Investigating The Thermal And Nonthermal Properties Of Galaxy Clusters With Radio Observations

A DISSERTATION
SUBMITTED TO THE FACULTY OF THE GRADUATE SCHOOL
OF THE UNIVERSITY OF MINNESOTA
BY

Damon Patrick Farnsworth

IN PARTIAL FULFILLMENT OF THE REQUIREMENTS
FOR THE DEGREE OF
Doctor of Philosophy

Dr. Lawrence Rudnick, Advisor

December, 2013

Acknowledgements

Most of the credit goes to my wife, Mary, for inspiring me and keeping me focused (whether or not I wanted to be), and to Elsa for giving me even more of a reason to graduate. My family has always been there for me − especially my dad, grandma, and grandpa − and I will always be grateful for their love and support.

I'd like to thank my advisor Lawrence Rudnick for his monumental contributions to my work over the years, and for always asking the question, "Yeah, but where's the science?" Thanks go to the members of my thesis committee − Terry Jones, Tom Jones, and Bob Lysak − and the faculty, staff, and graduate students in the School of Physics and Astronomy at the University of Minnesota. Special thanks to Steve for letting me keep his Socorro sketchbook.

I gratefully acknowledge assistance and comments from Rainer Beck, Michiel Brentjens, Rossella Cassano, Dominique Eckert, Peter Frick, Bryan Gaensler, Gabriele Giovannini, Thomas Jones, Leonia Kogan, Frazer Owen, Mariachiara Rossetti, Craig Sarazin, Dominick Schnitzeler, Dmitry Sokoloff, Rodion Stepanov, and Tiziana Venturi. Partial support for this work at the University of Minnesota was provided by the U.S. National Science Foundation through grants AST-09008668 and AST-1211595, and through award GSSP 09-0007 from the National Radio Astronomy Observatory (NRAO). The GBT and VLA are operated by NRAO, facilities of the National Science Foundation operated under cooperative agreement by Associated Universities, Inc. The Westerbork Synthesis Radio Telescope is operated by the ASTRON (Netherlands Institute for Radio Astronomy) with support from the Netherlands Foundation for Scientific Research (NWO). We acknowledge the use of NASA's *SkyView* facility[1] located at NASA Goddard Space Flight Center. This research has made use of the NASA/IPAC Extragalactic

[1] http://skyview.gsfc.nasa.gov

Database (NED) which is operated by the Jet Propulsion Laboratory, California Institute of Technology, under contract with the National Aeronautics and Space Administration. This research has made use of the VizieR catalogue access tool, CDS, Strasbourg, France. This research has made use of the X-Rays Clusters Database (BAX) which is operated by the Laboratoire d'Astrophysique de Tarbes-Toulouse (LATT), under contract with the Centre National d'Etudes Spatiales (CNES).

Dedication

For MSF, EMF, PNF, CLF, AMM, and BEM − thanks for believing in me.

Abstract

This thesis presents my recent investigations of the tenuous intracluster medium (ICM) in galaxy clusters using radio observations. The ICM is composed primarily of thermal and nonthermal plasma populations, permeated by magnetic fields which influence their evolution. Radio observations provide unique probes of the properties of the ICM, allowing for estimation of particle densities, magnetic field strengths, and even yielding clues to the physical mechanisms of particle acceleration. A major theme of this dissertation is that faint diffuse radio emission may contribute a significant amount of the synchrotron luminosity in galaxy clusters, yet goes unobserved due to an underappreciated deficiency of interferometric radio telescopes. Some of the current physical models do not account for this low surface brightness synchrotron emission, which may hold the key to distinguishing between competing models of relativistic particle acceleration and magnetic field amplification in these low density environments.

I first discuss the use of polarization observations to probe magnetized plasmas, exploring various methods of Faraday rotation measure determination. I demonstrate that methods such as traditional fitting of models to polarization angle only (without consideration of the fractional polarization) or the novel Rotation Measure Synthesis may yield erroneous results in the presence of complex Faraday structure. The best way to more accurately recover the true Faraday structure is by fitting models directly to the observables $Q(\lambda^2)$ and $U(\lambda^2)$, using radio polarization observations of the southern lobe of the radio galaxy 3C33 as an example.

Next I exhibit results from a 1.4 GHz GBT study of twelve merging galaxy clusters. After subtraction of confusion from Galactic foreground and extragalactic background radio sources, eleven of the twelve clusters exhibited a significant excess of diffuse emission over that found by previous interferometric studies. Faint large-scale radio emission in clusters may be commonly missed by interferometric studies, particularly at low redshifts, and this has serious implications for models of halo generation. I also provide supporting evidence for the notion that the total radio emission in clusters may not depend strongly on the particular structure (e.g., halo, relic). The energy for particle

acceleration is channeled from the merger and tied observationally to the thermal state of the ICM, and can result in a variety of radio structures.

I then present the results of snapshot VLA observations of the minor merging cluster A2142 at 1.4 GHz. New evidence of large scale ICM sloshing has been discovered in this cluster, further supported by an apparent 2 Mpc radio halo discovered as part of our recent GBT study. My VLA observations confirm the presence of a Mpc-scale halo in the sloshing core of A2142, which extends beyond the central cold fronts − a phenomenon unobserved in systems lacking major merging activity. This new halo appears to be comprised of multiple components, with a sharply peaked mini-halo type structure in the core, and a faint, extended giant radio halo type structure extending beyond the core region. The VLA observations do not recover the full halo extent observed by previous GBT observations, illustrating a weakness of interferometric cluster observations that may be underestimated in the literature. Preliminary spectral analysis finds a steep spectrum ($\alpha > 1.5$) to the core emission, possibly indicating a turbulent origin for the cosmic ray production in that region.

Finally, I discuss preliminary findings of a recent GBT study of nine clusters, chosen to span a wide range of dynamical activity. I found evidence for low surface brightness emission missed by interferometers in eight of the nine clusters, including two new radio structures. Additionally, I found more evidence that the total radio luminosity of clusters hosting diffuse emission follows the radio − X-ray correlation regardless of the structure of the radio emission (e.g., halo, relic, or combination).

Contents

List of Tables

List of Figures

Chapter 1

Introduction

The overall theme of this dissertation is the use of radio observations to investigate the physical properties of the thermal and nonthermal plasma in and around galaxy clusters. In this introduction I begin with a general discussion of cosmic large scale structure and general properties of galaxy clusters, including a summary on the dominant form of ordinary matter in clusters − a tenuous thermal plasma called the intracluster medium. Next I paint a picture of the nonthermal component of galaxy clusters, beginning with the physics of synchrotron radiation from diffuse relativistic plasmas, and then giving an overview of the various types of diffuse synchrotron structures in clusters − halos, relics, and mini-halos. Finally, I give a short description of each chapter inside this volume, and supply context within the framework of the dissertation.

1.1 Overview

The formation and evolution of large scale structure of the Universe is dominated by the flow of dark matter (DM), which collapses under gravity into a filamentary structure called the cosmic web. Ordinary (baryonic) matter moves in the gravitational potential of the dark matter distribution, onto and along the cosmic filaments. At the intersection of cosmic filaments − where the densest concentrations of dark matter exist − lie the largest virialized systems in the Universe, massive clusters of galaxies. Hosting hundreds to thousands of galaxies, most of the ordinary matter (i.e., baryonic) in clusters resides not in stars and galaxies, but in a diffuse, magnetized thermal plasma called the

intracluster medium (ICM).

There is also a nonthermal component of matter in clusters, relativistic particles called cosmic rays (CRs). Cosmic rays exist in the jets and lobes originating from active galaxies, but there is also a population of CRs permeating the ICM that is not associated with individual galaxies. During the process of cluster assembly, whereby smaller subclusters accrete along cosmic filaments onto clusters, shocks associated with the structure formation liberate gravitational energy to heat the gas, amplify magnetic fields, and accelerate particles to relativistic velocities. The cosmic ray electrons (CRe) are most strongly deflected by the magnetic field, and as they do so they emit synchrotron radiation observable at radio frequencies ($\lesssim$100 GHz). Diffuse radio synchrotron emission, on scales of 100s to 1000s of kpc, is observed in and around some clusters as structures called giant radio halos (GRHs), mini-halos (MHs), and relics. The relative locations, morphologies, and polarization properties of these structures suggest they are of different physical origins.

1.1.1 Galaxy Clusters - A Thermal Picture

Large scale structure in the Universe is believed to form by a hierarchical process of gravitational collapse and merging of dark matter. This is supported by weak lensing observations which have revealed the 3D structure of dark matter on scales exceeding tens of Mpc (e.g., Taylor et al. 2004; Massey et al. 2007). Baryonic matter then follows the gravitational potential of the dark matter, inside which groups or clusters of galaxies form and then merge via gravitational attraction to form ever growing structures. Numerical simulations (e.g., Cen & Ostriker 1999; Davé et al. 2001) predict that on the largest scales, matter in the nearby Universe exists in a filamentary structure called the Cosmic Web. At the intersection of cosmic filaments are galaxy clusters, formed through multiple merging events over cosmic time. Filamentary large scale structure is observed in the distribution of galaxies (e.g., Colless et al. 2001), but the diffuse gas which likely permeates the cosmic filaments eludes direct detection. The mergers which build up the clusters drive shock waves through the ICM, heating the gas and generating turbulence. At roughly $10^7 - 10^9$ K, the ICM is most easily observable by X-ray telescopes through its thermal bremsstrahlung emission. Signs of recent merging activity may be seen in X-rays, such as elongated or spiral gas morphology or sharp discontinuities in the X-ray

emission (marking shocks and cold fronts).

Eventually the major merging activity in a cluster may cease − although there is likely continued accretion at a lower rate onto all clusters − and the cluster will reach a "relaxed" state. This is usually observed by the presence of a cool, dense core in the X-ray gas, accompanied by a central dominant galaxy. In these central galaxies an active galactic nucleus (AGN) is usually present, from which relativistic jets inject energy into the surrounding "cool core" environment.

Magnetic fields are coupled to the thermal ICM, with typical strengths of roughly $0.1-1$ μG but exceeding 10 μG in the center of some cool core clusters (Govoni & Feretti 2004). Observed to be roughly dependent upon the thermal gas density, magnetic field strengths generally decline with increasing cluster radius. These fields are ordered on a wide range of scales, from a few kpc to hundreds of kpc. The origin of seed magnetic fields in clusters is still a mystery; they may stem from the early Universe, or perhaps have been injected into the ICM by galactic processes such as AGN jets and star formation. Over time these seed fields have been amplified by merging processes during cluster assembly. Magnetic fields in clusters provide a component of pressure to the ICM, and play a role in cluster dynamics and evolution. Their influence on cosmic rays provides a coupling between the thermal and nonthermal particle populations of the ICM, and hinders transport processes such as gas mixing, heat conduction, and CR propagation (e.g., ZuHone et al. 2013 and references therein).

1.1.2 Synchrotron Theory and Nonthermal Emission in Clusters

Synchrotron emission results from the motion of cosmic rays in a magnetic field, where the power radiated is a function of the particle energy, $E \propto \gamma$, where $\gamma = 1/\sqrt{1 - v^2/c^2}$ is the Lorentz factor, and the magnetic field strength, B. With typical cluster magnetic field strengths of 0.1-1 μG, most ICM synchrotron emission is from the CRe. For a homogeneous and isotropic ensemble of relativistic electrons with a power-law distribution of energies, $E(\gamma) \propto \gamma^{-\delta}$, the spectrum of the synchrotron emission is $f(\nu) \propto \nu^{-\alpha}$, with $\alpha = (\delta - 1)/2$. Typical astrophysical radio sources are observed to have a spectral slope of $\alpha \sim 0.7$. Synchrotron losses more strongly affect the particles of higher energy, resulting in a steepening of the synchrotron spectrum at high frequencies indicative of aging of the radio source. Because synchrotron emission is linearly polarized, properties

of the magnetic field such as strength and orientation may be estimated; we will discuss this topic in greater detail in Chapter 2.

Many galaxies are observed to emit radio synchrotron radiation, associated with physical phenomena such as star formation or AGN jets. Additionally, diffuse synchrotron emission − not associated with any galaxy − on scales of 100s to 1000s of kpc has been observed in roughly 80 clusters of various dynamical activity. The three main types of diffuse radio structures in clusters are halos, mini-halos, and peripheral relics, generally distinguished by their size, location, and polarization properties. We now summarize the current understanding of each of these types, with an emphasis on radio halos because they are most relevant to this dissertation. The reader is referred to Feretti et al. (2012) for a thorough review of diffuse radio emission in galaxy clusters.

Halos

Giant radio halos are diffuse synchrotron structures coincident with the cluster ICM, with typical sizes of ∼1 Mpc. Observed in about one-third of X-ray bright clusters (Ferrari et al. 2008) and typically regular in shape (i.e., roughly circular), halos are not observed to be polarized, although this may be due to observational effects such as projection (internal depolarization) or inadequate resolution (beam depolarization). Recent observations have discovered halos of smaller size or irregular/clumpy morphology, with similar properties as GRHs. Halos are found exclusively in merging clusters, which suggests that energy from mergers is somehow channeled into relativistic particles and magnetic fields. An observed correlation between the radio and X-ray luminosities of clusters hosting radio halos further supports the merger origin as well as a connection between the thermal and nonthermal properties of the ICM (e.g., Cassano et al. 2007). Halos possess relatively steep synchrotron spectra, with a median index of $\alpha \approx 1.2$.

The origin of the cosmic ray electrons in halos is currently a topic of debate, with the two leading theories being (1) turbulent reacceleration, and (2) secondary production from hadronic collisions (see Brunetti 2011 for a thorough discussion). In the turbulent reacceleration model, mildly relativistic electrons are reaccelerated by shock-induced magnetohydrodynamic (MHD) turbulence via the second-order Fermi acceleration mechanism. The seed population of low energy CRe is likely injected into the ICM

by AGN jets and perhaps, at a low level, by merger shocks (which are much more efficient at accelerating CRp than CRe). An alternative model postulates that cosmic ray protons collide with the thermal protons in the ICM, producing so-called "secondary" CRe and γ-rays as byproducts. While the production of secondary CRe through such hadronic collisions is almost certainly taking place in clusters, the relative contribution to the nonthermal ICM is suspect due to the lack of observational evidence such as predicted γ-ray emission. We note that γ-rays are also predicted by primary models of CR production (e.g., shocks), but at much lower levels than predicted by secondary models because they do not require the same number of CRp. Additionally, hadronic models of radio halo generation require magnetic field strengths and/or proton densities at cluster peripheries that are not supported by current observations.

Recent observations at sub-GHz frequencies with the GMRT have discovered a population of so-called ultra-steep spectrum radio halos (USSRHs), with spectral indices of $\alpha > 1.5$; only about five USSRHs are currently known (e.g., Feretti et al. 2012). Predicted by turbulent reacceleration models of halo generation, USSRHs may form in clusters undergoing less energetic mergers where high energy CRe are less efficiently produced − thus resulting in a deficiency of flux at high frequencies.

A current puzzle is the observed bimodal distribution of radio halos in merging clusters: either a halo exists with radio luminosity near that predicted by the empirical radio − X-ray correlation, or no radio halo is observed at all (e.g., Brunetti et al. 2009, Brown et al. 2011). Perhaps there is a minimum mass or X-ray temperature required for halo generation, or perhaps halos undergo an evolutionary cycle related to the merging activity whereby radio halos power up and then dissipate with the ICM turbulence (e.g., Donnert et al. 2013).

Mini-halos

Mini-halos are a class of diffuse radio structures that occur in cool-core clusters harboring a central dominant radio galaxy. Typically a few hundred kpc in extent, mini-halos also have steep synchrotron spectra. Recent observations (e.g., Mazzotta & Giacintucci (2008)) of mini-halos in clusters with sloshing ICM cores have found the MH emission to be bounded by X-ray cold fronts − sharp discontinuities in the X-ray emission interpreted as contact edges separating regions of gas with different entropies. Simulations

suggest that gas sloshing in cluster cores may generate sufficient turbulence to reaccelerate mildly relativistic electrons and amplify magnetic fields, powering the radio mini-halos (e.g., ZuHone et al. 2013).

Peripheral Relics

Observed at the periphery of roughly 40 clusters, radio relics are elongated structures up to and exceeding 1 Mpc in extent, typically with steep spectral indices ($\alpha \gtrsim 1$) and high degree of linear polarization ($\sim$25%). The peripheral location of these relics indicates the presence of μG magnetic fields and cosmic rays at cluster outskirts, with the current body of evidence (observational and theoretical) supporting a merger shock origin (e.g., Enßlin et al. 1998). In this scenario, large scale shocks associated with cluster mergers may re-accelerate mildly relativistic electrons or generate turbulence in the wake, which can also re-accelerate CRe. This is supported by observations, which show spectral steepening behind the leading edge of some relics − indicative of aging of the relativistic particles as the shock propagates outward (e.g., CIZAJ2242.8+5301; van Weeren et al. 2010).

1.2 The Chapters

The bulk of this dissertation is represented in the following four chapters. In Chapter 2 I present results of a polarization study of nearly 600 compact radio sources at 350 MHz with the Westerbork Synthesis Radio Telescope (WSRT). Therein I apply the principles of Faraday rotation to a subsample of polarized sources, and compare various techniques of rotation measure determination − a way to probe magnetized thermal plasma such as that which composes the ICM. Chapter 3 discusses the results from a study of low surface brightness radio emission in twelve X-ray bright clusters with the 100-m Green Bank Telescope. I compare the thermal properties (e.g., X-ray luminosity, dynamical state) of the observed clusters with their nonthermal properties (e.g., size and luminosity of diffuse radio structures) and comment on the role of faint, diffuse radio emission in systems without major merging activity. In Chapter 4 I present preliminary findings on VLA observations of the minor merging cluster Abell 2142, recently suggested to harbor sloshing of the thermal ICM on Mpc-scales. I searched for Mpc-scale radio emission in

A2142, and investigated the possibility that the large scale ICM sloshing may generate sufficient turbulence to amplify magnetic fields and accelerate cosmic rays on similar spatial scales − a previously unobserved phenomenon. Chapter 5 discusses preliminary findings on a recent GBT study of nine galaxy clusters chosen to span a wide range of dynamical activity. The broad goal of this ongoing project is to investigate low surface brightness radio emission in clusters, which may be commonly missed by interferometers for clusters at low redshift. I then investigate the relationship between the total thermal (X-ray) and nonthermal (radio) luminosities of galaxy clusters.

Chapter 2

Integrated Polarization of Sources at $\lambda \sim$1m and New Rotation Measure Ambiguities

A slightly modified version of this chapter appears in The Astronomical Journal: Farnsworth, D., Rudnick, L., & Brown, S. 2011, AJ, 141, 191.

2.1 Introduction

By characterizing the Faraday structure in radio synchrotron sources, properties of the magneto-ionic medium can be probed, such as magnetic field strength and orientation, as well as distribution of the relativistic and thermal electron populations. Radio arrays such as the Westerbork Synthesis Radio Telescope (WSRT), the Expanded Very Large Array (EVLA), the Low Frequency Array (LOFAR), the Australia Telescope Compact Array (ATCA), the Allen Telescope Array (ATA), and the planned Australian Square Kilometer Array Pathfinder (ASKAP) are well suited for Faraday structure studies due to their enhanced λ^2 sampling capabilities, e.g., wide relative bandwidth ($\Delta\lambda^2/\lambda^2_{min}$), and high spectral resolution ($\delta\lambda^2$).

We represent the complex linear polarization by

$$\mathbf{P} = Ipe^{2i\chi} = Q + iU \equiv I(q + iu) \tag{2.1}$$

where p and χ are the degree and angle of polarization, given by

$$p = \frac{P}{I} = \sqrt{q^2 + u^2} \tag{2.2}$$

$$\chi = \frac{1}{2} \arctan \frac{U}{Q} \tag{2.3}$$

and I, Q, U are the Stokes parameters for the total and orthogonal components of the linearly polarized intensities. We use q, u to represent the fractional values Q/I, U/I.

Traditionally, most polarization studies have determined rotation measures by fitting

$$\chi(\lambda^2) = \chi_0 + \lambda^2 \mathrm{RM}, \tag{2.4}$$

where RM is the Faraday rotation measure, with little or no attention paid to the behavior of the fractional polarization. A common practice has been to restrict RM fitting to regions of λ^2 space where $p(\lambda^2)$ is constant or decreases monotonically (e.g., Simard-Normandin et al. 1981), which would occur for a foreground rotating or depolarizing screen. This is sometimes done even when data showing a rise in $p(\lambda^2)$ at shorter wavelengths exists, ignoring evidence that multiple RM components may be present. Others restrict their fitting to $\lambda < \lambda_{1/2}$ (defined by $p(\lambda_{1/2})/p(0) = 0.5$), beyond which Burn (1966) suggests that significant non-linear behavior in $\chi(\lambda^2)$ is expected (e.g., Haves 1975). In other cases, significant non-linear behavior in $\chi(\lambda^2)$ is observed (e.g., Morris & Berge 1964, Roy et al. 2005), but no modeling of this anomalous behavior is made and the RM from the poor linear fit to $\chi(\lambda^2)$ is reported. Others require that p is above some threshold and/or that a minimum signal-to-noise value is present in the observations but do not report the behavior of $p(\lambda^2)$, which may hold information regarding the underlying Faraday structure (e.g., Clarke et al. 2001, Brown et al. 2007).

The only situation where $\mathrm{d}\chi/\mathrm{d}\lambda^2$ and $p(\lambda^2)$ are constant, and therefore unimportant in determining the Faraday structure, is when there is a single uniform Faraday screen completely in the foreground. In all other cases, including all or most physically realistic ones, more sophisticated modeling is required. For example, Fletcher et al. (2004) consider both polarization degree and angle in their study of the magnetic field of M31. In addition, Rossetti et al. (2008) and Fanti et al. (2004) employed simple models of

depolarization and χ rotation to examine Compact Steep-Spectrum (CSS) sources at $\lambda \leq 21$ cm. We will briefly summarize some of the classic models where $p(\lambda^2) \neq$ constant. For a detailed discussion on depolarization effects, we refer the reader to Sokoloff et al. (1998).

If the thermal electrons are spatially coincident with the relativistic, synchrotron emitting electrons, e.g., then

$$p(\lambda^2) \propto \frac{\sin(\lambda^2 \mathrm{F_c})}{\lambda^2 \mathrm{F_c}}. \tag{2.5}$$

as in the uniform slab model of Gardner & Whiteoak (1966), where $\mathrm{F_c}$ is the Faraday depth through the slab; $\mathrm{F_c}$ can be thought of as an "internal" RM. Cioffi & Jones (1980) showed that the observed depolarization and χ rotation can have considerable differences depending on the geometry assumed, even for simple cases such as cylinders and spheres.

For a foreground screen consisting of many unresolved components with a random distribution of RMs, Burn (1966) modeled the observed fractional polarization as

$$p(\lambda^2) \propto \exp(-2\sigma_{RM}^2 \lambda^4) \tag{2.6}$$

where σ_{RM}^2 is the variance of a Gaussian dispersion in RM across this so-called "mottled" screen. Modifications to this model have been proposed, e.g., by Rossetti et al. (2008) who include the effect of filling factors.

Two interfering foreground RM components will also produce non-λ^2 behavior in angle, and changes in fractional polarization that can rise or fall with increasing wavelength. Goldstein & Reed (1984) describe the observed polarized flux from two such components as:

$$P_{obs} = P_1[1 + k^2 + 2k\cos(\chi_1 - \chi_2)]^{1/2} \tag{2.7}$$

where $k = P_2/P_1 \leq 1$ is the ratio of the the polarized fluxes, χ_1 and χ_2 are the polarization angles at the observation frequency.

With adequately sampled data in λ^2 space, all of the above cases can, in principle, be distinguished. In practice, however, λ^2 sampling is inadequate to map out the Faraday structure, and even the large fractional bandwidths of the WSRT or the EVLA can be insufficient. As we will illustrate below, determination of the Faraday structure requires

observations which detect the *variations* in both $p(\lambda^2)$ and $\mathrm{d}\chi/\mathrm{d}\lambda^2$. In particular, the result $\mathrm{d}\chi/\mathrm{d}\lambda^2 \approx$ constant can occur over a substantial range in λ^2 even with underlying Faraday structure. Whether or not failure to diagnose the presence of underlying Faraday structure is acceptable depends on the particular scientific goals, as we discuss further below.

In Section 2.2 we present our WSRT observations at 350 MHz and the determination and removal of the off-axis instrumental polarization. We present the results of our polarization and Faraday structure analyses in Section 2.3. There we characterize the depolarization of our sample of 585 compact sources and give a brief overview of the polarization diagnostics and Faraday structure modeling employed. We then detail the modeling results on seven sources with significant 350 MHz polarization and the discrepancies between fitting $q(\lambda^2)$ and $u(\lambda^2)$ and other other techniques. In Section 2.4 we use the results of some simple experiments to demonstrate some of the inadequacies of common RM determination methods such as $\chi(\lambda^2)$ fitting and RM Synthesis. We also offer some recommendations for reliable RM determinations. A discussion of our findings, including the science implications of RM ambiguities, is presented in Section 2.5.

2.2 Westerbork 350 MHz Observations and Instrumental Polarization

2.2.1 Observations and Data Reduction

We observed six fields with the WSRT in 2008 and 2009, originally selected for possible large-scale diffuse polarization found in the NRAO Very Large Array Sky Survey (NVSS, Condon et al. 1998) through a reprocessing by Rudnick & Brown (2009). To minimize the contribution of polarized Galactic foreground emission, we have selected fields with $|b| \gtrsim 42°$. Observations were made in spectral line mode with a central frequency of 345 MHz, 70 MHz bandwidth, and 1024 channels over 8 intermediate frequency (IF) sub-bands, yielding full Stokes parameters. Even though the central frequency is 345 MHz, we will continue to refer to this band as the 350 MHz band to comply with the established convention. Various array configurations were used and are shown in Table

2.1. The nominal synthesized beam size varies with array configuration and observing frequency, but is approximately $70''$ in RA for our observations. Due to the East-West array configuration, the beam becomes elongated in the North-South direction by a factor of $\csc(\delta)$.

We will now summarize the key elements of the data reduction and calibration process; for a complete description we refer the reader to Brown & Rudnick (2009). All reduction was done using standard techniques in AIPS, correctly accounting for the WSRT linearly polarized feeds, and including several iterations of amplitude and phase self calibration for total intensity. Flux calibrators were observed, and are listed in Table 2.1. The AIPS procedure LPCAL was used to correct for polarization leakage between the X and Y orthogonal linear polarization receivers. Additionally, calculation of a time-independent phase correction between linear polarizations X and Y was attempted for each channel using a polarized calibrator observed during the run. The polarized calibrator 3C345 was used for all fields except Field B, for which DA240 was used instead. Unfortunately, a solution was not found for every channel, rendering those channels without a solution useless for Stokes U measurement.

Cleaning and imaging were also done in AIPS, where 4°x4° images in Stokes I, Q, and U were created for each channel. The community is just beginning to experiment with the much simpler problem of multifrequency synthesis/cleaning in total intensity, where one or two spectral parameters can be used to characterize the frequency dependence, and the biases there have not yet been characterized. Q and U have much more complex behavior as a function of frequency and will require extensive experimentation in the future. Therefore, each channel and Stokes quantity was cleaned separately in AIPS with IMAGR using a loop gain of 0.1 and 15,000 clean components per field. Images of Stokes V (circular polarization) were made to verify that no leakage into V was present, under the assumption that it is negligible for typical astrophysical sources. Typical channel sky RMS values of ∼3-5 mJy/beam were obtained in the cleaned I images, and ∼1-3 mJy/beam for the Q, U images. All images for a field with sky RMS ≤ 5 mJy/beam (uncorrected for primary beam attenuation) were convolved to a common beamsize, allowing channel averaging to be performed as described below.

Average images of Stokes I, Q, and U for each of the eight IFs were constructed from the individual channel images, along with a total intensity map averaged over all

eight IFs. The number of channels used for each band average image is listed in Table 2.2. Channels with imaging problems, such as strong artifacts due to radio frequency interference (RFI), were excluded. In addition, U imaging was not performed on channels where no X-Y phase correction was found. We supplemented these data using images from the NVSS to provide measurements of Stokes I, Q, U at 1.4 GHz. The NVSS images were convolved to the corresponding WSRT field's beamsize. See Table 2.1 for an overview of the field properties, including common beam convolution sizes. The Coma fields were imaged using a (somewhat smaller than nominal) restoring beam of $70''$x$70''$ as part of another study (Brown & Rudnick, 2011).

Total intensity images of the six fields are shown in Figure 2.1. Images of the linear polarization at RM=0, taken from the results of RM Synthesis (see Section 2.3.2), are shown in Figure 2.2. Note that the polarization maps at RM=0 are pervaded by diffuse Galactic emission (e.g., Brentjens & de Bruyn 2005, Schnitzeler et al. 2009, Wolleben et al. 2010, Bernardi et al. 2010).

2.2.2 Instrumental Polarization of WSRT at 350 MHz

To identify sources with either real or instrumental polarization, we first selected sources in each field with $I/\sigma_I \geq 30$ in the all-IF Stokes I image, yielding 585 total sources for the six fields. We then extracted Stokes I, Q, U from each of the WSRT individual IF and NVSS images, at the peak location in the all-IF Stokes I image. A background subtraction was performed for each measurement using a rectangular region about the source, of inner dimension $1\times$ the synthesized beam dimensions and outer dimension $2\times$ the synthesized beam dimensions. The RMS deviation within each annulus was adopted as the statistical error in each measurement.

For the purpose of illustrating the instrumental polarization, we apply the simplest bias correction to the polarization amplitude:

$$P_{corr} = \sqrt{P_{meas}^2 - \sigma_P^2}, \tag{2.8}$$

which is an approximation to the "most probable estimator" of Wardle & Kronberg (1974), good for $P_{corr}/\sigma_P > 0.5$. This most probable estimator is the best available for $P_{corr}/\sigma_P > 0.7$ (Simmons & Stewart 1985), and we only report results well above this

limit. We use a propagated error calculation for σ_P based on the observed errors in Q and U.

Figure 2.3 shows $p_{corr} \equiv P_{corr}/I$, averaged over multiple IFs, vs. off-axis radius for the WSRT data set, illustrating the instrumental enhancement of fractional polarization with radius as mentioned previously by de Bruyn & Brentjens (2005) and investigated at 1.4 GHz by Popping & Braun (2008). In this work, we determined the instrumental polarization behavior in both Q and U for each IF in order to perform a first order correction. For each IF, we first selected from the 585 initial sources those satisfying $P_{meas}/\sigma_P \geq 2$ and plot q and u as a function of their locations relative to the pointing center (Figure 2.4). In several IFs there is a clear quadrupole pattern, in general possessing a greater magnitude in q than u. The observed q quadrupole pattern is oriented coincident with the orientation of the X and Y linear dipole feeds on the WSRT, which face the sky perpendicular to each other and form Stokes Q by the linear combination of XX^* and YY^*. The observed u quadrupole pattern, which is formed from a linear combination of XY^* and YX^*, is offset 45° on the sky with respect to the q pattern, as one would expect.

To quantitatively model the instrumental polarization for each IF, we made the following cuts to the data. Outside $4500''$ the instrumental polarization rises sharply and we do not attempt any correction beyond that limit, cutting the total number of sources from 585 to 335[1] . We then required $P_{meas}/\sigma_P \geq 2$, yielding roughly 100 sources per IF. For each IF we fit a double cosine function to each set of q and u of the form

$$f(r, PA) = Ae^{Br}cos(2PA + C), \tag{2.9}$$

which includes the distance from the pointing center, r, and position angle, PA, of the source. This yielded 16 total sets of parameters, which are given in Table 2.3. We then produced corrected Q, U observations for each source by subtracting the modeled instrumental contribution.

The instrumental polarization is weak near the pointing axis, generally much less than 1%, but grows to as much as 6% in q near R_{pb} (half power radius of the primary beam) for the odd numbered IFs. In u the instrumental contribution is <3% at R_{pb} for

[1] This includes 36 duplicated sources observed at different off-axis positions due to the multiple pointings for the Coma field.

all IFs.

By examining Figure 2.5, one can see evidence of the 17 MHz modulation, as found by Popping & Braun (2008), in the q models for IFs 1, 3, 5, and 7, which are separated by ≈17 MHz. In these IFs, the instrumental polarization is stronger by factor of roughly 2-3 at R_{pb} over the neighboring even numbered IFs. This effect is much less pronounced in u, as seen in Figure 2.5.

After correction for instrumental polarization, there is still a significant polarized flux bias from a variety of factors which differ from one IF to another, including the noise bias (including random noise and residual sidelobe structures) and non-quadrupole components to the instrumental polarization as a function of IF and two-dimensional location within the primary beam. These are not well modeled by Equation 2.8, so in order to make a practical model for the polarized flux bias we took an empirical approach and measured the median (p_{med350}) and RMS scatter ($p_{scatter350}$) among the 350 MHz IFs of the polarized fraction for each of 335 sources with $r < 4500''$. We expect that residual instrumental polarizations, sidelobe structures, and noise will all vary from IF to IF, and that $p_{scatter350}$ will therefore provide an estimate of all of these contributions. On the other hand, p_{med350} provides an estimate of the true polarized flux, along with a bias related to $p_{scatter350}$. These are plotted vs. each other in Figure 2.6. Different symbols represent different levels of NVSS polarized flux for the same sources.

There was no significant difference in the distribution as a whole between sources with no NVSS polarization and sources with moderate or strong NVSS polarization. Therefore, the bulk of p_{med350} values are likely due to the instrumental contributions described above, as opposed to intrinsic polarizations. We fit the distribution and found

$$p_{med350} = \sqrt{(1.57 \times p_{scatter350})^2 + (0.006)^2} \tag{2.10}$$

We then adopted this calculated value as the effective polarization bias to be subtracted in quadrature from each of the measurements when doing statistical analyses. If a source had an intrinsic polarization equal to $1.5 \times p_{scatter350}$ which would add in quadrature to the calculated value of p_{med350}, then the source would be found on average at the dotted line in Figure 2.6. Only three sources out of 335 exceed this value (and at least two do

have well-behaved polarization behaviors), so we adopt this as our upper limit for the purposes of calculating depolarization ratios.

We note that changes to the empirical fit in Equation 2.10 will have a small effect on the statistical analyses in which it is employed. For example, if the fit value of p_{med350} is overestimated the above procedure may eliminate some sources that have significant real structure in $p(\lambda^2)$. However, the number of such sources is small, as discussed further below, so we ignore that issue in order to examine the depolarization properties of the sample as a whole in the following section. Since the residual bias correction from Equation 2.10 is not applied in the individual source modeling described in Section 2.3.2, it has no effect on the outcome of those analyses.

2.3 Results

2.3.1 Polarization Properties of the Overall Sample

Starting with the sample of 335 sources discussed above, we determined their polarized fluxes in the 1.4 GHz NVSS survey. We first convolved the NVSS I, Q and U images to the same beamsize as used in each corresponding WSRT field, then measured the I, Q and U fluxes at the locations of each total intensity peak in I at 350 MHz. Background subtraction and error estimation were performed using the same rectangular region about the source as described previously for our WSRT measurements. We then calculated the polarized flux (and fractional polarization) after correcting for the noise bias, according to Equation 2.8. After correction, we found that 102 of the 335 sources had significant polarizations at 1.4 GHz ($P_{corr1.4}/\sigma_{P1.4} > 2$), and for each we calculated the upper limit to their polarized fractions at 350 MHz. These are plotted in Figure 2.7.

The upper limits on the 350 MHz polarized fractions are largely independent of the fractional polarizations at 1.4 GHz. There is a rough upper limit to the distribution visible in Figure 2.7 likely due to the fact that at low fluxes, only large values of $p_{1.4}$ can be detected, and the upper limits on p_{350} will therefore also be high. Lines of unity slope on this diagram indicate specific depolarization ratios ($p_{350}/p_{1.4}$). Upper limits to the depolarization ratios vary from <0.03 to <2, with a median of <0.3 .

In Figure 2.8 we plot the median upper limit to the depolarization ratio as a function

of $p_{1.4}$. The decreasing values indicate the observational bias that we can only measure low depolarization upper limits for the highest values of $p_{1.4}$. The median upper limit for the 20 highest $p_{1.4}$ sources is $\sim$0.2.

2.3.2 Model Fitting of Individual Sources

Source Selection

From the set of 335 sources (with $r < 4500''$ and $I/\sigma_I > 30$ at 350 MHz, and disregarding $p_{1.4}$), we identified a subset based on their Faraday Dispersion Function (FDF) using the RM Synthesis technique (Brentjens & de Bruyn, 2005). This allows for the best signal to noise averaging of all the data, since $Q(\lambda^2)$ and $U(\lambda^2)$ can be summed as vectors after correcting for each assumed RM.

The observed FDF, $\tilde{F}(\phi)$, is constructed (using the formalism of Brentjens & de Bruyn 2005) thusly:

$$\tilde{F}(\phi) = F(\phi) * R(\phi) = K \sum_i^N w_i P_i e^{-2i\phi(\lambda^2 - \lambda_0^2)} \quad (2.11)$$

$$R(\phi) = K \sum_i^N w_i e^{-2i\phi(\lambda^2 - \lambda_0^2)} \quad (2.12)$$

$$K = \left(\sum_i^N w_i \right)^{-1} \quad (2.13)$$

at an arbitrary Faraday depth, ϕ, which replaces the usual rotation measure; in practice one chooses a range of Faraday depths to reconstruct a Faraday spectrum. The quantities P_i and w_i are the observed vector polarization and applied weight, respectively, at locations of sampled λ^2. The quantity λ_0^2 is the mean λ^2 of the set of observations, and the reconstructed FDF is represented at $\lambda^2 = \lambda_0^2$. Note that the actual $F(\phi)$ is obtained by deconvolving the Rotation Measure Spread Function (RMSF, $R(\phi)$), which is the normalized response function in Faraday space, from the observed $\tilde{F}(\phi)$. We briefly discuss the deconvolution procedure, RM Clean, in Section 2.3.2. Unless otherwise noted, all FDFs and RMSFs in this study were constructed using uniform weighting. For this paper we use an over-tilde to represent transformed polarization quantities unless otherwise noted, e.g., $\tilde{P}$ represents the magnitude of the FDF, $\tilde{Q}$ represents the real part

of the FDF, and so on.

We used all channels where sky noise in Stokes Q and U were $\leq$ 5 mJy/beam (uncorrected for primary beam attenuation), with the number of channels listed in Table 2.2. A typical RMSF for the WSRT 350 MHz band is shown in Figure 2.9; this RMSF was constructed using roughly 400 channels across the full band. The main lobe of each RMSF had a characteristic FWHM $\sim$12 rad/m^2. Nominal RM Synthesis capabilities of the WSRT 350 MHz band are given in Table 2.4. We note that no instrumental polarization correction has been applied to the data used to construct these FDFs, since the corrections were determined only when the channels were averaged within each IF band.

A coarse initial search over Faraday depths between $\pm$1000 rad/m^2 was performed at a resolution of 10 rad/m^2. Once we had determined that no significant power existed outside a Faraday depth of $\pm$200 rad/m^2, we performed a finer search between $\pm$200 rad/m^2 with a resolution of 1 rad/m^2.

To make an initial cut to the set of sources, the location (ϕ_{max}) and amplitude ($\tilde{P}_{max}$) of the peak in $\tilde{P}(\phi)$ were determined for each source, and those with a peak amplitude of $\tilde{P}_{max} \geq 3$ mJy/beam/RMSF (uncorrected for primary beam attenuation) were selected. In all, 116 of the original 335 sources passed this criterion, with a minimum signal to noise in $\tilde{P}_{max}$ of 3.4. This removed many sources from the sample whose observed polarization may be enhanced artificially, e.g., by noise, which places power at all Faraday depths in the FDF. We note that many of these remaining detections are due to instrumental polarization which is not corrected in the all-channel FDF.

For each of these 116 sources, we then examined the IF averaged Q and U measurements, corrected for instrumental polarization. Because sources could have different fractional polarizations for different IFs, we did not demand that they have strong signals in all IFs. Sources with at least four of the eight IFs satisfying $P/\sigma_P \geq 2$, and $U/\sigma_U \geq 4$ were then selected from the list of 116. We used only the U data for this cut because of the greater uncertainty in the instrumental correction for Q and the presence of occasional spuriously high Q values. Sources which exhibited a regular modulation in $p(\lambda^2)$ corresponding to to the $\sim$17 MHz modulation found by Popping & Braun (2008) were excluded. All such sources were found beyond $R \sim 4000''$, evidence of residual instrumental polarization not fully accounted for by our model. Only three sources met

all of these criteria. To those, we added four additional sources for modeling based on their high ratios of $p_{med350}/p_{scatter350}$, putting them at or above the upper limit line shown in Figure 2.6. These seven sources selected for modeling are listed in Table 2.5 along with selected properties from the literature. Plots of $q(\lambda^2)$ and $u(\lambda^2)$ are shown in Figure 2.10.

A Note on Bandwidth Depolarization

The NVSS data at 1.4 GHz were constructed from two 42 MHz wide bands, centered at 1364.9 MHz and 1435.1 MHz. Bandwidth depolarization for sources with $|\mathrm{RM}| \lesssim 50$ rad/m^2 would yield $(p_0 - p)/p_0 \lesssim 2\%$ in the NVSS (Condon et al., 1998). Any source with |RM| high enough to suffer significant bandwidth depolarization in the NVSS would be severely depolarized in the IF averaged 350 MHz data, and would not have been selected for further investigation.

Modeling Techniques

As can be seen in Figure 2.10 the sources found to have sufficient polarization for modeling all showed structure in $q(\lambda^2)$ and $u(\lambda^2)$ inconsistent with a simple Faraday screen. A simple screen would result in sine and cosine waves in q and u with matched frequencies and amplitudes. In order to measure the Faraday structure of these sources, we therefore explored a variety of techniques. In particular, we used: A. Linear fit to $\chi(\lambda^2)$; B. RM Synthesis/Clean; C. Model fitting to q, u vs. λ^2 using a two component foreground screen; and D. Model fitting using a single foreground screen with a mean RM and a separate depolarizing function. We have omitted an internal Faraday dispersion model for the following reason: internal depolarization in the Milky Way and nearby galaxies arises because the synchrotron and thermal plasmas are well mixed (Sokoloff et al., 1998). This is not true for extragalactic sources, where the depolarization almost always arises with Faraday variations across the beam (e.g., Tribble 1991 and references therein). We now briefly discuss each of the models employed followed by the results.

A. $\chi(\lambda^2)$. We determined the RM for each source using the most common method, minimizing the sum of the weighted residuals (i.e. chi-squared statistic, χ^2) from fitting Equation 2.4 to the observed polarization angles $\chi(\lambda^2)$. There were often a number of different solutions with comparable values of χ^2_{min} based on our choices for the nπ

ambiguities. We therefore made these choices to most closely match the results for the RM for the foreground depolarizing screen model described below. We calculated the errors in RM by the standard propagation of errors from the residuals to the fit, not from the errors in the original data points. Note that the reduced χ^2 values, $\chi^2_\nu \equiv \chi^2/dof$ (where dof = degrees of freedom), as listed in Tables 2.6 - 2.12 are generally quite high, suggesting that these are not good fits, despite the apparently small derived errors in RM.

B. RM Synthesis/Clean. For each of the seven sources the FDF was constructed using the q,u data, this time using the instrumental polarization corrected IF samples from the WSRT observations plus the NVSS data point. Uniform weighting for all λ^2 samples was applied; we experimented with various weighting of the WSRT and NVSS samples used as input for RM Synthesis, but found negligible differences in the RM Clean solutions. A representative RMSF is shown in Figure 2.11, displaying the sidelobe structure due to the sparse λ^2 sampling. The range of Faraday depth for the constructed FDF was this time limited to ± 50 rad/m^2, reflecting the maximum RM due to the λ^2 separation of the IF averaged samples. The full-channel FDFs were first searched for significant power beyond ± 50 rad/m^2 to ensure that this range of Faraday depths was large enough. Our custom version of RM Clean (Brentjens & de Bruyn 2005, Heald et al. 2009) was used to deconvolve the complex RMSF from the FDF, drastically reducing sidelobes and producing a more lucid representation of the Faraday structure. We used a gain factor of 0.1 and stopping criteria of either 200 iterations or a peak to RMS ratio of 1.5 in the residuals of $\tilde{p}$. These convergence criteria were found to strike the optimal balance between minimizing the residuals and limiting spurious clean components.

The location (RM) and amplitude ($\tilde{p}_0$) of the two most dominant features in each cleaned FDF were extracted by Gaussian fitting to the cleaned Faraday spectrum. To reduce polarization bias, which would enhance the amplitude of $\tilde{p}_0$ solutions, we subtracted the mean of the residuals in $\tilde{p}$ before performing the Gaussian fitting. As determined in some of our experiments, and also noted by Frick et al. (2010), the method of RM Synthesis/Clean has difficulty reproducing the correct phase information in the presence of multiple RM components. For this reason, we have neglected χ in the solutions by fitting to $\tilde{p}$ only. To exclude possible residual instrumental RM, which manifest near

± 42 rad/m^2 due to the 17 MHz modulation investigated by Popping & Braun (2008), we searched for components in the range |RM| < 40 rad/m^2. The RM Synthesis/Clean solutions for each source are summarized in Tables 2.6 - 2.12.

C. 2 component models for $q(\lambda^2)$, $u(\lambda^2)$. This fit involves six parameters, with the amplitude of the fractional polarization, p_0, intrinsic polarization angle, χ_0, and RM to be determined for each of two components. Because we expected (and sometimes found) multiple minima in χ^2 in this six dimensional space, we minimized χ^2 through a direct search of parameter space. The explored ranges were tailored somewhat to the individual sources, but typical values were polarized fraction (0, 0.1), RM (-25, 25) rad/m^2, and χ_0 (0, 180) degrees. The values presented in Tables 2.6 - 2.12 represent the minimum of χ^2 over these ranges. Note that there are no nπ ambiguities when fits are done in q,u space. A slice through this χ^2 surface for the two RM parameters for 3C33S is shown as an example in Figure 2.12. Each value in this space represents the minimum value of χ^2 for fixed values of the two RMs, with all other parameters allowed to float.

The errors in RM were calculated by normalizing χ^2_{min}, defining $\tilde{\chi}^2_{min} \equiv dof$. We then found the range of each of the two RMs for which the value of the normalized $\tilde{\chi}^2 \leq (dof + 1)$, allowing the other five parameters to float. In a number of cases, there were additional minima within the $\tilde{\chi}^2 < (dof + 1)$ range, so no errors are quoted and these RM values are shown in brackets. This procedure, of determining errors by adding 1 to the χ^2_{min} has a long history in the astrophysical literature (e.g., Avni 1976, Wall 1996), but has very serious problems as discussed below. The probability contour levels in Figure 2.12 were assigned using the χ^2 distribution for one degree of freedom (Lampton et al., 1976) as is appropriate when assigning errors to each individual RM, and allowing the other RM and all other parameters to float.

D. Foreground rotation and depolarizing screen models for $q(\lambda^2)$, $u(\lambda^2)$. We followed a procedure similar to that of the two component model, finding the minimum χ^2 for the three parameter function

$$\begin{aligned} \mathbf{p}(\lambda^2) &= q(\lambda^2) + iu(\lambda^2) \\ &= p_0 \exp(-2\sigma^2_{RM}\lambda^4) \exp[2i(\chi_0 + \lambda^2 \mathrm{RM})] \end{aligned} \tag{2.14}$$

similar to that described by Burn (1966). Errors in RM were determined in the same way as the two component model.

We quote errors on RM using methods similar to those in the literature, so that our uncertainties can be compared to them. However, it is very rare in the literature to find χ^2 values quoted for the fits, and therefore difficult to evaluate whether the models used are appropriate or not. As we will show below, it is possible to get quite robust $\chi(\lambda^2) \propto \lambda^2$ behavior given an apparent RM quite different from the actual RMs for two component models. *Therefore, RM determinations using only $\chi(\lambda^2)$ and ignoring the fractional polarization behavior can provide no guidance regarding the appropriateness of the fit.*

The χ^2_ν values in Tables 2.6 - 2.12 are often much greater than unity, showing that these models are not an adequate representation of the data. In that case, the meaning of our errors is unclear. Our normalization of $\tilde{\chi}^2_{min} \equiv dof$ produces much more conservative errors than simply adding 1 to χ^2_{min}. However, as pointed out by Lampton et al. (1976), this method produces the equivalent of a ratio of variances distribution, which has a very different probability distribution than χ^2 itself. In particular, they say *"We stress again that if ($\chi^2_{min} >> dof$),* no *formalism which uses distributions describing random fluctuations can provide the proper error estimator."* Given this, our errors must be accepted only in the sense of providing comparisons to the literature, and our recommendations for future work are described in Section 2.4.3.

Model Results and Comparisons

The results of the various RM determinations for each source are shown in Tables 2.6 - 2.12 and in Figures 2.13 - 2.19. Oscillation visible in the restored $\tilde{p}(\phi)$ profile (e.g., Figure 2.18) arises from the sinusoidal residuals in $\tilde{q}(\phi)$ and $\tilde{u}(\phi)$, which are added to the clean components, and provides a measure of the noise level in $\tilde{p}(\phi)$. In our tests, more aggressive cleaning reduced the oscillation in $\tilde{p}$ by placing power in the clean components randomly across ϕ (thus reducing the residuals and producing nicer plots), but did not significantly change the amplitudes or Faraday depths of the major RM components as reported for each source. If we look at the RM of the strongest component, we find that different models yield consistent results for some but not all sources. We give a brief discussion of the modeling results for each source here, and a more extensive

discussion of 3C33S in the following subsection. One goal of this investigation is to explore the effect that ignoring the effects of depolarization, including the presence of multiple strong RM components, may have on the findings of the traditional linear $\chi(\lambda^2)$ method. We compare our findings with those of Taylor et al. (2009) for sources where RMs were reported in their study. Where appropriate, we use data from the VLA FIRST (Faint Images of the Radio Sky at Twenty centimeters; Becker et al. 1995) survey to supplement our analysis.

NVSS J010616+125116. This source is resolved as a double source (separation $\sim$60″) in the original NVSS image, but appears as a single source when convolved to the WSRT field resolution (325″x70″). We adopt the name of the brighter NVSS source (peak $I_{1.4}$=102 mJy/beam); the secondary source is NVSS J010615+124210 (peak $I_{1.4}$=72 mJy/beam); the two sources have similar $p_{1.4}$. The dominant RM is found near -9 rad/m^2 for the linear $\chi(\lambda^2)$, depolarizing screen, and RM Synth/Clean methods. The two component model, however, finds the dominant RM component near -5 rad/m^2. It is possible that the relatively strong secondary RM component found near +2 rad/m^2 in the two component fit has drawn the other solutions away from the true intrinsic Faraday structure. The presence of multiple minima in the χ^2 surface, however, casts uncertainty on the two component result. For comparison, Taylor et al. (2009) determined the RM of NVSS J010616+125116 to be -16.8 ± 14.7 rad/m^2; no RM was reported for NVSS J010615+124210.

3C33S. This source is also known as NVSS J010850+131831. The dominant RM found by the linear $\chi(\lambda^2)$, depolarizing screen, and RM Synth/Clean methods are near -7 rad/m^2. This is in disagreement with the two component modeling, which finds no significant component near -7 rad/m^2; rather, the dominant component is found near -3 rad/m^2 with a relatively strong second component near 0 rad/m^2. For comparison, Taylor et al. (2009) determined the RM to be 3.4 ± 1.9 rad/m^2. In addition, Law et al. (2011) performed RM Synthesis on 3C33S using two bands, each 100 MHz wide, centered at 1.43 and 2.01 GHz with the ATA. After cleaning they found a single RM at -12.3 ± 0.4 rad/m^2. That they found a single RM is not unexpected, considering the FWHM of their RMSF of 141 rad/m^2, but the RM value found would not fit our 350 MHz observations. Given the high signal to noise in our Q, U data, this is the strongest case yet for interference between two strong RM components causing other methods

to misinterpret the true Faraday structure. In the next section, we will use idealized models to demonstrate how this comes about.

NVSS J011136+132437. The dominant RM component is found near -11 rad/m^2 for the linear $\chi(\lambda^2)$ and depolarizing screen models. The two component method finds equal amplitudes for both RM components, with one near -11 rad/m^2 and the other near -24 rad/m^2. It doesn't appear that a secondary component has affected the outcome of the single component methods. RM Synth/Clean nearly agrees, finding the dominant RM component at -13 rad/m^2. The secondary RM component found by RM Synth/-Clean and the two component model are in disagreement, however, in both location and relative amplitude. All methods have a high χ^2_ν, suggesting that no solution is to be trusted. For comparison, Taylor et al. (2009) determined the RM to be -13.8 ± 3.3 rad/m^2, in agreement with our findings.

NVSS J011204+124118. The dominant RM is found near +20 rad/m^2 for the linear $\chi(\lambda^2)$, depolarizing screen, and two component models. The two component fit finds a secondary component with $p_{02}/p_{01} > 0.5$ near -2 rad/m^2, but it doesn't appear to have affected the outcome of the single RM methods. RM Clean finds the dominant RM component near -33 rad/m^2, but three other peaks of significant amplitude are found in the Faraday spectrum, including relatively strong components near +34 and +17 rad/m^2. Taylor et al. (2009) do not report a RM for this source.

NVSS J125630+270108. All four methods find the dominant RM component to lie near +4.5 rad/m^2. Secondary components for RM Synthesis and the two component method are of relatively weak amplitude, and likely do not contribute significantly to the solutions found by the single RM methods. Due to the lack of depolarization from 1.4 GHz to 350 MHz, it is not surprising that the traditional linear fit to $\chi(\lambda^2)$ is in agreement with the other methods. Taylor et al. (2009) do not report a RM for this particular source (unresolved in both NVSS and FIRST), but using their data we determined the weighted mean RM of the 17 sources within 2° (with an entry in Taylor et al. 2009) to be $\approx 2.5 \pm 1$ rad/m^2. This suggests that a Galactic foreground (rotating) screen is the single dominant component of Faraday structure for this source, a situation which is unique in our modeling results.

NVSS J162408+605400. The dominant RM component is found to lie near -17 rad/m^2 for the linear $\chi(\lambda^2)$ and depolarizing screen models, while RM Synth/Clean

finds the dominant component near -15 rad/m^2. The two component model shows two equal amplitude RM components near -17 rad/m^2 and -18 rad/m^2. The presence of multiple minima in the χ^2 surface casts uncertainty on the two component solution. Taylor et al. (2009) do not report a RM for this source. The oscillation visible in the cleaned FDF shown in Figure 2.18 is due to the low amplitude of the clean components relative to the amplitude of the residuals in RM Clean. As mentioned in the beginning of this section, cleaning further would reduce the level of apparent oscillation in the cleaned FDF, but would not appreciably change the locations or amplitudes of the fitted RM components.

NVSS J162740+603900. The dominant RM component is found by the linear $\chi(\lambda^2)$, depolarizing screen, and RM Synth/Clean methods to be near -7 rad/m^2. The cleaned FDF displays three strong RM features, near -7, +4, and +15 rad/m^2, but it is likely that the components at -7 and +4 rad/m^2 are blended, contributing power to each other and increasing their peak amplitudes. These results contrast with the two component method, which finds two dominant RM components of equal amplitude near +4.5 and +15 rad/m^2. Again, it seems likely that two RM components are interfering in a way which confounds the other methods. Taylor et al. (2009) do not report a RM for this source.

A comparison between the different methods of determining RMs for each source are shown in Figure 2.20. As expected, the linear $\chi(\lambda^2)$ and depolarizing screen fits agree well for the dominant RM value since $n\pi$ angle shifts were inserted into the data for the $\chi(\lambda^2)$ fits to best match the depolarizing screen models. The RM of the dominant component found by RM Synth/Clean agrees fairly well with the linear $\chi(\lambda^2)$ fit method for six of the seven sources, although only three agree within the formal errors. The dominant RM found by the two component model fit, however, finds agreement with the linear $\chi(\lambda^2)$ fit method in only four of the seven sources analyzed. It is apparent that in six of the seven sources the traditional linear fit to $\chi(\lambda^2)$ is incapable of providing a description of the source's true Faraday structure, instead providing what may be referred to as a "characteristic" RM. This is due to the fact that fitting to $\chi(\lambda^2)$ does not consider the behavior of $p(\lambda^2)$, which is variable in most of our sources when the measurements across a large range of λ^2 are considered. One must consider depolarization models, such as the depolarizing screen or interference between multiple

RM components, if the true Faraday structure is to be described.

We note that the χ^2_ν values for these fits are quite high in many cases, suggesting more complicated models would be needed to properly fit the data. Some of the data appear anomalous when the apparent behavior of neighboring points is taken into account. These data could be contaminated by residual instrumental problems; we have attempted to incorporate these effects into our errors. Given infinite resources, our instrumental errors would approach zero; polarization calibration is notoriously difficult at low frequencies and we must therefore proceed with our best effort, given the current technological limitations. By removing "anomalous" data we would be biasing the solutions toward simple Faraday structures in the model fitting and degrading the ability of RM Synthesis to resolve multiple components closely spaced in Faraday depth. In addition, we found that some of the discrepancies between the fits were due to flaws in the techniques themselves, which we discuss in Section 2.3.3 using the case of 3C33S.

2.3.3 3C33 South

3C33S is the southern lobe of the $z = 0.059$ radio galaxy 3C33 near the pointing center of the Aries-Pisces field. At an off-axis radius of $\sim$650″, its mean p of $\sim$4% in the 350 MHz band is well above the mean WSRT instrumental contribution of $\lesssim$0.5% at that radius. In the NVSS image, convolved to the common beamsize used for our WSRT images, 3C33S displays a fractional polarization of 10%. Prior studies at λ6 cm and λ2 cm by Rudnick et al. (1981), which resolve the structure of the lobe, find the fractional polarization ranging from $\sim$15% at the radio peak to more than $\sim$60% in the lower surface brightness regions. Previous studies have quoted an integrated RM of -12 rad/m^2 for 3C33 (e.g., Berge & Seielstad 1967, Simard-Normandin et al. 1981), although this RM determination may be contaminated by the northern lobe. Rudnick (1988) finds the RM to be $\approx$-7 rad/m^2 in the southern hotspot region using unpublished 20 cm and 6 cm data.

Table 2.7 and Figure 2.14 summarize the modeling results for 3C33S. The model fit for the depolarizing screen also yielded RM $= -7 \pm 0.15$ rad/m^2, as did the $\chi(\lambda^2)$ fit alone (RM $= -6.8 \pm 0.17$ rad/m^2). Similarly, RM Synthesis/Clean found a dominant component with $p = 2.5\%$ at -6.7 rad/m^2, with a weaker $p = 0.6\%$ component at +8 rad/m^2. This result is robust for various weighting of the NVSS sample with respect

to the WSRT samples before computing the FDF. While increasing the weighting of the NVSS sample can have a large effect on the sidelobe level and structure in the RMSF and, hence, the constructed FDF, RM Clean yields a similar solution each time: a dominant peak near -7 rad/m^2 and a secondary peak near +8 rad/m^2. Thus, there appears to be good agreement between the literature, depolarizing screen, $\chi(\lambda^2)$ and RM Synthesis/Clean results that the dominant RM component in 3C33S is at -7 rad/m^2. Weaker RM components in the FDF, such as the $p = 0.4\%$ one at +23 rad/m^2, are increasingly unreliable (see Figure 2.14).

However, our two component fit to these same data give quite different values, -3 and 0 rad/m^2. Which of these determinations is correct? While direct comparison of the χ^2_ν values for the best model fits is inappropriate, it is clear from Figure 2.14 that the two component model provides a better fit to the data than the depolarizing screen model. It does a much better job of explaining the two longest wavelength observations (particularly in q), where p rises from a minimum near $\lambda^2 \sim 0.8$ m^2. The observation of a minimum in p is compelling evidence against a simple depolarizing screen. In any case, a slight change in the errors assigned to the original data points could change the relative goodness of fit for these two alternatives. Polarization data at $\lambda = 9$ cm (Rudnick et al., 1983) agrees in p with our two component and depolarizing screen models, but have been excluded from the fits since they were integrated over both lobes and therefore not reliable for these purposes.

We note that such a discrepancy can be quite important depending on the scientific issues under investigation. First, these two models (a single component at -7 rad/m^2 or two components, at -3 and 0 rad/m^2) represent quite different physical structures in the source. For example, the magnetic field in 3C33S very closely tracks the bow-shocked shape leading edge (Rudnick, 1988), and a small toroidal sheath could give rise to two dominant RM components. Alternatively, the surrounding medium might have a depolarizing screen with very fine scale structure ($\ll 1''$, $\sim$1 kpc) that is independent of the geometry of the source. If we were not interested in the Faraday structure, we could simply look at the weighted mean of the two component fit, which yields -1.7 rad/m^2. However, the difference between this value and the -7 rad/m^2 from other models represents a factor of greater than 4 in any derived densities or magnetic field strengths. If similar discrepancies are found at shorter wavelengths, e.g., 1 GHz, then

the physical parameters involved would be $\sim$10$\times$ larger.

The discrepancy between the -7 rad/m^2 and weighted -1.7 rad/m^2 fits is not due to the inaccuracies of the measurements, as determined from the formal errors. The error in our $\chi(\lambda^2)$ fit is small (RM $= -6.8 \pm 0.17$) and the errors in the two component fit are even smaller (RM $= -2.9 \pm 0.1$). Thus, using our linear $\chi(\lambda^2)$ fit we would have ruled out the two component weighted mean with high confidence. Similarly, our RM Synth/Clean results would have ruled out the two component fit. It might be further argued that we shouldn't have expected to distinguish between values of -7 and -1.7 using this method, since the FWHM of the RMSF's main lobe is $\sim$12 rad/m^2. This argument ignores the standard practice of quoting uncertainties in the location of a peak at a value of $\sim$FWHM/(2$\times$signal:noise). In the case of 3C33S, the error in the dominant RM peak (from Gaussian fitting to the cleaned FDF) is 0.06 rad/m^2. Again, we would have ruled out the (unresolved) combination of peaks near -3, 0 rad/m^2 with high confidence.

Because the discrepancies between the results of various models, in particular RM Synthesis/Clean, were much larger than our calculated errors, we carried out a series of experiments with infinite signal to noise models using two RM components.

2.4 Experiments with two RM components

2.4.1 RM Synthesis

Although many different polarization diagnostic experiments could (and should) be done, we focused on two-component models for several reasons. First, a two-component model produced a good fit to the 3C33S data. Second, two Faraday components might be a reasonable expectation for double radio galaxies that are unresolved. In addition, when angular resolution becomes sufficient to resolve depolarizing Faraday screens, there will always be places where the beam overlaps two neighboring structures, producing two Faraday components. Finally, recent work by Law et al. (2011), where RM Synth/Clean was performed on 37 polarized radio sources using the Allen Telescope Array (ATA), showed that two or more components were detected with high confidence in $\sim$25% of their sources. We now discuss a few simple experiments to demonstrate some of the potential pitfalls when RM Synthesis/Clean is employed.

Our first experiment was to adopt a model fixed to the best two-component fit to the 3C33S data, with components at -3 and 0 rad/m^2. Synthetic q,u spectra were constructed for the same NVSS + 8-WSRT λ^2 locations as in our previously discussed observations. The results of RM Synth/Clean are shown in Figure 2.21. It bears a remarkable resemblance to the observed FDF for 3C33S, displaying a single dominant peak near RM ~ -7 rad/m^2 and a low amplitude secondary feature near RM $\sim +8$ rad/m^2, even though the input RMs were at -3 and 0 rad/m^2. Thus, the FDF, with or without cleaning, produces RM power at what we can now state is the wrong value, since we know the input model parameters. This is true whether you examine the clean components at high RM resolution or their convolved version which reflects more closely the limitations in resolving multiple RM components. In the convolved case, one would expect the FDF to still reflect the weighted mean of the input components; it does not.

Another case, demonstrating the impact of the relative phase of the two polarized components, involves using two components of equal amplitude with RMs of -15 and 0 rad/m^2. These are separated by more than the FWHM of the RMSF, 12 rad/m^2, constructed from ~ 400 channels in the WSRT 350 MHz band and shown in Figure 2.9. Nominally, then, they should appear well-separated in the FDF. Figure 2.22 shows the results of using four different values for the difference in χ_0 for the two components. In three cases, RM Synthesis/Clean successfully resolved the two components. In the fourth case, with a difference in χ_0 of 90°, the raw FDF was dominated by a single peak near the mean RM of -7.5 rad/m^2, along with considerable sidelobe power. Cleaning produced an apparent triple component structure, with power at RMs of -17, +2 and -7.5 rad/m^2, instead of the input values of -15 and 0 rad/m^2.

We have also asked colleagues to run these and other models through their own RM Synthesis and cleaning programs, to verify that coding problems were not at fault. *The above problems with RM Synthesis and Clean are robust to its exact implementation.* They occur when the separation of the RMs is on the order of the FWHM of the RMSF, $2\sqrt{3}/\Delta\lambda^2$. Under these conditions, the number of cycles of Q and U within the bandwidth differ by one or less for the two components. RM synthesis is therefore not able to reliably resolve them into separate Fourier components. *However, the two components do not simply blend in this case, as two nearby sources would blend in total intensity. Instead, they interfere to create complicated structures in $Q(\lambda^2)$, $U(\lambda^2)$ (i.e.*

$P(\lambda^2)$ and $\chi(\lambda^2)$) which causes RM Synthesis to put power at values other than the input RM. In some cases, RM Clean is able to recover from this interference; in other cases it is not.

Some of the shortcomings of RM Synthesis arise not from a fault in the technique, but rather a limit of our measurement abilities. One can use radio aperture synthesis as an analogy from which to draw insight; limitations in baseline sampling for aperture synthesis are in some ways analogous to limitations in λ^2 sampling for RM Synthesis. However, the RM interference that we have illustrated here is considerably more complicated. These experiments reflect the interference between two RM components and are reminiscent of other types of interference that are better understood. Polarization canals (Shukurov & Berkhuijsen, 2003), e.g., do not represent actual dips in polarization, but simply the interference, in one beam, between two components separated by 90° in polarization angle at some observed wavelength. Similarly, rotation measure involves the trend of $\chi(\lambda^2)$ over a range of wavelengths, and the mapping between multiple RM components and $\chi(\lambda^2)$ is not yet fully understood. This illustrates the need for sufficiently broad λ^2 coverage in polarization observations when performing RM experiments, where detection of potential maxima or minima in $p(\lambda^2)$ is also critical to help diagnose the Faraday structure. These methods are also subject to a variety of degeneracies, some of which we illustrate in the following section.

2.4.2 Pseudo-λ^2 behavior

Another insidious quality of two component models is that they commonly produce

$$RM(\lambda^2) \equiv d\chi(\lambda^2)/d\lambda^2 \;\approx\; constant \tag{2.15}$$

over substantial ranges in λ^2 space. Although it may be obvious that sparsely sampled data (especially using only two or three λ^2 data points) could lead to mistakes, it is assumed that continuous sampling over a significant range of wavelengths (e.g., $(\lambda^2_{max}$-$\lambda^2_{min})/\lambda^2 > 0.25$) can verify whether RM($\lambda^2$) $\approx$ constant. This is not always true, as we now illustrate.

Figure 2.23 shows five different models, all of which produce excellent RM(λ^2) $\approx$ constant over the WSRT 350 MHz band, which covers $\sim$35% in λ^2 space. In addition,

three of these models would also yield the same excellent λ^2 behavior with an additional point at 1.4 GHz (e.g., NVSS). The model parameters are listed in Table 2.13. If one were examining the behavior of $\chi(\lambda^2)$ alone, as is done in most of the existing literature, there are a wide variety of two component models which easily fit the data but have very different values of RM than the one observed. The key to ruling out such two component models, and thus to have a reliable determination of RM, lies in their $p(\lambda^2)$ behavior, which is quite different for each model. A better way to avoid these mistakes is to simply fit the function $\mathbf{p} = pe^{2i\chi} = q + iu$ to the $q(\lambda^2)$ and $u(\lambda^2)$ data, and determine whether a satisfactory fit has been achieved.

It is tempting to assume that there is a "short wavelength" limit where these problems can be safely ignored. We now show that is not true. First, we define a "short wavelength" set of observations as one in which there is reasonable sampling in λ^2 space and $\lambda^2_{min} \ll \lambda^2_{max}$. Thus, one can verify whether RM(λ^2) $\approx$ constant down to effectively zero wavelength. The models described in Table 2.14 and shown in Figure 2.24 demonstrate that this does not exclude two component models with RMs very different than the ones measured by fitting RM(λ^2) = constant. In the examples shown, the $\chi(\lambda^2)$ data alone follow very closely a constant RM = 1000 rad/m^2. However, they actually contain components that range from -50 to 1650 rad/m^2. Again, the key is to examine the $p(\lambda^2)$ behavior, as seen in Figure 2.24, or better, as noted before, to fit a model directly to the $q(\lambda^2)$ and $u(\lambda^2)$ data.

We also show in Figure 2.24 the full RM(λ^2) for these models. The wide variations in this number show that when there are two interfering components, measuring the RM using data at closely spaced wavelengths, or only using very sparse sampling, can render the observed RM virtually meaningless.

2.4.3 Recommendations regarding RM measurements

There is no simple prescription for producing reliable rotation measures because it depends on the specific scientific goals. We begin the discussion of those issues below, but here we simply offer some general guidelines to inform the future practice of Faraday structure determinations:

- Fitting of models to $q(\lambda^2)$ and $u(\lambda^2)$ (or equivalently, $p(\lambda^2)$ and $\chi(\lambda^2)$) is the only reliable way to determine the underlying Faraday structure. In particular, results derived from $\chi(\lambda^2)$ alone or RM Synthesis alone are subject to large ambiguities.

- RM Synthesis/Clean, as it is currently implemented, can serve as a first order indicator of the location of power in Faraday depth space, and guide more detailed modeling.

- Plots of q vs. u provide another useful diagnostic of the appropriateness of any models.

- Results for RM determinations should always specify not only the formal errors, but also the χ^2 or RMS residuals of the fits. This, along with documenting the coverage in λ^2 space, will allow for an analysis of what ambiguities are permitted by the data.

- The allowable space for ambiguities can be significantly reduced by broadening the λ^2 coverage, increasing the sampling, and ensuring that regions of λ^2 space are observed where $\mathrm{RM}(\lambda^2) \neq$ constant and $p(\lambda^2) \neq$ constant.

- Scientifically useful results are possible in the presence of ambiguities if the underlying assumptions are both documented and valid, as discussed in Section 2.5.

- Alternative methods of parameter determination, such as Maximum Likelihood, should be considered in the presence of low signal to noise. In this case, least squares fitting may yield a low χ^2_ν statistic, but may not necessarily yield the appropriate solution. For example, Guidetti et al. (2008) use four frequency samples in a linear fit to $\chi(\lambda^2)$ to determine RMs for a number of cluster sources. In the limit of infinite signal to noise, it doesn't matter how closely spaced the points are; with four points and two parameters, i.e. dof=2, $\chi^2_\nu \approx 1$ would truly signify a good fit. However, we note that for each source two of their samples are at nearly the same frequency, and these measurements agree within errors. This essentially guarantees a value for χ^2_ν of order unity, perhaps giving false confidence in the appropriateness of the model. Thus, if minimization of χ^2_ν is to be used, we caution that the effective degrees of freedom should first be carefully considered.

2.5 Discussion

2.5.1 Depolarization

The median depolarization ratio between 350 MHz and 1.4 GHz for our seven modeled sources is $p_{350}/p_{1.4} \sim 0.3$. This is the same as the median of the upper limits for our sample as a whole. If this depolarization is due to a random foreground screen (and not to the interference between two components), then this corresponds to a Burn law $\sigma_{RM} \sim 1$ rad/m^2 , where the depolarization is $\exp(-2\sigma_{RM}^2\lambda^4)$. It is likely that the overall sample is even more depolarized, since we observed the upper limits to drop as the polarization fraction at 1.4 GHz increased (see Figure 2.8). This result has two implications, one for observations at low frequencies and one concerning the environment of radio galaxies.

Assuming a Faraday dispersion as above, we can estimate, e.g., the depolarization that would be observed by LOFAR[2] which has a high frequency band covering 120-240 MHz, and a low frequency band covering 30-80 MHz. If the Burn law were to remain roughly accurate for integrated polarizations, then the depolarization would peak at 0.008 at the high end of the high frequency band, and drop by many orders of magnitude at low frequencies, essentially making polarizations undetectable. However, as pointed out by Tribble (1991), the falloff from a Gaussian depolarizing screen is likely to be considerably slower, dominated by the small patches around extrema in RM, where the RM gradient is near zero. If we start with a characteristic integrated polarization of $\sim$3% at 1.4 GHz and extrapolate with only a λ^2 dependence from our depolarization results at 350 MHz, then we would expect fractional polarizations of 0.1% - 0.5% in LOFAR's high band, and 0.01% - 0.05% in the low band. These are not likely to be detectable. It is not clear, at present, whether even well-resolved extragalactic sources will have small enough Faraday dispersions to be observed in polarization at these low frequencies.

Using the more physical units introduced by Garrington et al. (1991), our observed characteristic lower limit to the Faraday dispersion is $\sim$1.5 cm^{-3} μG pc. For the purposes of calculating some very rough estimates of what these limits mean for field

[2] http://www.lofar.org

strengths around radio galaxies, we assume that the depolarization occurs in a foreground screen completely unaffected by the radio galaxy. Assume that we need ∼10 independent patches across a 100 kpc source in order to depolarize it, and a fiducial electron density of n_e=10^{-3} cm^{-3}. The resulting magnetic field is then B/μG $\geq$ $0.1(n_e/10^{-3})(r/10)$(cm^3 kpc^{-1}), where r is a typical scale size of magnetic field fluctuations and we have ignored the $\sqrt{N}$ averaging along each line of sight for this order of magnitude calculation. Fields of this strength are less than those found in clusters of galaxies, but greater than expected in the more filamentary WHIM outside of clusters (Ryu et al., 2008), especially if one factors in the much lower densities in those regions.

Thus, radio galaxies appear to be associated with thermal, magnetized plasmas with much higher values of n_eB than expected for filamentary regions, but similar to those found in clusters. This could result because of the bias for radio galaxies to be found in high density regions (de Zotti et al., 2010). Alternatively, effects very local to the parent galaxy, such as emission-line regions (e.g., Pedelty et al. 1989) could be responsible for the ubiquitous depolarization. This leaves very few radio galaxies available to probe cosmological filaments, except, perhaps some Mpc-scale sources (Saripalli, 2009). As we seek to understand the causes of the ∼1.5 cm^{-3} μG pc limits, however, it will also be important to readdress the questions of internal depolarization, e.g., due to a mixing layer (Bicknell et al., 1990) between the radio source (with possibly much higher fields) and its low density environment.

2.5.2 Science Implications of RM Ambiguity

We have shown that there is considerable ambiguity (sometimes >100%) in the determinations of RMs using the methods universally used in the literature, and even in the more recent RM Synthesis technique. We now briefly examine the implications this has for different types of scientific investigations.

Galactic Foreground

The use of polarized extragalactic sources to characterize the magnetic field structure of our Galaxy has a long history (e.g., Simard-Normandin & Kronberg 1980, Brown & Taylor 2001) plus a major recent advancement (Taylor et al., 2009). Our investigations do not reveal any (signed) bias in RM determinations, therefore, we would expect that

the average RM of a group of extragalactic sources in some area of the sky should be a fair measure of the true value. However, the structure function of galactic fluctuations will have contributions from the RM ambiguities discussed here, as well as attempts to measure the intrinsic differences in RM between sources, especially on the smallest scales.

Fluctuations through Galaxy Clusters

The situation with respect to cluster measurements is much more complicated. The clusters are expected to have fields that are tangled on scales substantially smaller than the cluster. Therefore the mean RM of a distant extragalactic source seen through the cluster should be zero, but the scatter in such RMs should be larger than for background sources not seen through clusters (e.g., Kim et al. 1991, Clarke et al. 2001, Bonafede et al. 2010). In this case, the quantity being measured is the RM scatter, which will be increased because of the ambiguities discussed in this paper. In the ideal world, this scatter should be no different for sources seen through clusters ("the sample") than for sources not seen through clusters ("the control"), so again the measurements should be unbiased.

However, unless the sample and control have exactly the same properties, both intrinsically and in terms of the observations leading to their RMs, it is impossible to know how the RM ambiguities would affect their comparison. For example, if RM determinations include a short wavelength point for some sources, as opposed to others, a different range of possible underlying RMs will be present for the two cases. Or, if the sources in the sample or control are statistically different physically (e.g., FRI vs. FRII sources), then the ambiguities can have different effects and contaminate the test. All of these problems are present in the well-cited studies by Kim et al. (1990), Kim et al. (1991), and Clarke et al. (2001), as discussed by Rudnick & Blundell (2004). Similar contamination can be present if RMs from one experiment are compared to RMs from another, with different wavelength coverage, different editing for non-λ^2 behavior, etc. (e.g., Johnston-Hollitt & Ekers 2004). Since our modelling shows that RMs can be affected by factors of order unity, it is not possible to assess the reliability of these cluster background experiments. Two types of studies are required to address this issue. First, the prevalence of multiple RM components within observing beams must be estimated;

Pizzo et al. (2011) found multiple components at $\sim 15''$ resolution in all three radio galaxies near the center of Abell 2255. Second, statistical predictors are needed to quantify the likely errors in RM for a given distribution of multiple components.

Faraday structure of radio galaxies

Increasingly detailed studies of the Faraday structure of individual radio galaxies are now becoming available (e.g., Laing & Bridle 1987, Zavala & Taylor 2002, Laing et al. 2006, O'Sullivan & Gabuzda 2008, Govoni et al. 2010). In many cases, the rotation measures are assumed to be entirely in the unperturbed foreground, and thus a fair measure of the magnetic field structure of the environment, usually a cluster of galaxies. However, as suggested by Bicknell et al. (1990) and Rudnick & Blundell (2003), and now demonstrated convincingly by Laing et al. (2008), the radio source itself may change the observed RM structure. This issue aside, the question remains how the newly described RM ambiguities could affect these measurements.

The studies of individual radio galaxies involve higher order characterizations of the RM distribution, such as the structure function, so they are much more sensitive to possible ambiguities. In addition to increasing the overall scatter in RMs, contributions from ambiguities are likely to change as a function of scale. If we assume an unperturbed foreground screen, then when the observing beam is much smaller than the smallest angular scale of RM variations, a single component dominates and the RM determination can be free of ambiguities. Feain et al. (2009) took advantage of this situation in a Faraday structure study of the radio lobes of Centaurus A, using background sources.

In the limit where the observing beam is much larger than the characteristic scale of variations, then we approach the Burn limit of a depolarizing screen, and the effect of ambiguities is minimized. However, as pointed out by Tribble (1991), the situation is typically much more complicated, and the observed polarized emission will be dominated by regions where the angular RM distribution is at an extremum, with only small gradients. The emission is then a complicated function of the beam size and the angular structure of the magnetic field fluctuations. Detailed modeling is required in such cases, and it is not certain whether a clear diagnosis of the Faraday structure is possible, in practice. In particular, we may not be able to distinguish between the physically distinct cases of fully external screens, thin mixing layers of relativistic and thermal emission or

fully mixed plasmas (e.g., Cioffi & Jones 1980).

The intermediate situation, where two or three different RM components dominate within an individual observing beam, is the most sensitive to the ambiguities discussed in this paper. The resulting complex interference patterns in λ^2 space can give rise to erroneous RMs, and will increase the observed scatter preferentially on these angular scales. This situation will necessarily arise whenever the minimum angular scale of RM fluctuations is being approached. The only effective way to deal with this will be using Monte Carlo or numerical simulations (e.g., Guidetti et al. 2008, Guidetti et al. 2010), where we expect there to be differences in shape between the input structure function and the observed structure function on scales of the order of the beamsize.

2.6 Conclusions

We have presented our polarization analysis of compact radio sources observed with the WSRT at 350 MHz. Using the observations of 585 sources in six fields, we computed a simple analytic model of the off-axis instrumental polarization (which can rise to several percent in q at the primary beam radius). After correction of the observations using this model, only a small fraction of the sources were determined to have significant polarization at this frequency. By supplementing our observations with data from the NVSS, we have assessed the depolarization of our sample, finding the median depolarization ratio from 1.4 GHz for the strongest sources to be $p_{350}/p_{1.4} < 0.2$.

We modeled the Faraday structure of seven sources using various methods, including the traditional linear fit to $\chi(\lambda^2)$, as well as q, u vs. λ^2 fitting to two simple depolarization models – a foreground screen and two interfering RM components. In addition, we applied the novel Rotation Measure Synthesis and RM Clean techniques. A comparison of the RMs determined by various methods has shown agreement in many sources, and yet failure to reproduce the q, u observations casts doubt upon the validity of those solutions. In only one of the seven sources modeled, where depolarization from 1.4 GHz was not present, did the linear $\chi(\lambda^2)$ fit offer a solution that sufficiently reproduced the q, u observations. Of the remaining six sources, RM Synthesis/Clean suggested multiple significant ($p_{02}/p_{01} \geq 0.5$) RM components in three sources, while the two-component model found a significant secondary RM component in all six. Thus, a "characteristic"

RM may be said to exist for any source, but the true Faraday structure may not always be adequately described by this alone. This point is well demonstrated by our detailed analysis of the southern lobe of the radio galaxy 3C33. Previous studies, as well as our own linear $\chi(\lambda^2)$ fit and RM Synthesis/Clean analyses have found a single, dominant RM of -7 rad/m^2, in sharp contrast to the q, u observations which strongly suggest two significant RM components near -3 and 0 rad/m^2.

To further explore the possible shortcomings of the linear $\chi(\lambda^2)$ fit and RM Synthesis/Clean methods, we have performed a few simple experiments. By constructing synthetic q, u spectra using the best fit two-component model for 3C33S, we find that RM Synthesis may place power at incorrect Faraday depths when multiple, closely spaced RM components interfere. In this case, both RM Synthesis and the linear $\chi(\lambda^2)$ fit find a consistent solution, but one that does not agree with the known model inputs. The vulnerability of RM Synthesis is further demonstrated by a second experiment, which illustrates the role of phase in RM ambiguity. In this experiment, we show that two RM components, separated by more than the FWHM of the RMSF, may still yield an incorrect solution under RM Synthesis depending upon the relative phase (i.e. intrinsic polarization angle) between the two components. A third experiment shows the dangers of a common assumption, that RM determinations made at high frequencies are sufficient. We show that the λ^2 coverage must be broadened as much as possible to explore the true depolarization behavior of the source.

With modeling of our WSRT observations and experiments on synthetic observations, we have touched upon some of the ambiguities that exist in rotation measure determinations. We caution that care must be taken when designing RM experiments and choosing one or more methods of analysis, stressing the importance of considering both degree and angle of polarization (or equivalently, q and u) over as wide a range of λ^2 space as possible to see a more global picture of the polarization behavior and produce a more accurate description of the Faraday structure.

Table 2.1 Summary Of WSRT 350 MHz Observations

Field	RA (J2000)	DEC (J2000)	b[1] (°)	Array Config.	Exposure (Hours)	Common Beam (″)	Calibrators
Aries-Pisces	01:09:14.30	+13:09:58.0	-49	Mini-short	12	325 x 70	3C147, 3C295
Coma SW	12:54:08.00	+26:42:00.0	+89	Special[2]	12	70 x 70	3C147, 3C295
Coma NW	12:54:08.00	+27:58:00.0	+88	Special[2]	12	70 x 70	3C147, 3C295
Coma NE	12:59:52.00	+27:58:00.0	+88	Special[2]	12	70 x 70	3C147, 3C295
A	14:53:00.00	+40:25:00.0	+62	Maxi-short	4.2	125 x 70	3C147, 3C48
B	16:20:00.00	+60:12:00.0	+42	Maxi-short	12	105 x 70	3C48, 3C295

[1]Approximate Galactic latitude at field center

[2]Special array configuration is 36m+54m+72m+90m.

Table 2.2 Number of 78 kHz Channels Used For IF Band Averaging

Field	Stokes	IF1 (376.4)[1]	IF2 (367.7)	IF3 (358.9)	IF4 (350.2)	IF5 (341.4)	IF6 (332.7)	IF7 (323.9)	IF8 (315.2)
Aries-Pisces	I	100	97	68	79	100	99	64	32
	Q	100	99	76	79	100	99	64	32
	U	69	96	58	24	85	28	64	32
Coma SW	I	101	101	59	62	101	98	96	92
	Q	101	100	58	69	100	97	97	97
	U	86	52	[7][2]	40	96	38	39	59
Coma NW	I	101	101	70	96	101	99	99	93
	Q	101	100	73	79	99	97	98	96
	U	91	84	21	75	100	27	78	32
Coma NE	I	101	101	56	29	101	99	91	87
	Q	101	100	64	62	100	98	96	95
	U	98	85	[5][2]	16	99	54	68	57
A	I	92	101	71	96	96	99	101	88
	Q	95	101	76	96	96	99	101	88
	U	30	[1][2]	26	78	65	[2][2]	17	88
B	I	86	94	42	41	100	92	90	70
	Q	86	97	64	76	101	97	101	93
	U	52	98	76	88	101	97	101	69

[1]IF band central frequencies are given below IF number in MHz.

[2]Bracketed values identify IFs where U averaging was not performed due to too few channels.

Table 2.3 Model Fit Parameters for Instrumental Polarization

IF	Fractional Stokes	A (%)	B ($\times 10^{-3}/''$)	C (°)
1	Q	0.08	1.1	83
	U	8×10^{-8}	3.7	81
2	Q	0.03	1.1	99
	U	0.007	1.3	48
3	Q	0.02	1.2	92
	U	0.03	0.75	43
4	Q	0.10	0.64	109
	U	0.30	0.26	47
5	Q	0.34	0.51	90
	U	0.004	1.3	33
6	Q	0.29	0.4	91
	U	0.008	0.7	4
7	Q	0.15	0.78	85
	U	0.13	0.13	16
8	Q	0.0005	1.9	108
	U	0.06	0.65	62

Table 2.4 RM Synthesis Capabilities of WSRT

Frequency (MHz)	$\langle\lambda^2\rangle$ (m^2)	$\Delta\lambda^2$ (m^2)	λ^2_{min} (m^2)	$\delta\lambda^2$ (m^2)	$\delta\phi$ (rad/m^2)	max-scale (rad/m^2)	$\lvert\phi_{max}\rvert$ (rad/m^2)
310-380	0.76	0.31	0.62	3.1×10^{-4}	12	5.0	5700

Table 2.5 Table of Modeled Sources

Source	RA (J2000)	DEC (J2000)	Off-axis Radius ($''$)	Pos. Angle (°)
NVSS J010616+125116[1]	01:06:16.8	+12:53:22	2786	250
3C33S[2]	01:08:50.7	+13:18:43	649	326
NVSS J011136+132437	01:11:36.2	+13:25:41	2268	65
NVSS J011204+124118	01:12:04.5	+12:42:39	2962	123
NVSS J125630+270108	12:56:30.5	+27:01:10	3816	150
NVSS J162408+605400	16:24:08.8	+60:54:04	3134	35
NVSS J162740+603900	16:27:41.0	+60:39:05	3783	63

[1]Resolved as double source in unconvolved NVSS image (with NVSS J010615+125210)

[2]NVSS J010850+131831

Table 2.6 Modeling results for NVSS J010616+125116

Model	RM_1 (err) (rad/m^2)	p_{01} (%)	χ_{01} (°)	RM_2 (err) (rad/m^2)	p_{02} (%)	χ_{02} (°)	σ^2_{RM} (rad/m^2)	χ^2_ν
Linear $\chi(\lambda^2)$	-9.6 (0.12)	-	80	-	-	-	-	1.2
Screen	-9.5 (5)	10.5	78	-	-	-	1.2	10.2
RM Synth/Clean	-9.1 (0.04)	3.1	-	11.5 (0.2)	0.5	-	-	-
Two Component[1]	[-5.0]	4.0	75	[2.0]	2.2	65	-	8.8

[1]Brackets indicate multiple minima in χ^2 surface – no RM error reported.

Table 2.7 Modeling results for 3C33S

Model	RM_1 (err) (rad/m^2)	p_{01} (%)	χ_{01} (°)	RM_2 (err) (rad/m^2)	p_{02} (%)	χ_{02} (°)	σ^2_{RM} (rad/m^2)	χ^2_ν
Linear $\chi(\lambda^2)$	-6.8 (0.17)	-	80	-	-	-	-	3.9
Screen	-7.0 (0.15)	8.5	86	-	-	-	1.0	6.0
RM Synth/Clean	-6.7 (0.06)	2.6	-	8.0 (0.1)	0.9	-	-	-
Two Component	-2.9 (0.1)	6.7	85	-0.05 (0.2)	4.8	49	-	2.1

Table 2.8 Modeling results for NVSS J011136+132437

Model	RM_1 (err) (rad/m^2)	p_{01} (%)	χ_{01} (°)	RM_2 (err) (rad/m^2)	p_{02} (%)	χ_{02} (°)	σ^2_{RM} (rad/m^2)	χ^2_ν
Linear $\chi(\lambda^2)$	-10.8 (0.31)	-	130	-	-	-	-	6.5
Screen	-10.75 (2.5)	5.5	130	-	-	-	1.2	9.3
RM Synth/Clean	-13.1 (0.1)	2.0	-	26.0 (0.3)	0.6	-	-	-
Two Component	-11.2 (0.5)	1.5	140	-24.2 (0.6)	1.5	175	-	7.9

Table 2.9 Modeling results for NVSS J011204+124118

Model	RM_1 (err) (rad/m^2)	p_{01} (%)	χ_{01} (°)	RM_2 (err) (rad/m^2)	p_{02} (%)	χ_{02} (°)	σ^2_{RM} (rad/m^2)	χ^2_ν
Linear $\chi(\lambda^2)$	20 (1.9)	-	60	-	-	-	-	12.0
Screen	19.5 (0.5)	7.5	94	-	-	-	1.0	1.9
RM Synth/Clean[1]	-32.8 (0.3)	2.1	-	34.4 (0.5)	1.7	-	-	-
Two Component[2]	[19.5]	2.7	95	[-2.0]	1.5	160	-	2.12

[1]Four strong features exist in the cleaned FDF, including one near 17 rad/m^2 .

[2]Brackets indicate multiple minima in χ^2 surface – no RM error reported.

Table 2.10 Modeling results for NVSS J125630+270108

Model	RM_1 (err) (rad/m^2)	p_{01} (%)	χ_{01} (°)	RM_2 (err) (rad/m^2)	p_{02} (%)	χ_{02} (°)	σ^2_{RM} (rad/m^2)	χ^2_ν
Linear $\chi(\lambda^2)$	4.6 (0.31)	-	-175	-	-	-	-	0.9
Screen	4.5 (0.25)	1.0	4	-	-	-	0.0	1.03
RM Synth/Clean	4.8 (0.3)	1.1	-	-17.7 (1.3)	0.2	-	-	-
Two Component	4.5 (0.25)	1.5	10	-4.0	0.5	130	-	0.851

Table 2.11 Modeling results for NVSS J162408+605400

Model	RM_1 (err) (rad/m^2)	p_{01} (%)	χ_{01} (°)	RM_2 (err) (rad/m^2)	p_{02} (%)	χ_{02} (°)	σ^2_{RM} (rad/m^2)	χ^2_ν
Linear $\chi(\lambda^2)$	-16.8 (0.4)	-	65	-	-	-	-	3.2
Screen	-17 (0.15)	5.5	64	-	-	-	1.4	1.2
RM Synth/Clean	-14.6 (1.5)	0.5	-	10.3 (0.4)	0.2	-	-	-
Two Component[1]	[-17.0]	2.5	95	[-18.0]	2.5	55	-	1.99

[1]Brackets indicate multiple minima in χ^2 surface – no RM error reported.

Table 2.12 Modeling results for NVSS J162740+603900

Model	RM_1 (err) (rad/m^2)	p_{01} (%)	χ_{01} (°)	RM_2 (err) (rad/m^2)	p_{02} (%)	χ_{02} (°)	σ^2_{RM} (rad/m^2)	χ^2_ν
Linear $\chi(\lambda^2)$	-7.8 (1.5)	-	65	-	-	-	-	4.0
Screen[1]	[-7.0]	2.0	34	-	-	-	1.0	1.8
RM Synth/Clean[2]	-6.4 (0.8)	0.5	-	14.6 (0.5)	0.4	-	-	-
Two Component	4.3 (0.5)	1.0	133	15.0 (0.5)	1.0	160	-	1.58

[1]Brackets indicate multiple minima in χ^2 surface – no RM error reported.

[2]Three strong RM components are present in FDF, including one near 4 rad/m^2.

Table 2.13 Model Parameters for Long Wavelength Pseudo-λ^2 Experiment[1]

Model ID	RM_1 (rad/m^2)	RM_2 (rad/m^2)	p_1 (%)	p_2 (%)	χ_1 (°)	χ_2 (°)
Mod1	1	-	1	0	90	-
Mod2	-0.5	2	0.66	1	-43	-123
Mod3	-4.4	6.3	1	1	-30	-145
Mod4	1	2	1.1	.55	-75	3
Mod5	-97	99	1	1	-35	35

[1]See Figure 2.23.

Table 2.14 Model Parameters for Short Wavelength Pseudo-λ^2 Experiment[1]

Model ID	RM_1 (rad/m^2)	RM_2 (rad/m^2)	p_1 (%)	p_2 (%)	χ_1 (°)	χ_2 (°)
S1	1110	750	0.7	0.35	-92	92
S2	1650	500	0.5	0.55	-110	102
S3	1400	-50	0.665	0.35	76	125
S4	1000	-	1	0	88.85	-

[1]See Figure 2.24.

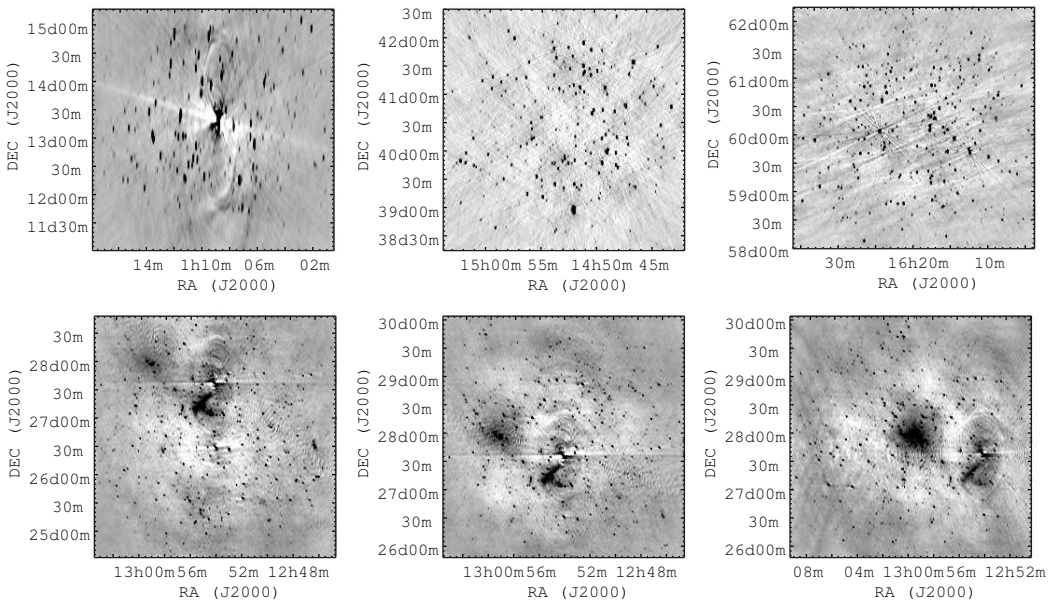

Figure 2.1 Total intensity images of the six fields observed at 350 MHz with the WSRT. Top row, from left: Aries-Pisces, Field A, Field B. Bottom row, from left: Coma SW, Coma NW, Coma NE (See Table 2.1). Images are 4x4 degrees. Diffuse emission from the Coma halo and relic are visible in the Coma images. Also visible are residual imaging artifacts near the strongest sources, common for the WSRT.

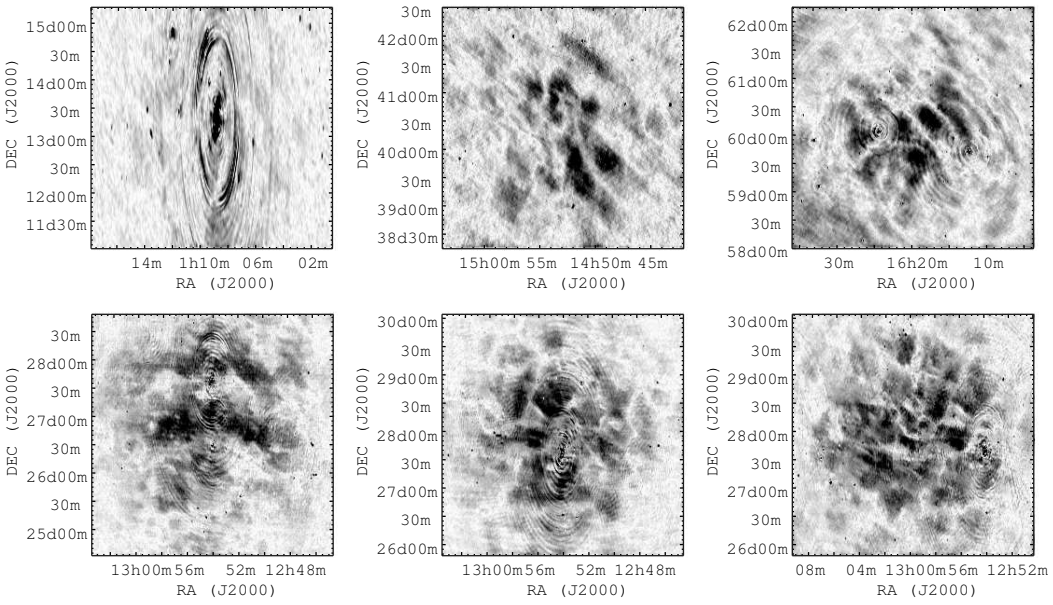

Figure 2.2 Linear polarization images at RM=0 of the six fields, taken from the results of RM Synthesis, observed at 350 MHz with the WSRT. Top row, from left: Aries-Pisces, Field A, Field B. Bottom row, from left: Coma SW, Coma NW, Coma NE (See Table 2.1). Images are 4x4 degrees. Note the diffuse Galactic emission which pervades each field. Also visible are residual imaging artifacts near the strongest sources, common for the WSRT.

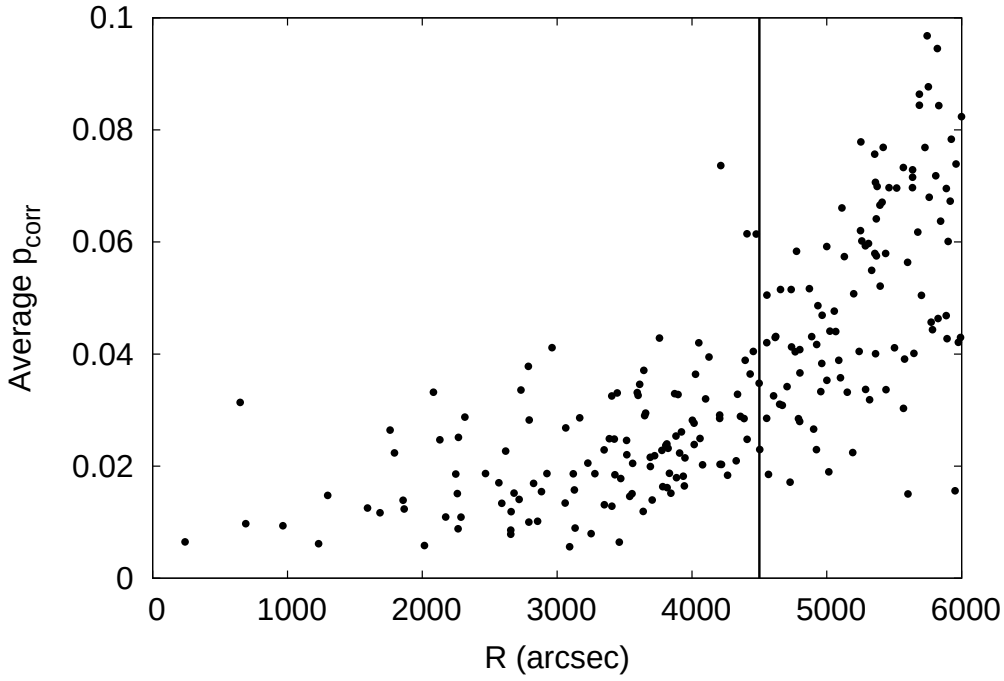

Figure 2.3 Plot of average p_{corr} at 350 MHz for sources with at least six of the eight IF measurements satisfying $P_{meas}/\sigma_P \geq 1.2$ before instrumental correction has been applied. The instrumental polarization increases with off-axis radius. The vertical line at $4500''$ corresponds to the radial limit of our instrumental polarization model fitting.

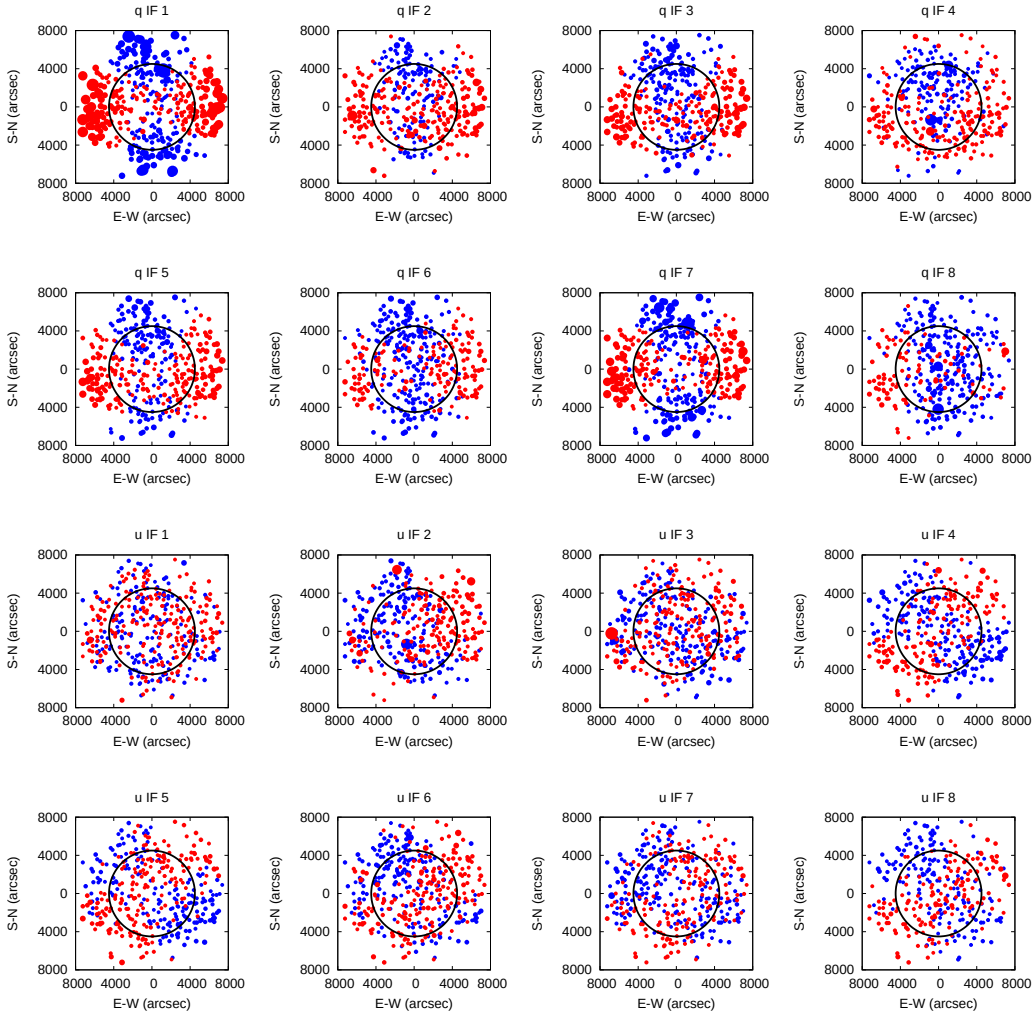

Figure 2.4 Plot of q and u measurements for sources with $P_{obs}/\sigma_P \geq 1.2$ from all six fields as projected on the sky, illustrating the radial and azimuthal behavior of off-axis instrumental polarization. Blue points are negative, red points are non-negative; the point size is related to the magnitude of the measurement. The quadrupole pattern described in the text is apparent. The black circle, of radius $4500''$, surrounds the region used for model fitting of instrumental polarization.

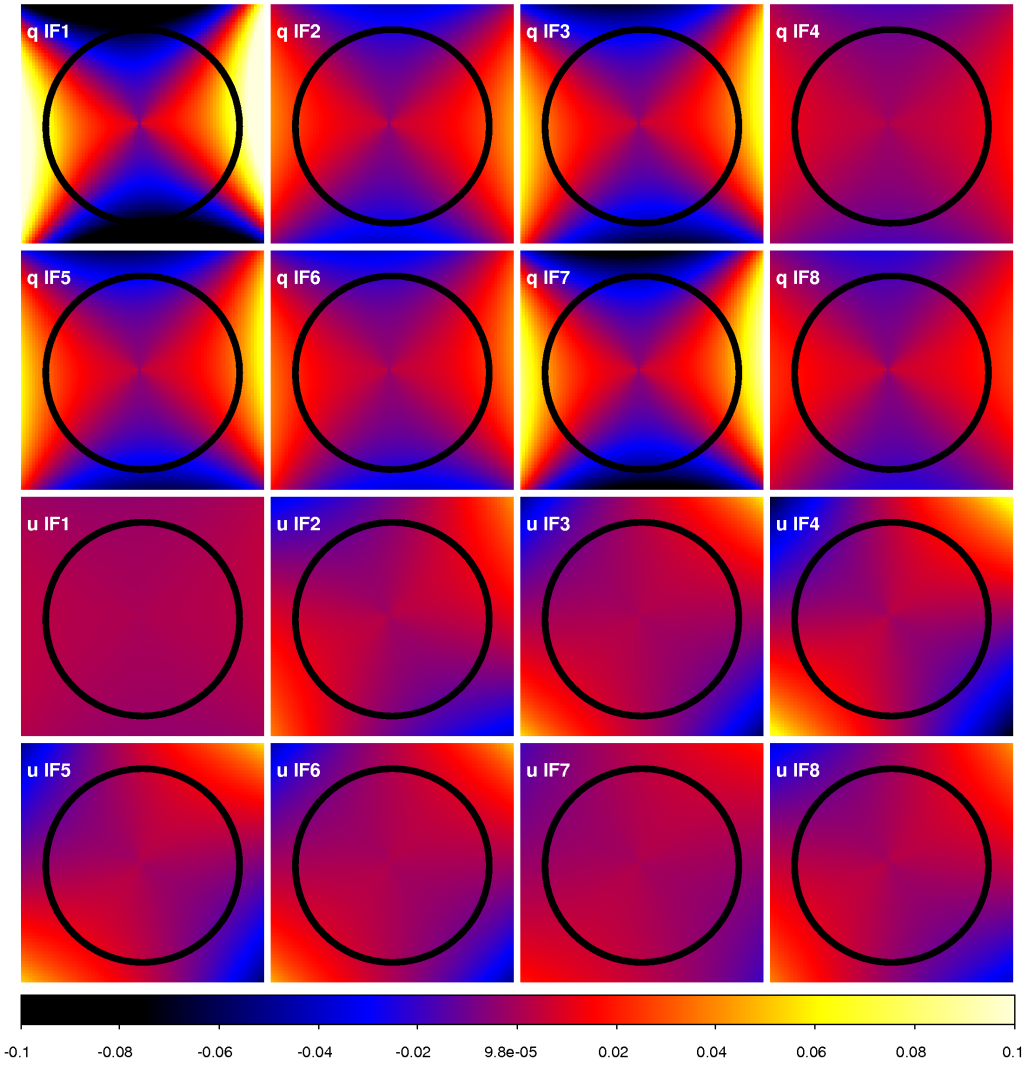

Figure 2.5 Model fits to the instrumental polarization of WSRT at 350 MHz as projected onto the sky (North is up, East is left). Top row: q for IF1 - IF4. Second row: q for IF5 - IF8. Third row: u for IF1 - IF4. Bottom Row: u for IF5 - IF8. The frequency dependence can be seen in q by noting the increased amplitude in the odd numbered IFs. The black circle is of radius $4500''$.

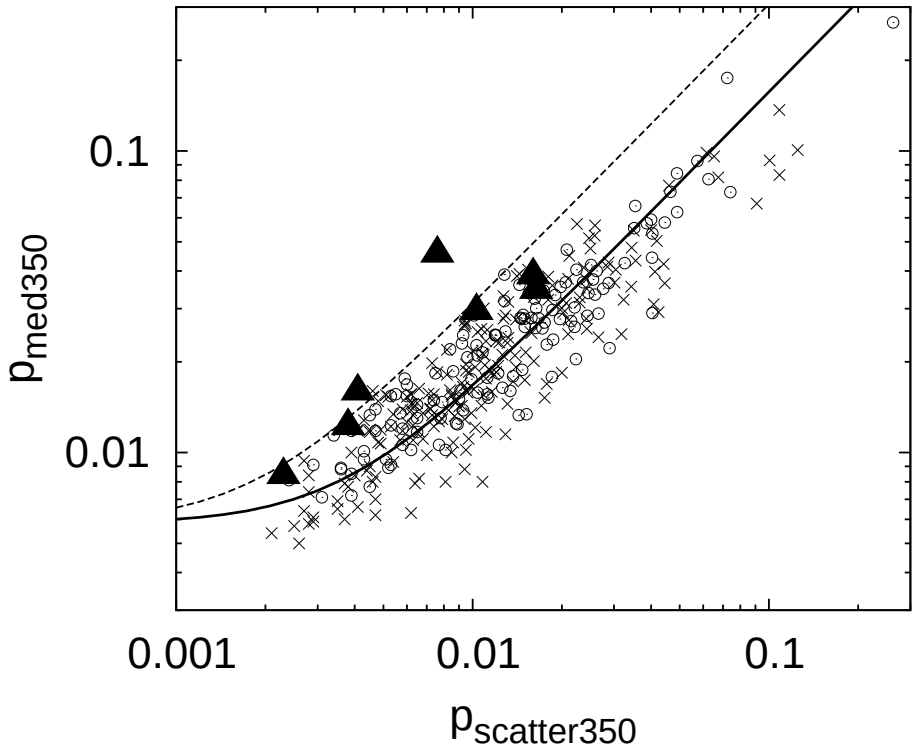

Figure 2.6 Plot of the median of p in the eight WSRT IFs vs. the RMS scatter of p among the IFs, to determine the polarization bias remaining after correction for instrumental polarization. Circles represent sources exhibiting no polarization in the NVSS. Xs represent sources exhibiting moderate or strong polarization in the NVSS. Solid triangles show sources chosen for modeling as described in the text. The solid line is the best fit for all bands for each of the 335 sources used to model the instrumental polarization, and the dashed line shows the defined upper limit discussed in the text.

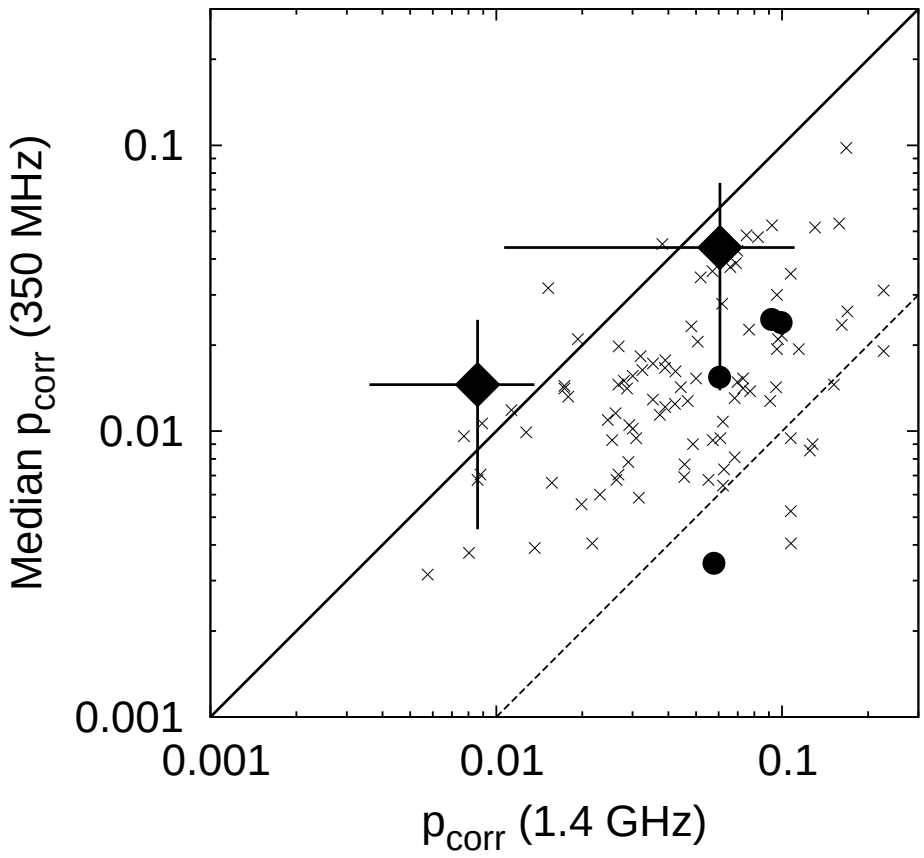

Figure 2.7 Plot of bias corrected median p_{350} vs. bias corrected $p_{1.4}$ for 102 sources with significant polarization at 1.4 GHz, defined as $P/\sigma_P > 2$. Xs represent upper limits at 350 MHz for the median fractional polarization. Solid symbols represent the sources we modeled, except for NVSS J162740+603900 which did not have a significant detection in polarization at 1.4 GHz. Circles represent sources whose median 350 MHz values are formally upper limits, although they were clearly detected in some IF bands. Diamonds are significant detections at both bands, shown with their errors.

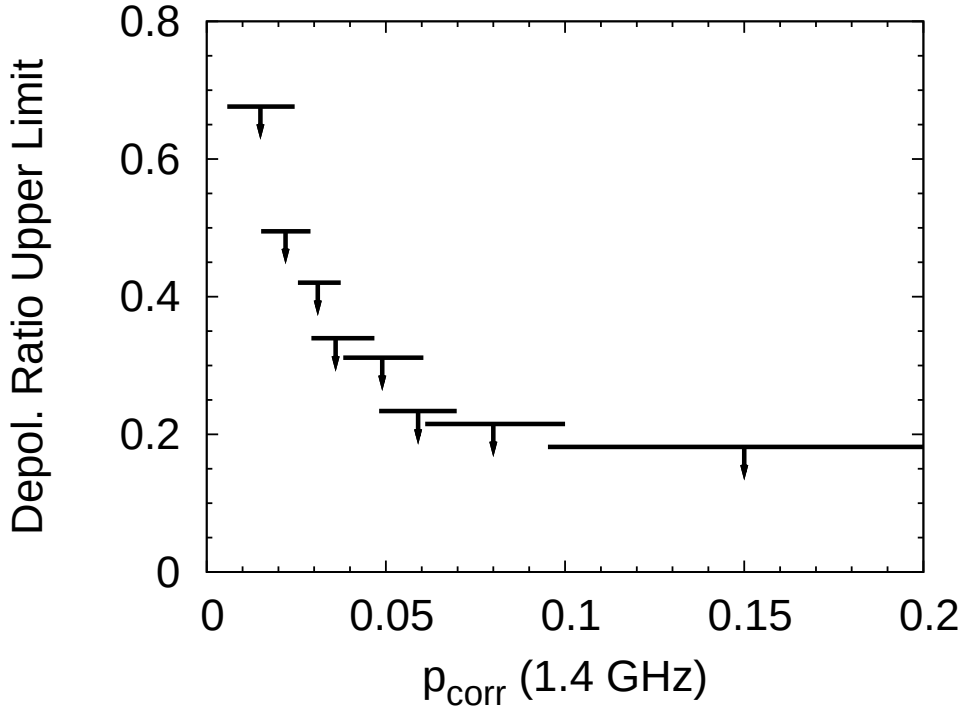

Figure 2.8 Plot of the upper limits to depolarization ratio from 1.4 GHz to 350 MHz vs. $p_{1.4}$ for the set of 335 sources described in Section 2.3.1. Depolarization ratio is defined as $p_{350}/p_{1.4}$.

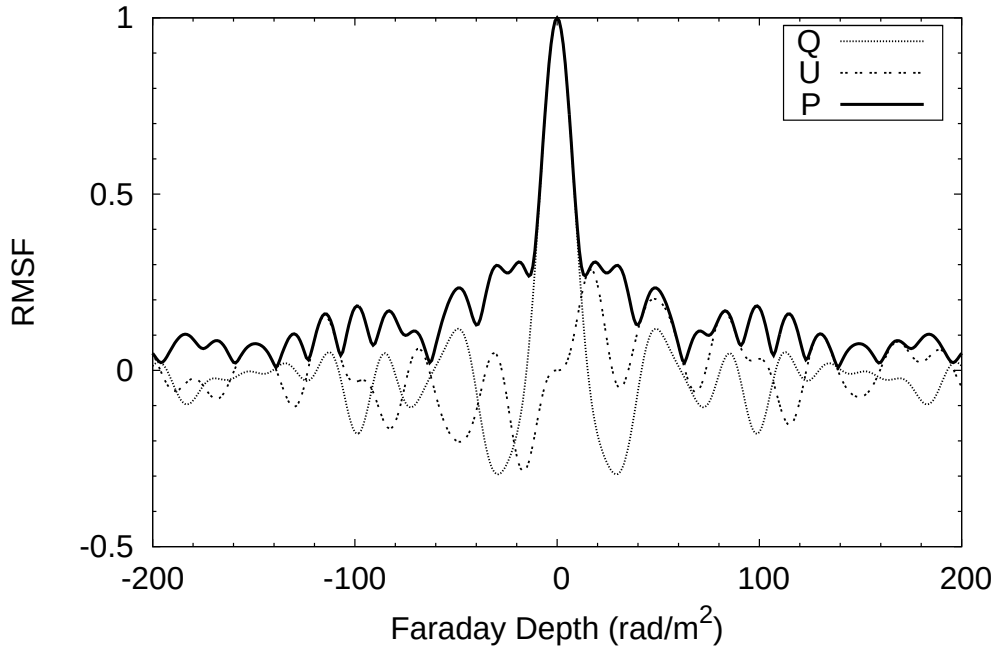

Figure 2.9 Rotation Measure Spread Function for a typical set of channels in the WSRT 350 MHz band. The RMSF is the normalized (unitless), complex response to polarized emission in Faraday space for a given set of λ^2 sampling. Roughly 400 channels were used to construct this RMSF.

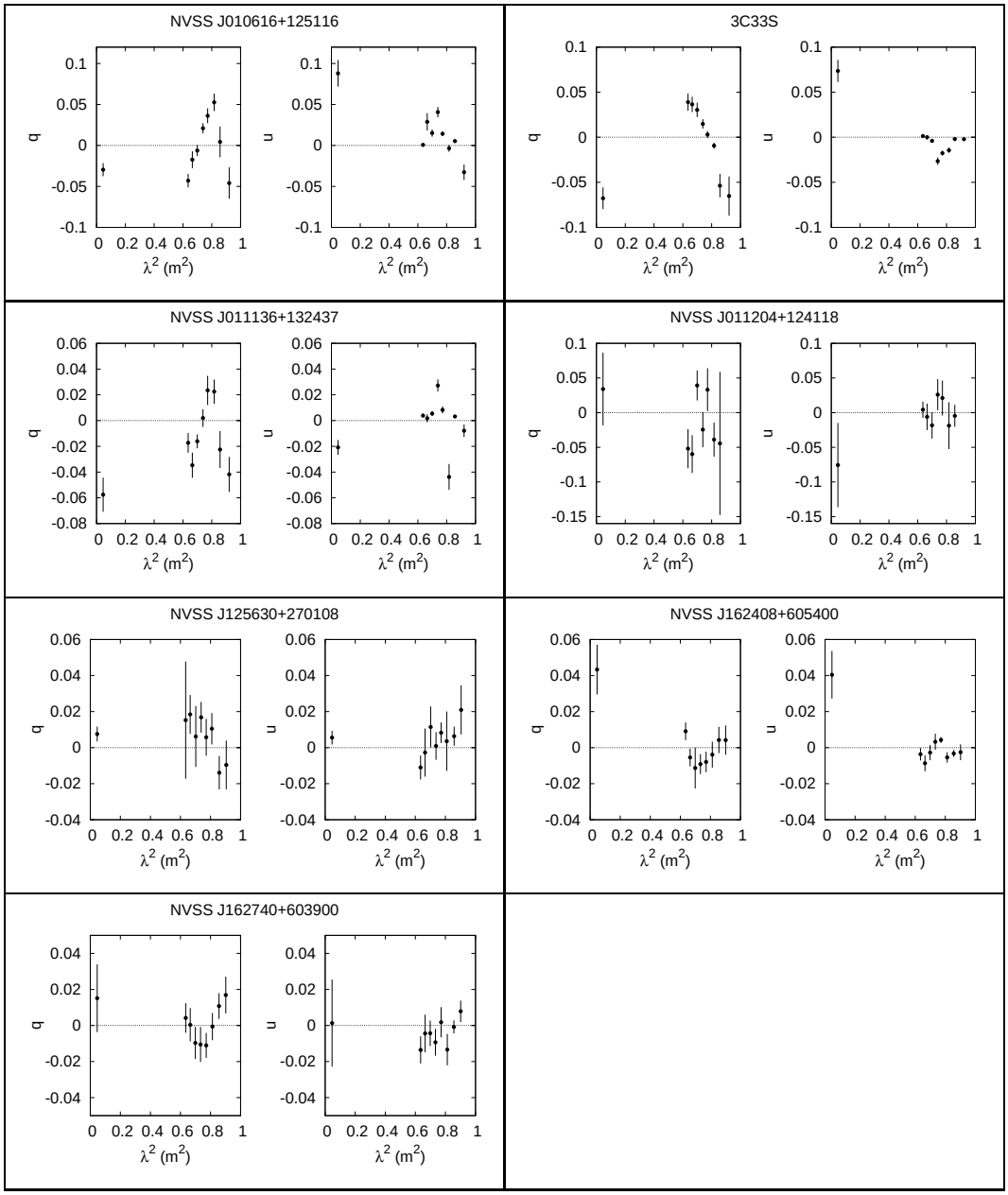

Figure 2.10 Observed NVSS + WSRT IF band averaged $q(\lambda^2)$ and $u(\lambda^2)$ for the seven sources modeled. Background subtraction and removal of WSRT instrumental polarization has been performed for each source, as described in the text.

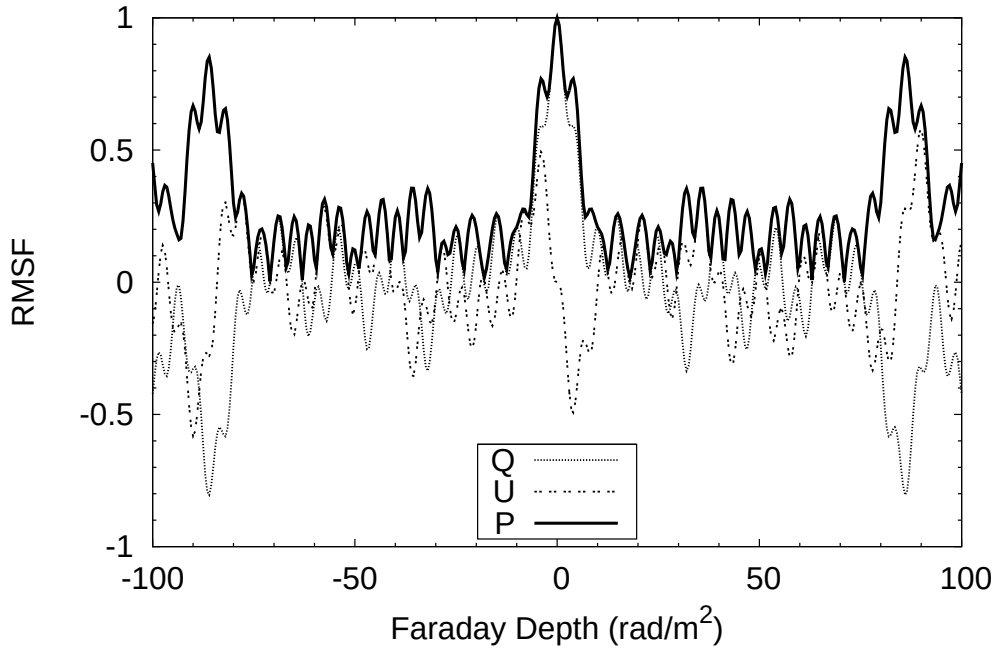

Figure 2.11 Rotation Measure Spread Function for a typical set of NVSS + 8 WSRT IF measurements. The RMSF is the normalized (unitless), complex response to polarized emission in Faraday space for a given set of λ^2 sampling.

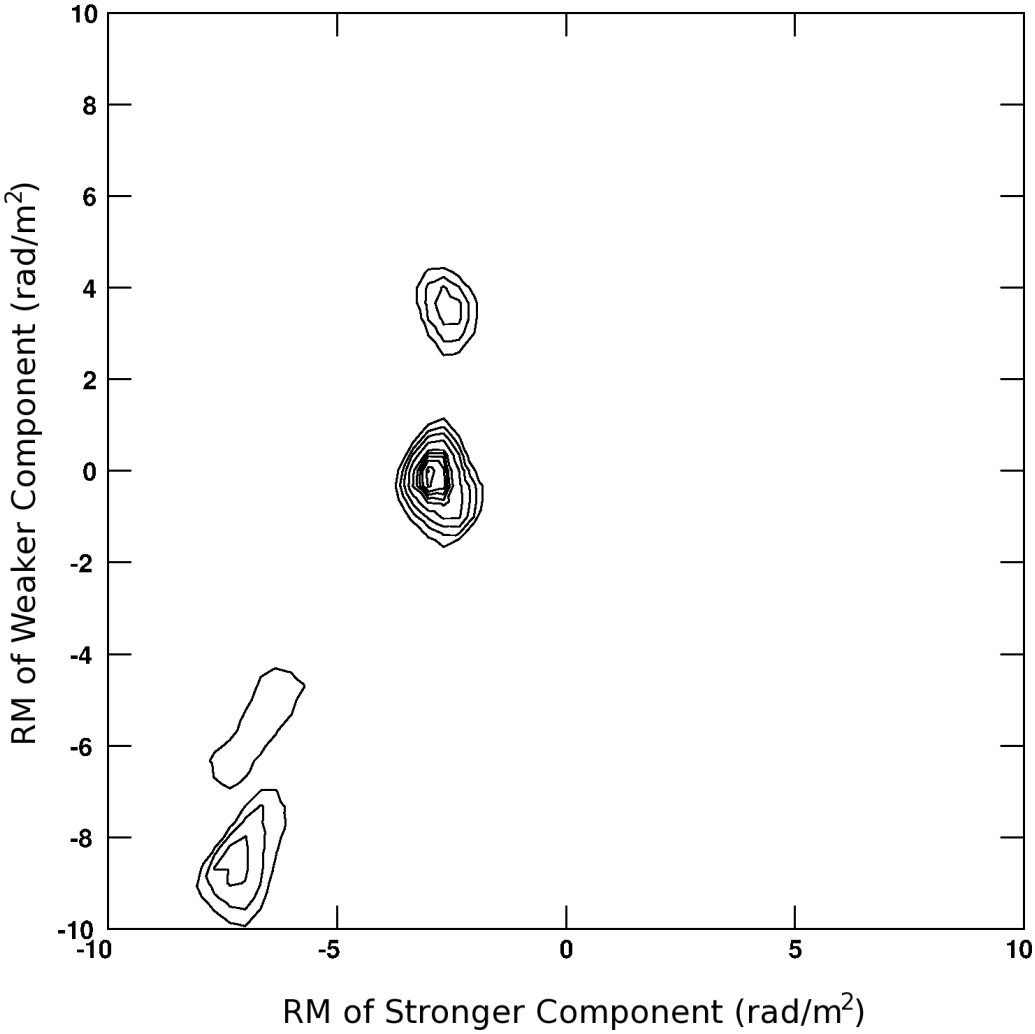

Figure 2.12 A cut through the χ^2 surface for our q, u vs. λ^2 model grid search for 3C33S. The contours show the deepest minima in the surface, with the best fit RMs near -3 rad/m^2 (stronger component) and 0 rad/m^2 (weaker component). Contour levels are at the probabilities of 10^{-6}, 10^{-5}, 10^{-4}, 10^{-3}, 10^{-2}, 2.5×10^{-2}, 5×10^{-6}, 10^{-1}.

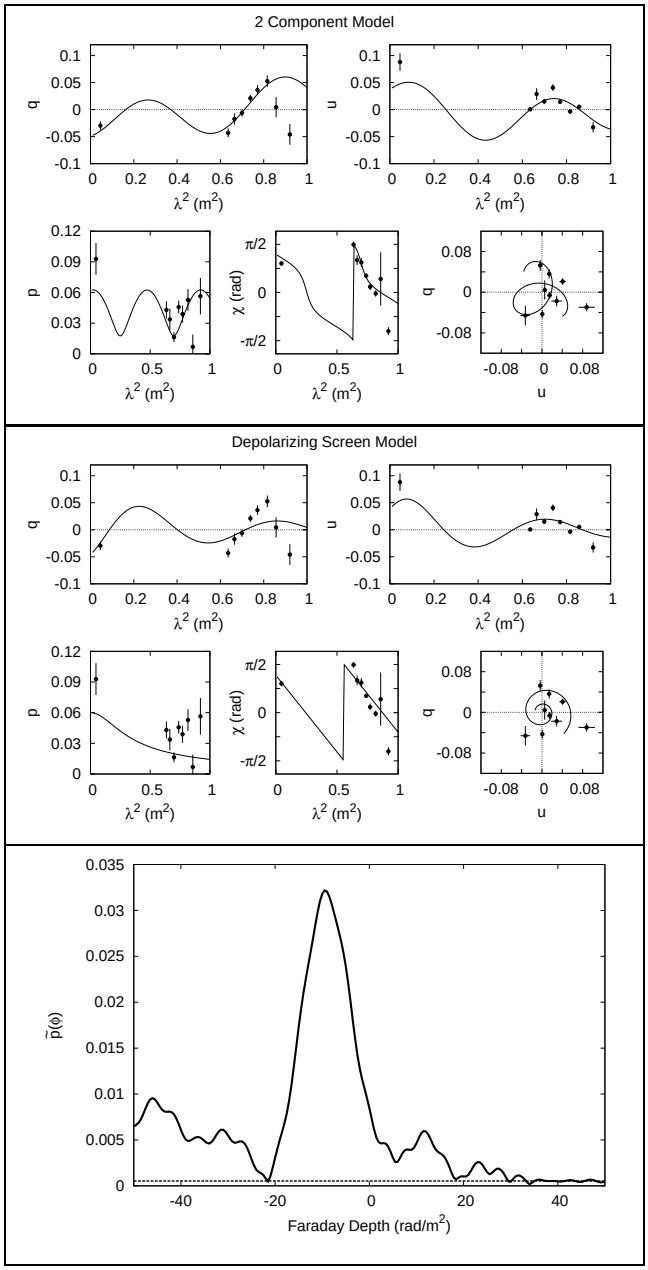

Figure 2.13 Polarization diagnostics for NVSS J010616+125116. Model fits (lines) are plotted over the observed data (points). Top panel: two component model. Middle panel: depolarizing screen. Bottom panel: magnitude of the cleaned fractional FDF (solid line) and rms of the residuals (horizontal dashed line). The linear $\chi(\lambda^2)$ fit is omitted since it is nearly identical to the depolarizing screen.

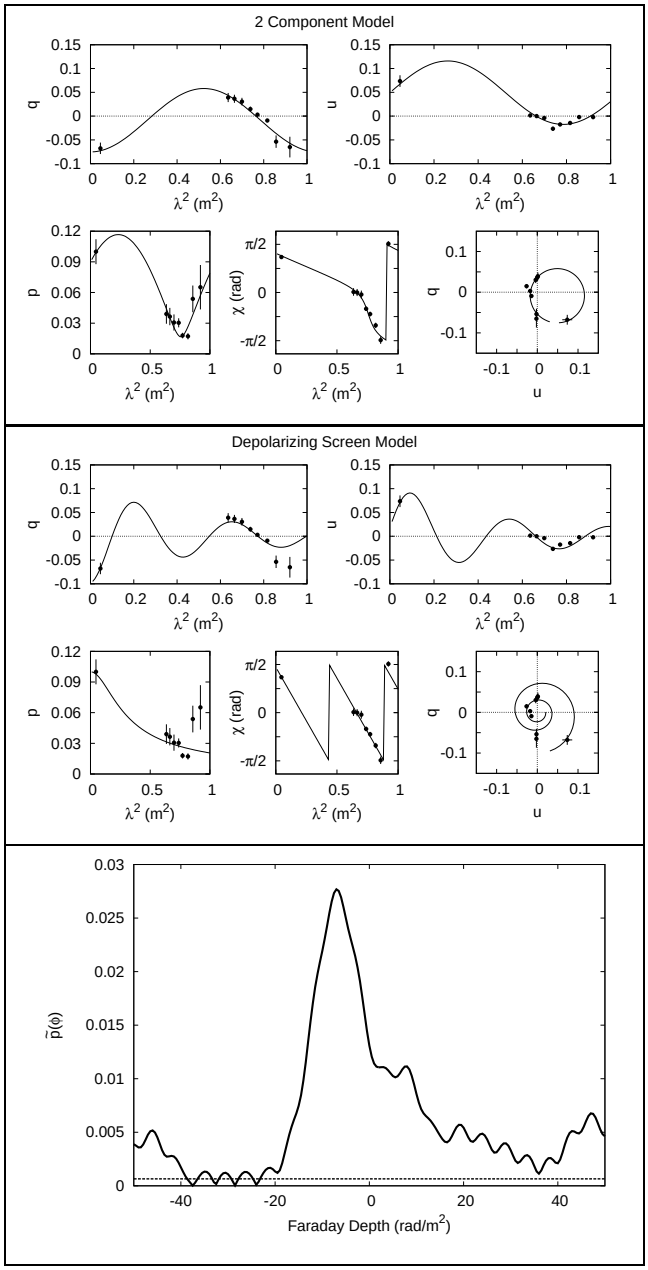

Figure 2.14 Polarization diagnostics for 3C33S. Same layout as Figure 2.13.

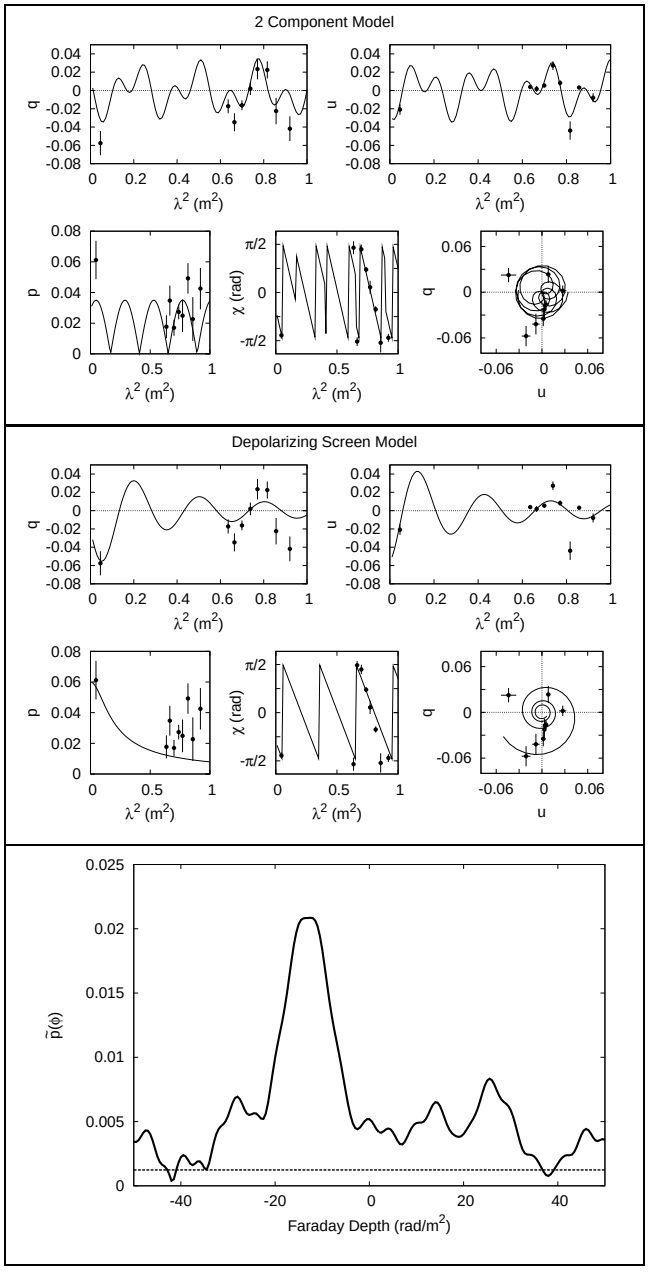

Figure 2.15 Polarization diagnostics for NVSS J011136+132437. Same layout as Figure 2.13.

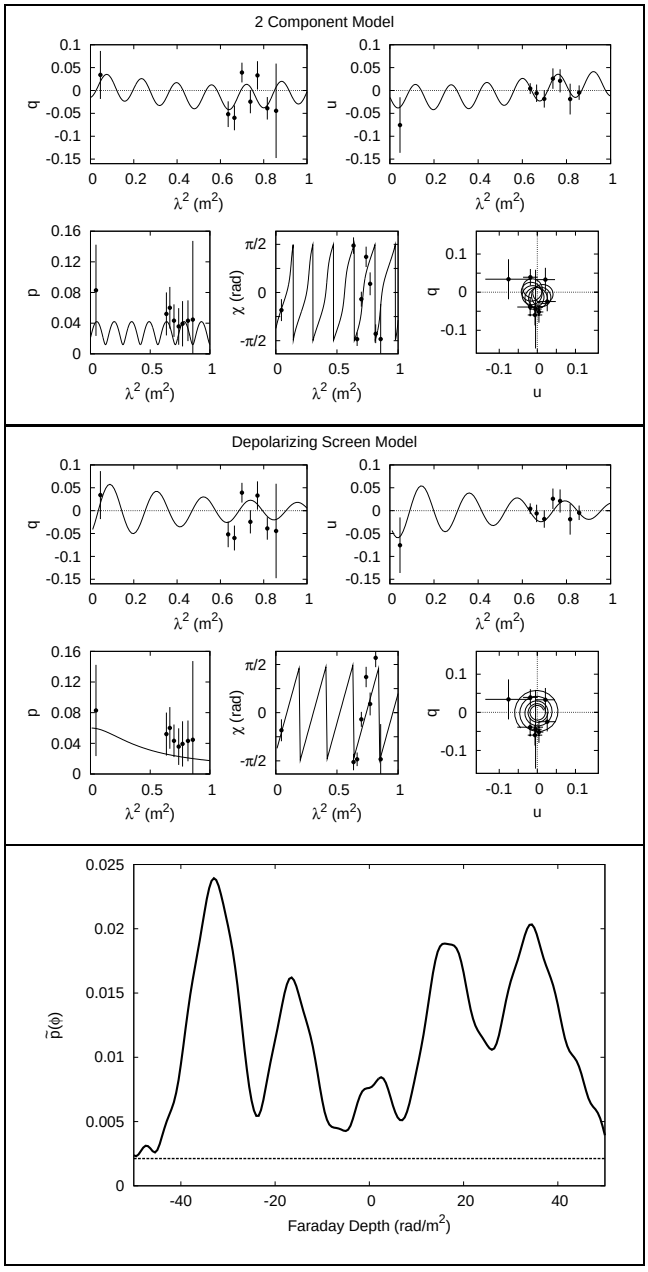

Figure 2.16 Polarization diagnostics for NVSS J011204+124118. Same layout as Figure 2.13.

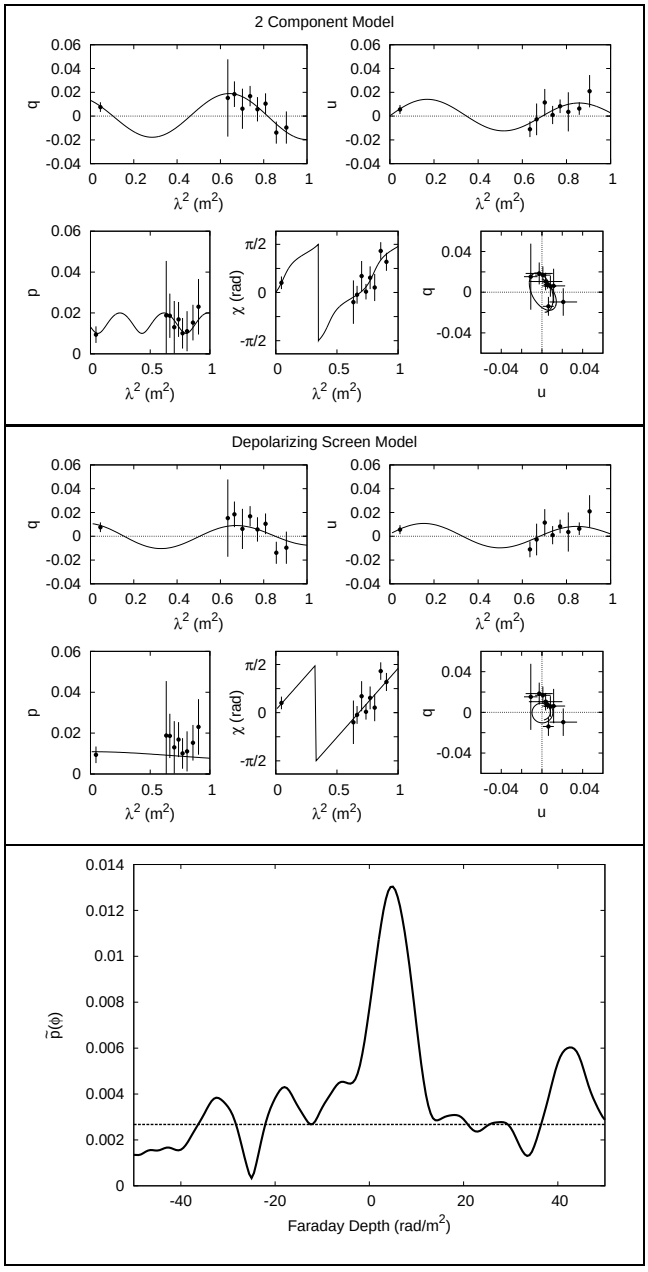

Figure 2.17 Polarization diagnostics for NVSS J125630+270108. Same layout as Figure 2.13.

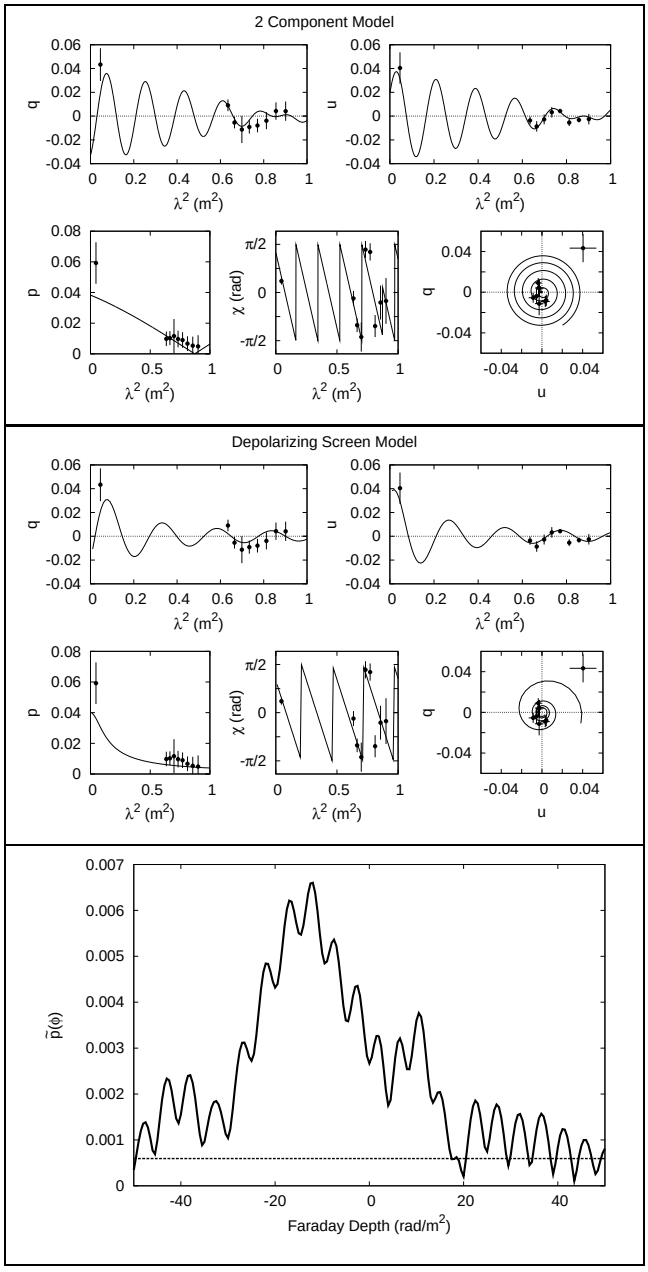

Figure 2.18 Polarization diagnostics for NVSS J162408+605400. Same layout as Figure 2.13.

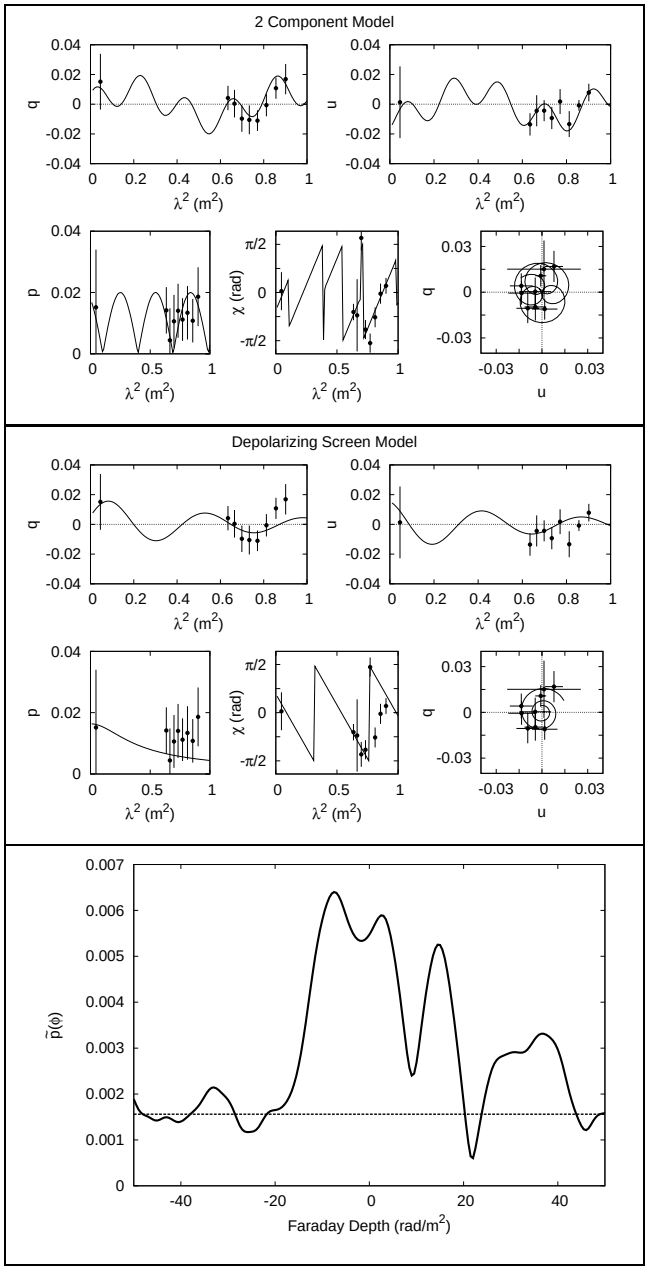

Figure 2.19 Polarization diagnostics for NVSS J162740+603900. Same layout as Figure 2.13.

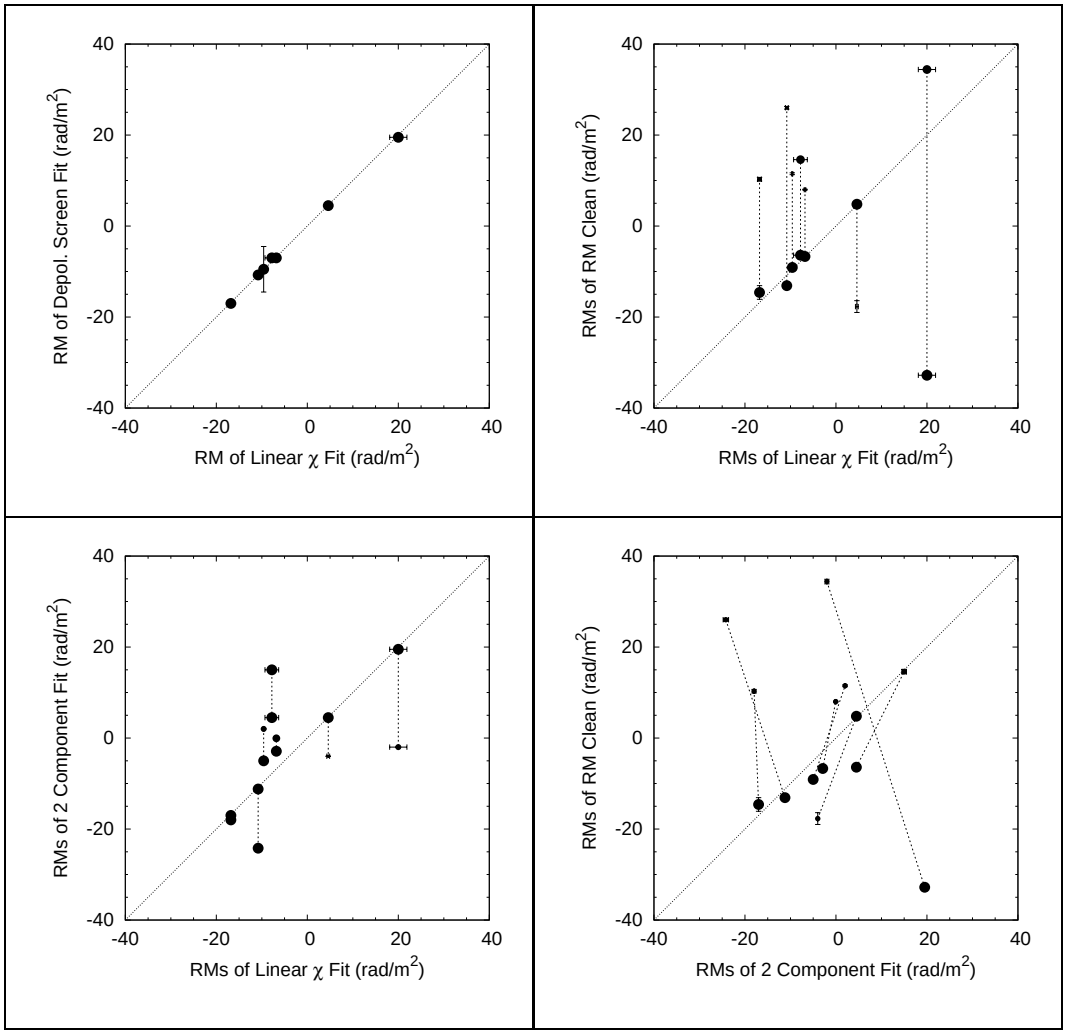

Figure 2.20 Comparison of the methods for RM determination for the seven modeled sources. **Upper left:** depolarizing screen vs. $\chi(\lambda^2)$ fit. **Upper right:** RM Synth/Clean vs. $\chi(\lambda^2)$ fit. **Lower left:** two component fit vs. $\chi(\lambda^2)$ fit. The two strongest RMs are plotted for RM Synthesis/Clean and two-component model fitting, connected by thick dashed lines for each source. Pointsize for the primary component is fixed, while the pointsize of the secondary component (relative to that of the primary) is proportional to the ratio of amplitudes for the RM components (i.e. p_2/p_1), as listed in Tables 2.6-2.12. **Lower right:** RM Synth/Clean vs. two component fit. Large and small points show RM_1 and RM_2, respectively, as listed in Tables 2.6-2.12. Errors from the fitting techniques are plotted, but are smaller than the pointsize for most sources.

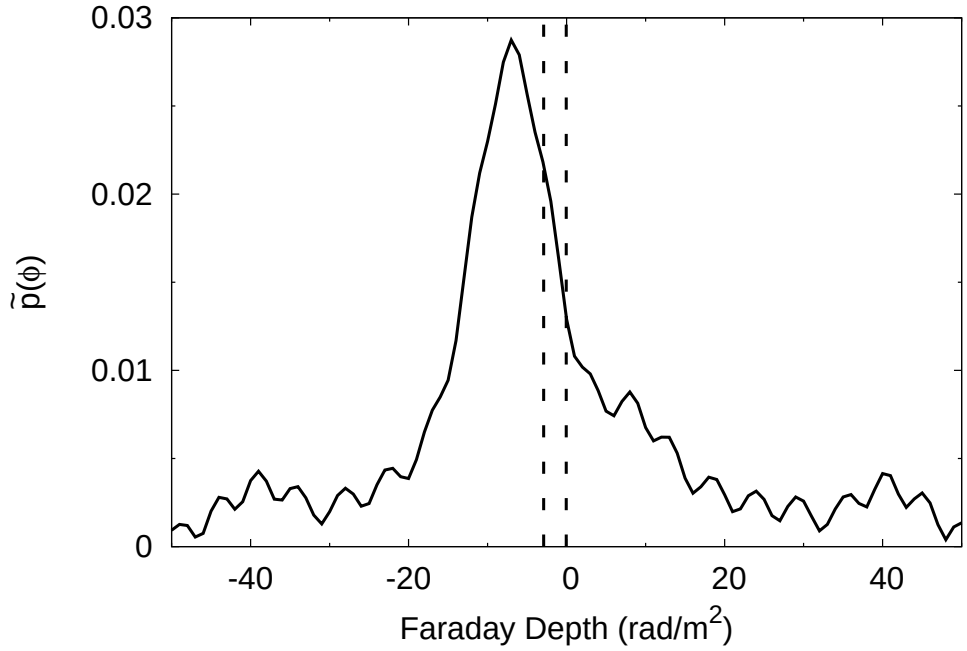

Figure 2.21 Cleaned FDF for the best fit two-component model of 3C33S. The two input RM components are at -2.9 and -0.05 rad/m^2 as discussed in the text, but the dominant peak in the Faraday spectrum is near -7 rad/m^2 with a secondary feature near +8 rad/m^2. Vertical dashed lines show the location of the two input RMs, -2.9 and -0.05 rad/m^2.

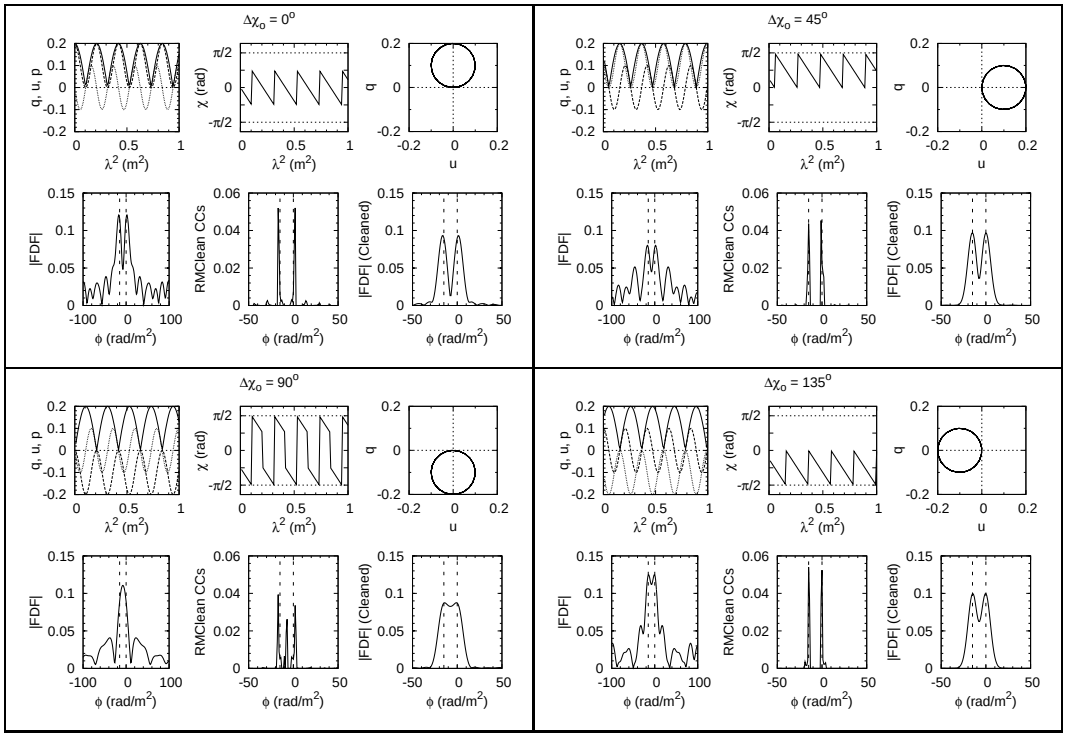

Figure 2.22 Illustration of the effect of relative phase between two RM components upon the results of RM Synthesis/Clean for various $\Delta\chi_0$ configurations. Although the two components are separated by more than the FWHM (12 rad/m^2) of the RMSF, RM Synthesis/Clean, using the same channels as in Figure 2.9, fails to properly reproduce the solution for certain relative phases. The model RMs are at -15, 0 rad/m^2, shown by vertical dashed lines in the FDFs. Plotted in each panel are: **top left:** Fractional polarization, q (dashed), u (dotted), p (solid); **top center:** polarization angle (radians); **top right:** q vs. u; **bottom left:** Dirty FDF; **bottom center:** RM Clean clean components; **bottom right:** Cleaned FDF.

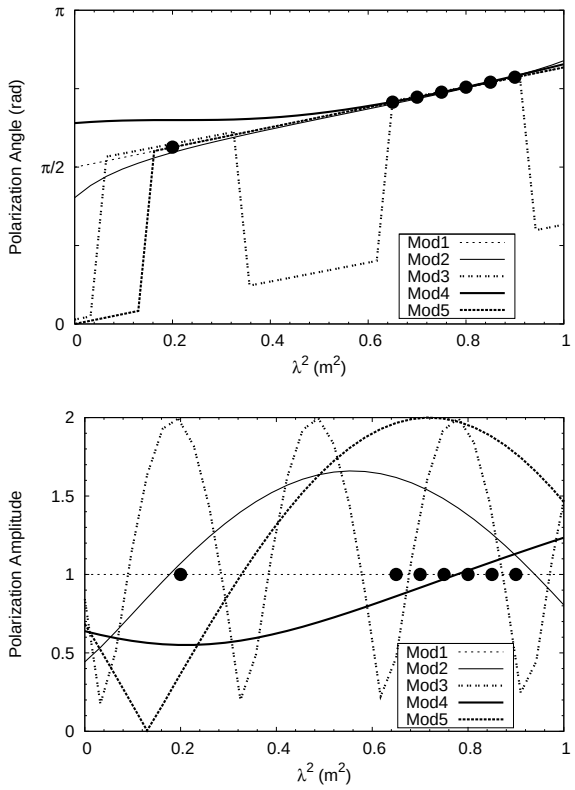

Figure 2.23 Various models illustrating the importance of considering polarization amplitude as well as angle in the long wavelength regime. A linear fit to $\chi(\lambda^2)$ yields the same "characteristic" RM in each case, but inspection of the amplitude behavior reveals the complicated nature of the various Faraday structures listed in Table 2.13. Top: Polarization angle vs. λ^2. Bottom: Polarization amplitude vs. λ^2.

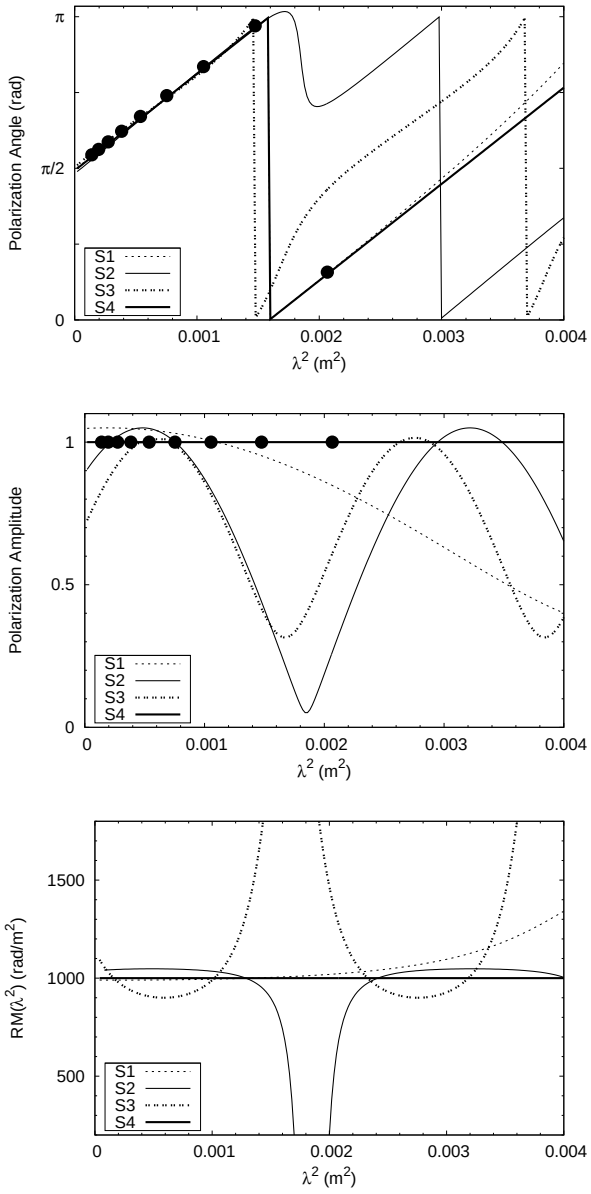

Figure 2.24 Various models illustrating the importance of considering polarization amplitude as well as angle in the short wavelength regime. A linear fit to $\chi(\lambda^2)$ yields the same "characteristic" RM in each case, but inspection of the amplitude behavior reveals the complicated nature of the various Faraday structures listed in Table 2.14. Top: Polarization angle vs. λ^2. Center: Polarization amplitude vs. λ^2. Bottom: RM(λ^2).

Chapter 3

Discovery of Megaparsec-Scale, Low Surface Brightness Nonthermal Emission in Merging Galaxy Clusters Using the Green Bank Telescope

A slightly modified version of this chapter appears in The Astrophysical Journal: Farnsworth, D., Rudnick, L., Brown, S., & Brunetti, G. 2013, ApJ, 779, 189.

3.1 Introduction

Diffuse radio synchrotron emission, on scales of hundreds to thousands of kpc, is observed in some galaxy clusters, illuminating the presence of magnetic fields and relativistic (GeV) electrons. The various morphologies of the observed structures are suggestive of multiple physical origins. Those extended radio structures not directly associated with individual galaxies (e.g., jets and lobes of radio galaxies) are tied directly to the thermal intracluster medium (ICM), and are dubbed radio halos and radio relics (see Feretti et al. 2012 for a review). Perhaps the best known example is the Coma cluster,

which contains both a Mpc-scale halo and a peripheral relic (e.g., Willson 1970; Jaffe & Rudnick 1979; Giovannini et al. 1985; Deiss et al. 1997; Brown & Rudnick 2011). Halos and relics have relatively steep radio synchrotron spectral indices of $\alpha > 1$, where we define the flux density $S_\nu \propto \nu^{-\alpha}$.

Radio halos are historically observed to be unpolarized, Mpc-scale smooth structures co-located with the X-ray ICM, observed in $\sim$1/3 of the most X-ray luminous clusters (Ferrari et al. 2008), with a few tens of radio halos observed. The central radio surface brightnesses of halos are fairly similar, with typical values ranging from $\sim$0.5 to a few μJy arcsec^{-2} (e.g., Murgia et al. 2009; Murgia et al. 2010); this low characteristic surface brightness makes halo detection an observational challenge. As the number of halo detections rises, so does the realization that radio halos are not all the same; their sizes range from hundreds to thousands of kpc, and their morphologies range from round to elongated and smooth to clumpy (e.g., Girardi et al. 2011; Bonafede et al. 2012; Boschin et al. 2012, Venturi et al. 2013). The radio luminosity in halos is well correlated with halo extent (e.g., Cassano et al. 2007; Murgia et al. 2009) and X-ray properties such as luminosity and temperature (e.g., Cassano et al. 2006).

Peripheral relics are typically elongated structures, up to and exceeding 1 Mpc in extent, found at the outskirts of a few tens of clusters. In the NVSS[1] sample, peripheral relics were found in $\sim$11% of clusters with 0.1-2.4 keV X-ray luminosity $L_X > 5\times10^{44}$ erg s^{-1} (Giovannini & Feretti 2002). Often highly polarized (i.e, a few tens of percent), observations of these relics provide strong evidence of μG magnetic fields and cosmic rays (CRs) at cluster peripheries. Predicted by cosmological simulations, peripheral relics are most likely tracers of merger or accretion processes, whereby the CRs are directly accelerated (or reaccelerated) by the resultant shocks, which also order and amplify the magnetic field (e.g., Hoeft et al. 2011; Kang et al. 2012).

There is much debate regarding the acceleration mechanism of the cosmic ray electrons (CRe) in halos, but it is now widely believed to occur in-situ due to the relatively short synchrotron lifetimes of the CRe compared to the diffusion timescales required to fill the cluster volume ($\sim$10 Mpc^3). The two most likely origins of CRe in halos are re-acceleration of mildly relativistic electrons by merger-induced turbulence − also known as the turbulent re-acceleration model − and as decay products of collisions between

[1] National Radio Astronomy Observatory (NRAO) VLA Sky Survey

the thermal ICM protons and long-lived cosmic ray protons (CRp) − also known as the hadronic model of secondary CRe. See Brunetti (2011) for a recent review.

Clues to the dominant mechanism of CRe production in halos, which may be a function of the cluster's mass or merger state (e.g., Brunetti & Lazarian 2011), can be gleaned from observables such as number counts and integrated spectral indices of halos. There is an observed bimodality in the presence of radio halos for clusters with X-ray luminosity $>5\times10^{44}$ erg s^{-1}, i.e., these clusters either have a halo with radio luminosity that correlates well with X-ray luminosity, or no radio halo at all at levels below $\sim$10% of their expected radio luminosity (Brunetti et al. 2009). This is interpreted as evidence for an evolutionary cycle whereby clusters transition between radio halo "on" and "off" states driven by merger-induced turbulence (e.g., Brunetti et al. 2009; Enßlin et al. 2011; Donnert et al. 2013). Additionally, a correlation has been recently observed between the radio luminosity and integrated SZ signal for clusters, further strengthening the thermal-nonthermal relationship in clusters (Basu 2012; Cassano et al. 2013).

In addition, turbulent re-acceleration models alone predict the presence of a population of ultra-steep spectrum (USS) halos, with $\alpha \gtrsim 1.5$, in clusters undergoing less energetic mergers (e.g., Cassano et al. 2006; Brunetti et al. 2008); for this reason, many radio halos are expected to be discovered at sub-GHz frequencies (e.g., Cassano 2010). To date, only about five USS halos are known (e.g., Feretti et al. 2012); future sensitive surveys at $\sim$100 MHz, e.g., by the Low Frequency Array[2] (LOFAR), are expected to make great contributions to this issue.

3.1.1 Detection Bias At Low z And The Case For Single Dish Observations

It is well known that radio interferometers suffer from the so-called "missing spacings problem," whereby the lack of sampling at short baselines results in decreased sensitivity to emission that is smooth on large spatial scales – e.g., Mpc-scale radio halos. Separate from the point source sensitivity of an interferometer − which is dependent only on the total collecting area and receiver properties − this problem is often times understated and ill-quantified, so we conducted a simple experiment to quantify the sensitivity of the NVSS to emission on various spatial scales.

[2] www.lofar.org

The NVSS, which has been used as a finding survey for halos and relics (e.g.Giovannini et al. 1999), was conducted using short "snapshots" which resulted in only modest u-v coverage at short spacings. As a result, the NVSS is increasingly insensitive to larger scale features, and an upper limit of $\sim 15'$ is often quoted in the literature. To estimate this effect more quantitatively, and to separate it from other issues such as signal:noise, we inserted very bright two-dimensional Gaussian components into two representative sets of NVSS u-v data at declinations of 74° and 18°, respectively. We then constructed and cleaned the images, and measured the total flux in boxes drawn manually around the source as seen in the clean image. The results of this experiment are shown in Figure 3.1. We find that the recovered flux falls to half of its true value at $\sim$10-11$'$ for snapshot observations, which will depend weakly on declination and the exact u-v coverage, field overlaps, true source shape, etc. At size scales of $15'$, only $\sim$10% of the flux is recovered. This experiment was conducted using a 1000 Jy Gaussian; clean biases and other difficulties in detecting extended sources would occur at brightness levels near the detection limit.

This is important at low redshift because at $z = 0.1$ (0.05), a 1 Mpc halo would subtend roughly 9 (17) arcminutes. One would then expect that surveys such as NVSS and WENSS[3] , which seek to maximize sky coverage by reducing integration times, might miss a significant number of radio halos at low redshift. Furthermore, halo detections will be biased towards those with high surface brightness or spatially concentrated emission – possibly excluding clusters of certain dynamical qualities. The loss of flux on large scales by interferometers can be mitigated somewhat by improving the u-v coverage for short baselines, either using longer integration times or compact arrays − thus, "filling" the aperture more completely − although increasing the integration time does not reduce the minimum baseline length. It is thus likely that the sizes and luminosities of halos at low redshift are underestimated. The lack of short spacings for interferometers can be alleviated by combining single dish data (effectively zero baseline length) with the interferometer data (e.g., Stanimirovic 2002; Fletcher et al. 2011). Single-dish observations are the only way to recover the total flux of such highly extended sources,

[3] The Westerbork Northern Sky Survey

but suffer more from confusion from point source background and diffuse Galactic foreground. For example, at 1.4 GHz the extragalactic point source confusion has an rms[4] of $\sim$90 μJy beam^{-1} for the Karl G. Jansky Very Large Array (VLA) in D-configuration (45″ beam), but $\sim$13 mJy beam^{-1} for the Robert C. Byrd Green Bank Telescope (GBT; 9′ beam, nominal). We will demonstrate that much of this confusion can be successfully removed, allowing these extended, low surface brightness halos to be observed where interferometers have failed.

Throughout this paper, unless otherwise stated, we assume $H_0 = 70$ km s^{-1} Mpc^{-1}, $\Omega_\Lambda = 0.7$, $\Omega_m = 0.3$. We use L_X to denote the 0.1-2.4 keV X-ray luminosity unless otherwise noted. All linear (angular) sizes reported are deconvolved (observed) quantities unless otherwise noted.

3.2 Observations and Data Reduction

3.2.1 GBT Observations

We observed twelve Abell galaxy clusters with the 100-m GBT between June and September 2009 (see Table 3.1). The clusters were selected due to the possibility of extended radio polarization features present in reprocessed NVSS data (Rudnick & Brown 2009), and restricted to $z \lesssim 0.1$ in order to (at least slightly) resolve structure on Mpc scales; we also included two clusters with $z > 0.1$ because they were serendipitously located in the same field of view as some of our sample members. A brief summary of relevant parameters for each cluster is listed in Table 3.2. The observations were taken with the GBT's Spectrometer in full polarization mode with a 50 MHz bandpass centered on 1.41 GHz. To create an image of each field we first employed on-the-fly mapping to create 1-D stripes of constant Declination. Each stripe was made from three successive "back and forth" scans, where Declination was held constant as the GBT was driven at a rate of 0.1° s^{-1} in Right Ascension, sampling at 2.4′ intervals. In anticipation of necessary baseline removal due to low spatial frequency gain drifts and foreground (atmospheric and Galactic) emission on scales of $\gtrsim$0.5°, our scans subtended

[4] Estimated using Equation 3E6 in Essential Radio Astronomy by Condon, J. & Ransom, S.; http://www.cv.nrao.edu/course/astr534/ERA.shtml

at least a few degrees in Right Ascension (see Table 3.1). In order to adequately sample the GBT beam, the constant Declination stripes were separated by $3.3'$. Similar observations were made each night for flux and polarization calibrators.

We give an overview here of the reduction procedure; for a more detailed discussion, see Brown & Rudnick (2011). Using an internal correlated calibrator signal ($\sim$19 K) we determined the relative X and Y dipole gains and internal X-Y phase offset. From each triplet of back and forth scans, the pair whose difference yielded the lowest rms value were averaged together to construct a stripe – thus mitigating instabilities due to receiver or atmospheric fluctuations. This yielded fully calibrated stripes with sky position and Stokes I, Q, U, V in units of surface brightness (i.e., Kelvin). Nominal I, Q, U Gaussian beam dimensions and scalings of K/(Jy beam^{-1}) were determined using the calibrator source 3C286. We note the dimensions of our beam ($\approx 9.5'$) are larger than the $9' \pm 0.1'$ listed in the GBT Proposal Guide[5] . This is likely due to a combination of factors such as: 1) the on-the-fly mapping technique, which smears the beam in the direction of telescope motion; 2) scan separation of $3.3'$ in Declination; 3) interpolation onto a regular grid to create each map. Parallactic angle correction was performed to transform the Stokes Q and U amplitudes from telescope to sky values. Due to insufficient parallactic angle coverage of a polarized calibrator, the full Mueller matrix was not computed, resulting in $\sim$1% deviations of our Q/I, U/I amplitudes with respect to the VLA calibrator manual values for 3C286. Since we were only sensitive to very high fractional polarizations ($\gtrsim$30%) for our low surface brightness features, no correction for the instrumental polarization was made. We verified that the V (circular polarization) stripes were consistent with zero to ensure that no significant residual polarization leakage remained.

Stripe Baseline Removal

Linear baseline subtraction in I, Q, U for each stripe was performed to remove the effects of receiver drifts and smooth atmospheric and Galactic foregrounds, which vary on scales $\gtrsim 30'$ (larger than the clusters observed). The "sky" for each GBT stripe was isolated by subtracting a preliminary point source model stripe, constructed from the $45''$ resolution NVSS survey. To create the NVSS stripe for each Stokes parameter, we

[5] https://science.nrao.edu/facilities/gbt/proposing

convolved the NVSS image to the nominal GBT beam measured from our 3C286 images, then interpolated to the GBT stripe sample positions. The desired linear baseline was then fit to the residuals and removed from the original stripe. Because Galactic emission is a source of confusion in some of the fields, we experimented with higher order polynomial (e.g., cubic) baseline fitting. We found that the baseline could not be well fit with higher order (i.e., >1) polynomial functions, which introduced large scale artefacts in many cases, and so we used linear baseline fitting only. This preliminary subtraction was meant only to help set the background "zero" level for each stripe and allow for image construction from the set of stripes; because the GBT gains, beam dimensions, and position correction varied slightly between fields, we later performed a more careful point source subtraction using the constructed GBT images after optimization of these parameters for each individual field.

GBT Imaging and Subtraction

The calibrated and baseline subtracted stripes were then used to create I, Q, U images for each field via interpolation with a square pixel scale of $2'$. Once the GBT images were constructed, we attempted to remove the contribution of point sources more carefully, enhancing the procedure described above; this was necessary because of small pointing errors and because the GBT beam properties vary slightly from field to field. Since we are not limited by extragalactic point source confusion in polarization, image subtraction was performed only for the total intensity data.

We now describe the subtraction method for the total intensity images. To mitigate the contribution of the NVSS image noise ($\sigma_{rms} = 0.45$ mJy beam^{-1}, $45''$ resolution), which is $\approx$5.5 mJy beam^{-1} at the nominal $9'$ GBT resolution, we first clipped each full resolution NVSS image at $3\sigma_{rms} = 1.35$ mJy beam^{-1}. The clipping procedure results in a small loss of flux for compact sources; the residual errors due to this are much less than the other sources of error in the final images. We then optimized a set of six parameters to yield the lowest GBT-NVSS rms residuals around several moderately bright ($\sim$100 mJy beam^{-1}) sources in the vicinity of each target. The parameters fit were: beam major and minor FWHM dimensions, θ_{Bmaj} and θ_{Bmin}, and position angle, ϕ_{Bpa}; x and y image shift; and flux scaling (Kelvin to Jy beam^{-1}). In general, the shifts applied to each GBT image were $\lesssim$0.5 pixels in Right Ascension and zero pixels in Declination.

The optimized scaling from Kelvin to Jy beam^{-1} was applied to each GBT image; the flux scaling varied by $\lesssim$2% from field to field.

Figure 3.2 illustrates the point source removal process for the A2319 field, displaying the input NVSS and GBT images, and the resulting GBT-NVSS residual image which shows a diffuse halo-like structure along with patchy Galactic emission and typical subtraction artefacts.

A final zero-level subtraction was performed on each residual image to minimize the contribution from the local Galactic foreground, which could contaminate the measurement of the diffuse emission associated with the cluster (e.g., halo or relic). We first calculated and subtracted an initial estimate of the mean background level within an aperture of area >10 beams placed around the cluster with inner radius $\sim$1 Mpc. Potential detections were then identified by examining contour maps of the images for coherent structures above the 2σ level. All fields except for A2056 exhibited a potential detection; the residual images for A400 and A3744 contained possible extended emission associated with each cluster, but suffered from strong subtraction artefacts due to the presence of embedded radio galaxies. For the images with potential detections, the following iterative method was employed: define a "background" aperture located just outside the $2\sigma_{rms}$ contour of the potential detection, made as large as possible (but $\gtrsim$10$\times$ the area of the cluster aperture) while excluding residual artefacts, e.g., of a bright radio galaxy >30$'$ away); calculate the mean and σ_{rms} of the background aperture; subtract the mean of the background aperture from the entire image and adopt the σ_{rms} for the next iteration. For fields where no potential detection was apparent, the same iterative process was employed, but the background aperture was defined with an inner radius of 0.5 Mpc and an outer radius of $\sim$1.5 Mpc at the cluster redshift (again excluding artefacts). After each iteration, the field was reassessed for the presence of a potential detection. This process was repeated until the absolute value of the mean background level was $\lesssim$0.1 mJy beam^{-1} and changed by $\lesssim$10% between iterations; typically less than five iterations were required per field. The background level removed was generally less than a few mJy beam^{-1} for each field.

For fields where significant patchy Galactic emission was present near the cluster (i.e., A1367, A2142, and A2319), a final, more careful background subtraction was performed; we describe this process in the discussion of each relevant field in Section 3.3

and illustrate the results in Figure 3.3. The adopted value of σ_{map} (reported in Table 3.1) was then calculated within a background aperture on the final image.

The NVSS is partially sensitive to extended emission, and it is inevitable that some of our desired diffuse flux will be subtracted in some sources; we address this point for particular clusters in Section 3.3.

Residual artefacts due to non-Gaussianity of the GBT beam, imperfect image alignment, scaling, scan baseline removal, etc., remained after subtraction. This is most noticeable for bright (>100 mJy beam^{-1}) or particularly extended radio sources where the amplitudes of these artefacts are observed to be roughly 2-5% of the original peak flux. This mainly posed a problem for clusters with an embedded RG, of which there are two in our sample. We address these issues in Section 3.3.

For the polarization imaging, we used our GBT observations of the polarized calibrator source 3C286 to quantify the beam properties in Q $(610'' \times 510'', 180°)$ and U $(590'' \times 530'', 45°)$. Each Q, U image was then convolved to a common beam size $(10.5' \times 10.0', 0°)$, which we adopted as our "effective" GBT polarization beam. Images for P (linear polarization intensity) and χ (linear polarization angle) were then constructed in the usual way, i.e.:

$$P = \sqrt{Q^2 + U^2} \tag{3.1}$$

$$\chi = \frac{1}{2} \arctan \frac{U}{Q}. \tag{3.2}$$

No correction was made for the polarized noise bias since our only detection, A1367, was at a high signal to noise ratio.

3.2.2 VLA Observations of A2319

Abell 2319 was observed on the recently upgraded VLA in its D-configuration at 1.4 GHz for three 7-hour sessions on March 27, March 28, and April 5, 2010 with 20 newly-configured antennas. Two pointings were used, centered at 19h21m15s, 43°52′ and 19h20m45s, 44°03′, with the northwest field added because of residuals seen from a beta-function fit to the Rosat PSPC X-ray data (Feretti et al. 1997).

Data were taken in two bands of 128 MHz bandwidth each, centered at 1328 and

1860 MHz. Due to interference and receiver problems only the lower frequency band is presented here, and approximately 30% of those data were also flagged as problematic. Calibration and self-cal using both amplitude and phase were performed in CASA[6] . Imaging and deconvolution were also performed in CASA resulting in two maps with resolutions of $43'' \times 39''$ at -66°. The maps were exported into AIPS[7] to be primary beam corrected and interpolated onto a single grid centered at the first pointing above. Compact sources totaling 1.1 Jy within $1000''$ of the map center were removed from the map using the multiscale filtering technique described by Rudnick (2002), with a box size of $207''$. The residual image was then convolved to a $240''$ circular beam to increase the signal:noise, resulting in a sensitivity of 3 mJy beam^{-1}.

3.3 Results

From the GBT residual images we identified detections of diffuse radio emission, requiring the 3σ contour to be extended in at least one dimension with respect to the GBT beam for all detections. This identification was done separately in total intensity and polarization.

After point source subtraction, nine of the twelve clusters exhibited one or more detections of excess diffuse emission, including one in polarization as well. For the detections we measured the angular dimensions and radio fluxes within the 3σ contours. For the halo dimensions we adopt the following notation: θ_{maj} and θ_{min} are the major and minor axis angular widths as measured from the 3σ contours. The 3σ sizes were used to compare with those in the literature, where available, as listed in Table 3.2. I_{peak} and $S_{1.4}$ are the peak and integrated 1.4 GHz Stokes I fluxes, respectively, and P_{peak} and P_{int} are the peak and integrated polarized intensities, respectively. We also noted the location of the diffuse radio structure relative to the X-ray emission (e.g., centrally or peripherally located) in order to classify the nature of the emission (e.g., halo or relic).

If we assume elliptical Gaussianity to the diffuse intrinsic flux profile and a circular

[6] The *Common Astronomy Software Applications* package; http://casa.nrao.edu
[7] Astronomical Image Processing System; http://www.aips.nrao.edu

Gaussian beam (valid to <2%) of effective FWHM

$$\theta_{Beff} = \sqrt{\theta_{Bmaj} \times \theta_{Bmin}}, \tag{3.3}$$

we can estimate the deconvolved major and minor angular dimensions of the 3σ contours, θ'_{maj} and θ'_{min}, as:

$$\theta'_{maj,min} \approx \sqrt{\theta^2_{maj,min} - \Delta^2_{Beff}}, \tag{3.4}$$

where we define Δ_{Beff} as the full width of the effective circular Gaussian beam at the normalized amplitude of the 3σ contour, i.e., $3\sigma/I_{peak}$. Thus, when $I_{peak} = 6\sigma$, $\Delta_{Beff} = \theta_{Beff}$, and so on. The deconvolved angular dimensions can then be converted to linear size. L_{maj} and L_{min} are the deconvolved major and minor 3σ dimensions of our detections in kpc, and we define the largest linear scale as LLS $= L_{maj}$. For sources unresolved along the minor axis, we adopt 1/2 the beam width as an upper limit to the deconvolved linear size.

The 3σ sizes, measured angular and deconvolved linear, and fluxes for the total intensity detections are reported in Table 3.3. The integrated fluxes within the 3σ contours should be considered "biased" estimates due to the likelihood that considerable emission lies below the 3σ noise level. Errors for the angular dimensions reflect the sizes of the 2σ and 4σ contours. We report the sizes, measured and deconvolved, and fluxes for the polarization detection in Table 3.4. Errors to the integrated flux within 3σ contours, reported in Tables 3.3 and 3.4, are calculated as $\sigma_{map} \times \sqrt{N_{beams}}$, where N_{beams} is the area of the 3σ contour in beams.

3.3.1 Individual Sources

We now discuss the individual fields, including those with likely contamination, and add information from the literature. For each field we illustrate our GBT detections – for total intensity we overlay the NVSS raw image (greyscale) with the 1.4 GHz GBT-NVSS contours (red) and X-ray contours (blue). The X-ray images are from the Rosat All Sky Survey[8] (RASS) unless otherwise noted.

[8] http://heasarc.gsfc.nasa.gov/docs/rosat/rass.html

Abell 119

A119 ($z = 0.0444$) is a merging cluster, as suggested by optical analyses (e.g., Way et al. 1997; Tian et al. 2012), which show multiple substructures and are suggestive of a dynamically young system with merging along the line of sight. Markevitch et al. (1998) found evidence for a mild merger shock in ASCA X-ray data. Preliminary X-ray observations with $XMM - Newton$ (Whitaker et al. 2003) show a long, cool filament ($\sim$4 keV) stretching to the N/NE of the core, further demonstrating that this system is likely undergoing a merger. Short *Chandra* observations suggest the presence of a cold front and possible merger shock to the north of the core, indicative of a state of near core passage in the merger (Sarazin 2006).

There is no previously known detection of halo or relic type radio emission. Giovannini & Feretti (2000) found no diffuse flux at 0.3 GHz with the VLA ($60'' \times 55''$ HPBW and $\sigma_{noise} = 5.0$ mJy beam^{-1}). There is no evidence of halo emission in the 74 MHz VLA Low-Frequency Sky Survey redux (VLSSr; Lane et al. 2012) image ($80''$ resolution).

In the GBT-NVSS residual image we found an extended structure with largest linear scale (LLS) $\sim$1100 kpc and $S_{1.4} = 243$ mJy as measured from the 3σ contours (Figure 3.4). 3C29 is located at the cluster periphery, so the residual artefacts resulting from subtraction of this bright source do not appear to significantly contaminate the cluster diffuse emission. There are multiple possibilities for the physical nature of the diffuse emission; the location of the radio structure, coincident with the X-ray emission, suggests a possible halo origin. However, much or all of this diffuse flux is likely from the two tailed radio galaxies (TRGs) clearly visible in the NVSS image; it is probable that the extended radio tails have a low surface brightness component that NVSS has missed and that the GBT is picking up this missing flux. We can not rule out halo or relic type emission, and therefore consider this as "unclassified" detection, worthy of deep followup interferometric observations.

A400

Abell 400 (z=0.0244), which contains the bright double TRG system 3C75 ($z = 0.0232$), is believed to be undergoing a merger of two subgroups (Eilek & Owen 2002 and references therein). No diffuse ICM emission is apparent in NVSS or VLSSr images.

Due to the presence of the extremely bright 3C75 (>5 Jy beam^{-1} peak in the NVSS image convolved to the GBT beam), strong subtraction artefacts (∼13% of the peak in the residual image) prevented direct measurement of diffuse halo-type emission. To place a limit upon the diffuse radio emission, we integrated the fluxes inside an aperture of radius 500 kpc in both the convolved NVSS image and our GBT image. Comparison shows an excess of 352 mJy in the GBT image, which is ∼6% of the integrated NVSS flux of 6.04 Jy. It is difficult to determine how much, if any, of this is ICM emission because there is likely a contribution from the extended radio tails of 3C75. We therefore report this as an upper limit to diffuse halo emission.

Abell 1367

A1367 ($z = 0.022$), part of a filamentary supercluster structure with the Coma cluster, is a merging cluster which hosts a well known peripheral relic to the northwest. A temperature structure analysis using X-ray observations was performed by Donnelly et al. (1998), which suggested a merger of two subclusters along a SE-NW line, with the lower luminosity component to the NW. This interpretation is supported by the optical analysis of Cortese et al. (2004) which suggests the NW component is in an early merging phase with the SE component; additional merging subclusters are also present, demonstrating the active dynamical state of this system. Ghizzardi et al. (2010) detected an X-ray brightness discontinuity – which they label a "merging" cold front – ∼350″ south of the X-ray center (∼70″ from the peak) using *XMM-Newton*.

Diffuse radio emission was first detected at 1.4 GHz by Gavazzi & Trinchieri (1983) and observed again by Gavazzi & Jaffe (1987), each time labeled a radio halo. Enßlin et al. (1998) re-labeled the radio structure a relic, noting the peripheral location and irregular shape of the radio structure; they predict a small polarization of ∼4% due to the low expected viewing angle of the relic. No known halo-type radio emission associated with the cluster has been detected.

In both the total intensity (GBT-NVSS residual) and polarization images, the relic is clearly visible but adjacent to a ridge of Galactic emission that runs through the cluster. This confusing feature makes quantitative analysis difficult, and so it was removed by subtracting a large-scale Gaussian component from the total intensity and polarization images, similar to the method for A2319 (described in Section 3.3.1); see Figure 3.3.

In total intensity we find a diffuse structure at the location of the known relic with LLS $\sim$ 600 kpc and $S_{1.4}$ = 232 mJy as measured from the 4σ contours, which we use as a conservative estimate of the relic boundary due to the presence of a peculiar residual feature which does not appear to be directly associated with the relic itself; see the left panel of Figure 3.5. This arc-shaped residual feature, which is no longer a coherent structure above the 4σ level and invisible above the 5σ level, could be: a) Galactic emission not removed by our large-scale subtraction effort; b) a GBT beam side-lobe effect of 3C264; c) an NVSS imaging artefact, a common feature around many bright sources; d) cluster halo-type emission. There is tentative evidence for a bridge of emission from the relic extending SE towards the main cluster.

The relic is also detected in linear polarization, with an integrated flux of 25.4 mJy (17.5 mJy beam^{-1} peak; $\sigma_P = 1.3$ mJy beam^{-1}). Because the signal to noise ratio was sufficiently high, correction for polarization bias was unnecessary. We find a fractional polarization of roughly 18% (15%) at the location of peak polarized (total) intensity – much higher than that predicted by Enßlin et al. (1998). In the right panel of Figure 3.5 we overlay the RASS X-ray image with the GBT-NVSS total intensity and GBT polarized intensity contours.

Due to the presence of the extended radio galaxy 3C264, strong subtraction artefacts prevented direct measurement of diffuse halo-type emission. To place a limit upon the diffuse radio emission, we integrated the flux inside an aperture of radius 500 kpc in the GBT-NVSS residual image, measuring 148 mJy. It is difficult to determine how much, if any, of this is halo-type emission because there is likely a large contribution from the extended radio tails of 3C264. We therefore report this as an upper limit to diffuse halo emission.

A2056

A2056 ($z = 0.0846$) is a poorly studied member of the Corona-Borealis Supercluster (CrB-SC; e.g., Small et al. 1998). With a relatively low X-ray luminosity of $L_X \approx 1.2 \times 10^{44}$ erg s^{-1}, it is expected to host a very faint – if any – radio halo ($P_{1.4} \sim 5 \times 10^{20}$ W Hz^{-1}) by the $P_{1.4}$ - L_X correlation. It exhibits no diffuse emission in the NVSS image, and does not display any significant evidence of diffuse radio emission in the GBT residual image. We classify this as a "clean" non-detection due to the lack of residual subtraction artefacts from strong RGs present in A400 and A3744.

To estimate an upper limit to its radio halo flux we have injected synthetic Gaussian halos (e.g., Brunetti et al. 2007; Venturi et al. 2008; Rudnick & Lemmerman 2009). We simulate a radio halo by constructing a circular Gaussian halo with a FWHM = 1 Mpc, convolved with the GBT beam for the A2056 field. We then add scaled versions of this model to the original residual image until a detection (i.e., a coherent structure resolved in at least one dimension at the 3σ contour) is observed. Our halo simulation method is illustrated in Figure 3.6. The synthetic halo is unambiguously detected when a Gaussian of peak flux 8 mJy beam^{-1} is injected, so we adopt a peak value of 7 mJy beam^{-1} as the upper limit for a non-detection. To estimate a conservative upper limit for the 1.4 GHz radio luminosity, we use the total integrated flux of the model Gaussian with 7 mJy beam^{-1} peak flux (i.e., integrate the model to infinity with zero noise). The integrated flux of 15.7 mJy corresponds to an upper limit for the radio halo power of $P_{1.4} = 2.79 \times 10^{23}$ W Hz^{-1} – more than two orders of magnitude above the value predicted by the observed X-ray correlation.

Abell 2061

A2061 ($z = 0.0784$) is a CrB-SC member believed to be in a pre-merger state with the nearby cluster A2067; at their mean redshift of $z = 0.0762$, the projected distance between A2061 and A2067 is 2.5 Mpc and Rines & Diaferio (2006) note they are separated by only $\sim$600 km s^{-1} in redshift. Marini et al. (2004) suggest the presence of an internal shock $\sim 3'$ between the A2061 cluster core and a galaxy group infalling from the NE of the X-ray peak, as evidenced by an X-ray temperature jump in their *BeppoSAX* data; its presence is further supported by preliminary *Chandra* observations (Hogge et al.

2013).

A radio relic $\sim 17'$ to the SW of the X-ray peak was discovered in the WENSS and NVSS images by Kempner & Sarazin (2001), with reported fluxes of 104 mJy and 19 mJy at 327 MHz and 1400 MHz, respectively; these measurements yield a spectral index of $\alpha = 1.17 \pm 0.23$. Using the WSRT, van Weeren et al. (2011) measured the 1382 and 1714 MHz fluxes for the relic to be 27.6 and 21.2 mJy, respectively; combining their measurements with those of the literature they derived a spectral index of $\alpha = 1.03 \pm 0.09$ for the relic. The projected dimensions of the relic are estimated to be 675×320 kpc (van Weeren et al. 2011).

We detect the SW relic in the GBT total intensity image; it is not detected in our polarization image. It is marginally resolved, and the deconvolved 3σ dimensions in Table 3.3 are thus unreliable. However, it already has a measured size of 675 kpc $\times$ 320 kpc (van Weeren et al. 2011). We measure 25.3 mJy of integrated flux within the 3σ contours of the GBT residual image; this value includes $\sim$6 mJy of integrated relic flux present in the NVSS image above the clipping value of 1.35 mJy beam^{-1} which we have added back in to the residual image. Our integrated flux value for the relic is consistent, within errors, with the 27.6 mJy at 1382 MHz measured by van Weeren et al. (2011).

A radio halo was discovered in reprocessed WENSS data by Rudnick & Lemmerman (2009), who measured the 327 MHz fluxes for the halo and relic to be 270 mJy and 120 mJy, respectively, within separate apertures of radius 500 kpc. They noted that their total fluxes are suspect "because of extensive nearby emission" present in the image.

Using the GBT, we have now made the first detection at 1.4 GHz of the radio halo, measuring 16.9 mJy of integrated flux within the 3σ contours; see Figure 3.7. The elongated halo morphology, with a largest linear extent of $\sim$1700 kpc, displays the fingerlike extension towards the NE, also seen at 327 MHz by Rudnick & Lemmerman (2009) which may be associated with the NE X-ray plume originally seen in Rosat-PSPC images (Marini et al. 2004). The halo classification is tentative, since relics, internal shocks, small scale turbulent regions, etc., associated with the extension to the NE may be unresolved by the GBT, appearing to be a coherent, Mpc-scale structure. There appears to be a blending of the SW relic with the halo in the GBT image or perhaps a

bridge of emission joining the two structures, as evident in Figure 3.7.

No evidence of a radio halo was found by van Weeren et al. (2011) at 1382 MHz with the WSRT, although a few small patches of diffuse radio emission are apparent in their WSRT image at the location of our GBT halo detection. Their 1σ rms sensitivity of 22 μJy $(32'' \times 16'' \text{ beam})^{-1}$ equates to a 3σ detection limit of $\approx$41 mJy beam^{-1} at the GBT resolution ($570'' \times 560''$), well above the peak flux of 13.5 mJy beam^{-1} observed in our GBT image. Thus, it is not surprising that the radio halo was not detected by van Weeren et al. (2011).

To explore the possibility of an inter-cluster filament between A2061 and A2067, we show the GBT view of the A2061-A2067 system at $11'$ resolution in Figure 3.8. At the 2σ level we see an apparent bridge of emission between the clusters.

We also reprocessed the WENSS data to mitigate residual contamination from point sources; once convolved to the GBT resolution, this yielded a more reliable estimate of the 327 MHz halo flux within our GBT halo boundary (defined by the 3σ contour) to be 250$\pm$42 mJy. By combining the new 327 MHz halo flux with our 1.4 GHz measurement, we derive an integrated flux spectral index of $\alpha_{0.3}^{1.4} \approx 1.8 \pm 0.3$ for the halo. This results in a tentative classification of the halo in A2061 as an ultra steep spectrum source, a class of objects whose spectral behavior has serious implications for the nature of halo generation – we will return to this topic in Section 3.6.2. We note that the WENSS image shows the halo to extend several arcminutes northeast beyond the GBT halo boundary, and reiterate that our spectral index estimate is for the emission within the boundary defined by our GBT 3σ contour.

Abell 2065

A2065 ($z = 0.0726$) is also part of CrB-SC. Markevitch et al. (1999) suggest A2065 is in the late stage of an ongoing merger, as evidenced by ROSAT and ASCA X-ray observations which show a double gas density peak about two central galaxies that appear to have survived a merger shock passage. Similarly, Belsole et al. (2005) used *XMM-Newton* X-ray observations to label A2065 an ongoing merger of two subclusters in a compact phase, the evolutionary state of mergers where resultant strong shocks in the ICM are most easily detected. They also state that the relatively cool main core suggests that the colliding object was probably of smaller mass, but that the quality

of their observations are not good enough to be certain. Chatzikos et al. (2006) used *Chandra* to detect a discontinuity they identify as a probable cold front and two "cold" cores coinciding with the cluster cD galaxies. They suggest that evidence of shocks to the SE of the merger appear in the temperature maps, and that the deprojected density distribution in that region indicates the presence of a supersonic flow with $M \approx 1.7$; the quality of the data do not allow them to definitively distinguish between the shock wave and cold front interpretation for the discontinuity. Bourdin & Mazzotta (2008) detected a bow-like feature with *XMM-Newton* that corresponds to the discontinuity detected by Chatzikos et al. (2006). The X-ray brightness discontinuity is also detected $\sim$100″ SE of the X-ray center by Ghizzardi et al. (2010) in an *XMM-Newton* study, where it is classified as a cold front. There is no known detection of diffuse radio emission in the literature for this cluster.

We detect a smooth diffuse structure of $S_{1.4} = 32.9$ mJy, roughly 1 Mpc in extent, within the 3σ contours; see Figure 3.9. Due to its $\sim$1 Mpc size and peak location, which is roughly coincident with the X-ray peak, we classify this structure as a possible giant radio halo. The location of our radio centroid is $\sim$3.5′ (290 kpc) SE of the X-ray peak in the RASS image, which corresponds roughly to the location of the *Chandra* surface brightness discontinuity observed by Chatzikos et al. (2006).

Abell 2067

A2067 ($z = 0.073858$), a relatively low X-ray luminosity cluster ($L_X \sim 4 \times 10^{43}$ erg s^{-1} in the 0.1-2.4 keV band), displays an elongated morphology in the RASS image. Marini et al. (2004) used *BeppoSAX* X-ray observations to estimate the ICM gas temperature to be $kT \sim 1.5$ keV. Likely in a pre-merger state with A2061, there appear to be internal dynamics as well; this is suggested by the presence of two dominant galaxies – one near the X-ray peak and the other $\sim$4.3′ to the south along an X-ray extension illuminating a galaxy overdensity (Marini et al. 2004). There is no previous detection of diffuse radio emission in the literature

We detect a marginally resolved feature in total intensity $\sim$12′ to the north of the X-ray peak; see Figure 3.7. Within the 3σ contours, we measure a flux of 12.4 mJy and LLS of $\sim$800 kpc. We classify our detection as a possible radio relic based on its peripheral location with respect to the X-ray ICM emission; there is no evidence for a

giant radio halo.

Abell 2069

A2069 ($z = 0.116$) is undergoing a merger between two main X-ray components separated by $\sim 9'$; Owers et al. (2009) detected a cold front in the smaller component, A2069B ($z = 0.1178$). They suggest the cold front has arisen due to gas sloshing after an encounter with A2069A, with the subcluster motion primarily in the plane of the sky.

We have made the first detection of Mpc-scale radio emission in A2069, and classify this as a possible radio halo due to its coincidence with the diffuse X-rays; see Figure 3.10. The radio emission, $\sim$2.8 Mpc long with integrated flux of 28.8 mJy, coincides roughly with the elongated X-ray emission connecting and surrounding the two main cluster components. The radio peak is offset to the north of the X-ray peak (and location of A2069A) by $\sim 4'$ ($\sim$700 kpc in projection), in the direction of A2069 and its cold front. The radio halo axial ratio, as measured by the 3σ contour, is $L_{maj}/L_{min} \approx 3$, which is at the high end for typical halos. Another possible scenario is the existence of one or more merger-induced radio relics or small scale halo-like structures. Rudnick & Lemmerman (2009) provide an upper limit at 327 MHz of 70 mJy for the diffuse flux within a 500 kpc radius of the X-ray centroid. Using an aperture of 500 kpc radius centered at the location of the X-ray centroid we measure a GBT 1.4 GHz flux density of 10.7 mJy; this yields an upper limit to the spectral index from 327 MHz to 1.4 GHz of $\alpha_{0.3}^{1.4} \lesssim 1.3$ in this region.

Giovannini et al. (1999) detected a diffuse radio structure $\sim$6 Mpc SE of the cluster center in the NVSS survey, but classify it as "uncertain" in type, although they speculate that it could be a relic; estimates of the flux and dimensions are absent. By inspection of their radio image, this feature appears to be $\sim 5'$ in extent, and corresponds to an unresolved radio feature in our GBT-NVSS residual image (not shown) that is $\sim 30'$ ($\sim$4 Mpc in projection) SE of our halo-like detection. There is no significant X-ray emission at this location. It could be a peripheral relic, as Owers et al. (2009) mentions that the X-ray structure of A2069A is elongated in this direction (SE-NW). Inspection of the NVSS full resolution image reveals several radio galaxies in the vicinity (between this feature and the cluster core, about 15-20$'$ SE of the cluster core) and a corresponding

feature in our residual image, so perhaps this is some diffuse emission from one or more TRGs.

Abell 2073

A2073 ($z = 0.1717$) is a poorly studied cluster in the direction of CrB-SC but likely too distant to be dynamically associated. Flin & Krywult (2006) find evidence of substructure in the optical galaxy distribution, and suggest this may be a dynamically young system. This cluster has not been studied in detail in X-rays, although it does have an integrated X-ray flux listed in Ebeling et al. (2000), with a corresponding 0.1-2.4 keV X-ray luminosity of 1.9×10^{44} erg s^{-1}. There is no known detection of diffuse radio emission in this cluster.

We detect an extended radio feature of 21.7 mJy within the 3σ contours, with a LLS of 2.5 Mpc; see Figure 3.11. The peak of the radio flux is to the north of the X-ray peak by $\sim$5.5$'$ ($\sim$700 kpc in projection). Given the peripheral location of the radio structure with respect to the X-ray ICM emission, we classify this as a possible relic source.

Abell 2142

A2142 ($z = 0.0894$), whose diffuse X-ray emission is elongated SE-NW, was the first cluster where X-ray cold fronts were discovered with *Chandra* (Markevitch et al. 2000). The origin(s) of the two *Chandra* cold fronts near the X-ray core has long been debated (e.g., Markevitch et al. 2000; Markevitch & Vikhlinin 2007); it is now widely accepted that gas sloshing in the core is at least partly responsible. Optical analysis by Owers et al. (2011) shows evidence of minor merging activity which they suggest may also play a role in the formation of the cold fronts. This merging activity could be inducing turbulence and creating an extended, low surface brightness radio halo. Recent *XMM-Newton* observations have revealed a third X-ray cold front nearly 1 Mpc SE of the core (Rossetti et al. 2013), the largest CF to cluster center distance known to date.

A2142 was originally suggested to host a radio halo by Harris et al. (1977). Giovannini et al. (1999) detected diffuse emission in the NVSS with a size of $\sim$350 kpc but reported no flux measurement. VLA observations by Giovannini & Feretti (2000) yielded a 1.4 GHz flux of 18.3 mJy and an extent of 270 kpc (roughly $3' \times 4'$) to the diffuse synchrotron emission, located in the core just north of the southern central cold

front detected by *Chandra*. The sub-Mpc extent of the diffuse emission led to its classification as a mini-halo (MH), although A2142 lacks other qualities typically observed in MH systems – such as a relaxed X-ray ICM morphology and central AGN (e.g., Govoni et al. (2009)).

We reduced confusion from nearby large-scale Galactic emission by subtracting a large-scale Gaussian component from the total intensity image, similar to the method for A2319 (described in Section 3.3.1); see Figure 3.3.

In order to represent the total diffuse emission, we added back in the $\sim$4 mJy of diffuse emission from the NVSS which had been subtracted. Within the 3σ contours we measure a structure elongated in the same SE-NW orientation as the diffuse X-rays, with LLS of $\sim$2.2 Mpc and $S_{1.4} = 64.0$ mJy; see Figure 3.12. This halo-like structure extends beyond the *XMM-Newton* cold front to the SE, hinting at a possible connection between the two phenomena.

Abell 2319

A2319 ($z = 0.0559$) is a merging cluster which hosts a well known GRH. Ghizzardi et al. (2010) detected an X-ray brightness discontinuity, which they label a "merging" cold front, $\sim$150″ SE of the X-ray center using *XMM-Newton*.

Feretti et al. (1997) studied A2319 in detail at 20 cm and 90 cm with the VLA and WSRT, providing halo flux and size measurements at multiple frequencies. Noting that they likely miss low surface brightness emission due to missing short baselines, they report an integrated flux at 1.4 GHz of 153 mJy and an average surface brightness of $\sim$0.45 μJy arcsec^{-2} after subtraction of discrete sources. They report a largest linear extent of 1320 kpc, which yields 1030 kpc in our cosmology. Giovannini et al. (1999) reported a flux of 23 mJy and an extent of 420 kpc (310 kpc in our cosmology), measured from the NVSS image. We estimate that roughly 12 mJy of diffuse flux remained in the raw resolution NVSS image after 3σ clipping, which would then be absent from our GBT-NVSS residuals. This is only $\sim$3% of the integrated flux in our residual image, and so we have chosen not to attempt a recovery of this lost flux as we did for A2142.

We attempted to mitigate the large scale Galactic emission, which is patchy on $\sim$1° scales. To do this, we modeled the Galactic emission in the vicinity of A2319 as a very large vertical Gaussian (3600″ $\times$ 580″), convolved with the GBT beam. This

was subtracted from the original GBT-NVSS residual image, and the background level of the residual image was then rezeroed in the cluster vicinity. The Galactic structure evident in Figures 3.2 was greatly reduced, and the effective map rms lowered by nearly a factor of two; see also Figure 3.3.

Within the 3σ contours we measure a LLS of 2 Mpc and an integrated flux of 328 mJy (see Figure 3.13, left panel), more than twice the integrated flux found by Feretti et al. (1997). We used the 0.4 GHz and 0.6 GHz flux measurements reported in Feretti et al. (1997) and our 1.4 GHz flux measurement to derive a single spectral index from 0.4 GHz to 1.4 GHz of $\alpha_{0.4}^{1.4} = 1.2$ with only a slight steepening at 0.6 GHz, contrary to the report of Feretti et al. (1997).

The halo is also detected in our VLA image (Figure 3.13, right panel), which shows an extension to the NW in the direction of the X-ray excess found by Feretti et al. (1997). The residual, diffuse flux within $1000''$ of the center is 270±25 mJy, although the noise value is only a rough estimate. Approximately 50 mJy of diffuse emission was also removed by the filtering process, yielding a total diffuse flux of approximately 320 mJy, virtually the same as determined by our GBT measurements. A more precise measurement of the diffuse structure and total flux will be made combining these measurements with higher resolution (C-configuration) data in a future publication.

A3744

A3744 (z=0.0381) is a poorly studied cluster whose diffuse X-ray emission, concentrated near the cluster center, has 0.1-2.4 keV luminosity $L_X \approx 1.8 \times 10^{43}$ erg s^{-1} (Böhringer et al. 2004). The cluster contains two bright tailed radio galaxies, NGC 7016 and NGC 7018, near the cluster center. Rudnick & Brown (2009), after a reprocessing of the NVSS polarization data, found large scale polarization features coincident with the tailed radio galaxies. In addition they found a polarized structure ∼1.8 Mpc east of the cluster center, ∼1.4 Mpc in extent, which seems to have no total intensity counterpart. They suggest that this could be a peripheral relic structure, a rarity in clusters with such low L_X.

Due to the strong subtraction artefacts (∼10% of the peak value in the residual image) from the bright radio galaxies, we estimated an upper limit to diffuse cluster emission by measuring the integrated fluxes inside an aperture of radius 500 kpc in

both the NVSS image (convolved to the GBT beam) and our GBT image (no NVSS subtraction). Comparison revealed an excess of 1.14 Jy in the GBT image, which is $\sim$11% of the integrated NVSS flux of 10.5 Jy. As we are unable to separate the radio galaxy flux from the GBT measurement, we report this as an upper limit to the diffuse flux.

Although we detect the (unresolved) central radio galaxies in polarization, we do not detect – in either total intensity nor polarization – a structure corresponding to the peripheral Mpc-scale polarization feature reported in Rudnick & Brown (2009).

3.3.2 Residual Contamination From Faint Radio Galaxies

It is likely that some of the residual flux in our GBT detections comes from faint cluster radio galaxies that are below the NVSS detection limit and, hence, not subtracted in our procedure. We evaluate this contribution for each halo detection by using cluster radio luminosity functions (RLFs) and, for three of the clusters, deep interferometric data.

The published luminosity functions (Ledlow & Owen 1996; Miller & Owen 2003; Branchesi et al. 2006) use data from low and high redshift clusters with completeness down to a minimum 1.4 GHz luminosity limit of $\sim 8\times10^{21}$ W Hz^{-1} (in a ΛCDM cosmology) and some (incomplete) information down to $\sim 2.5\times10^{21}$ W Hz^{-1}. To then derive estimates for each GBT cluster, we focused on data from A2255 and 19 other nearby clusters to compute scalings between galaxy numbers, N_{gal}, and X-ray luminosities, L_X (e.g., Bahcall 1977; Abramopoulos & Ku 1983). We then integrated the radio galaxy luminosity function between 2.5×10^{21} W Hz^{-1} and the corresponding luminosity limit of the NVSS for that cluster (determined by NVSS 1.35 mJy flux clipping level). This integrated luminosity – which we boosted by a scaling of $L_X^{0.5}$ – was then converted to 1.4 GHz flux at the cluster distance, yielding an estimate of the residual contamination not accounted for in our NVSS subtraction; we list these values in Table 3.5. Due to variations in RLF determination, $N_{gal} - L_X$ scaling, etc., our estimates of residual contamination vary by a factor of $\sim$1.5 for each field (reflected in the table values). It should be noted that these estimates are biased low because the luminosity functions that we use are cut off at 2.5×10^{21} W Hz^{-1}. Although the contribution of elliptical galaxies is found to drop off at these levels (e.g., Ledlow & Owen 1996), we do not know

the contribution from starburst galaxies at such low luminosities. The cases most likely to be problematic are those where the residual flux is only about twice as large as the estimated contamination level: A2061, A2065, and A2069.

To compare these estimates of residual contamination with direct observations, we analyzed deep interferometric images of three of the five clusters with halo detections, A2061, A2065, and A2142. For A2061 we used a 1.3 GHz GMRT image graciously provided by T. Venturi and S. Bardelli (unpublished), with a characteristic 1σ rms sensitivity of $\sim$25 μJy beam^{-1} ($3'' \times 2.5''$ resolution); for A2065 we reduced and imaged archival 1.4 GHz VLA data (Program AD0375, L-band, C-configuration) with a characteristic 1σ rms sensitivity of $\sim$75 μJy beam^{-1} ($15'' \times 14''$ resolution); for A2142 we used snapshot 1.5 GHz VLA data (Program VLA11B-156; L-band, C-configuration) with a characteristic 1σ rms sensitivity of 90 μJy beam^{-1} ($11''$ resolution). These images are nearly an order of magnitude deeper than the NVSS, and are near or below the luminosity limit of the published radio luminosity functions used above. We used the AIPS task SAD to extract radio galaxy locations and fluxes, and established cluster membership based on published redshifts in the SDSS catalog. Where available, spectroscopic redshifts were used; for a few sources the photometric redshift errors made their cluster membership uncertain, so we estimate the residual contamination with and without these sources. To summarize:

- For A2061 we find that the NVSS subtraction missed roughly 1.4 mJy of faint RG flux, much lower than the 9-13 mJy estimated by extrapolation of the published RLFs. This lowers our estimate of the halo flux in A2061 from 16.9 mJy to about 15.4 mJy.

- For A2065 we find that the NVSS subtraction missed roughly 5-9 mJy[9] of faint RG flux. This is in reasonable agreement with the 11-15 mJy estimated by extrapolation of the published RLFs. This lowers our estimate of the halo flux in A2065 from 32.9 mJy to 23-28 mJy.

- For A2142 we find that the NVSS subtraction missed roughly 8.3 mJy of faint RG flux. This is roughly a factor of two lower than the estimation of residual

[9] The uncertainty comes from the inclusion/exclusion of two RGs whose large photometric redshifts (with large errors) make their cluster membership uncertain.

contamination using published RLFs, and lowers our estimate of the halo flux in A2142 from 64.0 mJy to 55.7 mJy.

Thus we conclude that the level of contamination for each cluster that is expected from the published RLFs is likely an overestimate, although the unknown contribution from starforming galaxies is an issue that needs further investigation. This is most problematic for the low surface brightness detections in A2061 and A2069.

3.3.3 Tentative Classification Summary

We now summarize the classifications of our total intensity detections. Because we are resolution limited these classifications are considered tentative except where already classified by interferometric observations:

- *Radio Halos* − A2319 hosts a well known "classical" GRH for which we have increased the observed size and luminosity, as well as observed the NW extension. A2142 has now been detected as a 2 Mpc radio halo structure, in addition to the smaller, possible MH previously seen. We have made three new 1.4 GHz detections of radio halos: A2065 and A2069 (both entirely new radio halo detections), and A2061, whose radio halo has previously been detected only at 327 MHz. The diffuse detections in A2061 and A2069 may be multi-structure (e.g., halo+relic) systems.

- *Radio Relics* − A1367 and A2061 harbor known relics which we have detected in this study. We have tentatively classified our detections in A2067 and A2073 as relics due to their peripheral location relative to the X-ray emission, although interferometer observations are necessary for proper diagnosis.

- *Unclassified* − A119, A400, and A3744 each contain an excess of extended emission, some of which is very likely associated with the diffuse tails of the cluster TRGs missed by interferometers. Due to inadequate resolution, however, halo or relic type emission associated with the ICM of these merging clusters can not be ruled out. Deep interferometric observations are desired.

3.4 Analysis and Scaling Relations

In order to bring our detections into context we looked at various aspects of the diffuse radio structures: measured quantities such as physical size and surface brightness, and derived quantities such as radio luminosity and volume-averaged synchrotron emissivity.

For the five tentative halo detections, we complemented our image analysis by extracting azimuthally averaged radio flux profiles to measure characteristic sizes and explore the physical mechanisms responsible for cosmic ray production. The radial profiles were extracted from the GBT residual images using concentric annuli of width $60''$ centered on the radio centroid, yielding an average flux and standard deviation within the annulus as a function of radius. Because the point sources were already absent in our GBT residual images, only minimal masking was needed, e.g., in the presence of significant subtraction artefacts (e.g., from a nearby strong point source) or closely separated diffuse structures (e.g., the halo and relic in A2061). The average radio flux as a function of radius for each of the halo detections is shown in Figure 3.14.

Finally, for each of the halo detections we measured the X-ray concentration, a good indicator of merger activity level (e.g., Cassano et al. 2010a).

3.4.1 X-ray/Radio Luminosity Correlation

There is a known correlation between radio and X-ray luminosity for clusters hosting radio halos (e.g., Cassano et al. 2006; Brunetti et al. 2009). For each of our detections and upper limits, we plot in Figure 3.15 the 1.4 GHz radio power measured from the 3σ contours, $P_{1.4}$, vs. the literature 0.1-2.4 keV X-ray luminosity, L_X, along with the clusters in Brunetti et al. (2009). To supplement the sample of low L_X clusters where some of our clusters reside we have included clusters from Giovannini et al. (2009) and Giacintucci et al. (2011). We note that the classification of the diffuse radio structure in A1213 as a halo (Giovannini et al. 2009) is suspect − primarily due to its small size and unusual morphology − so we have omitted it from the plot. Our halo detections agree well with the observed correlation; in fact, our revised halo powers for A2142 and A2319 improve their agreement with the correlation predictions. It is apparent that the contribution of large scale, low surface brightness emission can be a significant fraction of the total radio halo power for some clusters. Our upper limits to $P_{1.4}$ for the three

non-detections are well above the observed correlation and provide little insight to the low L_X region they inhabit.

3.4.2 Radio Halo Sizes and Emissivities

The sizes of halos show a correlation with radio luminosity (e.g., Cassano et al. 2007). We now explore various measures of halo size which appear in the literature in order to compare our results with previous ones. A brief description of each characteristic halo size follows, but we refer the reader to Appendix 3.5 for further details on the methodologies employed. Note that for the following measures of size (i.e., LLS, R_H, and R_{85}), we assume a Gaussian halo profile unless otherwise stated (i.e., R_e for an exponential profile).

- The largest linear scale (**LLS**) – typically measured directly from an image's 3σ isophotes – is common in the literature. In Figure 3.16 we plot $P_{1.4}$ vs. LLS for our halo detections with 42 radio halos compiled from the literature by Feretti et al. (2012). We note that LLS can be heavily dependent upon the sensitivity of the observations.

- Another measure of halo size can be determined from the radio isophotes, following the technique of Cassano et al. (2007). Given the deconvolved major and minor widths of the 3σ contours, L_{maj} and L_{min}, we can calculate an effective halo radius ($\boldsymbol{R_H}$) by $R_H = \frac{1}{2}\sqrt{L_{maj} \times L_{min}}$. We plot our detections with the sample and derived correlation for $P_{1.4}$ vs. R_H from Cassano et al. (2007) in Figure 3.17.

- Another characteristic size of the halo can be estimated by the radius enclosing 85% of the total integrated flux ($\boldsymbol{R_{85}}$) as in Cassano et al. (2007). This measure of the halo extent is less sensitive to map noise than R_H. For each of the halo detections, we measured the observed R_{85} from the azimuthally averaged radial profiles and deconvolved it from the GBT beam using Equation 3.4. Because R_{85} is measured from the azimuthally averaged radial profile rather than directly from the image, this size measure is less sensitive to image noise than either LLS or R_H. This can result in a measurement of $R_{85} >$ LLS/2 as we see in A2065. Cassano et al. (2007) found that $R_{85} \approx R_H$ for their halo sample.

- The e-folding radius ($\boldsymbol{R_e}$) of a model halo with an assumed exponential radial flux profile can be fit to the observed radial flux profile (see Appendix 3.5) as done by Orrú et al. (2007), Murgia et al. (2009), Murgia et al. (2010), and Vacca et al. (2011). We plot the model central surface brightness, I_0, vs. R_e for each halo in Figure 3.18, along with the exponential halo and mini-halo results of Murgia et al. (2009), Murgia et al. (2010), and Vacca et al. (2011).

When considering LLS and R_H, each of our halo detections is overly large for its radio luminosity when compared to halos in the literature. As these measures of size are somewhat dependent upon sensitivity, it is not surprising that the GBT is able to detect low surface brightness emission to large cluster radii. If we consider R_e, however, we see that the likely single-structure halos A2065, A2142, and A2319 are at the high end for halo size when compared to the sample of Murgia et al. (2009), but not anomalously so. The likely multi-structure halos in A2061 and A2069, however, have very large R_e for their respective central surface brightnesses, hinting at a complex nature of the diffuse emission. A summary of the various sizes measured for our halo detections is given in Table 3.6.

Murgia et al. (2009) estimate the volume-averaged synchrotron emissivity for the exponential flux profile by assuming all the flux comes from a sphere of radius $3R_e$:

$$\langle J_{1.4} \rangle_e \approx 7.7 \times 10^{-41} (1+z)^{3+\alpha} \frac{I_0}{R_e} \tag{3.5}$$

where $\langle J_{1.4} \rangle_e$ is in erg s^{-1} cm^{-3} Hz^{-1}, I_0 is the central surface brightness in units of μJy arcsec^{-2}, R_e is in kpc, $(1+z)^{3+\alpha}$ is a factor which accounts for the k-correction and cosmological dimming of surface brightness with redshift, z, and α is the spectral index. We calculate the volume-averaged emissivities for each of our halo detections using the corresponding exponential halo model, adopting $\alpha = 1$ for comparison with the values of Murgia et al. (2009). The calculated emissivities of our sample, listed in Table 3.8, are one to two orders of magnitude smaller for most of our halo detections than the bulk of the sample in Murgia et al. (2009). Figure 3.19 displays a histogram of emissivities for our sample, along with halos and mini-halos from Murgia et al. (2009) for comparison, to illustrate this result.

3.5 Model Fitting To Radial Flux Profiles

Here we give details of the radial flux profile fitting. We use a method similar to that of Murgia et al. (2009), Murgia et al. (2010), and Vacca et al. (2011), who investigated the diffuse emission in a sample of twenty halos and mini-halos by fitting model halos of exponential radial form to their radio observations. They estimated the central (peak) surface brightness, I_0, and the e-folding radius (i.e., the radius at which $I(r)$ falls to I_0/e), R_e, by fitting the model flux profile, convolved with a Gaussian beam, to azimuthally averaged radial profiles of their observed halo emission. This was done by first constructing a 2-D synthetic image of the exponential halo, convolving with their beam, extracting the synthetic radial profile, and then evaluating the model radial profile with respect to their observations. By iterating over many (R_e,I_0) pairs they then found the optimal model which would best fit the observed data.

Similarly, we have modeled the intrinsic flux profiles using models of exponential form with the intent of evaluating the flux profiles at large radii (low surface brightness), where our GBT observations provide an advantage over existing interferometer studies. We employ the same exponential model as Murgia et al. (2009),

$$I(r) = I_0 e^{-r/R_e}, \tag{3.6}$$

where I_0 and R_e are the intrinsic (i.e., deconvolved) central surface brightness and e-folding radius, respectively.

For each model we constructed a synthetic "infinite resolution" image, convolved it with the GBT beam for that field, extracted the model radial profile, and compared it with the observed radial profile. Iterating over many (R_e,I_0) pairs enabled us to find the optimal exponential halo model.

The integrated halo flux is then computed as

$$S = \int_0^R 2\pi I(r) r dr, \tag{3.7}$$

which is analytically integrable for the simple profile assumed. For the exponential fit to the radial flux profile we analytically calculate the integrated model flux to a sufficiently large radius; as a check, we verify that this integrated model flux is consistent with

the observed cumulative flux from the azimuthally averaged radial profile used for R_{85} determination. As discussed in Section 3.4.2, we then use the formalism of Murgia et al. (2009) to estimate the volume-averaged synchrotron emissivity for the exponential flux profile by assuming all the flux comes from a sphere of radius $3R_e$ (see Equation 3.5).

We illustrate the radial fits in Figure 3.20 and report the deconvolved fitting results and calculated emissivities in Table 3.8; note that for the exponential model, $R_{85,mod} \approx 3.38R_e$. Figure 3.21 shows R_{85} and $R_{85,mod}$ vs. R_H for the halo detections, illustrating that $R_H \approx R_{85}$ is not universal, contrary to the findings of Cassano et al. (2007). Additionally, Figure 3.21 suggests that the assumption of an exponential radial profile tends to estimate a value of R_{85} larger than that observed directly from the extracted radial flux profile.

3.5.1 X-ray Concentration

We have calculated the X-ray concentration parameter (e.g., Santos et al. 2008; Cassano et al. 2010a; Brown et al. 2011) for each cluster with a tentative halo detection. Following Cassano et al. (2010a), we adopt the definition

$$c_X = \frac{S_X(r < 100 \text{ kpc})}{S_X(r < 500 \text{ kpc})}, \tag{3.8}$$

where S_X is the integrated X-ray flux within an aperture of specified radius. The concentration parameter is a measure of the dynamical disturbance of a cluster, and is a useful diagnostic of merger status. Cassano et al. (2010a) set $c_X = 0.2$ as the line between merging (low c_X) and non-merging (high c_X) clusters, while Brown et al. (2011) define $c_X = 0.156$ as that value.

Where available, we used Rosat PSPC images from *Skyview*[10] because of the higher resolution relative to the RASS images ($15''$/pixel for PSPC vs. $45''$/pixel for RASS). For A2065, the only halo detection without an available PSPC image on *Skyview*, the RASS image was used. Background subtraction was performed using statistics from a circular annulus centered on the cluster with inner and outer radii of one and two Mpc, respectively, after masking of X-ray point sources. A2061 required an irregular annulus in the 1-2 Mpc radial region due to nonuniform exposure in the region. This issue was

[10] http://skyview.gsfc.nasa.gov/

only present for $R > 1$ Mpc, and so did not affect the statistics of the 100 and 500 kpc apertures. A polygonal region including only areas of uniform exposure and absent of point sources was used, employing roughly 50% of the total annulus. Table 3.7 lists the concentration parameters calculated for the five halo detections.

Of the five halo detections, A2061, A2065, and A2069 have $c_X < 0.156$, qualifying them as merging in the scenarios of Cassano et al. (2010a) and Brown et al. (2011). Note that these are the three clusters with the lowest central radio surface brightnesses (each with $I_0 \lesssim 0.17$ μJy arcsec^{-2}) and, hence, the lowest volume averaged synchrotron emissivities among our detections. By this classification, these are the clusters with the highest level of dynamical disturbance, and thus are most likely to display a radio halo.

The other two clusters, A2142 ($c_X = 0.25$) and A2319 ($c_X = 0.18$) − the only two prior 1.4 GHz halo detections − would be classified in the definition of Brown et al. (2011) as non-merging clusters. Under the classification of Cassano et al. (2010a), however, A2319 would belong to the merging class. A2142 was once called a cool core cluster, contributing to the early classification of the diffuse emission found in the NVSS as a mini-halo. However, although it has a concentration index of 0.253, A2142 is now known to be dynamically active, with multiple cold fronts (e.g., Rossetti et al. 2013) and minor merging activity at various cluster radii from multiple optical subclusters (Owers et al. 2011). A2319 and A2142 are also the two halo detections with the highest central radio surface brightnesses (each with $I_0 \gtrsim 0.38$ μJy arcsec^{-2}) and, hence, the highest volume averaged synchrotron emissivities among our detections. In our small sample, low X-ray concentration correlates with low central radio surface brightness.

3.6 Discussion

The observed correlation between $P_{1.4}$ and L_X for clusters hosting a GRH is believed to reflect the role of the cluster merger history in the production of cosmic rays, whether by turbulent acceleration or secondary production (or both). Brunetti et al. (2009) used a sample of radio halos from the literature and the GMRT radio halo survey (Venturi et al. 2007; Venturi et al. 2008), which contained both radio halo detections and upper limits, to argue in favor of the primary mechanism of CRe generation. They describe a scenario of evolution to and from an "on-state" where the halo radio luminosity obeys

the observed correlation, dictated by the recent merger history of the cluster. For clusters with no recent or major merging activity, an "off-state" is expected at which the halo radio power is an order of magnitude or more below the "on-state" correlation value. This notion was supported by the radio power upper limits for non-detections in the GMRT radio halo survey. Brown et al. (2011) performed a stacking analysis on SUMSS[11] data, finding statistical detections of off-state halos in X-ray bright ($L_X > 5 \times 10^{44}$ erg s^{-1}) clusters, as predicted by Brunetti & Lazarian (2011).

Although our five halo detections agree well with the observed radio/X-ray luminosity correlation, they are all larger and fainter than typical radio halos. As a result, the inferred volume-averaged synchrotron emissivities and corresponding equipartition magnetic field strengths are much lower than values estimated by Murgia et al. (2009) for their sample of twelve radio halos. We note that if the tentative halos in A2061 and A2069 are composed of multiple structures (e.g., halo+relic) blended within the GBT beam, then the emissivities calculated here would be underestimated due to the overestimated filling factor. However, if they were confirmed by interferometric observations to be continuous radio structures, then they would be *extreme* cases of low emissivity halos.

3.6.1 Sensitivity Considerations And Halo Detectability

Radio halo statistics such as frequency of occurrence are important to address questions about halo bimodality and the physical mechanism(s) of halo generation (e.g., CR acceleration) and evolution (e.g., timescales).

The overall fraction of X-ray clusters hosting radio halos is small, <10% (∼40%) below (above) $L_X = 10^{44.9}$ erg s^{-1} (Cassano et al. 2008). However, the detection rate increases significantly if the sample is restricted to dynamically disturbed systems. In a statistical study of 32 disturbed clusters with $L_X \gtrsim 10^{44.7}$ erg s^{-1} and $0.2 \leq z \leq 0.32$, Cassano et al. (2010a) find a radio halo in 11 of 15 (∼73%). In this work, we find that this high fraction continues to lower luminosities; for the seven clusters with $L_X < 10^{44.9}$ erg s^{-1} which do not suffer confusion from bright radio galaxies, we detect four likely halos. Two of these are in A2061 and A2069, which are possibly multi-structure

[11] The 843 MHz Sydney University Molonglo Sky Survey; http://www.physics.usyd.edu.au/sifa/Main/SUMSS

(e.g., halo+relic) sources or contaminated by faint radio galaxies not accounted for in our subtraction procedure. We note that while our sample is neither unbiased nor large, our results are indeed consistent with a large occurrence of halos in merging systems.

Our success at halo detection at low X-ray luminosities (and hence, redshifts) is related to the superb surface brightness sensitivity of the GBT. For comparison, we can estimate the surface brightness capabilities of the GMRT using sensitivities and beam sizes from Venturi et al. (2008). The median (best) 3σ surface brightness sensitivity for their 23 GMRT observations at 610 MHz is 0.70 (0.095) μJy arcsec^{-2} at 610 MHz. With our 1.4 GHz GBT observations, we have achieved a median (best) 3σ sensitivity of 0.03 (0.018) μJy arcsec^{-2}. Assuming a synchrotron spectral index of $\alpha = 1.3$, the equivalent median (best) 3σ sensitivity for the GBT at 610 MHz would be 0.088 (0.053) μJy arcsec^{-2}, approximately eight (two) times better than the surface brightness sensitivity of the GMRT. We note that these sensitivity arguments are valid for sources that are well resolved.

In order to have unbiased statistics on clusters at low and high redshifts, it is thus critical to combine interferometric measurements, such as from the GMRT, complemented with single dish studies for low surface brightness and extended halos and the peripheries of brighter systems.

3.6.2 Nature of the Diffuse Emission

How can the radio/X-ray luminosities be in such good agreement with the classical picture of GRHs, while attributes such as size (alternatively, volume averaged emissivity) and surface brightness are not?

We argue here that the scaling of radio to X-ray luminosity for diffuse emission in clusters, tied to the thermal energy budget of the merger, is largely independent of the actual particle acceleration mechanism(s) in effect, e.g., shocks, turbulence, and hadronic collisions. While the majority of the LSS formation energy budget goes into shock heating and virialisation of the thermal gas, a portion of this energy is extracted into nonthermal components and then transferred into radiation. As we demonstrate in Appendix 3.6.3, this cycle leads to a natural correlation between nonthermal and thermal luminosities, where different mechanisms of particle acceleration resulting from mergers lead to similar scalings, e.g., between $P_{1.4}$ and L_X, but not necessarily to size.

For relics, the synchrotron emission scales with the shock acceleration (reacceleration) of CRe, which depends on the kinetic energy flux at shocks; this is intimately tied to the cluster dark matter (DM) potential and, hence, the thermal gas energy density and X-ray luminosity. For turbulent acceleration of CRe, the energy density in turbulence is again tied to that of the thermal gas due to the fact that merger shocks and oscillation of dark matter cores are the most important progenitor of large scale turbulence (not considering AGN jets which may stir the gas). In the case of secondary CRe resulting from hadronic collisions, the injection rate of CRe depends on the number density of the thermal and relativistic protons; observationally this is tied to the thermal gas density and X-ray luminosity.

We address a few possible scenarios which could account for the large sizes and low surface brightnesses of the halo-like emission regions (with a more detailed discussion of radio − X-ray scaling relationships given in Appendix 3.6.3):

- *Shocks and turbulence* − Simulations suggest that merger shocks and minor merging activity at cluster outskirts are likely to generate considerable peripheral turbulence, thus contributing significant nonthermal pressure and relatively efficient particle acceleration (e.g., Burns et al. 2010; Cavaliere et al. 2011; Vazza et al. 2011). For clusters such as A2319 and A2142, where halo emission has been previously seen but not to such large radii, we may be now picking up this extended, low surface brightness halo component previously unobserved in clusters.

- *Particle acceleration near X-ray cold fronts* − Five clusters in our sample contain one or more X-ray cold fronts, four of which host tentative large-scale, halo-like emission. The remaining cluster, A1367, exhibits excess large-scale emission in the vicinity of the cold front, but subtraction artefacts from the tailed radio galaxy 3C264 prevent us from distinguishing between halo-like emission and diffuse radio tails. These findings suggest a possible relationship between the physics of cold fronts and particle acceleration on large scales. Recent simulations by ZuHone et al. (2013) have shown that diffuse, halo-like radio emission may be generated by turbulence at X-ray cold fronts. Additionally, simulations (e.g., Iapichino et al. 2008; Dursi & Pfrommer 2008; Vazza et al. 2011) have shown significant turbulence to develop in the wake of a moving subcluster during a merger event (potentially

the same event responsible for the sloshing of the cluster core and corresponding cold front), possibly giving rise to turbulent particle acceleration.

- *Clumpy halos from multiple acceleration regions* − For less relaxed merging systems such as A2061 and A2069, evidenced by highly elongated radio and X-ray morphology and optical substructure, large scale turbulence believed to power GRHs may not have yet developed. Rather than a single, large-scale GRH structure, in dynamically young systems CR acceleration may occur in multiple regions associated with internal shocks and inhomogeneous turbulent regions producing a "clumpy" halo (e.g., Venturi et al. 2013); this morphology could be blended within the large GBT beam to give the appearance of a smooth Mpc-scale halo. As an example, the highly elongated, 2 Mpc radio structure in A2142 may arise from some combination of the multiple cold fronts present and the minor merging activity.

- *CR propagation* − Secondary models of CR acceleration have long suffered from an inability to explain the extent of very large radio halos (e.g., Brunetti 2004; Planck Collaboration et al. 2013a; Brunetti et al. 2012). This is due to the high content of CR protons required by such models at cluster peripheries (where the number density of thermal protons is very small), provided the magnetic field in these regions is not strong. However, low surface brightness halos require a smaller CRp energy density and may be powered by secondary CRe if the CR spatial distribution is very broad (Keshet & Loeb 2010).

The Ultra Steep Spectrum Halo in A2061

One prediction of the turbulent reacceleration model for halo generation, which includes turbulent reacceleration of CRe, is that the integrated radio spectrum of the halo should have a spectral index $\alpha > 1.5$ near GHz frequencies for a subset of clusters. While they are predicted to be numerous (e.g., Cassano et al. 2010b; Cassano et al. 2012), only a handful of these so-called Ultra Steep Spectrum (USS) radio halos have been observed with present radio telescopes. The prototype USS halo is A521, with $\alpha_{240MHz}^{1.4GHz} \sim 1.9$ (Brunetti et al. 2008; Dallacasa et al. 2009; Macario et al. 2013). The existence of USS is difficult to explain with purely hadronic models. USS halos are theorized to result

from conditions where turbulence is not strong enough to accelerate and maintain CRe at the energies necessary to emit at GHz frequencies, giving rise to a steep synchrotron spectrum. Cassano et al. (2010b) suggest that these USS halos should be more common in clusters with smaller mass and higher redshift, as a result of the smaller energetics of mergers and larger CRe energy losses, respectively. According to numerical simulations of turbulent acceleration in binary cluster-cluster mergers, USS radio halos are also naturally produced during the initial and final phases of the evolution of a radio halo during a merger event (Donnert et al. 2013). A USS halo in A2061 would provide more evidence for theories of turbulent halo generation. We note that the location of the peripheral relic to the SW of the cluster, suggested by van Weeren et al. (2011) to be a tracer of a shock wave from a prior cluster merger event, suggests a mature state of evolution for the merger event which created the relic-halo configuration. Sensitive interferometric observations over 100-1000 MHz frequencies are needed to resolve the synchrotron morphology and better measure the integrated radio spectrum.

A Possible Inter-cluster Filament In A2061-A2067

Simulations suggest that up to 50% of the baryonic matter at low redshift may reside in filamentary structures between galaxy clusters in a diffuse 10^5-10^7 K gas (e.g., Cen & Ostriker 1999) called the warm-hot intergalactic medium (WHIM). These filaments are presumed to funnel matter onto clusters through accretion. So far, however, these inter-cluster filaments have gone largely undetected due to the low temperatures and densities of the WHIM. Markevitch et al. (1998) found evidence for an inter-cluster filament in the A399-A401 system in their ASCA X-ray temperature map, and recent thermal SZ observations with Planck have further strengthened the case by detecting a hot (7 keV), diffuse gas bridge (Planck Collaboration et al. 2013b). That filament detection, however, is at 8×10^7 K − similar to the temperature of the gas in the clusters − making this unlikely to be a WHIM detection. Radio synchrotron emission holds promise for filament detection due to the relatively high efficiency of shocks in these low density regions (e.g., Brown 2011 for a concise review). Our tentative detection of an inter-cluster filament linking A2061 and A2067 is tantalizing, and warrants sensitive interferometric observations at $\lesssim$1 GHz.

3.6.3 Radio - X-ray Luminosity Scaling For Particle Acceleration

If gravity provides the energy budget for the nonthermal components in galaxy clusters, the luminosity of the diffuse emission should correlate with the thermal energy budget of the hosting clusters and this is expected independently of the precise mechanism that accelerates particles. The main concept here is that the energy budget of large scale structure formation is mainly channeled into the heating/virialisation of the hot gas, but that a fraction of this energy is also extracted into nonthermal components and then transferred into radiation. As we will show by considering the mechanisms of particle acceleration that are presently proposed for the origin of radio halos and relics, this cycle leads to a natural correlation between nonthermal and thermal luminosities (or cluster masses) that are not very different in slope and potentially also similar in normalization. In this case, if unresolved, relics and halos in a cluster may mix and contribute with similar importance (within an order of magnitude) to the observed radio emission. This is especially important for our paper because our observations do not have good spatial resolution. For example it should not be surprising to see that clusters like A2061 and A2069, whose diffuse radio emission is probably due to multiple components (e.g, halo+relic) not properly resolved by the GBT, follow the same correlation as classical radio halos (see Figure 3.15).

In the following we will adopt a simplified approach to derive expected thermal − nonthermal scaling relations resulting from different mechanisms that convert a fraction of the energy dissipated during mergers into particle acceleration.

Merger Shocks

The thermal energy budget in clusters is determined by the dark matter (DM) potential well. The gas traces the DM potential and is heated up to the virial temperature which is proportional to GM_v/R_v, where M_v and R_v are the virial mass and radius of the cluster, respectively. The gas reaches this temperature falling into the potential well where it is heated by shocks that form during the mass assembly of clusters. The energy flux through each shock is

$$\frac{dE_{sh}}{dt} \sim \rho_{gas} v_{sh}^3 S, \tag{3.9}$$

where ρ_{gas} is the gas density, v_{sh} is the shock velocity, and S is the shock surface area. Essentially a large fraction of this energy flux times the number of shocks determine the cluster temperature and gas energy density, yet a sizable fraction of this energy can also be converted into the acceleration (or reacceleration) of CRp and CRe (e.g., Ryu et al. 2003).

If we assume that radio relics are due to CRe accelerated at shock waves (the same shocks that heat up the gas), the energy flux generated in these CRe is

$$\frac{dE_{CRe}}{dt} \sim \eta_e \frac{dE_{sh}}{dt}, \tag{3.10}$$

where η_e is the acceleration efficiency of CRe (much smaller, typically $\leq 1\%$, than that in CRp); the acceleration efficiency depends on the shock Mach number and on the presence of pre-existing CRs in the upstream region (e.g., Kang et al. 2009), yet here we do not elaborate on this point. Under stationary conditions all of the energy injected in ultra-relativistic CRe is converted into synchrotron (B^2) and inverse Compton (B^2_{CMB}) radiation. In this case the synchrotron luminosity emitted by the downstream region[12] will be

$$L_{syn} \sim \frac{dE_{CRe}}{dt} \frac{B^2}{B^2 + B^2_{CMB}}. \tag{3.11}$$

In the case of strong B, essentially all of the energy will go into synchrotron radiation,

$$L_{syn} \sim \frac{dE_{CRe}}{dt}, \tag{3.12}$$

while for weak B only a small fraction of this energy will be in synchrotron,

$$L_{syn} \sim \frac{dE_{CRe}}{dt} \frac{B^2}{B^2_{CMB}}. \tag{3.13}$$

The velocity of the shocks from mergers is essentially of the order of the freefall velocity (e.g., Sarazin 2002),

$$v_{sh} \sim \sqrt{GM_v/R_v}, \tag{3.14}$$

[12] If we are observing at a frequency ν_o this region will extend to a distance from the shock surface $\sim v_d \tau_{age}(\nu_o)$ where v_d is the downstream velocity of the flow (in the reference frame of the shock) and τ_{age} is the lifetime of the CRe emitting at frequency ν_o in the downstream region.

and as a first approximation we can assume that the shock surface area scales with $S \propto R_v^2$ (proportional to the cluster "surface") and $\rho_{gas} \propto f_b$ (for f_b, the baryon fraction, we use virial matter density that is constant, i.e., independent of cluster mass).

So one has:

$$\begin{aligned} L_{syn} &\propto \eta_e f_b \left(\frac{GM_v}{R_v}\right)^{3/2} R_v^2 \frac{B^2}{B^2 + B_{CMB}^2} \\ &\propto \eta_e f_b M_v^{5/3} \frac{B^2}{B^2 + B_{CMB}^2} \end{aligned} \tag{3.15}$$

because $M_v \propto R_v^3$. Although here we have adopted a very basic approach, we note that Equation 3.15 is equivalent to Equation 32 in Hoeft & Brüggen (2007) in the case of strong shock approximation (and taking into account that Equation 3.15 refers to the bolometric synchrotron luminosity).

The magnetic field in galaxy clusters is likely connected with their thermal energy budget, $B^2 \propto \rho_{gas} T \propto f_b T \propto f_b M^{2/3}$, so in any case (i.e., weak or strong B) the synchrotron luminosity connected to CRe acceleration at shocks (e.g., relics) should depend on cluster M_v or alternatively on other "thermal" observables. One of the most common observables used as mass proxy is the X-ray luminosity of the cluster; note that throughout this appendix we will adopt the following notation for X-ray luminosities: bolometric luminosity, L_X, or in the 0.1-2.4 keV band, $L_{[0.1-2.4]}$.

Because $L_X \propto T^{\alpha_T}$ (where $\alpha_T \sim 3$, e.g., Arnaud & Evrard 1999; Pratt et al. 2009), the expected scaling is

$$\begin{aligned} L_{syn} &\propto \eta_e T^{5/2} f_b \frac{B^2}{B^2 + B_{CMB}^2} \\ &\propto \eta_e f_b L_X^{5/2\alpha_T} \frac{B^2}{B^2 + B_{CMB}^2} \end{aligned} \tag{3.16}$$

that in strong fields is

$$L_{syn} \propto \eta_e f_b L_X^{5/6} \tag{3.17}$$

and in weak fields is

$$L_{syn} \propto \eta_e f_b^2 L_X^{7/6}. \tag{3.18}$$

Equation 3.18 is equivalent to Equation 16 in Kempner & Sarazin (2001) if we assume

a strong shock ($\alpha = -1$ in their equation).

In our paper we use the X-ray luminosity in the 0.1-2.4 keV band. For hot clusters this approximately scales with L_X as $L_{[0.1-2.4]} \propto L_X^{1-0.6/\alpha_T}$ (e.g., Kushnir et al. 2009) implying scalings in the form $L_{syn} \propto L_{[0.1-2.4]}^{\frac{5/2}{\alpha_T-0.6}}$ and $L_{syn} \propto L_{[0.1-2.4]}^{\frac{7/2}{\alpha_T-0.6}}$ in the case of strong and weak magnetic fields, respectively ($\alpha_T \sim 3$). Note that slightly steeper scalings can be induced if we consider that the baryon fraction f_b weakly depends on cluster temperature (e.g., Dai et al. 2010).

Turbulence

One possibility for the origin of radio halos is that CRe are reaccelerated by turbulence in the ICM that can be generated during cluster mergers. In this case scaling relations between thermal and nonthermal properties depend on the scaling of turbulent energy vs. thermal energy. Regardless of the details, as a first approximation it is natural to assume that the energy injection rate of turbulent motions scales with the thermal energy density divided by a reference timescale, such as the cluster-cluster crossing time (e.g., Cassano & Brunetti 2005). In the following we closely follow the derivation from Cassano et al. (2007).

Under the hypothesis given above, the total energy flux in turbulence is

$$\frac{dE_{tu}}{dt} \propto V_{tu} \frac{\rho f_b T}{\tau_{cross}}, \tag{3.19}$$

where V_{tu} is the volume where turbulence "illuminates" the radio halo (the volume of the halo), ρf_b is the gas density within this volume, and $\tau_{cross} \sim R_v/v_i$ is a constant because the cluster-cluster impact velocity is $v_i \propto \sqrt{M_v/R_v}$.

A fraction of the turbulent energy flux is channeled into CRs (CRe and CRp); this fraction is the ratio of the damping rates of turbulence due to the interaction with a given species of particles divided by the total damping of the turbulence. For electrons the fraction is

$$f_{CRe} = \frac{\Gamma_{CRe}}{\Gamma_{th} + \Gamma_{CRp} + \Gamma_{CRe}} \propto X_e \sqrt{T}, \tag{3.20}$$

where X_e is the ratio of the CRe to thermal energy densities. The energy flux that will

be channeled into CRe is

$$\frac{dE_{CRe}}{dt} = f_{CRe}\frac{dE_{tu}}{dt}. \tag{3.21}$$

Under stationary conditions this energy flux will be essentially converted into synchrotron and inverse Compton radiation:

$$L_{syn} \propto f_{CRe} M_{tu} f_b T^{3/2} \frac{B^2}{B^2 + B^2_{CMB}} \tag{3.22}$$

where $M_{tu} = \rho V_{tu}$ is the cluster mass in the region of the halo. This can be calculated assuming hydrostatic equilibrium (isothermal gas; e.g., Sarazin 1986):

$$M_{tu} = \frac{3 k_B T R^3_{tu} \beta}{\mu m_p G}(R^2_{tu} + r^2_c)^{-1}, \tag{3.23}$$

where β and r_c are the beta-model exponent and the core radius of the cluster, respectively. Based on the analysis of Cassano et al. (2007) for 14 GRHs, $M_{tu} \propto T^a$, where $a \simeq 2 - 3$, implying a scaling between synchrotron and X-ray luminosities in the form (using $L_X \propto T^{\alpha_T}$, with $\alpha_T \sim 3$, as in the previous subsection):

$$L_{syn} \propto X_e f_b L_X^{\frac{3/2+a}{\alpha_T}} \frac{B^2}{B^2 + B^2_{CMB}}. \tag{3.24}$$

Under the assumption (as in the previous section) that the magnetic field energy density scales with the thermal energy density, Equation 3.24 implies scalings in the form $L_{syn} \propto X_e f_b L_X^{(3/2+a)/\alpha_T}$ and $L_{syn} \propto X_e f_b^2 L_X^{(5/2+a)/\alpha_T}$ for strong and weak fields, respectively. Similarly (converting L_X into $L_{[0.1-2.4]}$ as in the previous subsection), the model predicts $L_{syn} \propto X_e f_b L_X^{(3/2+a)/(\alpha_T - 0.6)}$ and $L_{syn} \propto X_e f_b^2 L_X^{(5/2+a)/(\alpha_T - 0.6)}$ for strong and weak fields, respectively ($\alpha_T \sim 3$).

Secondary CRe

An additional source of CRe in radio halos is provided by hadronic (CRp-p) collisions in the ICM. The energy injection rate of secondaries is

$$\frac{dE_{CRe}}{dt} \propto n_{th} \epsilon_{CRp} R^3_v \sigma_{pp}, \tag{3.25}$$

where σ_{pp} is the CRp-p cross-section, n_{th} is the thermal proton number density and ϵ_{CRp} is the energy density of CRp. Under stationary conditions, the total synchrotron luminosity emitted by this process is

$$L_{syn} \propto n_{th} \epsilon_{CRp} R_v^3 \frac{B^2}{B^2 + B_{CMB}^2} \tag{3.26}$$

and the bolometric X-ray luminosity is

$$L_X \propto n_{th}^2 R_v^3 T^{1/2}. \tag{3.27}$$

Consequently, defining X_p as the ratio of the CRp to thermal energy densities, we would expect (using $L_X \propto T^{\alpha_T}$ and $\alpha_T \sim 3$ as in the previous subsections) a simple scaling between synchrotron and bolometric X-ray luminosity of the hosting cluster in the form

$$L_{syn} \propto X_p L_X^{1+1/2\alpha_T} \frac{B^2}{B^2 + B_{CMB}^2}. \tag{3.28}$$

In the case of a strong B field, this is equivalent to the scaling derived by Kushnir et al. (2009), i.e., $L_{syn} \propto X_p L_X^{1+1/2\alpha_T}$ or $L_{syn} \propto X_p L_{[0.1-2.4]}^{(\alpha_T+0.5)/(\alpha_T-0.6)}$. The weak magnetic fields case in these models is ruled out by the γ-ray upper limits obtained for nearby galaxy clusters (e.g., Ackermann et al. 2010; Jeltema & Profumo 2011; Brunetti et al. 2012).

Finally, we note that, although not very different, hadronic and turbulent models predict different slopes for the nonthermal vs. thermal correlations in the case of radio halos. For example, if we focus on the L_{syn} vs. $L_{[0.1-2.4]}$ correlation using the same assumptions in the two models, in the case of strong magnetic fields the hadronic models predict a slope $\sim$1.45 while turbulent models predict a slope in the range $\sim$1.45-1.9. The slope becomes even steeper for weak fields in the turbulent model, $\sim$1.9–2.3; for reference, present observations give a slope of the correlation $= 2.10 \pm 0.17$ (Cassano et al. 2013).

3.7 Conclusions

We present results of a 1.4 GHz GBT study of twelve $z < 0.2$ Abell galaxy clusters with $L_X \sim 10^{43} - 10^{45}$ erg s^{-1}, each exhibiting some evidence of merging activity. After subtraction of point sources using images from the NVSS, we reach a median (best) 1σ rms sensitivity level of 0.01 (0.006) μJy arcsec^{-2}, and find a significant excess of diffuse emission in eleven clusters. These include two new halos and two new relics, increased sizes and integrated fluxes for known structures, and the tentative detection of an inter-cluster filament and ultra-steep spectrum radio halo in the Abell 2061-2067 system. Residual contamination from faint galaxies – e.g., starburst galaxies – is unknown, and could contribute significantly to the fainter detections. Sensitive interferometric observations are necessary to resolve the diffuse radio emission and further address the issue of residual contamination. We also present a determination of the sensitivity of the NVSS as a function of source size.

While all five of the halo-type detections agree with the observed $P_{1.4} - L_X$ correlation, their sizes are larger than typically observed for their radio luminosities, implying volume averaged synchrotron emissivities 1-2 orders of magnitude below the average of Murgia et al. (2009). We note, however, that for A2061 and A2069, the emissivities may be underestimated if these are multi-structure sources blended by the GBT beam.

The three new radio halo structures all have in common the presence of optical substructure, either an X-ray cold front or internal shock, and very low X-ray core concentration, implying all are in a relatively early stage of merging. Due to the poor resolution of the GBT images, it is not possible to distinguish between a low surface brightness GRH and a blend of multiple smaller-scale structures associated with the merging activity (e.g., internal shocks, turbulent patches), which can be blended within the $\sim 9.5'$ beam. If a blend of multiple synchrotron structures is present, then it is interesting that the integrated radio luminosity should agree with the observed correlation for GRHs, supporting the idea that the merger energy input to cosmic rays and magnetic fields may be relatively independent of the particular mechanisms of particle acceleration (see Appendix 3.6.3).

Table 3.1 Galaxy Clusters Observed

Source	z[a]	Scale (kpc/″)	R.A. (J2000)	Decl. (J2000)	Effective Beam $\theta_{Bmaj} \times \theta_{Bmin}, \phi_{Bpa}$	Local σ^{b}_{map} (mJy beam^{-1})
A119	0.0442	0.87	00:56:21.4	-01:15:47	$9.5' \times 9.3'$, 80°	6.0
A400	0.0244	0.49	02:57:38.6	+06:02:00	$9.5' \times 9.3'$, 100°	7.6
A1367	0.0220	0.44	11:44:29.5	+19:50:21	$9.5' \times 9.3'$, 80°	4.5
A2056	0.0846	1.59	15:19:12.3	+28:16:10	$9.5' \times 9.3'$, 100°	3.4
A2061	0.0784	1.48	15:21:15.3	+30:39:17	$9.5' \times 9.3'$, 100°	2.3
A2065	0.0726	1.38	15:22:42.6	+27:43:21	$9.5' \times 9.3'$, 100°	3.8
A2067	0.0739	1.40	15:23:14.8	+30:54:23	$9.5' \times 9.3'$, 100°	2.3
A2069	0.1160	2.10	15:23:57.9	+29:53:26	$9.5' \times 9.3'$, 100°	3.0
A2073	0.1717	2.92	15:25:41.5	+28:24:32	$9.5' \times 9.3'$, 80°	3.3
A2142	0.0909	1.69	15:58:16.1	+27:13:29	$9.5' \times 9.3'$, 80°	2.3
A2319	0.0557	1.08	19:20:45.3	+43:57:43	$9.7' \times 9.5'$, 110°	6.0
A3744	0.0381	0.76	21:07:13.8	-25:28:54	$9.5' \times 9.3'$, 100°	7.3

[a] Redshifts taken from the NASA/IPAC Extragalactic Database (NED)
[b] After baseline removal and point source subtraction

Table 3.2 Cluster Parameters From Literature[a]

Source	L_X (10^{44} erg s^{-1})	kT_X (keV)	$S_{1.4}$ (mJy)	$P_{1.4}$ (10^{24} W Hz^{-1})	LLS (kpc)	Class.	References
A119	1.648	5.1	–	–	–	–	1
A400	0.204	2.1	–	–	–	–	2
A1367	0.816	3.5	35	0.038	130	Relic	2, 10, 11
A2056	0.116	–	–	–	–	–	4
A2061H	2.015	5.6	–	–	N/A[b]	Halo	2, 7
A2061R	2.015	5.6	27.6	0.42	680	Relic	2, 6
A2065	2.520	8.4	–	–	–	–	2
A2067	0.439	3.1	–	–	–	–	3
A2069	4.551	7.9	–	–	–	–	2
A2073	1.908	5.6	–	–	–	–	3
A2142	10.58	11.0	18.3	0.38	200	Mini-halo	2, 9
A2319	6.995	9.9	153	1.13	1030	Halo	1, 8
A3744	0.180	–	–	–	–	–	5

[a] All parameters are corrected for cosmology, where applicable.
[b] The radio halo in A2061 was detected at 327 MHz by Rudnick & Lemmerman (2009) but no size was reported

Columns: (1) Cluster; (2) X-ray luminosity, 0.1-2.4 keV; (3) X-ray temperature; (4) Flux density, 1.4 GHz; (5) Radio luminosity, 1.4 GHz; (6) Largest linear scale of radio halo or relic type emission; (7) Classification of diffuse radio emission not associated with radio galaxies.

References: *X-ray:* (1) Ebeling et al. (1996); (2) Ebeling et al. (1998); (3) Ebeling et al. (2000); (4) Ledlow et al. (2003); (5) Böhringer et al. (2004); *Radio:* (6) van Weeren et al. (2011); (7) Rudnick & Lemmerman (2009); (8) Feretti et al. (1997); (9) Giovannini & Feretti (2000); (10) Gavazzi & Trinchieri (1983); (11) Gavazzi & Jaffe (1987)

Table 3.3 Total Intensity Results From 3σ Contours

Source	$P_{1.4}$ (10^{24} W Hz^{-1})	$S_{1.4}$ (mJy)	$\theta_{maj} \times \theta_{min}$ (arcmin)	$L_{maj} \times L_{min}$ (kpc)
A119	1.1	243±16	$27.2^{+1.8}_{-1.5} \times 15.5^{+0.5}_{-0.9}$	$1100^{+61}_{-55} \times <250^{a}$
A400	<0.48	$<352^{b}$	–	–
A1367H	<0.16	$<148^{b}$	–	–
A1367R[c]	0.25	232±28	$27.5^{+2.1}_{-2.1} \times 27.2^{+1.8}_{-1.7}$	$610^{+47}_{-50} \times 600^{+37}_{-37}$
A2056	<0.28	$<15.7^{d}$	–	–
A2061H	0.26	16.9±4.2	$21.0^{+2.8}_{-3.8} \times 10.3^{+2.0}_{-2.0}$	$1700^{+170}_{-280} \times 410^{+70}_{-70}$
A2061R	0.38	25.3±5.6	$15.8^{+1.5}_{-3.1} \times 13.7^{+2.3}_{-1.5}$	$760^{+350}_{-350} \times 290^{+170}_{-30}$
A2065	0.42	32.9±11	$16.7^{+4.3}_{-3.7} \times 16.3^{+5.7}_{-4.3}$	$1100^{+310}_{-270} \times 1000^{+460}_{-350}$
A2067	0.18	12.4±4.3	$14.2^{+8.8}_{-3.4} \times 10.5^{+3.2}_{-2.2}$	$840^{+790}_{-240} \times 240^{+250}_{-79}$
A2069	1.0	28.8±7.2	$23.7^{+2.8}_{-3.0} \times 12.0^{+1.8}_{-2.3}$	$2800^{+240}_{-290} \times 1000^{+170}_{-110}$
A2073	1.8	21.7±6.2	$17.5^{+6.2}_{-5.0} \times 11.8^{+3.0}_{-2.5}$	$2500^{+1100}_{-820} \times 1100^{+340}_{-250}$
A2142	1.3	64.0±6.1	$26.2^{+1.5}_{-1.7} \times 15.0^{+1.3}_{-1.3}$	$2200^{+68}_{-120} \times <480^{a}$
A2319	2.4	328±28	$34.7^{+3.3}_{-2.8} \times 27.3^{+2.2}_{-2.3}$	$2000^{+190}_{-160} \times 1400^{+100}_{-130}$
A3744	<0.16	$<1140^{b}$	–	–

[a] Upper limit for unresolved minor dimension (deconvolved) is set to one half the beam width

[b] Upper limit within 500 kpc radius of cluster center; may contain residual contamination from strong radio galaxies

[c] Measurements taken from the 4σ contours. Size errors reflect the dimensions of the 3σ and 5σ contours

[d] Assuming 1 Mpc Gaussian halo

Columns: (1) Cluster; (2) Radio luminosity at 1.4 Ghz; (3) Integrated 1.4 GHz total intensity flux; (4) Observed major and minor angular dimensions of the 3σ contour. Errors reflect the dimensions of the 2σ and 4σ contours (except A1367R); (5) Deconvolved major and minor linear dimensions of the 3σ contour. Errors reflect the dimensions of the 2σ and 4σ contours (except A1367R).

Table 3.4 Polarization Detection From 3σ Contours

Source	P^{a}_{int} (mJy)	$\theta_{maj} \times \theta_{min}$ (arcmin)	$L_{maj} \times L_{min}$ (kpc)
A1367R	25.4±4.5	27.0×17.0	590×210

[a] Integrated 1.4 GHz polarized flux within 3σ contours

Table 3.5 Potential Residual Contamination From Faint Radio Galaxies Below NVSS Limit

Source	NVSS Limit $P_{1.4}$ (W Hz^{-1})	Calculated Residual[a] (mJy)	Observed Residual[b] (mJy)
A2061	2.0×10^{22}	9-13	1.4
A2065	1.7×10^{22}	11-15	5.0-9.0[c]
A2069	4.7×10^{22}	8-13	-
A2142	2.8×10^{22}	14-25	8.3
A2319	1.0×10^{22}	12-17	-

[a] Calculated by integrating the RLF between 2.5×10^{21} W Hz^{-1} and the NVSS 3σ clipping level (1.35 mJy), whose equivalent luminosity is given in Column 2.

[b] Faint RG flux between 75 (225, 270) μJy and 1.35 mJy observed for A2061 (A2065, A2142) at the GMRT (VLA, VLA); equivalent limiting luminosity is 1.1×10^{21} (2.9×10^{21}, 5.6×10^{21}) W Hz^{-1}.

[c] Uncertainty due to two sources with large photometric redshift uncertainties

Table 3.6 Halo Sizes

Source	LLS (kpc)	R_H (kpc)	R_{85} (kpc)	R_e (kpc)
A2061H	1700	410	680	330
A2065	1100	520	870	270
A2069	2800	890	1120	730
A2142	2200	620	630	230
A2319	2000	840	650	300

Table 3.7 X-ray Concentration For Halo Detections

Source	c_X
A2061	0.071
A2065	0.11
A2069	0.071
A2142	0.25
A2319	0.18

Table 3.8 Surface brightness characteristics of halo detections from our radial profile fitting

Source	R_e (kpc)	I_0 (μJy arcsec^{-2})	$\langle J_{1.4} \rangle_e$ (erg s^{-1} cm^{-3} Hz^{-1})
A2061H	330	9.8×10^{-2}	3.1×10^{-44}
A2065	270	2.8×10^{-1}	1.1×10^{-43}
A2069	730	8.9×10^{-2}	1.4×10^{-44}
A2142	230	6.4×10^{-1}	3.0×10^{-43}
A2319	300	9.2×10^{-1}	2.9×10^{-43}

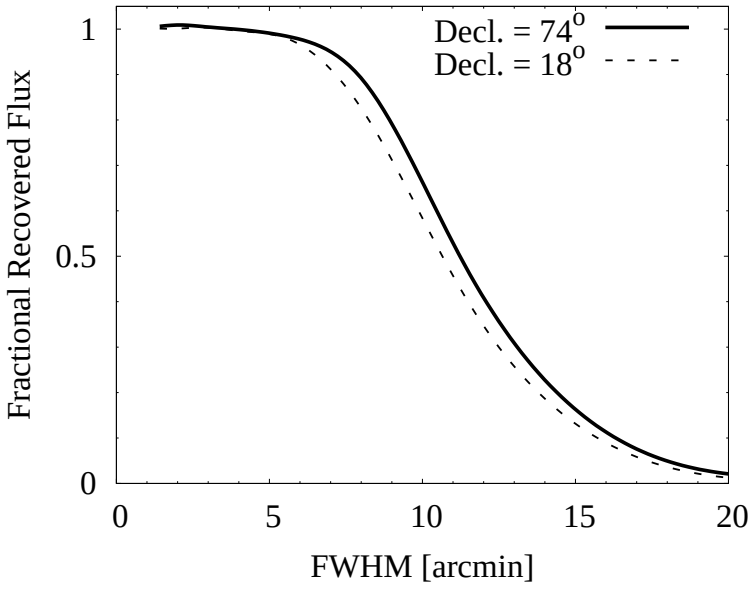

Figure 3.1 Fractional recovery of extended emission in the NVSS for two values of Declination (see text for details). For emission on scales $>11'$, less than 50% of the total flux is recovered.

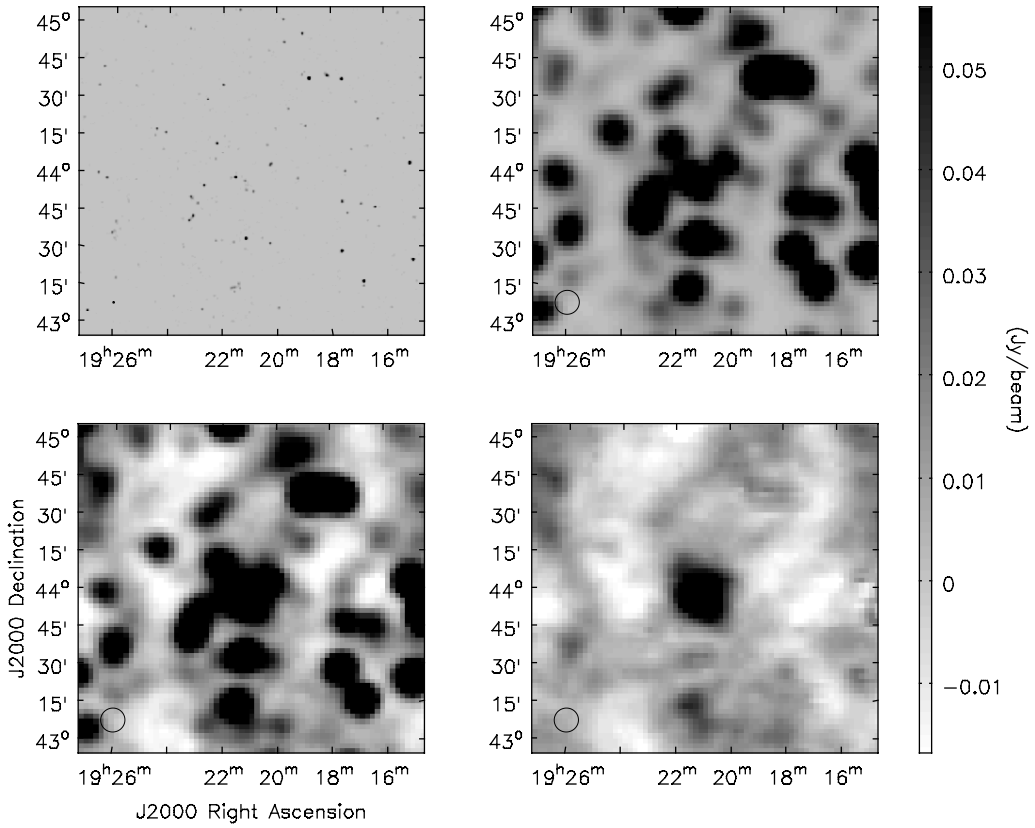

Figure 3.2 Illustration of the subtraction procedure. Top left: clipped NVSS image at 45″ resolution. Top right: clipped NVSS image convolved to the GBT beam. Bottom left: GBT image. Bottom right: GBT-NVSS residual image showing the radio halo in A2319. The corresponding beam is shown in the lower left of each image. The NVSS image has been clipped at $3\sigma = 1.35$ mJy (45″ beam)$^{-1}$.

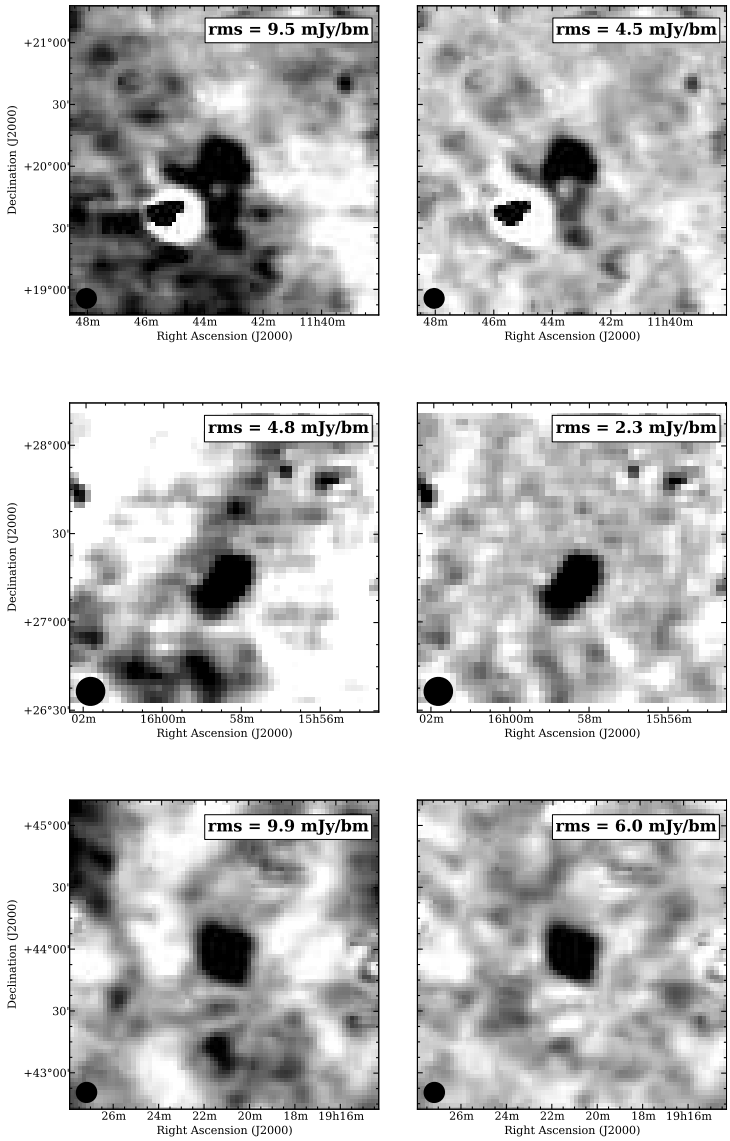

Figure 3.3 A1367 (top), A2142 (center), A2319 (bottom) before (left) and after (right) the nonlinear Galactic foreground subtraction procedure described in Section 3.3. For each image, a constant offset level has been added/subtracted to force the local background level to a mean of zero about the diffuse detection; the greyscale ranges from $-2\sigma_{map}$ to $6\sigma_{map}$, where σ_{map} for each field is the post-subtraction background rms (listed in Table 3.1). The GBT beam is shown in the lower left of each image.

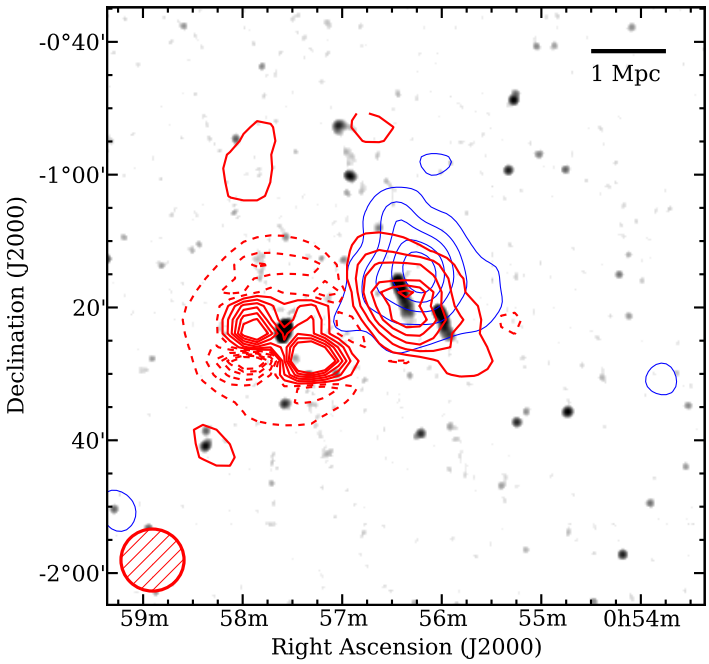

Figure 3.4 **A119**. NVSS image (greyscale), clipped at 1.35 mJy (45″ beam)$^{-1}$ with overlaid GBT-NVSS 1.4 GHz residuals (red contours) and RASS X-ray image (smoothed with a 5′ Gaussian kernel, blue contours). Radio contours are at $\pm(3,9,15,21,27,33)\times\sigma_{map}$ (negative contours dashed, if present). Strong artefacts from the bright RG 3C29 to the SE of the cluster remain after subtraction, but the integrated residual flux for 3C29 is <1% of the original flux. The GBT beam is shown in the lower left of the image.

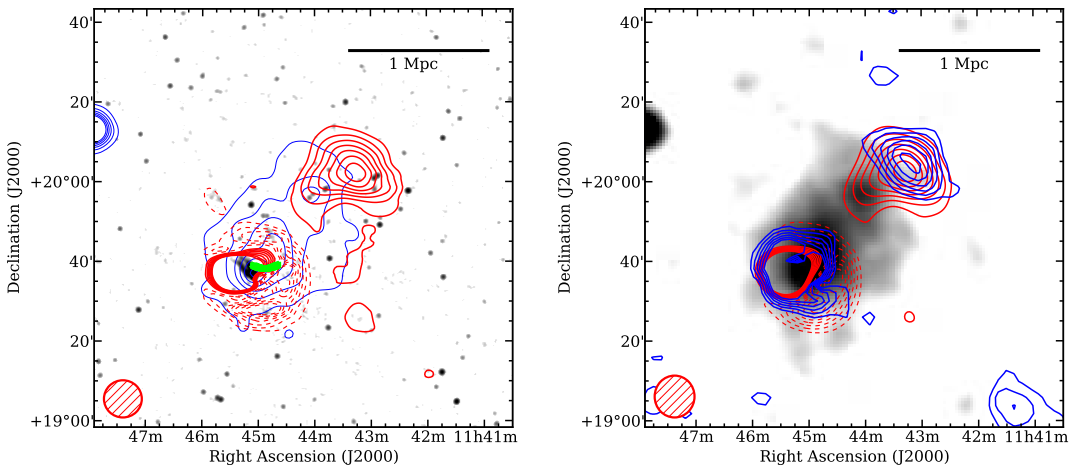

Figure 3.5 **A1367**. *Left:* NVSS image (greyscale), clipped at 1.35 mJy (45″ beam)$^{-1}$ with overlaid GBT-NVSS 1.4 GHz total intensity residuals (red contours) and RASS X-ray image (smoothed with a 5′ Gaussian kernel, blue contours). Radio contours are at $\pm$(4,7,10,13,16,19,22)$\times\sigma_{map}$ (negative contours dashed, if present). Strong artefacts from the bright NAT 3C264 to the SE of the cluster remain after subtraction, preventing us from unambiguously detecting halo emission. The X-ray cold front is shown as a green arc. *Right:* RASS X-ray image (smoothed with a 5′ Gaussian kernel, greyscale) with overlaid GBT 1.4 GHz polarized intensity (blue contours) and GBT-NVSS total intensity (red contours). Polarized intensity contours are at (3,5,7,9,11,13)$\times$1.3 mJy beam^{-1}; total intensity contours are at $\pm$(5,8,11,14,17,20,23)$\times$4.6 mJy beam^{-1} (negative contours dashed, if present); P and I are at the resolution of the "effective" GBT P beam ($10.5' \times 10'$), shown in the bottom left of the image.

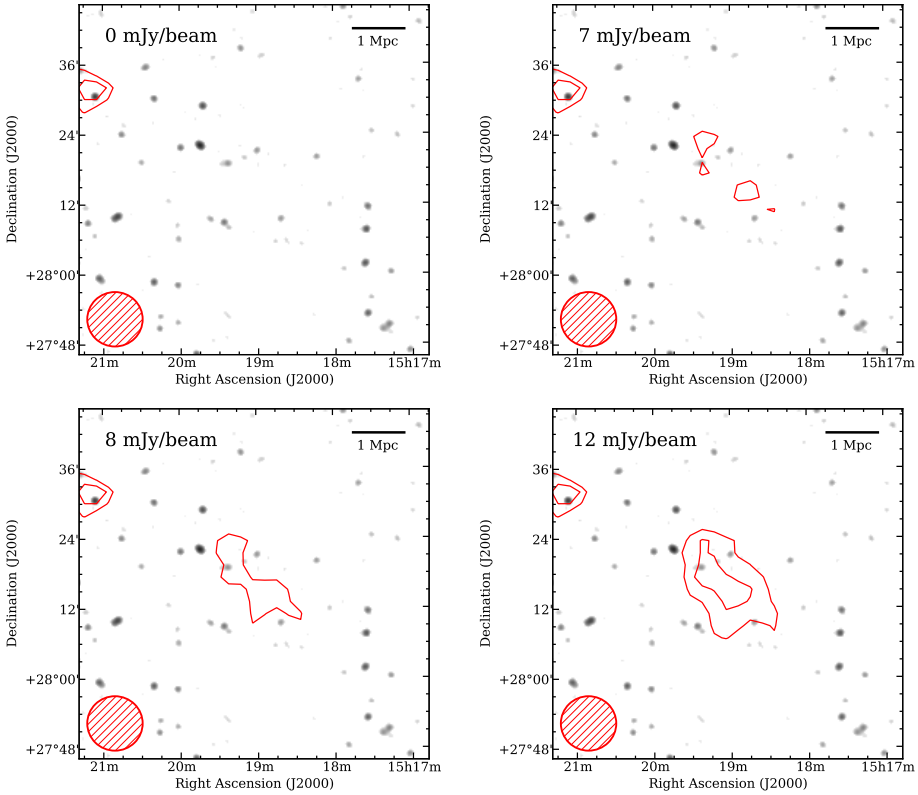

Figure 3.6 **A2056.** Determination of an upper limit to the radio halo flux of A2056 using injection of a synthetic Gaussian halo with FWHM = 1 Mpc (see text for details). Each image displays the NVSS image (greyscale), clipped at 1.35 mJy $(45'' \text{ beam})^{-1}$ with overlaid GBT-NVSS residuals plus injected halo (red contours). For each frame, the contour levels are at $\pm(3,4,5,...)\times\sigma_{map}$ (negative contours are dashed, if present), the peak level of the synthetic halo is stated in the upper left corner, and the GBT beam is shown in the lower left corner. The synthetic halo would be classified as a detection when injected with peak of 8 mJy beam^{-1}, so we adopt 7 mJy beam^{-1} as the peak flux of a non-detection. The feature displaying residual flux in the upper left is an unrelated radio galaxy.

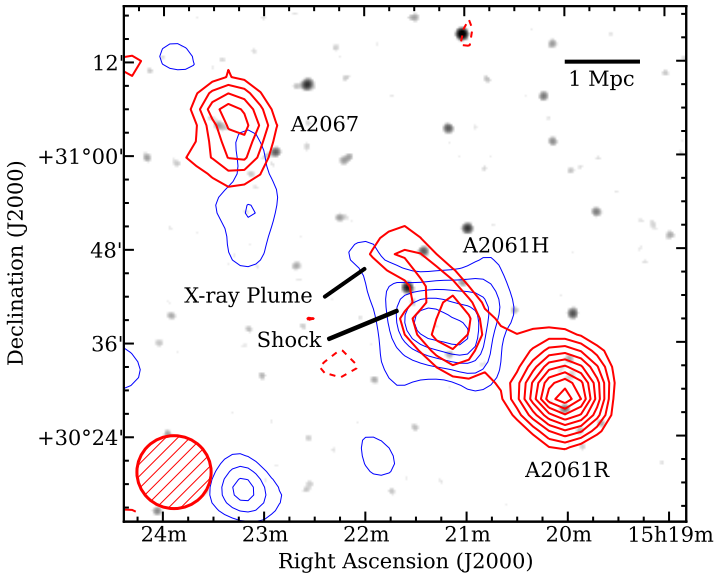

Figure 3.7 **A2061-A2067**. NVSS image (greyscale), clipped at 1.35 mJy (45″ beam)$^{-1}$ with overlaid GBT-NVSS 1.4 GHz residuals (red contours) and RASS X-ray image (smoothed with a 5′ Gaussian kernel, blue contours). The X-ray shock and plume are labeled. Radio contours are at $\pm(3,4,5,...)\times\sigma_{map}$ (negative contours dashed, if present). The GBT beam is shown in the lower left of the image.

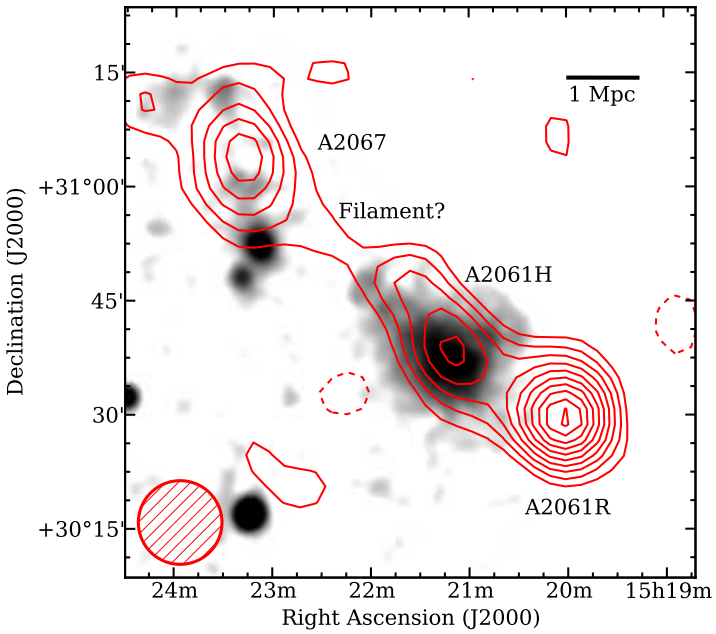

Figure 3.8 **Possible inter-cluster filament in A2061-A2067**. Rosat PSPC X-rays (smoothed with a 2′ Gaussian kernel, greyscale) with overlaid GBT-NVSS 1.4 GHz residuals (red contours). Radio contours are at ±(2,3,4,...)×2.4 mJy (11′ beam)$^{-1}$ (negative contours dashed, if present). The GBT beam is shown in the lower left of the image.

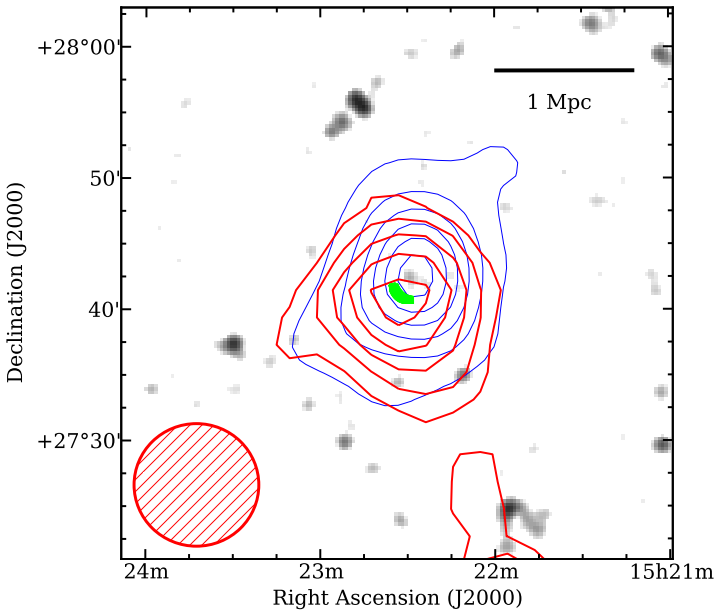

Figure 3.9 **A2065.** NVSS image (greyscale), clipped at 1.35 mJy (45″ beam)$^{-1}$ with overlaid GBT-NVSS 1.4 GHz residuals (red contours) and RASS X-ray (smoothed with a 5′ Gaussian kernel, blue contours). The X-ray cold front is shown as a green arc. Radio contours are at $\pm(3,4,5,...)\times\sigma_{map}$ (negative contours dashed, if present). The GBT beam is shown in the lower left of the image.

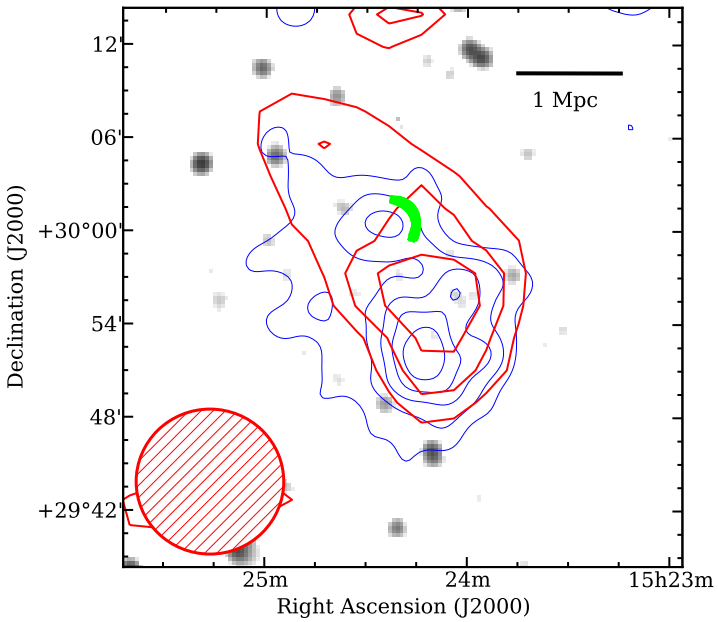

Figure 3.10 **A2069.** NVSS image (greyscale), clipped at 1.35 mJy (45″ beam)$^{-1}$ with overlaid GBT-NVSS 1.4 GHz residuals (red contours) and Rosat PSPC X-ray image (smoothed with a 2′ Gaussian kernel, blue contours). The X-ray cold front is shown as a green arc. Radio contours are at $\pm(3,4,5,...)\times\sigma_{map}$ (negative contours dashed, if present). The GBT beam is shown in the lower right of the image.

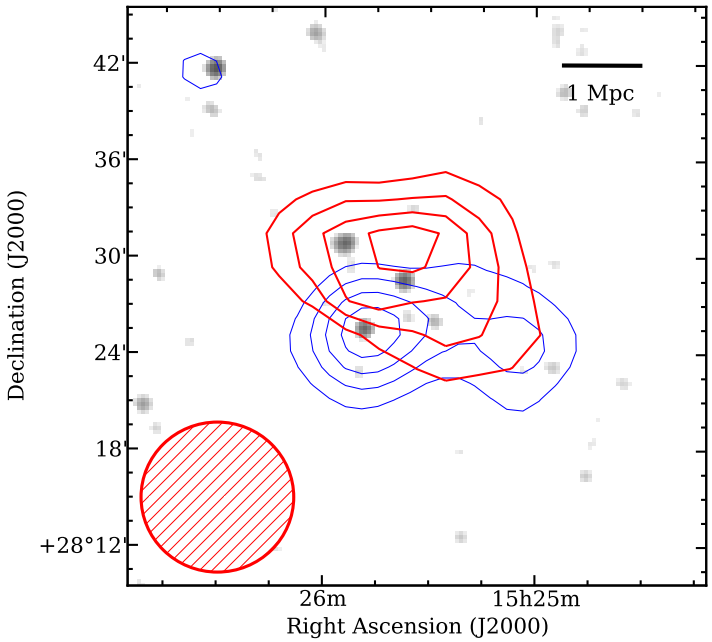

Figure 3.11 **A2073**. NVSS image (greyscale), clipped at 1.35 mJy (45″ beam)$^{-1}$ with overlaid GBT-NVSS 1.4 GHz residuals (red contours) and RASS X-ray image (smoothed with a 5′ Gaussian kernel, blue contours). Radio contours are at $\pm(3,4,5,...)\times\sigma_{map}$ (negative contours dashed, if present). The GBT beam is shown in the lower left of the image.

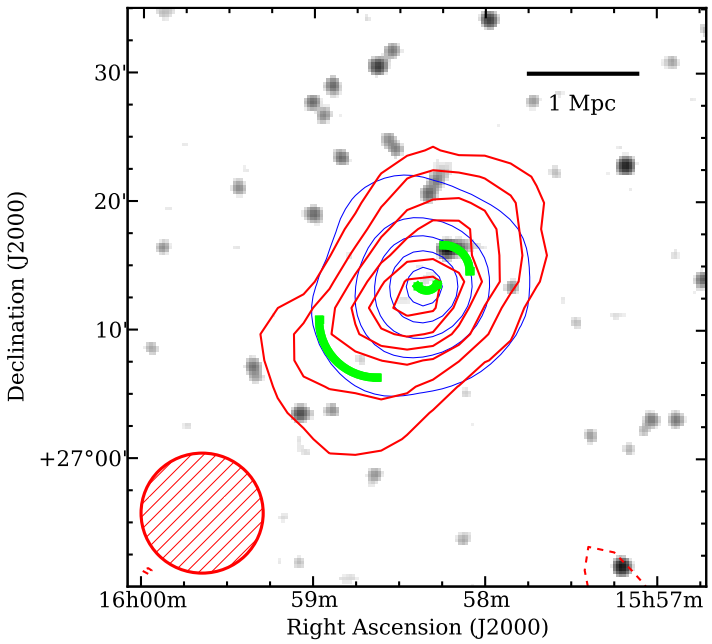

Figure 3.12 **A2142**. NVSS image (greyscale), clipped at 1.35 mJy (45″ beam)$^{-1}$ with overlaid GBT-NVSS (plus reconstructed NVSS halo; see text) 1.4 GHz residuals (red contours) and RASS X-ray image (smoothed with a 5′ Gaussian kernel, blue contours) in the A2142 region. Radio contours are at $\pm(3,6,9,...)\times\sigma_{map}$ (negative contours dashed, if present).

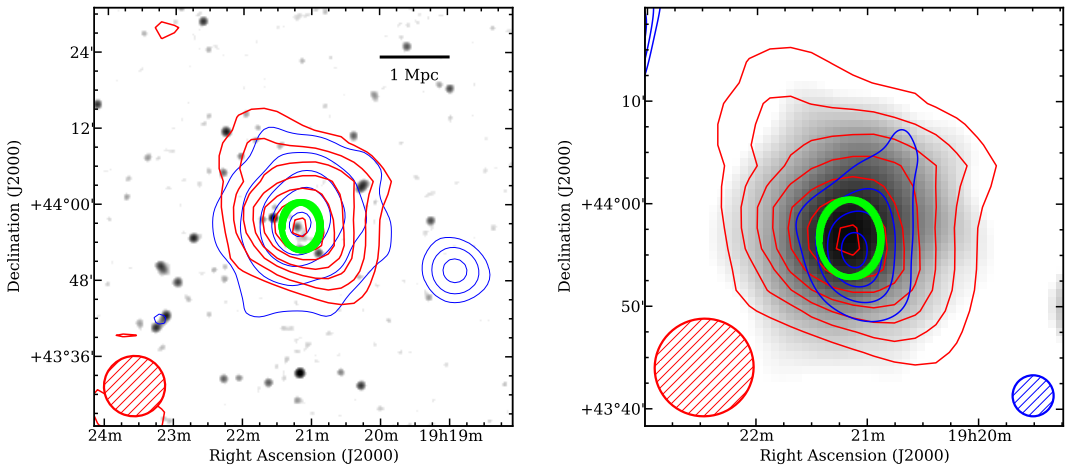

Figure 3.13 **A2319**. *Left:* NVSS image (greyscale), clipped at 1.35 mJy (45″ beam)$^{-1}$ with overlaid GBT-NVSS 1.4 GHz residuals (red contours) and RASS X-ray (smoothed with a 5′ Gaussian kernel, blue contours). Radio contours are at $\pm(3,6,9,...)\times\sigma_{map}$ (negative contours dashed, if present). The GBT beam is shown in the lower left of the image. *Right:* RASS X-ray image (greyscale, convolved with a 5′ Gaussian kernel) with overlaid VLA diffuse flux (blue contours) and GBT-NVSS residuals (red contours). The VLA contours are at (3,5,7,...)×3 mJy (240″ beam)$^{-1}$; the GBT-NVSS contours are the same as in the left panel.

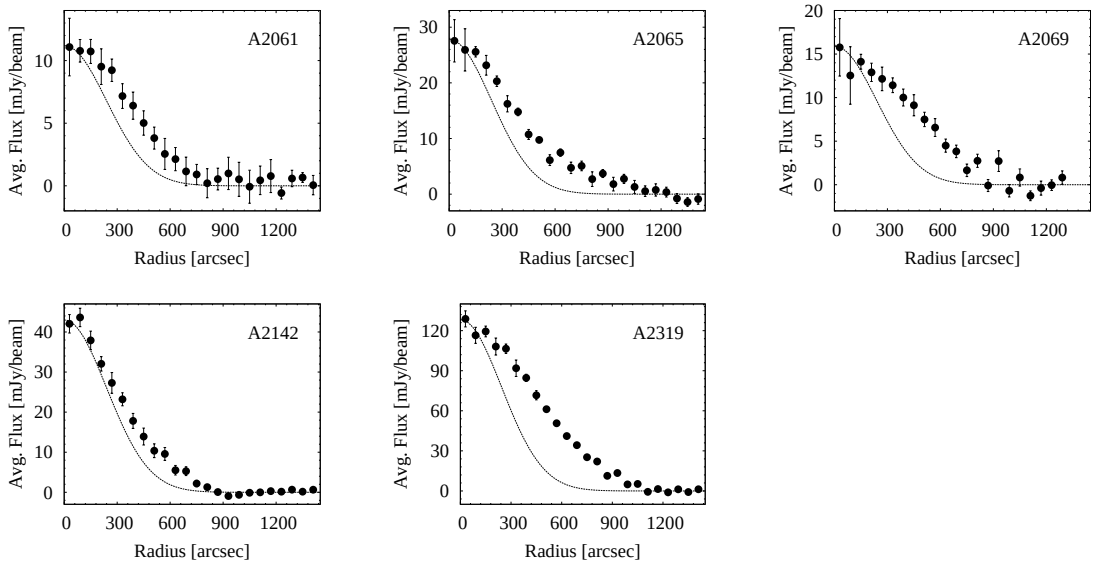

Figure 3.14 Azimuthally averaged radial flux profiles of the radio halo detections, as described in the text. Error bars represent the standard deviation of pixel fluxes within the radial bin. Note that the assumption of azimuthal symmetry allows the radial sampling to exceed the image pixel scale. The effective circular Gaussian beam profile is shown as a dashed line.

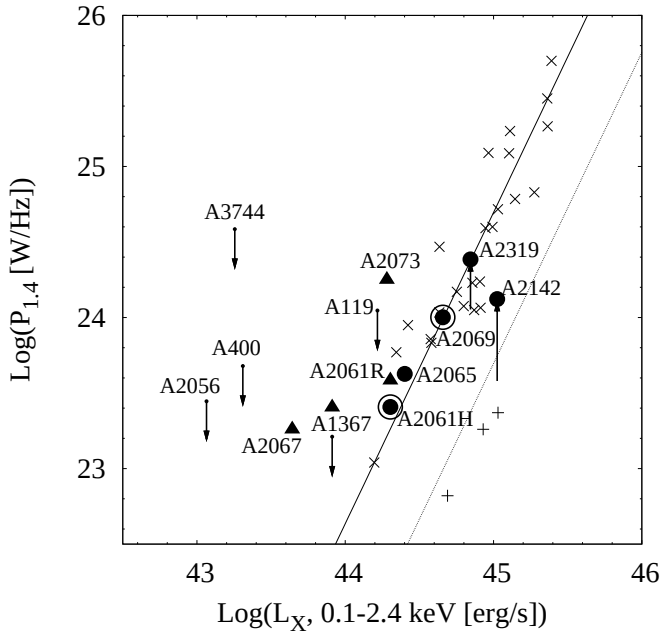

Figure 3.15 Plot of $P_{1.4}$ vs. L_X for halo detections. Xs are halos from the literature. Crosses are statistical detections of off-state halos from Brown et al. (2011). From this work are halos (filled circles) and relics (filled, upward triangles); the (possibly) multi-structure halos A2061H and A2069 are shown as filled circles surrounded by open circles. Upward arrows connecting previous (literature) $P_{1.4}$ measurements to those of this work are shown for A2142 and A2319. Values of $P_{1.4}$ for detections are from the integrated 3σ contours as described in the text. Downward solid arrows show upper limits of $P_{1.4}$ for A119, A400, A1367H, A2056, and A3744. All of our halo detections are well above the "off-state" halo detections of Brown et al. (2011) (approximate upper limit marked by the dashed line).

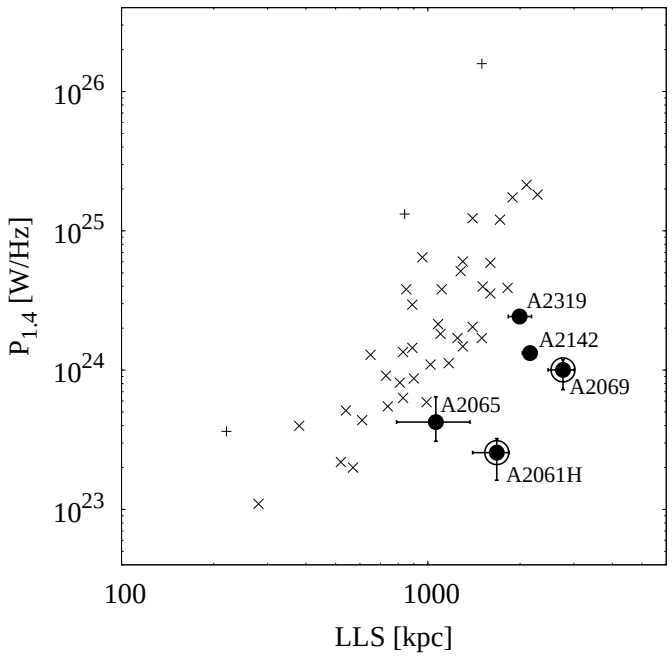

Figure 3.16 Plot of $P_{1.4}$ vs. LLS for radio halos. Our halo detections (filled circles) are shown, along with 42 literature halos (shown as ×s, except for three "peculiar" objects shown as +s) compiled in Feretti et al. (2012). The (possibly) multi-structure halos A2061H and A2069 are shown as filled circles surrounded by open circles. Error bars represent sizes and luminosities determined from 2σ and 4σ contours.

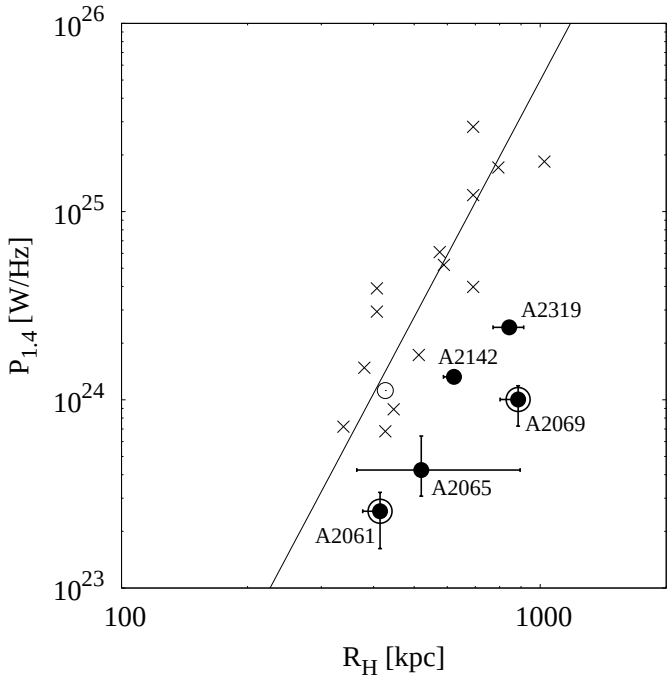

Figure 3.17 Plot of $P_{1.4}$ vs. R_H for radio halos, estimated from the 3σ contours. Xs − and an open circle for Abell 2319 − are halos from Cassano et al. (2007). The halo detections from this work are shown as filled circles. The (possibly) multi-structure halos A2061H and A2069 are shown as filled circles surrounded by open circles. Error bars represent sizes and luminosities determined from 2σ and 4σ contours. The correlation from Cassano et al. (2007) is drawn as a solid line.

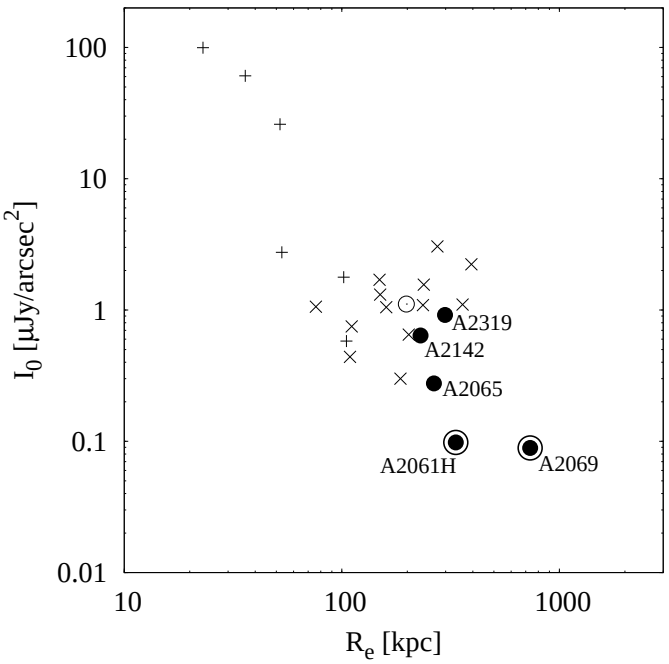

Figure 3.18 Plot of central surface brightness vs. e-folding radius (deconvolved quantities; see Table 3.8) for GBT halo detections at 1.4 GHz, calculated from fits of synthetic radial flux profiles to the observed radial profiles extracted from each radio image (filled circles). The (possibly) multi-structure halos A2061H and A2069 are shown as filled circles surrounded by open circles. Also plotted, from Murgia et al. (2009), Murgia et al. (2010), and Vacca et al. (2011), are halos (×s) and mini-halos (+s) with exponential radial form; their A2319 datum is marked with an open circle. In general, the volume averaged emissivity will be lower for objects with larger radius and lower central surface brightness.

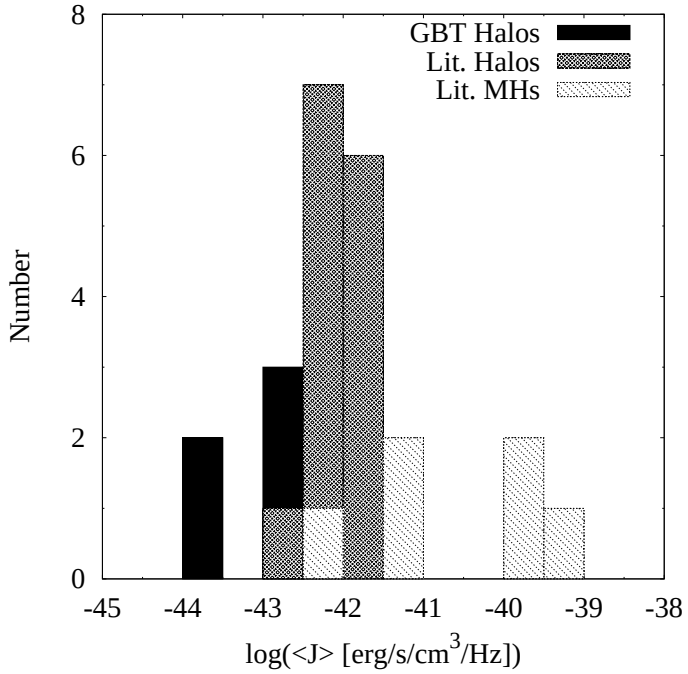

Figure 3.19 Histogram of volume averaged synchrotron emissivities for the halo detections of this work, from the results of the exponential flux profile fitting (see Appendix 3.5 and Table 3.8). Also shown are literature halo and mini-halo emissivities from Murgia et al. (2009), Murgia et al. (2010), and Vacca et al. (2011). The lowest emissivity bin is populated exclusively by A2061 and A2069.

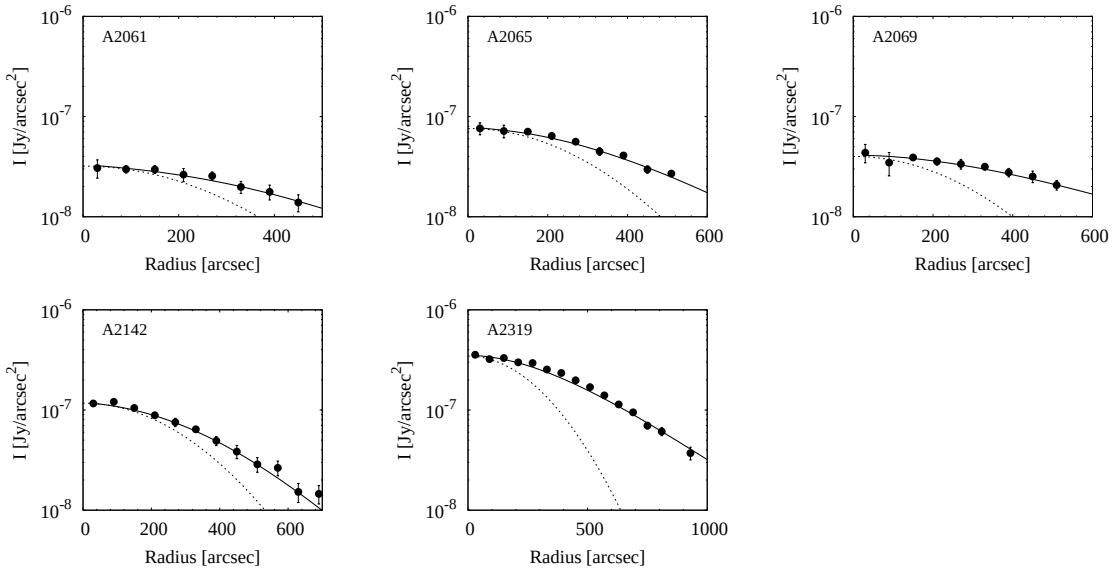

Figure 3.20 Fits to the azimuthally averaged brightness profiles of the radio halo detections. The exponential halo model fits (solid black line), from which I_0 and R_e are estimated (see text), are overlaid on the $\geq 2\sigma$ data (filled circles) used for the profile fitting. The effective circular Gaussian beam profile is shown (curved, dashed black line) to illustrate the extended nature of the halo detections. Note that the assumption of azimuthal symmetry allows the radial sampling to exceed the image pixel scale.

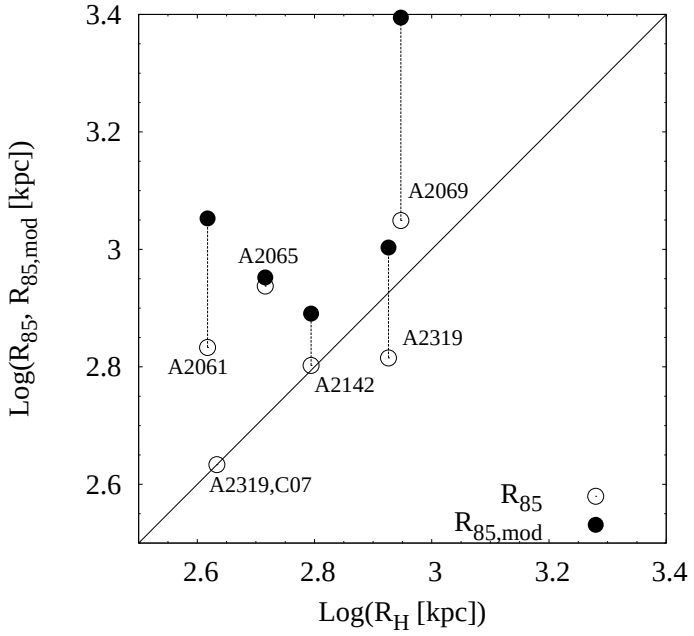

Figure 3.21 Plot of various measures of R_{85} vs. R_H for our radio halos. R_{85} (open circle) has been measured directly from the azimuthally averaged profiles, $R_{85,mod} \approx 3.38R_e$ (filled circle) is from the exponential model fitting to azimuthally averaged radial profiles; the various values for each halo are connected with a dashed line. The value of R_H for A2319 derived by Cassano et al. (2007) (from maps in Feretti et al. (1997)) is shown as the solitary open circle, assuming $R_H = R_{85}$.

Chapter 4

Cold Fronts, Large Scale Sloshing, and Mpc-scale Particle Acceleration in Abell 2142

4.1 Introduction

Giant radio halos are diffuse Mpc-scale radio synchrotron structures observed in roughly one-third of the most X-ray luminous galaxy clusters. In total, a few tens of GRHs are observed, exclusively in systems with recent merging activity. The synchrotron emission illuminates the presence of relativistic (GeV) electrons and μG magnetic fields. The low characteristic central surface brightness of GRHs (typically $\sim$0.5 to a few μJy arcsec^{-2} at GHz frequencies) makes halo detection an observational challenge.

The origin of the cosmic ray electrons (CRe) is a hotly debated topic, but characteristics of the halo radio synchrotron spectrum − such as index and curvature − may shed light upon the dominant acceleration mechanism in GRHs. Halos are observed to possess "steep" radio spectral indexes of $\alpha > 1$ at GHz frequencies, with a mean of $\alpha \approx 1.3$ ($S_\nu \propto \nu^{-\alpha}$). Recent observations at sub-GHz frequencies, primarily with the Giant Metrewave Radio Telescope (GMRT), have revealed a class of ultra steep spectrum radio halos (USSRHs), with spectral index $\alpha \gtrsim 1.5$ for $\nu \lesssim 1$ GHz. Detections of USSRHs are rare ($\lesssim$5 are known), but are expected to occur in minor to intermediate

merging systems where turbulent re-acceleration models exclusively predict that lower merger energy translates to a steeper CR energy (hence, synchrotron) spectrum.

Cold fronts in the thermal ICM of galaxy clusters are observed as surface brightness discontinuities in the X-ray emission and interpreted as contact edges separating regions of gas with different entropies. They are found in a large fraction of galaxy clusters with the majority of clusters harboring at least one CF (e.g., Ghizzardi et al. 2010). In merging systems, CFs may represent the discontinuity between hot shocked ICM and the low entropy gas of an interacting subcluster (remnant core). When found in relaxed cool-core clusters, CFs result from the relative motion of the low entropy core gas within the hotter outer gas after an off-axis merger has perturbed the gravitational potential − termed "sloshing" of the ICM.

Cold fronts have not previously been associated with the generation of Mpc-scale radio emission, but they have been suggested to play a role in the generation of radio mini-halos (MHs). These are diffuse radio structures up to a few hundred kpc in extent found at the center of some cool-core clusters. Several MHs appear to be bounded by one or more sloshing CFs − e.g., 2A 0335+0906 (Mazzotta et al. 2003), MS1455 and RXJ1720 (Mazzotta & Giacintucci 2008) − suggesting a link between the two phenomena. It has recently been suggested that the CRe production and magnetic field amplification which powers MHs may be related to the physics (e.g., shear-induced turbulence) associated with sloshing CFs. Recent simulations (ZuHone et al. 2013) have demonstrated that gas sloshing in cluster cores may generate sufficient turbulence to reaccelerate mildly relativistic electrons and amplify magnetic fields in the core. In the simulations, the regions which exhibit the most turbulence and strongest magnetic field amplification are, however, confined inside the sloshing CFs, and consequently the diffuse radio emission (on scales of a few hundred kpc) is expected to be confined within the same region. These simulations have also reproduced observables such as the steep synchrotron spectral index ($\alpha \gtrsim 1.5$) observed in mini-halos such as those found in Perseus and Ophiuchus. Recent observations at sub-GHz frequencies of the MH at the center of the Ophiuchus cluster suggest that a spatial gradient to the spectral index may exist in mini-halo systems, where the spectrum steepens with increasing distance from the center (Murgia et al. 2010).

4.1.1 Abell 2142

A2142 ($z = 0.091$) was the first cluster where X-ray cold fronts were discovered with *Chandra*, hosting two central cold fronts. While the CFs in A2142 were originally interpreted to belong to the remnant core class (Markevitch et al. 2000), subsequent X-ray (Markevitch & Vikhlinin 2007) and optical (Owers et al. 2011) analyses have led to the now dominant interpretation that they arise from sloshing of the ICM core. Recent *XMM-Newton* observations have revealed a third X-ray CF nearly 1 Mpc SE of the core (Rossetti et al. 2013), the largest CF-to-cluster-center distance known to date, interpreted as evidence of large-scale ICM sloshing from recent minor merging activity.

A2142 was originally suggested to host a radio halo by Harris et al. (1977), and was later observed to host a ∼300 kpc diffuse synchrotron structure in the core (Giovannini et al. 1999; Giovannini et al 2000). The location and sub-Mpc extent of the diffuse emission led to its classification as a mini-halo (MH), and although the two central cold fronts found by *Chandra* roughly bound the MH region − consistent with other MH systems (e.g., Mazzotta & Giacintucci 2008) − A2142 lacks other qualities typically observed in MH systems such as a relaxed X-ray ICM morphology and central AGN (e.g., Govoni et al. 2009).

Using confusion subtracted Green Bank Telescope (GBT) observations at 1.4 GHz, we recently discovered large scale radio emission elongated in the same SE-NW orientation as the diffuse X-rays, with a maximum extent of ∼2 Mpc (Farnsworth et al. 2013). The 1.4 GHz luminosity measured by the GBT places this radio halo just below the value predicted by the observed X-ray−radio luminosity correlation for GRHs, similar to the location of USSRHs in this phase space (Cassano et al. 2013). The large extent and low luminosity implies a volume averaged synchrotron emissivity more than an order of magnitude lower than is characteristic for GRHs (Farnsworth et al. 2013). As observed by the GBT, this halo-like structure extends to − and possibly beyond − the peripheral *XMM-Newton* CF to the SE (Figure 4.1), hinting at a possible connection between the two phenomena. A major goal of these followup VLA observations is to verify the GBT observation of a 2 Mpc halo in this system, and explore the physical connection between the diffuse radio emission and the X-ray cold fronts.

4.2 Observations and Data Reduction

A2142 was observed with the Karl G. Jansky Very Large Array (VLA) in D and C configurations at 1-2 GHz as part of NRAO observing program VLA11B-156. In this paper we will report only on the findings from the D-configuration data unless otherwise noted; the C-configuration data will be incorporated into a forthcoming paper.

The D-configuration data were acquired on October 9, November 6, and November 7, 2011. To recover the full extent of the GBT halo detection three pointings were acquired, with 28 minutes of integration time per pointing. Observations were made in spectral line mode with 16 spectral windows, each 64 MHz wide, spread across the full 1-2 GHz band. A bug in the backend system of the recently upgraded VLA led to the recording of only two seconds of every five second integration. The reduced time on source resulted in higher thermal noise and less complete u-v coverage, yielding drastically worse effective sensitivity for emission on all scales.

Standard data flagging and reduction techniques were performed with CASA, using the VLA calibrator sources J1331+3030 (3C286) and J1609+2641 for flux and phase calibration. After editing for RFI, roughly 45% of the total bandwidth remained, yielding $\sim$450 MHz over seven "clean" spectral windows. The useable data existed in two blocks, with $\sim$250 MHz and $\sim$200 MHz bandwidth centered at $\sim$1.38 GHz ("low" band) and $\sim$1.78 GHz ("high" band), respectively. We experimented with self-calibration (both phase and amplitude+phase), but determined that neither produced significant improvement and so self-calibration was not employed.

4.2.1 Imaging

To image with the full usable 450 MHz of bandwidth we implemented the multi-frequency multi-scale *clean* task in CASA, which also mosaiced the three pointings into a single image. To account for the frequency dependence of the emission across such a wide band we employed the MS-MFS *clean* algorithm (Rau & Cornwell 2011) in CASA with the number of Taylor expansion terms set to two (nterms=2). Multiscale cleaning was implemented, with scales of roughly 0, 1, 2, 4, 8 arcminutes specified. Correction for primary beam attenuation was performed using the CASA task *impbcor*. The full resolution ($34'' \times 32''$) image is shown in Figure 4.2 (both before and after correction for

primary beam attenuation).

Imaging The Diffuse Emission

Because imaging with the full bandwidth is considerably more challenging, technically, we have imaged the diffuse emission in the two separate sub-bands mentioned in Section 4.2. To isolate the diffuse cluster emission we first subtracted the contribution from radio galaxies. We identified the radio galaxy positions in the unpublished VLA C-configuration image at 1.6 GHz ($11''$ resolution, rms sensitivity of $\sigma \approx 90$ μJy beam^{-1}) constructed from the companion data mentioned previously. Using the CASA task *clean*, we then interactively cleaned (using zero scale) the locations containing radio galaxies with clean boxes (masks) of size of the synthesized beam. There are a number of blended or extended radio galaxies (i.e., tailed RGs) in the field, and these were carefully masked during the cleaning process. Once the radio galaxies were sufficiently removed (evaluated by-eye in an iterative cleaning process), *clean* was stopped and a model u-v data set representing the RG emission was created. The model u-v data set was then subtracted from the original u-v data, and the resulting u-v data set was then imaged with multi-scale *clean*. As before, correction for primary beam attenuation was performed using the CASA task *impbcor*. This procedure was done for the low and high band data sets, yielding images of the diffuse emission at 1.38 GHz and 1.78 GHz. To increase signal-to-noise for our analysis, we convolved the images to resolutions of $45''$ and $90''$. We list the effective beam and rms noise properties (after primary beam correction) in Table 4.5. The primary beam correction causes the map noise to increase outward from image center, so for those images we measure the effective map noise as near to the phase center as possible but outside of the cluster emission.

The results are shown in Figures 4.3 and 4.4, which display the diffuse emission at various resolutions (convolved to $45''$ and $90''$). In Figures 4.5 and 4.6, we overlay the VLA diffuse emission contours upon the X-ray image and show the locations of the three cold fronts.

4.3 Results

For our analysis of the diffuse radio emission, unless otherwise stated, we use the 90″ maps (Figures 4.5 and 4.6) for the best combination of signal-to-noise and resolution.

4.3.1 Morphology, Integrated Halo Flux and Spectral Properties

The peak of the halo flux is at the location of the known "mini-halo," but the emission is observed to extend across the southern central cold front. This is seen at both 1.38 and 1.78 GHz, and at all resolutions (see Figures 4.5 and 4.6). At high resolution the halo has a clumpy appearance, with an extended, low surface brightness component underlying the smaller but higher peaked central component. Thus it seems that the halo in A2142 may be some hybrid structure, composed of a "classical" MH-like emission region bounded by the central CFs, with an additional Mpc-scale halo. The halo does not appear to extend out to the SE peripheral cold front, as suggested by the GBT observations of Farnsworth et al. (2013).

The 1.38 GHz Image

At 1.38 GHz, within the 3σ contour level we find the radio halo to extend approximately $9.4'$ ($\sim$950 kpc in projection) in the SE-NW direction, along the same direction of the diffuse X-ray elongation. This is roughly half of the physical extent seen in the recent GBT study by Farnsworth et al. (2013). In the transverse direction (i.e., NE-SW) the halo's maximum extent is approximately $7.4'$ ($\sim$750 kpc). At 1.38 GHz we measure a total integrated halo flux of $S_{1.38} = 27.2 \pm 0.912$ mJy within the 3σ contour.

The 1.78 GHz Image

At 1.78 GHz, within the 3σ contour level we find the radio halo to have a similar extent to that seen at 1.38 GHz – roughly $9.4''$ by $7.4''$. The diffuse emission spans the southern central cold front at 1.78 GHz, extending in the southeast direction as was seen in the low band. At 1.78 GHz we measure a total integrated halo flux of $S_{1.78} = 18.6 \pm 0.632$ mJy within the 3σ contour.

Spectral Properties

To properly estimate the spectral index using the two frequency bands we must measure the fluxes within the same aperture, which we have constructed by drawing a polygon which encloses the 3σ contours of images at *both* frequencies. Within this same aperture we measure fluxes of $S_{1.38,tot} = 28.2 \pm 0.975$ mJy and $S_{1.78,tot} = 19.0 \pm 0.658$ mJy, yielding a spectral index for the halo of $\alpha_{1.38}^{1.78} = 1.55 \pm 0.04$. Note that the aperture is larger than each of the individual high/low band apertures, and that the flux within this aperture is slightly higher for each frequency than that measured in each respective aperture. This suggests that there may be more halo flux "hiding" beneath the noise in an extended low surface brightness component, a notion we further investigate with our radial profile analysis in Section 4.3.2.

Because the physical properties of the ICM bounded within the central CFs are expected to differ from those without, we estimate the spectral properties of the two regions. Inside the region bounded by the two central CFs we measure $S_{1.38,core} = 10.1 \pm 0.43$ mJy and $S_{1.78,core} = 7.0 \pm 0.29$ mJy, yielding a spectral index $\alpha_{1.38}^{1.78} = 1.44 \pm 0.05$. Due to insufficient signal-to-noise, we are unable to estimate the spectral index on the low surface brightness halo extension SE of the southern cold front.

4.3.2 Radial Profile

By extracting a radial profile from the 1.38 GHz image under the assumption of azimuthal symmetry, we may estimate properties such as total flux, various measures of size, central surface brightness, and volume averaged synchrotron emissivity. The radial profiles were extracted from the 1.38 GHz diffuse image using concentric annuli of width $16''$ centered on the radio centroid, yielding an average flux and standard deviation (in Jy beam^{-1}) within the annulus as a function of radius. The average radio flux and integrated flux as a function of radius for the halo at 1.38 GHz is shown in Figure 4.8. Inspection of Figure 4.8 reveals that the halo flux density at 1.38 GHz is approximately 31 mJy, higher than the value measured from the 3σ contours in the previous section but still much lower than the value of 64 mJy measured with the GBT (Farnsworth et al. 2013). From the radial profile we estimate the following two measures of halo size.

R_{85}, measured directly from the radial profile of integrated flux, represents the

radius enclosing 85% of the total halo flux and is less sensitive to map noise than measuring from the radio isophotes (Cassano et al. 2007). In the 90″ profile we measure $R_{85} \approx 400$ kpc, less than the value of 630 kpc measured with the GBT (Farnsworth et al. 2013).

R_e, the e-folding radius of a model halo with an assumed exponential radial flux profile, is fit to the observed radial flux profile (e.g., Orrú et al. 2007, Murgia et al. 2009). We refer the reader to Farnsworth et al. (2013) for the specifics of our procedure, and merely report our findings here. The fits were performed on the 1.38 GHz data at both 45″ and 90″ resolution, and the results are displayed in Figure 4.10 and Table 4.5. The results of the fitting procedure yield the deconvolved quantities $R_e = 110$ and 140 kpc and central surface brightness, I_0, of 0.90 and 0.75 μJy arcsec^{-2} for the 45″ and 90″ images, respectively. This demonstrates that the fitting procedure is fairly robust at various resolutions. We note that for the exponential halo model, $R_{85,model} \approx 3.38R_e \approx$ 440-470 kpc (depending on the image resolution analyzed), which agrees well with the value of R_{85} measured directly from the observed radial profile. These sizes differ by nearly a factor of two from the GBT study of Farnsworth et al. (2013), which found $R_e = 230$ kpc and $I_0 = 0.64$ μJy arcsec^{-2}, likely due to the additional largest scale component.

Following the prescription of Murgia et al. (2009), we estimate the volume-averaged synchrotron emissivity for the exponential flux profile by assuming all the flux comes from a sphere of radius $3R_e$:

$$\langle J_{1.4} \rangle_e \approx 7.7 \times 10^{-41} \ (1+z)^{3+\alpha} \frac{I_0}{R_e} \ (\text{erg s}^{-1} \text{ cm}^{-3} \text{ Hz}^{-1}) \tag{4.1}$$

where I_0 is in units of μJy arcsec^{-2}, R_e is in kpc, $(1+z)^{3+\alpha}$ is a factor which accounts for the k-correction and cosmological dimming of surface brightness with redshift, z, and α is the spectral index. Assuming $\alpha = 1.45$, we calculate $\langle J_{1.4} \rangle_e = 6.1 \times 10^{-43}$ erg s^{-1} cm^{-3} Hz^{-1}, a factor of two higher than the estimate of Farnsworth et al. (2013) on larger scales.

4.3.3 A Multi-component Halo?

We performed a simple experiment to explore the possibility of a multi-component halo by extracting a 1D slice across the 1.38 GHz image at 60″ resolution. The position of this slice, oriented SE-NW and shown in the top left panel of Figure 4.9, was chosen to intersect the peak of the radio emission, as well as all three X-ray cold fronts. We modeled the 1D flux profile as a sum of two Gaussian components, representing the smaller MH-like structure and the larger GRH-like structure. The results are shown in the lower panel of Figure 4.9. We find the model MH-like component to be contained within the central CFs, marginally resolved with a FWHM of approximately 69″ – this translates to a deconvolved size of ∼35 kpc at the redshift of A2142. The model GRH-like component is much larger, extending across both central cold fronts, with a FWHM of ∼400″ – about 650 kpc (deconvolved) at the redshift of A2142. We have not attempted to model the 2D structure of the halo, as the goal of this simple experiment was to illustrate the strong evidence that the radio halo is comprised of at least two discrete components. For comparison, in Figure 4.9 we also show the same slice along the 1.4 GHz GBT halo image from Farnsworth et al. (2013). It is readily seen that the GBT halo size is much larger, extending beyond the SE peripheral CF (left vertical line in Figure 4.9), but the gradient of the GBT flux appears to change near that CF location. This may be evidence for a third halo component, much larger and fainter, which is perhaps missing in the VLA data due to a lack of sensitivity to emission on such large scales.

4.4 Discussion

We have confirmed the GBT discovery by Farnsworth et al. (2013) of a Mpc-scale halo in the sloshing cluster A2142. More importantly, we have verified that the diffuse radio emission is not confined within the envelope of the sloshing core cold fronts. This is the first known detection of halo emission beyond the sloshing core CFs – contrary to observations of mini-halo systems such as 2A 0335+096 (Mazzotta et al. 2003), RXJ1720.1+26 and MS1455.0+2232 (Mazzotta & Giacintucci 2008) as well as MHD simulations of sloshing cool-core systems (ZuHone et al. 2013), which predict that the sloshing-induced turbulence responsible for CRe reacceleration and magnetic

field amplification is negligible outside of the cold fronts. We note that the sensitivities achieved in the aforementioned observational investigations were not sufficient to detect a low surface brightness halo component if one had been present.

The peak of the radio emission in our VLA images is located in the core region bounded by the cold fronts, and does display a sharp gradient in surface brightness leading up to the southern cold front. Outside of the southern cold front the radio emission has a somewhat flatter gradient, suggesting that different physical origins may exist for the radio emission on either side of the cold front. At high resolution the halo extension displays a clumpy appearance, as seen with increasing frequency for radio halos as more sensitive interferometric observations of clusters are acquired (e.g., Venturi et al. 2013), but this could be due to poor signal to noise. Perhaps the radio halo in A2142 is composed of multiple synchrotron components, with a MH-like structure in the core and a separate, large scale GRH-like component. In one possible scenario, the MH-like structure could be generated by the core sloshing, and a smooth, Mpc-scale halo component generated by large-scale ICM sloshing which has been triggered by recent minor merging activity (Owers et al. 2011, Rossetti et al. (2013)).

The spectral index of $\alpha_{1.38}^{1.78} \approx 1.5$ tentatively classifies A2142 as an ultra-steep spectrum radio halo, a prediction of turbulent reacceleration models for halo generation. Further observations at sub-GHz frequencies are required to measure the full synchrotron spectrum, which could also show curvature around 1 GHz − another prediction of turbulent reacceleration models.

While these VLA observations have confirmed the presence of a Mpc-scale halo in A2142, they have reproduced neither the 2 Mpc extent (see Figure 4.7) nor the ≈60 mJy of integrated halo flux seen at 1.4 GHz by the GBT study of Farnsworth et al. (2013). The other measures of halo radius, R_{85} and R_e, are also smaller than observed by the GBT, although the central surface brightness (deconvolved) observed by the VLA is higher by about 15%. Our modeling of the 1D flux profile in Section 4.3.3 has illustrated that the halo as seen by the VLA is at least two discrete components, with a MH-like structure bound by the central CFs and a larger GRH-like component. The GBT flux profile along the same line suggests that a third − much larger and fainter − halo component may exist, which is not seen by the VLA.

What is the nature of the discrepancy between the GBT and VLA observations of

the same cluster? As suggested in Section 4.3, there may be an extended, low surface brightness component to the halo that is missed by the interferometer. It is likely that these VLA observations suffer from missing short spacings, whereby sensitivity to flux on large spatial scales is reduced. This effect, drastic for "snapshot" observations such as the NVSS, was quantified by Farnsworth et al. (2013). For example, up to 50% of the total flux may be lost for emission on scales $>11'$. Longer VLA observations in D-configuration are necessary to fill in the short spacings and increase the sensitivity to large scale emission. Additionally, the union of single dish and interferometric observations would yield the best combination of resolution and sensitivity to extended emission; this is a difficult procedure, however, and requires great care.

4.4.1 Future Work

In order to image the full halo seen by the GBT, more completely measure the synchrotron spectrum, and explore the possibility of a 2 Mpc halo generated by large scale ICM sloshing, a number of observational tactics will be employed.

• With data already in hand, we will use the feathering technique to combine the single dish GBT data at 1.4 GHz with the interferometric VLA data. By integrating the GBT data we will effectively fill in the "zero spacing" in the u-v plane, greatly enhancing the sensitivity to large scale emission.

• We will incorporate the C-configuration VLA data at 1-2 GHz, currently in the reduction phase, into our imaging to provide better resolution as well as improve the u-v coverage (including some short baselines).

• Observations at 100-200 MHz with LOFAR will be acquired in early 2014, imaging the full halo at low frequencies where the halo emission becomes relatively bright due to the steep spectral index.

• Observations at 200-600 MHz with the GMRT have been acquired and are in the late stages of reduction and imaging.

• We have proposed deep VLA observations at 1-2 GHz and 2-4 GHz in C and D array configurations to augment these VLA data and better image the large scale component of the halo.

By observing the halo's radio spectrum from ∼100-4000 GHz we will be able to search for spectral features such as slope and curvature, allowing us to distinguish between

the two main models of halo generation in this system − turbulent reacceleration and hadronic collision. This will be done for the core region bounded by the central sloshing CFs as well as the region outside of the core, where we expect the physical conditions to be quite different.

In addition to the spectral modeling, we will perform a spatial correlation analysis between the radio and X-ray emission. This will provide us with another test of turbulent vs. hadronic models of halo generation, because hadronic models have difficulty reproducing the large extent to radio halos without invoking very high magnetic field strengths or proton densities at the cluster peripheries.

Finally, using data from *Planck* and AMI[1] we will explore at multiple resolutions the radio − S-Z correlation (e.g., Cassano et al. 2013) in A2142. By looking at radio − S-Z correlations of total flux and radial distribution, we will improve our understanding of the interplay between the thermal and nonthermal properties of the ICM in the regions inside and outside of the sloshing core.

4.5 Conclusions

We present results of a 1.5 GHz VLA study of the merging galaxy cluster Abell 2142. Recent observations by *XMM-Newton* and the Green Bank Telescope (GBT) have uncovered the most distant CF ever observed and a ∼2 Mpc radio halo, respectively, in a system that was previously observed to harbor only MH-like radio emission. The locations of the CFs and similar morphologies of the X-ray and radio emission suggests that the large scale sloshing of the thermal intracluster medium (ICM) − likely caused by an intermediate mass ratio merging event − may be responsible for cosmic ray (CR) acceleration and magnetic field amplification on similarly large scales. Our followup snapshot observations at 1-2 GHz with the VLA have confirmed the presence of Mpc-scale emission extending across at least one of the central CFs. This challenges the current paradigms of GRH generation − which predicts GRHs to occur preferentially in major merger systems − and MH generation, where the diffuse radio emission is bounded by the sloshing CFs. Spectral analysis finds the emission's spectral index to be ∼1.5 within the 1-2 GHz band, with a spatial gradient across the central cold

[1] The Arcminute Microkelvin Imager; http://www.mrao.cam.ac.uk/facilities/ami/

fronts. Sloshing of the ICM, previously linked to diffuse radio emission on scales of a few hundred kpc in some cool-core clusters, may provide an alternative mechanism for generating GRHs on Mpc scales. A2142 seems to be a unique hybrid system of halo-type components, with a MH-like structure existing within the sloshing core and a Mpc-scale, low surface brightness GRH-like component powered by the peripheral merging activity. The line between MH and GRH in clusters seems to be further blurred as the sensitivity and frequency coverage of radio telescopes improves. Further deep radio observations with emphasis on spectral coverage and short baselines − critical for recovery of extended emission − are required for this and other intermediate merger systems to further investigate this phenomenon.

Table 4.1. Summary of VLA Observations

Center Frequency (GHz)	Bandwidth (MHz)	Resolution	rms sensitivity (μJy beam^{-1})
1.56	450[a]	$34'' \times 32''$	110
1.38	250	$40'' \times 37''$	150
1.38	250	$45'' \times 45''$	170
1.38	250	$90'' \times 90''$	200
1.78	200	$32'' \times 29''$	70
1.78	200	$45'' \times 45''$	85
1.78	200	$90'' \times 90''$	135

Note. — Images at 1.38 and 1.78 GHz have had point sources subtracted as described in the text.
[a] 450 MHz total bandwidth in two blocks between 1.23 GHz and 1.88 GHz.

Table 4.2. Halo Properties From the 3σ Contours

Frequency (GHz)	S_ν (mJy)	Angular Dimensions (arcmin)	Linear Dimensions (kpc)
1.38	27.2 ± 0.9	9.4×7.4	950×750
1.78	18.6 ± 0.6	9.3×7.3	940×740

Note. — Notes go here.

Table 4.3. Surface Brightness Characteristics From Radial Profile and Fitting

Resolution (arcsec)	$S_{1.38}$ (mJy)	R_{85} (kpc)	R_e (kpc)	I_0 (μJy arcsec^{-2})
45	31	390	110	0.90
90	31	400	140	0.75

Note. — All relevant quantities are deconvolved. For the exponential model fit to the radial profile, $R_{85,model} \approx 3.38 R_e$.

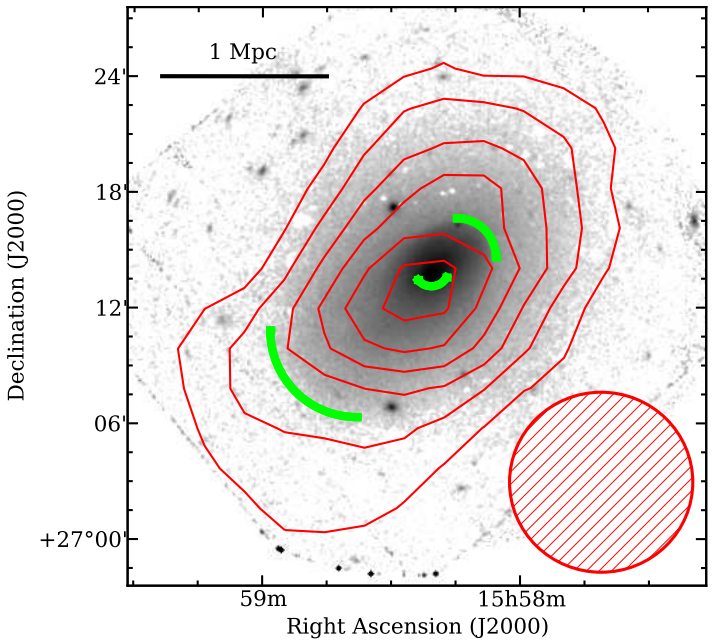

Figure 4.1 *XMM-Newton* X-rays (greyscale), overlaid with GBT 1.4 GHz diffuse emission (9.5′ resolution, red contours at (3,6,9,...)×2.3 mJy beam^{-1}). The X-ray cold fronts are shown as green arcs.

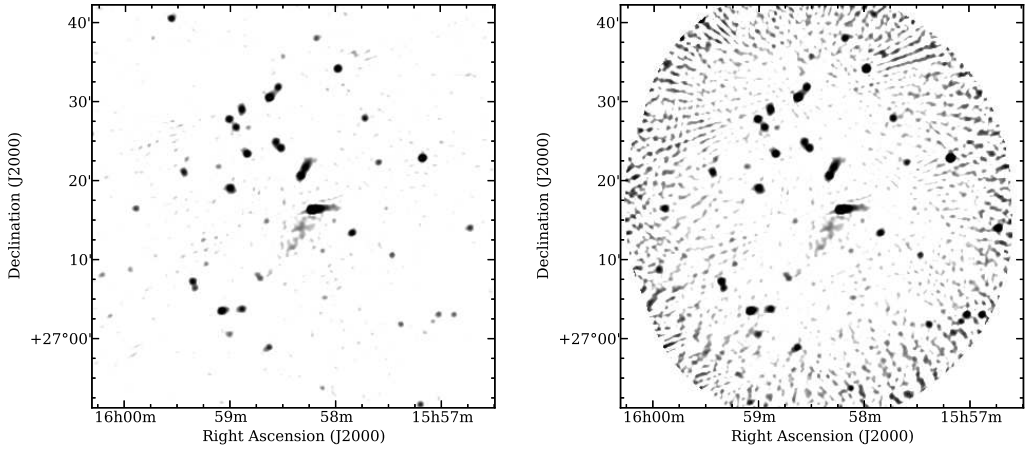

Figure 4.2 The A2142 field at 1.56 GHz constructed with MFMS clean using 450 MHz bandwidth. Shown are images of the field before (*left*) and after (*right*) correction for primary beam attenuation. For both panels the resolution is $34'' \times 32''$, and the greyscale goes from 200 μJy beam^{-1} to 3 mJy beam^{-1}. The radio halo is visible just south of image center.

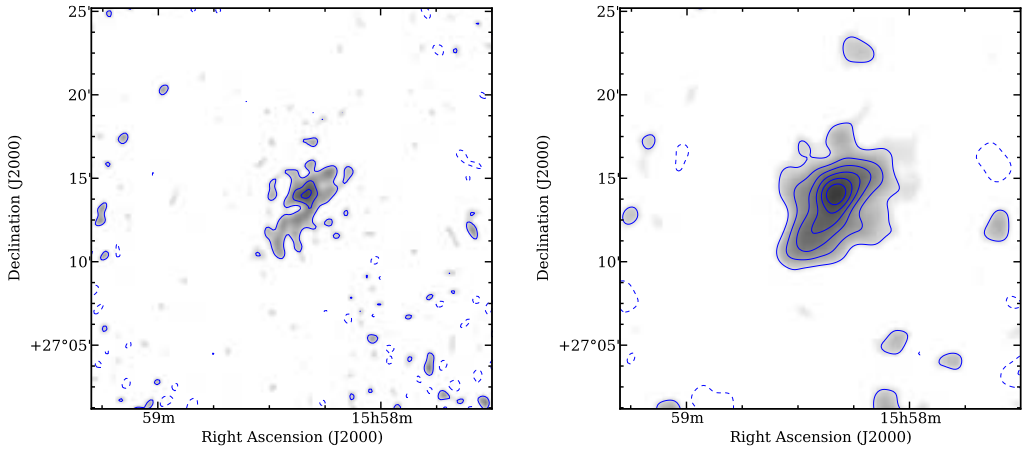

Figure 4.3 VLA 1.38 GHz diffuse emission (greyscale and contours) at 45″ (left), and 90″ (right) resolution. The contours are at $\pm(3,6,9,...)\times\sigma_{map}$.

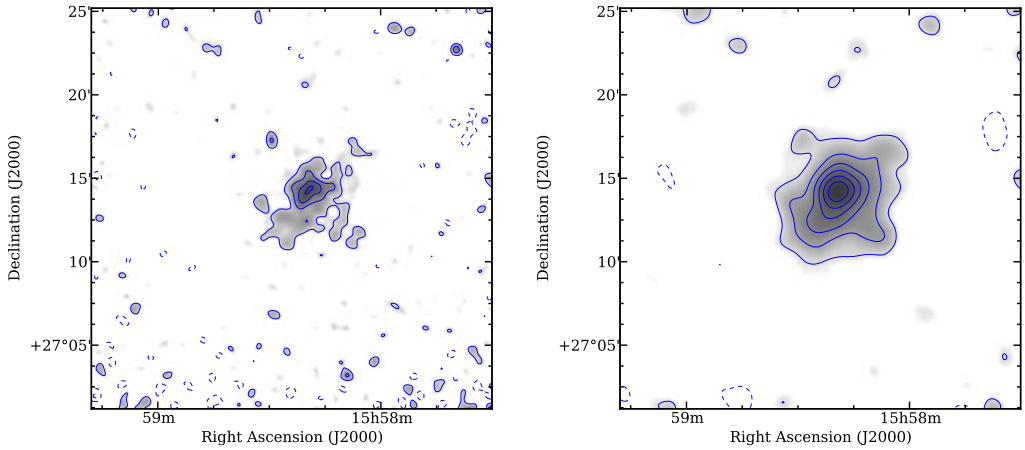

Figure 4.4 VLA 1.78 GHz diffuse emission (greyscale and contours) at 45″ (left), and 90″ (right) resolution. The contours are at $\pm(3,6,9,...)\times\sigma_{map}$.

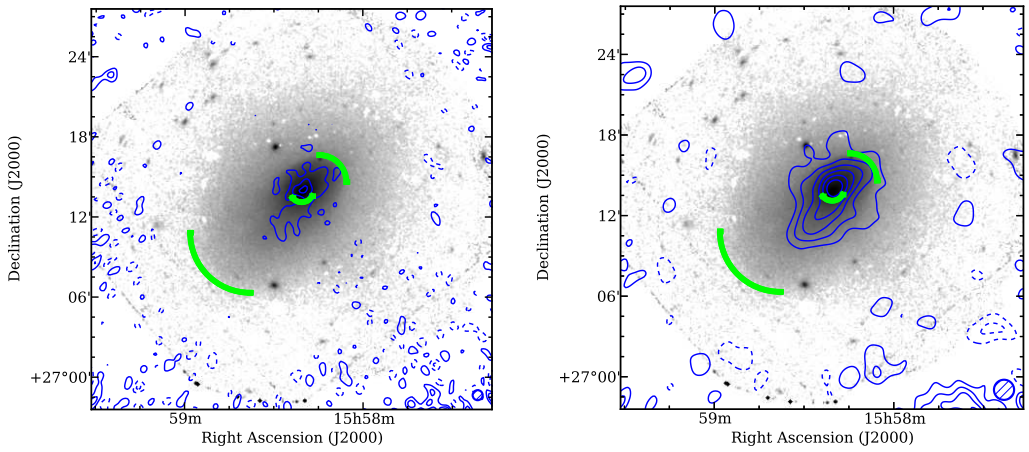

Figure 4.5 *XMM-Newton* X-rays (greyscale), overlaid with VLA 1.38 GHz diffuse emission at 45″ (left), and 90″ (right) resolution (blue contours at $\pm(3,6,9,...)\times\sigma_{map}$). The X-ray cold fronts are shown as green arcs.

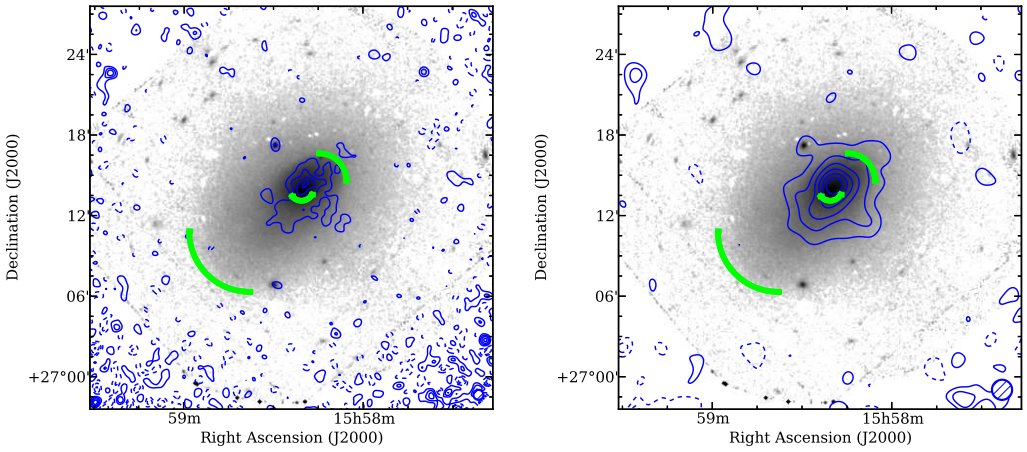

Figure 4.6 *XMM-Newton* X-rays (greyscale), overlaid with VLA 1.78 GHz diffuse emission at 45″ (left), and 90″ (right) resolution (blue contours at $\pm(3,6,9,...)\times\sigma_{map}$). The X-ray cold fronts are shown as green arcs.

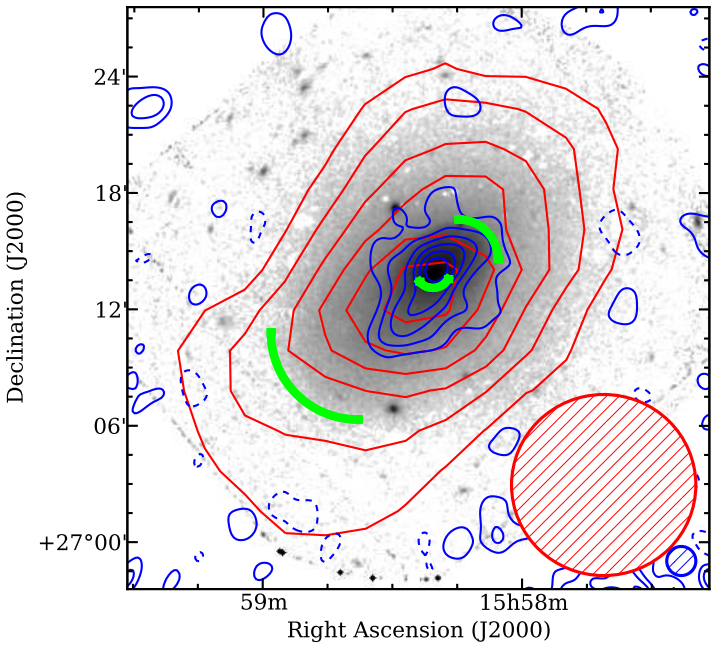

Figure 4.7 *XMM-Newton* X-rays (greyscale), overlaid with GBT 1.4 GHz diffuse emission (9.5′ resolution, red contours at (3,6,9,...)×2.3 mJy beam^{-1}) and VLA 1.4 GHz diffuse emission (90″ resolution, blue contours at ±(3,6,9,...)×200 μJy beam^{-1}). The X-ray cold fronts are shown as green arcs.

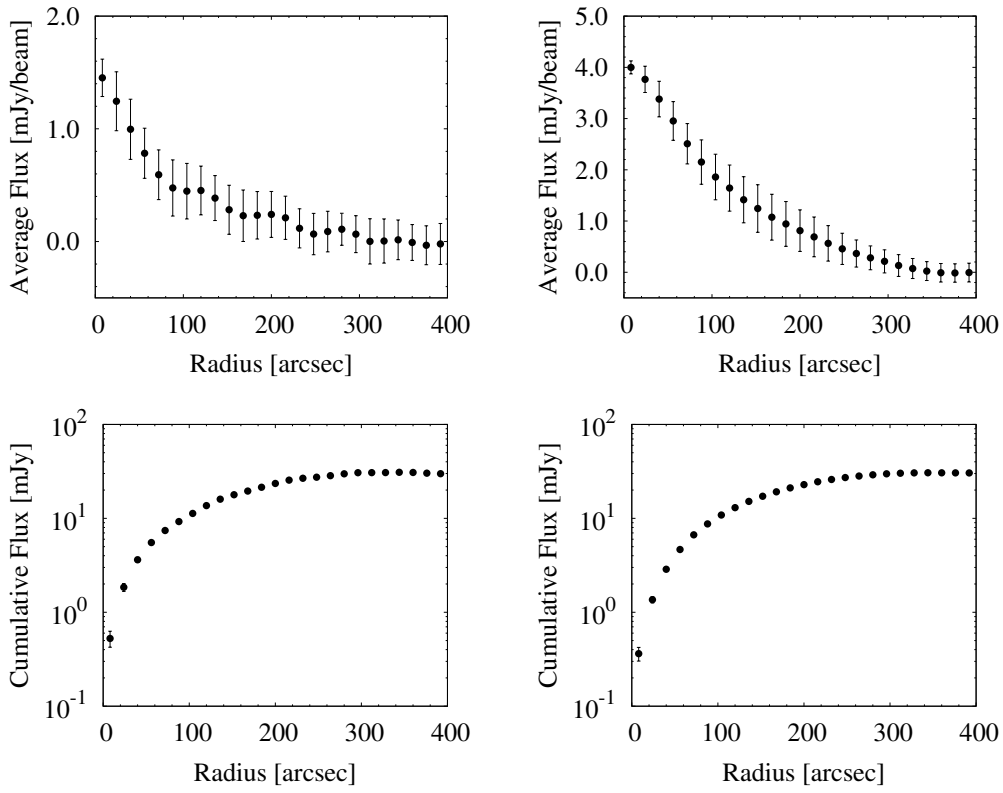

Figure 4.8 Azimuthally averaged radial profiles of average flux (top) and cumulative flux (bottom) of the diffuse emission at 1.38 GHz for the 45″ (left), and 90″ (right) resolution images.

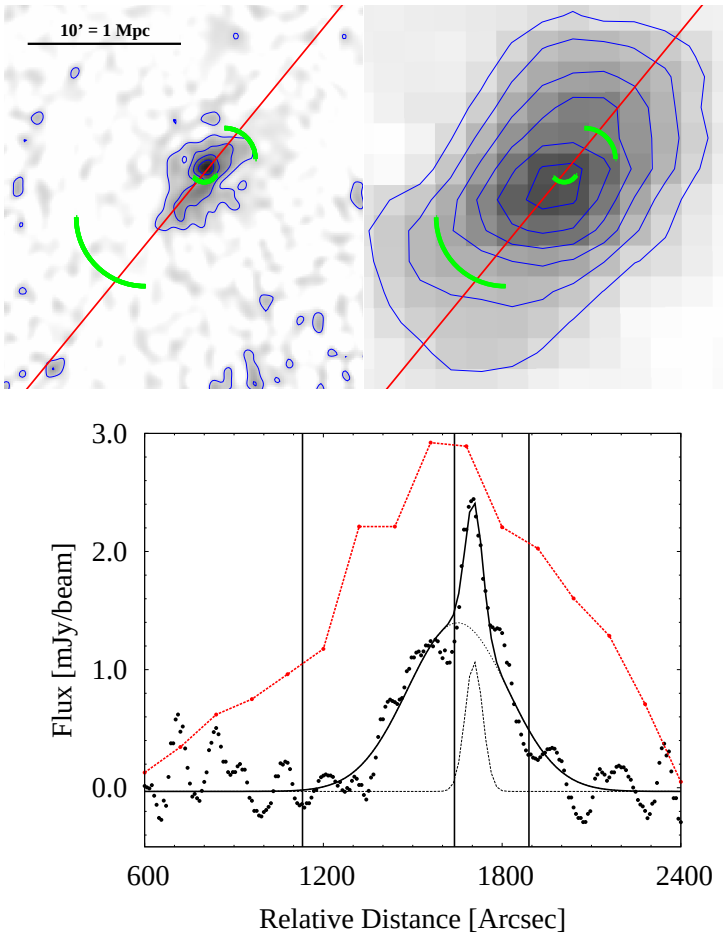

Figure 4.9 *Top:* VLA 1.38 GHz (60″ resolution, left) and 1.4 GHz GBT (9.5′ resolution, right) diffuse emission in greyscale and blue contours; overlaid are the positions of the X-ray cold fronts (green arcs) and 1D slice (red line) used for analysis. The VLA contour levels are at at (3,6,9,12)×170 μJy beam^{-1}) and the GBT contour levels are at (3,6,9,...)×2.3 mJy beam^{-1}). *Bottom:* 1D slice across the VLA image (black points) and GBT image (scaled by a factor of 1/15, red points+line) versus relative distance along slice. Shown are the results of the double Gaussian fitting, with the MH and GRH components (dashed black curves) and their sum (thick black curve). The locations of the three CFs are shown as vertical black lines.

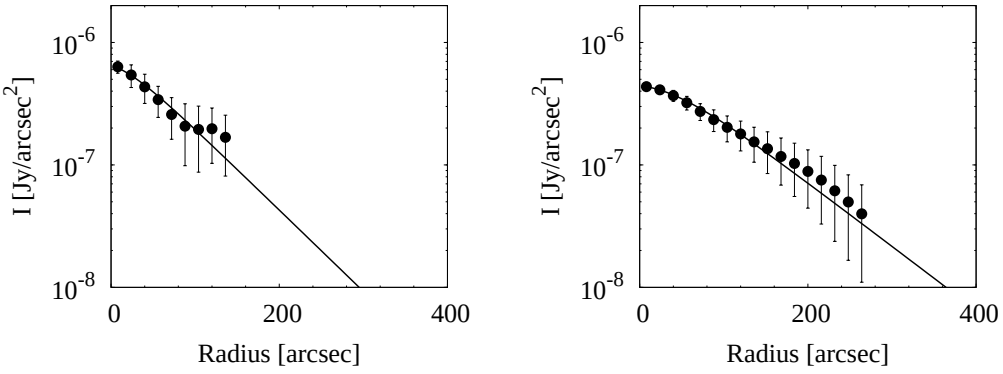

Figure 4.10 Azimuthally averaged radial profile of the 1.38 GHz radio flux for the 45″ (left), and 90″ (right) resolution images; points above $2\sigma_{map}$ are shown and error bars represent the standard deviation within that annulus. The best fitting exponential halo model is shown as a solid line.

Chapter 5

Low Surface Brightness Radio Emission in Galaxy Clusters

5.1 Introduction

As clusters of galaxies assemble at the intersections of large-scale structure filaments, the bulk of their baryons – the intracluster medium (ICM) – are shocked, heated and stirred into turbulence. During this process, a portion of the energy is channeled into amplification of magnetic fields and acceleration of cosmic rays (CR). This diffuse relativistic plasma is detected by its radio emission in the form of centrally located halos and peripheral relics.

Giant radio halos are diffuse Mpc-scale radio synchrotron structures observed in roughly one-third of X-ray luminous galaxy clusters. In total, a few tens of GRHs are observed, exclusively in systems with recent merging activity. The synchrotron emission illuminates the presence of relativistic (GeV) electrons and μG magnetic fields. The low characteristic central surface brightness of GRHs (typically $\sim$0.5 to a few μJy arcsec^{-2} at GHz frequencies) makes halo detection an observational challenge. Deep interferometric studies have shown that radio halos appear to have a bimodal luminosity distribution. (e.g., Brunetti et al. (2009)): the "on-state" of merging clusters with correlated X-ray and radio halo luminosities ($P_{1.4} \propto L_X^{2.06}$)[1] , and an "off-state" in which most, though

[1] L_X is the integrated luminosity 0.1-2.4 keV throughout.

not all, clusters appear relaxed (e.g., Brown et al. (2011)).

The CR electrons (CRe) lose energy to synchrotron and inverse Compton radiation against the CMB quickly enough that they cannot diffuse throughout the Mpc-scale volume. The two most popular, and hotly debated models (for a concise review, see Brunetti 2012 and references therein) for distributed, *in situ*, CRe acceleration are i) *primary* − direct acceleration via merger shocks and MHD turbulence, and ii) *secondary* − production via hadronic interactions between long-lived relativistic and thermal protons in the ICM. It is important to distinguish between these two processes because of their implications for ICM physics − the dissipation timescale for turbulence, the role of non-thermal pressure support that can affect cluster X-ray cosmology studies, the mixing of metals in the ICM, and the production of γ-rays along with the CRe. We note that for CRe turbulence provides *re*-acceleration; the source of the original seed CRs is still unclear.

A bimodal distribution arises naturally in the primary models, where the turbulence is expected to decay quickly post-merger, leading to an "off-state" for radio halos at a luminosity $\approx$10% of the "on-state" value. The prediction for secondary models is less clear; although the CR protons should continue to generate CRe at a steady rate, a separate prescription for the evolution of the magnetic field strength must be made. However, there are a handful of clusters with clear signs of recent mergers where a radio halo has not yet been detected (e.g., Cassano et al. 2010a; Russell et al. 2011), showing that we are still missing a key piece of the puzzle.

Peripheral relics are typically elongated structures, up to and exceeding 1 Mpc in extent, found at the outskirts of a few tens of clusters. In the NVSS[2] sample, peripheral relics were found in $\sim$11% of clusters with 0.1-2.4 keV X-ray luminosity $L_X > 5\times10^{44}$ erg s^{-1} (Giovannini & Feretti 2002). Often highly polarized (i.e, a few tens of percent), observations of these relics provide strong evidence of μG magnetic fields and cosmic rays (CRs) at cluster peripheries. Predicted by cosmological simulations, peripheral relics are most likely tracers of merger or accretion processes, whereby the CRs are directly accelerated (or reaccelerated) by the resultant shocks, which also order and amplify the magnetic field (e.g., Hoeft et al. 2011; Kang et al. 2012).

[2] National Radio Astronomy Observatory (NRAO) VLA Sky Survey

5.1.1 Faint Radio Emission In Clusters

Radio halo detection is challenging, because the emission is typically much fainter than both cluster radio galaxies and background radio sources. This reflects the weak ($\sim\mu G$) magnetic field strengths in clusters. The possibility of an even fainter undetected "off-state" was uncovered only recently (Brunetti et al. 2009), with the availability of sensitive upper limits using the GMRT. However, Brown et al. (2011) recently obtained a statistical measure of the "off-state" luminosity by stacking the radio emission from X-ray clusters using the SUMSS[3] survey at 843 MHz. This required the careful removal of more compact AGN emission and a rigorous use of controls. The statistical detection level was $\sim$10$\times$ lower than the observed radio/X-ray correlation, as expected in primary (re-)acceleration models.

Additional insight comes from our recent work on the Green Bank Telescope (GBT), where Farnsworth et al. (2013) discovered in a number of clusters low surface brightness emission much larger than what had been detected on interferometers. An example of this is the merging cool-core cluster Abell 2142, previously thought to contain only a faint 270 kpc mini-halo. Mini-halos (MHs) are diffuse radio structures seen in relatively relaxed, cool core (CC) clusters, extending roughly over the cooling region ($\sim$100 kpc). Their low surface brightness compared to the (typically) embedded cD radio galaxy makes them difficult to detect. The GBT observations at 1.4 GHz of Farnsworth et al. (2013) uncovered 5$\times$ more flux in a 2 Mpc halo-like structure, showing that Abell 2142 is actually an "on-state" GRH system.

Recently it has been observed that a number of clusters host diffuse radio emission which fits into neither the radio halo nor relic class. Some clusters seem to host a bridge of emission connecting a radio halo and relic, e.g., A2744 and A1300 (Venturi et al. 2013), RXCJ1314.4-2515 (Venturi et al. 2007), A521 (Brunetti et al. 2008), Coma (e.g., Brown & Rudnick 2011), and A3667 (Carretti et al. 2013). Farnsworth et al. (2013) observed in A1367 what appears to be a bridge of emission from the known relic towards the main cluster, but no halo was visible. One physical interpretation is shock (re)accelerated CRe which are subsequently accelerated further in the turbulent wake of the outward propagating merger shock (Venturi et al. 2013). Farnsworth et al.

[3] Sydney University Molonglo Sky Survey, http://www.physics.usyd.edu.au/sifa/Main/SUMSS

(2013) discovered similarly peculiar, low surface brightness emission in several clusters (e.g., A2061, A2065, A2069, A2142), but the poor resolution of the GBT prevented a more detailed morphological classification. They suggest that the radio luminosity of halo and relic type emission follow similar scalings, and that the "state" of the diffuse radio emission is primarily a function of total merger energy and time (i.e., cluster evolutionary state).

5.2 Observations and Data Reduction

We observed nine Abell galaxy clusters with the 100-m GBT between October 2012 and September 2013 (see Table 5.4.2). These clusters were selected to span a wide range of dynamical activity, from relaxed to merging, and were restricted to $z \lesssim 0.1$ in order to (at least slightly) resolve structure on Mpc scales after removal of compact emission. A brief summary of relevant parameters for each cluster is listed in Table 5.4.2. The observations were taken with the GBT's Spectrometer in full polarization mode with a 50 MHz bandpass centered on 1.41 GHz.

Each field was imaged using the on-the-fly mapping technique, acquiring 1-D scans of constant Declination separated by $3.3'$ to adequately sample the GBT beam. To improve signal to noise, each scan was repeated once in the opposite direction, where Declination was held constant as the GBT was driven at a rate of 0.1° s^{-1} in Right Ascension, sampling at $2.4'$ intervals. In anticipation of necessary baseline removal due to low spatial frequency gain drifts and foreground (atmospheric and Galactic) emission on scales of $\gtrsim 0.5^\circ$, our scans subtended at least a few degrees in Right Ascension. Similar observations were made each night for flux and polarization calibrators. We give an overview here of the reduction and imaging procedures; for more detailed discussions, see Brown & Rudnick (2011) and Farnsworth et al. (2013).

Using an internal calibrator signal ($\sim$19 K) simultaneously injected into both receivers we determined the relative X and Y dipole gains and internal X-Y phase offset. This yielded fully calibrated scans with sky position and Stokes I, Q, U, V in units of surface brightness (i.e., Kelvin). Linear baseline subtraction in I, Q, U for each stripe was performed to remove the effects of receiver drifts and smooth atmospheric and Galactic foregrounds, which vary on scales $\gtrsim 30'$ (larger than the clusters observed).

The calibrated and baseline subtracted stripes were then used to create I, Q, U images for each field via interpolation with a square pixel scale of $2'$.

Point source subtraction was carried out in the same manner as described in Farnsworth et al. (2013), whereby scaled and convolved images from the NVSS (first clipped at 3σ = 1.35 mJy beam^{-1}) of the corresponding fields were subtracted from the GBT images to yield residual emission maps. This was done in an iterative manner, optimizing for image alignment, GBT beam parameters, and Kelvin to Jy beam^{-1} scaling, which may vary slightly (a few percent) from field to field. The GBT beam parameters were assumed to be equal for all fields, with FWHM dimensions of $9.3' \times 9.2'$ and position angle of 100°. A final zero-level subtraction was performed on each residual image to minimize the contribution from the local Galactic foreground, which could contaminate the measurement of the diffuse emission associated with the cluster. The adopted value of σ_{map} (reported in Table 5.4.2) was then calculated within a background aperture on the final image.

5.3 Results

From the GBT-NVSS residual images we identified detections of diffuse radio emission, finding the $3\sigma_{map}$ contour to be extended in at least one dimension with respect to the GBT beam for all detections. In order to assess the candidate radio detection(s) and morphological classification(s) (e.g., halo, relic) for each field, we acquired Rosat PSPC X-ray images from the NASA SkyView[4] archive.

Figures 5.1−5.7 illustrate the findings, displaying GBT-NVSS residuals (red contours) and Rosat PSPC X-rays (smoothed by a $2'$ Gaussian kernel; blue contours) overlaid upon the NVSS image (clipped at 3σ = 1.35 mJy beam^{-1}; greyscale) for each cluster. The results are reported in Table 5.4.2, where the listed values of integrated flux are measured directly from the residual images, and do not include diffuse flux (not associated with any radio galaxy) that has been removed as a consequence of our NVSS subtraction. We now discuss each cluster in detail.

[4] http://skyview.gsfc.nasa.gov/cgi-bin/titlepage.pl

5.3.1 Abell 85

A85 (z=0551) is part of a well studied large-scale structure also including the clusters Abell 87 and Abell 89, with an associated 3 Mpc X-ray filament extending in a southeast direction (Durret et al. 1998). It is likely undergoing a merger with a small subcluster to the south, as evidenced by X-ray observations (e.g., Markevitch et al. (1998)). A85 displays a spiral feature in the *Chandra* X-ray image after subtraction of a beta-model (Rudnick et al., private communication), implying that merger-induced sloshing of the ICM may be present. Kempner et al. (2002) and Ghizzardi et al. (2010) have reported the presence of a merging cold front associated with the southern subcluster. Bagchi et al. (1998) and Young (2004) observed a radio relic $\sim 10'$ to the southwest of the main cluster, likely related to past merger activity. No halo-type radio emission has been observed in A85.

We detect a large scale radio structure offset from the X-ray peak by roughly $10'$ to the south (see Figure 5.1), with the peak of the radio emission roughly coincident with the merging cold front. With a peak of 45.7 mJy beam^{-1} the integrated flux (after subtraction of the NVSS relic) is observed to be 72.8 mJy. The morphology is somewhat irregular with an apparent low surface brightness extension to the east, although this may be a residual artefact from imperfect point source subtraction. As the radio peak is offset from the X-ray peak, this may be a previously unobserved relic, missed due to its low surface brightness. The emission extends north towards the cluster core, unusual for typical relics, and so this may be some blend of emission structures, such as a relic + bridge. Adding back in the 37.4 mJy of flux in the NVSS relic, we estimate 110.2 mJy of total diffuse radio flux in this cluster. Some of the flux near the peak of the residuals may be from the diffuse tails of a radio galaxy which is barely present in the NVSS image, but is seen in deeper VLA observations (Rudnick et al., unpublished).

Note that, due to negative artefacts (likely oversubtraction) from two 100 mJy radio galaxies to the northeast of the cluster, the total diffuse flux in A85 may be higher than we have estimated here.

5.3.2 Abell 399

A399 (z=0.0718) is likely in an early merger state with A401, with which it is separated by ∼3 Mpc in projection. Murgia et al. (2010) observed with the VLA a ∼570 radio kpc halo (∼420″ extent for the 3σ contour) with $S_{1.4} = 16.2$ mJy after point source subtraction.

In our GBT-NVSS residual image, we detect the halo with $S_{1.4} = 43.9$ mJy, noting that some diffuse emission present in the NVSS image has been subtracted (see Figure 5.2). By visual inspection of the sensitive, high resolution images of Murgia et al. (2010), we have identified the radio galaxies in the NVSS image and estimated that approximately 5.1 mJy of diffuse flux (not associated with any galaxy) present in the NVSS image has been subtracted in our confusion removal procedure. Thus, we estimate the total halo flux of A399 to be 49.0 mJy.

5.3.3 Abell 401

A401 (z=0.0737) is likely in an early merger state with A399. Bacchi et al. (2003) observed A399 at 1.4 GHz with the VLA in D-array, detecting a radio halo flux of 17.1 ± 0.1 mJy after subtraction of discrete radio sources. This is slightly lower than that detected in the NVSS by Giovannini et al. (1999); they attribute this difference to the subtraction of two emission peaks which they classify as unrelated. A399-A401 is the only known "double halo" system (Murgia et al. 2010).

In the GBT-NVSS residual image we observe the halo to have a flux density of $S_{1.4} = 78.3$ mJy, much higher than previous interferometer estimates. We note that the radio structure seems to be offset to the northwest of the X-ray centroid by about $5'$, bringing into question the morphological classification of this structure as a classical GRH; deep interferometric observations are required to investigate this further. By visual inspection of the residual image (Figure 5.2), it appears that we may have oversubtracted the tailed radio galaxy in the western part of the halo. It is possible that some halo flux present in the NVSS image has been subtracted, although the unknown contribution from the diffuse tails of the radio galaxy − likely not fully represented in the NVSS image but detected by the GBT − makes estimation of a correction impossible.

The A399-A401 Intracluster Bridge

X-ray analyses of the A399-A401 pair have uncovered a faint bridge of thermal emission between the two clusters, which may be evidence for an intracluster filament (e.g., Fujita et al. 2008 and references therein). We do not detect a bridge of radio emission in the GBT data, but place a 3σ upper limit on the 1.4 GHz surface brightness of 3.4×10^{-8} Jy arcsec^{-2}.

5.3.4 Abell 496

A496 (z=0.0329) was determined to have three cold fronts by Ghizzardi et al. (2010), likely related to sloshing of the ICM core. It has no known diffuse radio emission.

Due to the presence of three strong radio galaxies within $10'$ of the cluster X-ray peak, large residual artefacts remain in the GBT-NVSS image (see Figure 5.3). Consequently, we are unable to make a clean detection of diffuse cluster emission from the residual image. To estimate an upper limit to the diffuse cluster emission, we have integrated the flux within a typical cluster diameter of 1 Mpc. Within an aperture of radius 500 kpc about the cluster center, we measure a residual flux consistent with zero. A more proper upper limit will be obtained by injection of synthetic Gaussian halos (e.g., Farnsworth et al. 2013).

5.3.5 Abell 644

A644 (z=0.0704) has peculiar X-ray properties; outside the core (R ~75 kpc) it is consistent with a CC cluster, but the temperature profile rises inside the core (Buote et al. 2005), and is suggested to be of merger origin. It has no known diffuse radio emission.

In the GBT-NVSS residual image there is a feature, resolved in only one dimension, that appears to be associated with the cluster ICM (see Figure 5.4). The radio structure extends northeast from the core, the same direction in which a compression of the X-ray contours are observed in the PSPC image, suggesting a link between the dynamics of the ICM (e.g., sloshing, merging) and the nonthermal emission in that region. We measure a flux of 11.1 mJy within the 3σ contours for this structure, which could be a halo, relic, or combination of both.

Interestingly, there is an extended patch of emission $\sim 24'$ to the southeast of the X-ray peak ($\sim$2 Mpc in projection at the redshift of A644). There is no known galaxy cluster or group at this location, nor is there X-ray emission present in the PSPC image; this feature appears coincident with several radio galaxies of unknown redshifts. It is unlikely that this residual emission results entirely due to subtraction artefacts, as the GBT-NVSS residual flux of 25.5 ± 4.8 mJy is $\approx$20% of the NVSS flux within the same aperture − well above the characteristic $\pm$2% residual flux error for our subtraction method. Thus, we tentatively classify the southeast structure as a possible relic associated with A644, with a high degree of uncertainty.

5.3.6 Abell 2029

A2029 (z=0.0773) is a cool-core (CC) cluster, and is part of a supercluster structure with A2028 and A2033 (e.g., Gastaldello et al. (2010); Walker et al. (2012)). In X-ray observations it appears relaxed in the outer cluster regions but shows spiral features in the core which suggest sloshing due to a past merger (Clarke et al. (2004)). Govoni et al. (2009) discovered 18.8 mJy mini-halo with the VLA, which surrounds an extended cD galaxy for which they measure $S_{1.4}$=480 mJy.

Due to the presence of the strong radio galaxy in the cluster center, residual artefacts from the subtraction procedure prevent an unambiguous detection of diffuse emission. We have estimated an upper limit of 37 mJy to the diffuse emission within a radius of 500 kpc about the cluster center. This does not include any diffuse emission present in the NVSS, which has been removed by our subtraction procedure and cannot be cleanly estimated, and may be contaminated by a ridge of Galactic foreground emission (visible in Figure 5.5 and discussed in Gastaldello et al. 2010).

5.3.7 Abell 2033

A2033 (z=0.0818) is a poorly studied member of a supercluster structure with A2028 and A2029. It has a relaxed X-ray morphology in the Rosat image. There is no known diffuse radio emission in this cluster.

Due to the presence of a strong radio galaxy in the cluster center, residual artefacts from the subtraction procedure prevent an unambiguous detection of diffuse emission.

We have estimated an upper limit of 8.4 mJy to the diffuse emission within a radius of 500 kpc about the cluster center. This does not include any diffuse emission present in the NVSS, which has been removed by our subtraction procedure and cannot be cleanly estimated, and may be contaminated by what appears to be Galactic foreground emission (visible in Figure 5.5).

5.3.8 Abell 2256

A2256 (z=0.0581) is a merging cluster known to host a radio halo and radio relic (Clarke & Ensslin 2006). Sun et al. (2002) and Ghizzardi et al. (2010) report the presence of a merging cold front $\sim 5'$ south of the relic. Clarke & Ensslin (2006) used deep observations between 1-2 GHz with the VLA to measure a halo flux density of $S_{1.4} = 103.4$ mJy and a relic flux density of $S_{1.4} = 462$ mJy.

In the GBT-NVSS residual image we detect 438 mJy of flux associated with this cluster (see Figure 5.6). While the emission from the faint halo, not visible in NVSS, must be present, this detection is clearly dominated by relic emission not present in the NVSS image. This makes it impossible to estimate the halo flux directly. We estimate the amount of relic flux in the NVSS image to be 181 mJy, for which we add to the GBT-NVSS residual amount to yield 619 mJy of total diffuse emission (halo + relic) associated with the cluster. This is higher than the total halo+relic flux estimate of Clarke & Ensslin (2006) of 565 mJy; it is likely that we are picking up more of the faint radio halo, although residual contamination (e.g., from faint radio galaxy emission) may be a factor.

5.3.9 Abell 2255

A2255 (z=0.0806) is a merging cluster which has likely undergone a recent merger (e.g., Feretti et al. 1997), likely in the east-west direction (Sakelliou & Ponman 2006. This cluster has been studied extensively with radio telescopes, and shows multiple diffuse radio structures including a halo, multiple relics, radio filaments, and a halo-to-relic bridge structure (Pizzo et al. 2008; Pizzo & de Bruyn 2009; Pizzo et al. 2011).

In the GBT-NVSS residual image we distinguish four regions of interest, three of which are of extremely low surface brightness at the cluster periphery (see Figure 5.7).

Most of the residual flux is contained in a region somewhat cospatial with the X-ray emission (offset slightly to the north), and is likely a combination of the halo, bridge, and NE relic of Pizzo et al. (2008) and Pizzo & de Bruyn (2009). At the north end of the cluster, we find 44.0 mJy in an elongated low surface brightness structure extending northwest which is likely related to the filamentary NW relic of Pizzo & de Bruyn (2009). We also measure 19.1 mJy in a diffuse structure about $30'$ east of the cluster which is also present in the images of Pizzo & de Bruyn (2009) but dismissed as an imaging artefact. Finally, we observe 21.1 mJy in a low surface brightness structure $\sim 40'$ to the southwest of the cluster, for which there is also a hint of at 2 m in Pizzo & de Bruyn (2009) but is not mentioned.

5.4 Discussion and Concluding Remarks

Expanding on the work of Farnsworth et al. (2013), we have presented results of a further exploration of low surface brightness emission in galaxy clusters representing a wide range of merging activity with the 100-m Green Bank Telescope. In six of the nine clusters observed we detect diffuse emission above what is currently observed by interferometers, including new structures in A85 and A644. Our detections have occurred exclusively in clusters with merging activity, supporting the notion that radio halos are powered by merger energy. For two other clusters, A2029 and A2033, we can provide only upper limits to possible diffuse emission due to the presence strong confusion from Galactic foreground and bright embedded radio galaxies.

The poor resolution of the GBT prevents us from providing morphological classification for some of these structures, which may be multi-component structures blended within the GBT beam. In A85 we may be seeing a relic plus bridge of emission related to the merging activity with the southern subcluster. Similarly for A2255, we have detected the halo/bridge/relic structure seen by Pizzo et al. (2008), but have also seen multiple faint diffuse structures at the cluster periphery, such as an extension to the NW relic seen by Pizzo & de Bruyn (2009). In A644 we see an elongated radio feature which extends outward from the core, and may be some sort of halo+relic structure. For systems with halos or relics, we have increased the observed flux of these structures, where we are likely sensitive to faint emission not seen by the interferometers. In A399

and A401, a known binary halo system, we have detected much more emission (more than double) than previously found by interferometers. Similarly, in A2256 we have observed roughly 10% more combined flux from the halo and relic (blended by the GBT beam) than observed in a deep interferometric study.

Our results support the findings of Farnsworth et al. (2013) that nonthermal emission in clusters at low redshift ($z < 0.1$) may be missed often by interferometric observations. This low surface brightness emission may be in the form of faint halo extensions, halo-to-relic bridge structures or small scale particle acceleration regions associated with minor to moderate merging activity.

5.4.1 Nonthermal Luminosity of Clusters

Farnsworth et al. (2013) discuss the notion that the nonthermal ICM luminosity of clusters is tied to the thermal energy budget, which is, in turn, dependent upon the energy input by mergers. Thus the radio luminosity of a cluster is relatively independent of the exact type of radio structure (e.g., halo, relic), and may distributed between multiple diffuse structures. We test this concept by plotting our detections on the X-ray − radio luminosity correlation of Brunetti et al. (2008). Figure 5.8 illustrates that our detections all lie near the so-called "on-state" halo correlation for clusters, where recent merging activity has presumably channeled gravitational energy into cosmic rays and magnetic fields which are observed as diffuse nonthermal emission. The relatively large scatter in this correlation is perhaps a function of evolutionary state, which causes each cluster to move about the phase space as thermal and nonthermal energy is generated/dissipated (Donnert et al. 2013). To properly investigate this theory, more detailed information about the merger phase is required for each cluster.

5.4.2 Future Work

Our ongoing study proposes to address the following questions:

• Is low surface brightness emission commonly missed in clusters, particularly at low redshift? If so, what is the nature of this emission in the context of merger dynamics, particle acceleration, and cluster magnetic fields?

• What is the physical nature of the observed radio halo bimodality? What are the

timescales for halo generation and dissipation? That no radio halos have been observed far from the X-ray − radio luminosity correlation suggests that this timescale must be relatively short.

• Is the total nonthermal luminosity of a cluster really dependent only upon the thermal ICM properties and not upon the type of diffuse structures (e.g., halo, relic)?

These questions may be addressed by a combination of single dish and interferometric programs. Using single dish telescopes, a larger survey of clusters spanning a wide range of cluster dynamical states may be desirable to locate faint halos in the off-state luminosity region. Such a survey will be possible using data from GALFACTS[5] , a project with the Arecibo Radio Telescope which will primarily focus on diffuse Galactic emission, but will serendipitously observe roughly 700 galaxy clusters at $z < 0.3$ (the redshift at which a linear extent of 1 Mpc is just resolved). Additionally, single dish observations are the only way to recover the full radio flux of sufficiently extended structures, making these instruments critical for observations at low redshift. Deep followup observations at multiple frequencies with radio interferometers such as VLA, GMRT, and LOFAR are then necessary to resolve and classify the morphology of the emission structures (e.g., halos, relics) and diagnose the physical mechanism(s) at responsible for CRe production (i.e., turbulent reacceleration vs. hadronic collisions).

[5] Galactic Arecibo L-band Feed Array Continuum Transit Survey; http://www.ucalgary.ca/ras/GALFACTS

Table 5.1. Galaxy Clusters Observed

Source	z	Scale (kpc/″)	R.A. (J2000)	Decl. (J2000)	Local σ^a_{map} (mJy beam^{-1})
A85	0.0551	1.07	00h41m50.1s	-09d18m07s	4
A399	0.0718	1.37	02h57m56.4s	+13d00m59s	4
A401	0.0737	1.40	02h58m57.5s	+13d34m46s	4
A496	0.0329	0.656	04h33m38.4s	-13d15m33s	4
A644	0.0704	1.34	08h17m24.5s	-07d30m46s	3.5
A2029	0.0773	1.46	15h10m55.0s	+05d43m12s	4
A2033	0.0818	1.54	15h11m26.5s	+06d20m56s	4
A2256	0.0581	1.13	17h03m43.5s	+78d43m03s	4
A2255	0.0806	1.52	17h12m31.0s	+64d05m33s	4

Note. — Redshifts are taken from the NASA/IPAC Extragalactic Database
[a] After baseline removal and point source subtraction

Table 5.2. Cluster Parameters From The Literature

Source	L_X (10^{44} erg s^{-1})	kT_X (keV)	$S_{1.4}$ (mJy)	Classification	References
A85	8.38	6.2	50	Relic	1, 3
A399	6.40	5.8	16.2	Halo	2,4
A401	9.94	7.8	17.1	Halo	2,5
A496	3.54	4.7	–	–	1
A644	7.92	6.6	–	–	1
A2029	15.29	7.8	18.8	Mini-halo	2, 6
A2033	2.57	4.7	–	–	2
A2256	7.11	7.5	103.4[a], 462[b]	Halo, Relic	2, 7
A2255	4.94	7.3	44[a], 30[b]	Halo, Relics	2, 8

Note. — All parameters are corrected for cosmology, where applicable.
Columns: (1) Cluster; (2) X-ray luminosity, 0.1-2.4 keV; (3) X-ray temperature; (4) Flux density, 1.4 GHz; (5) Classification of diffuse radio emission not associated with radio galaxies; (6) References for X-ray and radio parameters.
References: *X-ray:* (1) Ebeling et al. (1996); (2) Ebeling et al. (1998); *Radio:* (3) Young (2004); (4) Murgia et al. (2010); (5) Bacchi et al. (2003); (6) Govoni et al. (2009); (7) Clarke & Ensslin (2006); (8) Pizzo & de Bruyn (2009)
[a] Estimated total halo flux
[b] Estimated total relic flux

Table 5.3. Total Intensity Results From 3σ Contours

Source	$P_{1.4}$ (10^{24} W Hz^{-1})	$S_{1.4}$ (mJy)	$\theta_{maj} \times \theta_{min}$ (arcmin)	I_{peak} (mJy beam^{-1})
A85	0.521	72.8 ± 7.6	17.8 × 15.0	45.7
A399	0.552	43.9 ± 6.3	17.5 × 13.7	33.6
A401	1.04	78.3 ± 8.0	26.0 × 20.0	37.9
A496	–	–	–	–
A644	0.134	11.1 ± 3.3	13.0 × 6.2	18.0
A2029	<0.54	<37[a]	–	–
A2033	<0.14	<8.4[a]	–	–
A2256	3.54	438 ± 10.3	28.7 × 25.3	224.1
A2255	1.96	122 ± 8.5	27.0 × 19.2	65.5

Note. — The integrated fluxes reported here represent values measured directly from the GBT-NVSS residual images, and do not account for any diffuse emission lost in the subtraction procedure. Upper limits to $S_{1.4}$ are measured within 500 kpc of the cluster center. See text for details.

[a] Likely contaminated by Galactic foreground emission.

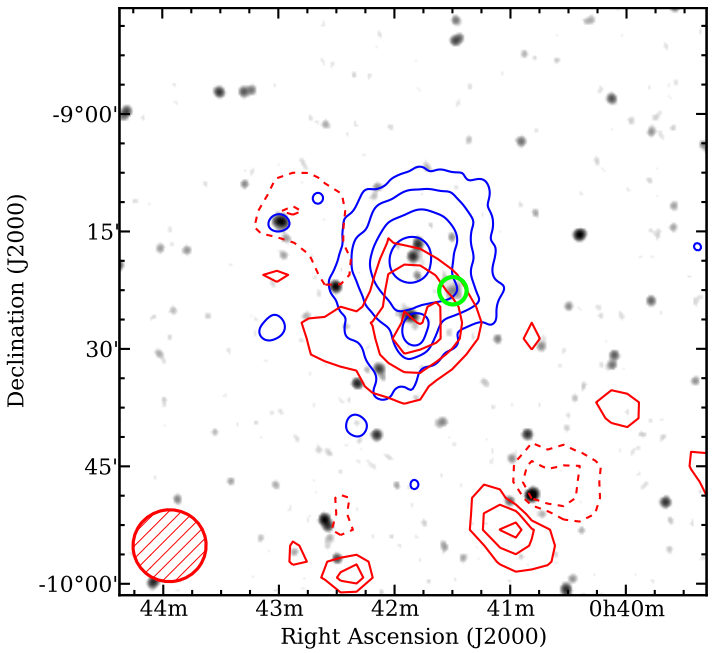

Figure 5.1 **Abell 85.** NVSS image (greyscale; clipped at 1.35 mJy (45″ beam)$^{-1}$) with overlaid GBT-NVSS 1.4 GHz residuals (red contours) and PSPC X-ray image (smoothed with a 2′ Gaussian kernel, blue contours) in the A85 region. Radio contours are at $\pm$(3,6,9,...)$\times\sigma_{map}$ (negative contours dashed, if present). The location of the relic present in the NVSS image is shown as a green circle. The GBT beam is shown in the lower left of the image.

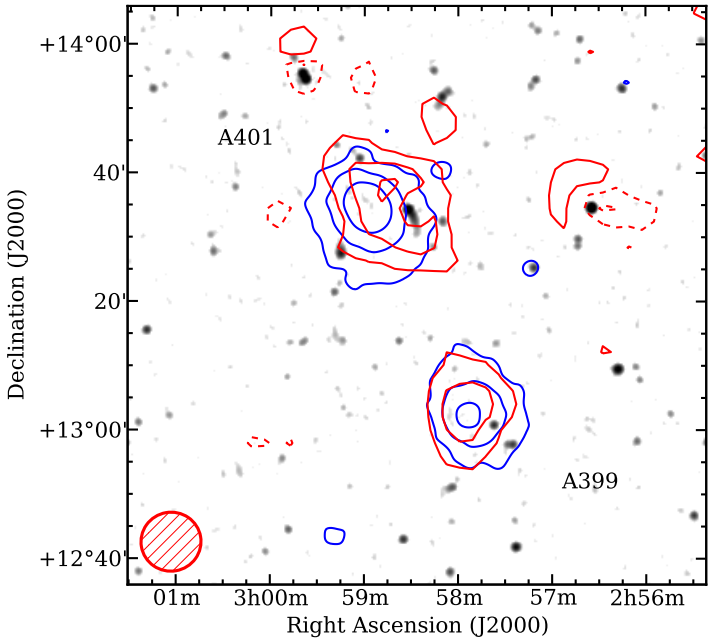

Figure 5.2 **The Abell 399 – Abell A401 system.** NVSS image (greyscale; clipped at 1.35 mJy (45″ beam)$^{-1}$) with overlaid GBT-NVSS 1.4 GHz residuals (red contours) and PSPC X-ray image (smoothed with a 2′ Gaussian kernel, blue contours) in the A399-A401 region. Radio contours are at $\pm$(3,6,9,...)$\times\sigma_{map}$ (negative contours dashed, if present). The GBT beam is shown in the lower left of the image.

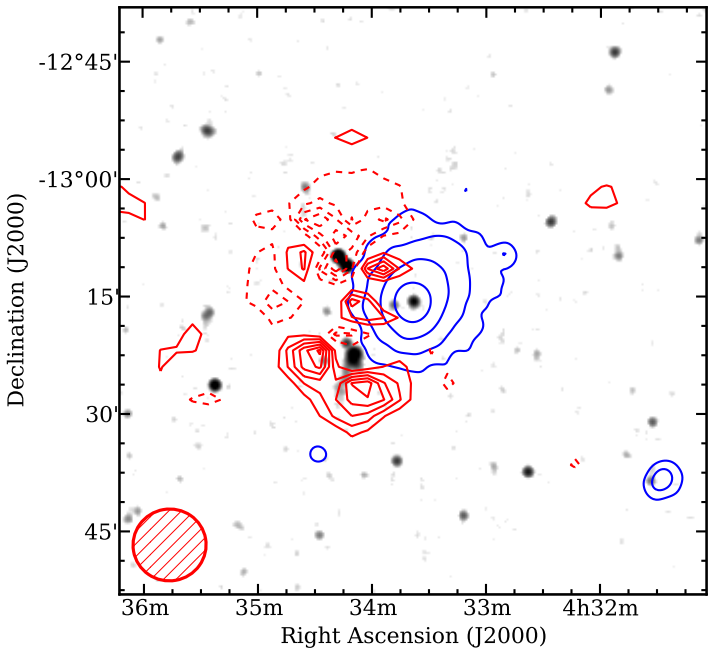

Figure 5.3 **Abell 496.** NVSS image (greyscale; clipped at 1.35 mJy (45″ beam)$^{-1}$) with overlaid GBT-NVSS 1.4 GHz residuals (red contours) and PSPC X-ray image (smoothed with a 2′ Gaussian kernel, blue contours) in the A496 region. Radio contours are at $\pm$(3,6,9,...)$\times\sigma_{map}$ (negative contours dashed, if present). The GBT beam is shown in the lower left of the image.

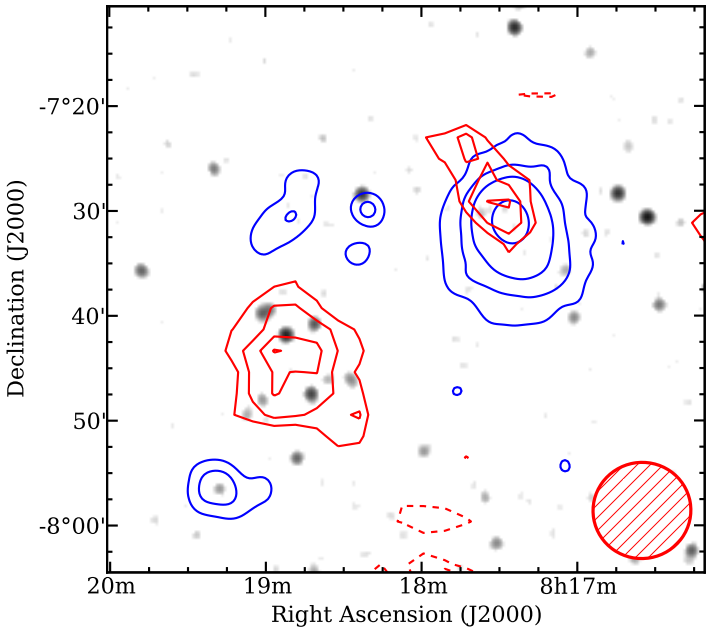

Figure 5.4 **Abell 644.** NVSS image (greyscale; clipped at 1.35 mJy (45″ beam)$^{-1}$) with overlaid GBT-NVSS 1.4 GHz residuals (red contours) and PSPC X-ray image (smoothed with a 2′ Gaussian kernel, blue contours) in the A644 region. Radio contours are at $\pm$(3,4,5,...)$\times\sigma_{map}$ (negative contours dashed, if present). The GBT beam is shown in the lower right of the image.

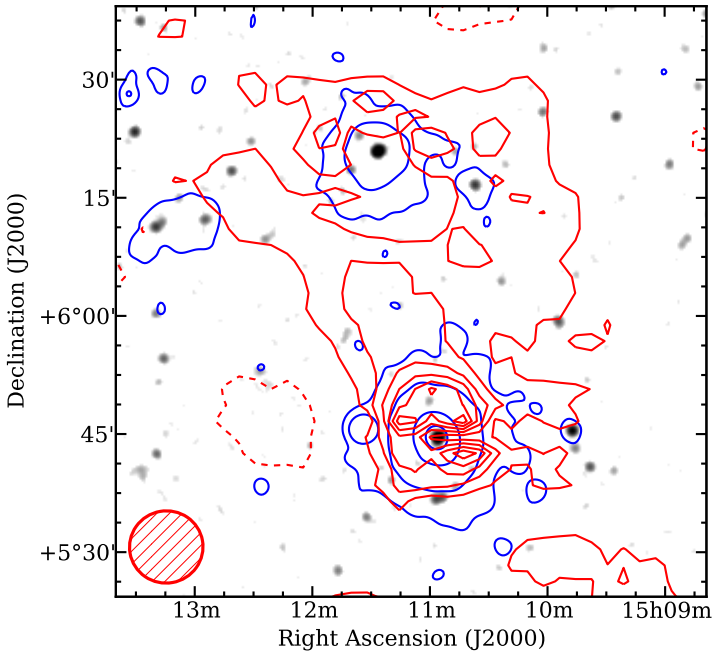

Figure 5.5 **Abell 2029 and A2033.** NVSS image (greyscale; clipped at 1.35 mJy (45″ beam)$^{-1}$) with overlaid GBT-NVSS 1.4 GHz residuals (red contours) and PSPC X-ray image (smoothed with a 2′ Gaussian kernel, blue contours) in the A2029 (south) and A2033 (north) region. Radio contours are at $\pm$(3,6,9,...)$\times\sigma_{map}$ (negative contours dashed, if present). The ridge of Galactic foreground emission is clearly visible at the lowest radio contour. The GBT beam is shown in the lower left of the image.

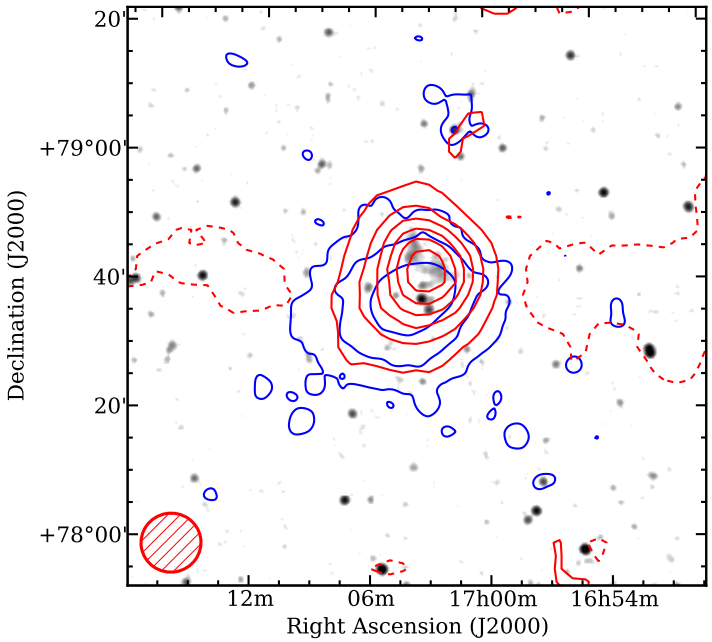

Figure 5.6 **Abell 2256.** NVSS image (greyscale; clipped at 1.35 mJy (45″ beam)$^{-1}$) with overlaid GBT-NVSS 1.4 GHz residuals (red contours) and PSPC X-ray image (smoothed with a 2′ Gaussian kernel, blue contours) in the A2256 region. Radio contours are at $\pm$(3,12,21,30,...)$\times\sigma_{map}$ (negative contours dashed, if present). The GBT beam is shown in the lower left of the image.

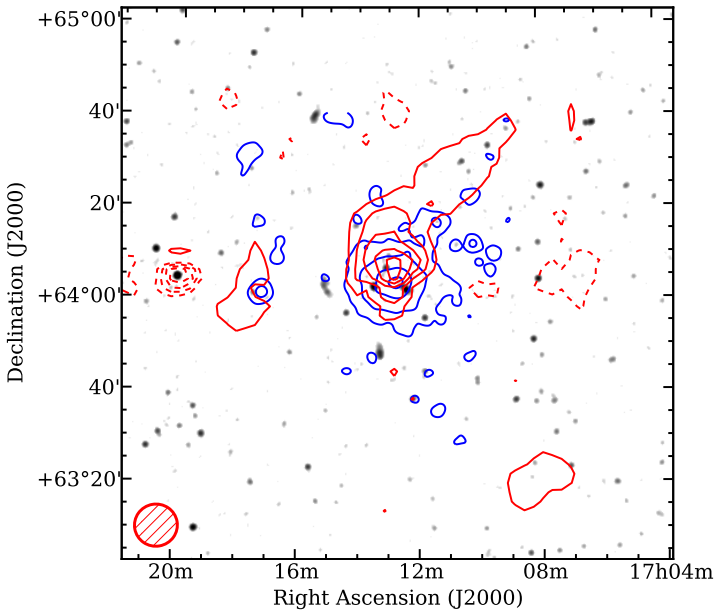

Figure 5.7 **Abell 2255.** NVSS image (greyscale; clipped at 1.35 mJy (45″ beam)$^{-1}$) with overlaid GBT-NVSS 1.4 GHz residuals (red contours) and PSPC X-ray image (smoothed with a 2′ Gaussian kernel, blue contours) in the A2255 region. Radio contours are at $\pm$(3,6,9,...)$\times\sigma_{map}$ (negative contours dashed, if present). The GBT beam is shown in the lower left of the image.

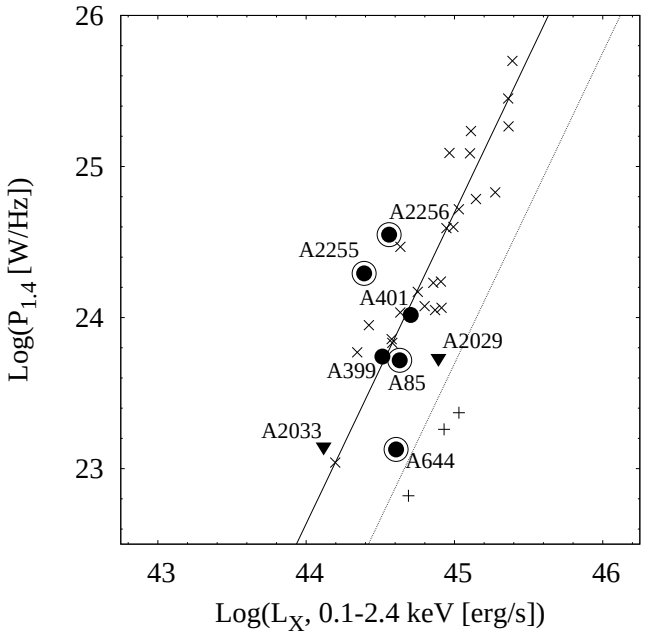

Figure 5.8 Plot of $P_{1.4}$ vs. L_X for halo detections. Xs are halos from the literature. Crosses are statistical detections of off-state halos from Brown et al. (2011). From this work are halos (filled circles), and upper limits (filled, downward triangles); the candidates for multi-structure objects (i.e., A85, A644, A2255, A2256) are shown as filled circles surrounded by open circles. The values plotted here are measured directly from the GBT-NVSS residual images and do not reflect any diffuse emission lost in the subtraction process.

Chapter 6

Conclusions

6.1 Summary Of Results

• In Chapter 2 I discussed the use of polarization observations to probe magnetized plasmas, exploring various methods of Faraday rotation measure determination. I determined that methods such as traditional fitting of models to polarization angle only (without consideration of the fractional polarization) or the novel Rotation Measure Synthesis may yield erroneous results in the presence of complex Faraday structure. It seems that the best way to more accurately recover the true Faraday structure is by fitting models directly to the observables $Q(\lambda^2)$ and $U(\lambda^2)$, using radio polarization observations of the southern lobe of the radio galaxy 3C33 as an example.

• In Chapter 3 I exhibited results from a 1.4 GHz GBT study of twelve merging galaxy clusters. After subtraction of confusion from Galactic foreground and extragalactic background radio sources, eleven of the twelve clusters exhibited a significant excess of diffuse emission over that found by previous interferometric studies. Faint large-scale radio emission in clusters may be commonly missed by interferometric studies, particularly at low redshifts, and this has serious implications for models of halo generation. I also provide supporting evidence for the notion that the total radio emission in clusters may not depend strongly on the particular state (e.g., halo, relic), as the energy for particle acceleration is channeled from the merger and tied observationally to the thermal state of the ICM.

• In Chapter 4 I presented the results of snapshot VLA observations of the minor

merging cluster A2142 at 1.4 GHz. New evidence of large scale ICM sloshing has been discovered in this cluster, further supported by an apparent 2 Mpc radio halo discovered as part of our recent GBT study (Chapter 3). My VLA observations confirm the presence of a Mpc-scale halo in the sloshing core of A2142, which extends beyond the central cold fronts − a phenomenon unobserved in systems lacking major merging activity. This new halo appears to be comprised of multiple components, with a sharply peaked MH-type structure in the core, and a faint, extended GRH-like structure extending beyond the core region. The VLA observations do not recover the full halo extent observed by previous GBT observations (Chapter 3), illustrating a weakness of interferometric cluster observations that may be underestimated in the literature. Preliminary spectral analysis finds a steep spectrum ($\alpha > 1.5$) to the core emission, possibly indicating a turbulent origin for the cosmic ray production in that region.

• In Chapter 5 I discussed preliminary findings of a recent GBT study of nine clusters, chosen to span a wide range of dynamical activity. I found evidence for low surface brightness emission missed by interferometers in eight of the nine clusters, including two new radio structures. As in Chapter 3, I found that the total radio luminosity of clusters hosting diffuse emission follows the radio − X-ray correlation regardless of the state of the radio emission (e.g., halo, relic, or combination).

6.2 Final Thoughts

Throughout this dissertation we have explored the thermal and nonthermal properties of galaxy clusters, primarily with radio observations. The work presented here represents our significant contribution to the current understanding of plasma physics in galaxy clusters. Through radio polarization studies properties of the thermal ICM − such as magnetic field strength and thermal electron density − may be probed, but special care must be taken with many standard analysis methods (e.g., polarization angle fitting and Rotation Measure Synthesis) to avoid misinterpretation of the observations.

In the nonthermal regime, large scale, low surface brightness synchrotron emission may be commonly missed by current interferometric studies. This unobserved emission may represent a significant amount of the total radio luminosity in some clusters (e.g.,

minor merging clusters), challenging the current paradigm of the nonthermal properties of these systems. Turbulence on Mpc-scales may exist in minor merging systems, e.g., generated by large scale ICM sloshing, and this may be sufficient to drive cosmic ray acceleration and magnetic field amplification/ordering on similarly large scales. Alternatively, galaxy clusters may host a faint, extended halo component powered by hadronic collisions between thermal and relativistic protons. To address this possibility, future cluster surveys – especially those at low redshift – must improve their sensitivity to faint extended emission. This may be accomplished for interferometric studies either by vastly increasing the acquisition of short baselines by interferometers, or, preferably, the inclusion of single dish observations to recover the total system flux. Additionally, radio observations must be acquired across a wide range of frequencies, e.g., 50 MHz to a few GHz, in order to properly characterize the synchrotron spectrum and distinguish between competing particle acceleration models.

6.3 Future Work

6.3.1 Galaxy Clusters: Cosmic Ray Acceleration And Magnetism

Improved Surveys

To address the competing models of particle acceleration in galaxy clusters, large surveys at a wide range of frequencies must be undertaken. Several such surveys with various radio interferometers are either underway or in the planning phase. The GMRT is currently conducting an all-sky survey at 150 MHz, and will cover about 37,000 square degrees of the northern sky with an rms sensitivity of 5-7 mJy beam^{-1}. LOFAR is planning to survey the entire accessible sky at frequencies of 15, 30, 60, 120 MHz and 1000 square degrees at 200 MHz. ASKAP will be used for several surveys at various frequencies between 700 MHz and 1.8 GHz; this includes EMU and POSSUM at 1.4 GHz, which will map a large fraction of the sky in total intensity and polarization, respectively. NRAO is currently considering an all-sky survey at 350 MHz with the VLA's new wideband low frequency receiver system.

These surveys (and many others that I have not mentioned) will play a crucial role in improving our understanding of the nonthermal physics of galaxy clusters. Not only

will they likely detect many of the copious ultra-steep spectrum radio halos predicted to exist but currently evading detection at GHz frequencies, they will allow us to fully characterize the synchrotron spectra of the diffuse emission and distinguish between models of particle acceleration. We will also investigate the correlation between X-ray luminosity and radio luminosity at a wide range of radio frequencies, improving our understanding of the interplay between the thermal and nonthermal particle populations in clusters. POSSUM's sights are aimed directly at investigating astrophysical magnetism through Faraday rotation analysis, and clusters are a big part of their plans.

GALFACTS

This all-Arecibo sky survey at 1.4 GHz is currently underway using the largest single-aperture telescope in the world, the 300-m Arecibo Radio Telescope at the Arecibo Observatory in Puerto Rico. Designed with the primary goal of investigating the Milky Way galaxy, I am part of a team that will take advantage of the serendipitous observations by this survey of hundreds of galaxy clusters with $z < 0.3$. The redshift range is chosen to probe 1) the era of heightened cluster merging activity ($0.2 < z < 0.3$) and 2) the low redshift ($z < 0.2$) regime where the lack of sensitivity to Mpc-scale emission by radio interferometers causes halo emission to go undetected. The superb resolution ($\sim 3'$) and sensitivity (<1 mJy beam^{-1}) will allow us to improve upon the GBT cluster projects described in this thesis (Chapters 3 and 5). Our search for faint cluster emission will first start with a targeted sample of X-ray luminous clusters, where radio emission is expected due to the associated merging activity. We will then conduct a blind survey of the full GALFACTS data set, thus removing any bias toward dynamical activity. These projects will provide stringent tests on the observed bimodality of radio halos, and refine upper limits to the synchrotron emissivity of quiescent clusters.

6.3.2 Beyond Clusters: The Cosmic Web

While galaxy clusters harbor much of the baryonic matter at low redshift, roughly 50% of the baryons observed at high redshift are still undetected in the local Universe. Theory and simulations predict that most of this unseen matter likely exists in a filamentary network of low density magnetized thermal plasma (warm-hot intergalactic medium; WHIM) called the cosmic web. These filaments are presumed to be shock heated to

$10^5 - 10^7$ K through accretion processes onto and along the filaments. The same shocks that heat the plasma are also expected to energize a significant nonthermal population of relativistic particles and magnetic fields (e.g., Keshet et al. 2004; Ryu et al. 2008). Radio observations currently hold the most promise for detection of the diffuse cosmic web. The synchrotron signature of shocks in filaments is expected to trace the distribution of the thermal matter, and characterization of the nonthermal properties will be crucial to understanding the thermal and nonthermal pressures, magnetic fields, and cosmic ray acceleration efficiencies in these low density environments. Brown (2011) highlights some of the methods by which direct and statistical detections of the WHIM are likely to occur in the next decade or two. I now describe some of my plans for statistical investigation of the Cosmic Web.

Cross Correlation Methods

The synchrotron signature of shocks in the cosmic web should be correlated with the distribution of matter in large scale structure (e.g., Keshet et al. 2004). Following our pilot project (Brown et al. 2010), which involved the cross-correlation of Bonn 1.4 GHz radio images with 2MASS galaxy distributions, our team will use multiple radio surveys − such as GALFACTS and VLSSr − to perform these experiments. By illuminating these cosmic filaments, we will characterize the nonthermal properties of large scale filaments − such as synchrotron emissivities, magnetic field strengths, and CR acceleration mechanisms − and probe the distribution of large scale thermal matter.

Angular Power Spectra

Keshet et al. (2004) also suggest that the synchrotron signature of shocks in large scale structure will be detectable in angular power spectra of the extragalactic radio background, particularly below 500 MHz. This should be easily observable within forthcoming surveys by telescopes such as LOFAR and SKA, but it may also be detectable using current surveys. Our team will measure the angular power spectrum in low frequency surveys such as VLSSr and WENSS. The exquisite sensitivity of GALFACTS may also allow a detection from this experiment, and it will also be pursued. These experiments will illuminate the large scale distribution of the missing baryons.

References

Abramopoulos, F., & Ku, W. H.-M. 1983, ApJ, 271, 446

Ackermann,M., Ajello, M., Allafort, A., et al. 2010, ApJ, 717, L71

Arnaud, M., & Evrard, A. E. 1999, MNRAS, 305, 631

Avni, Y. 1976, ApJ, 210, 642

Bacchi, M., Feretti, L., Giovannini, G., & Govoni, F. 2003, A&A, 400, 465

Bagchi, J., Pislar, V., & Lima Neto, G. B. 1998, MNRAS, 296, L23

Bahcall, N. A. 1977, ApJ, 217, L77

Basu, K. 2012, MNRAS, 421, L112

Becker, R. H., White, R. L., & Helfand, D. J. 1995, ApJ, 450, 559

Belsole, E., Sauvageot, J.-L., Pratt, G. W., & Bourdin, H. 2005, Advances in Space Research, 36, 630

Berge, G. L., & Seielstad, G. A. 1967, ApJ, 148, 367

Bernardi, G., et al. 2010, A&A, 522, A67

Bicknell, G. V., Cameron, R. A., & Gingold, R. A. 1990, ApJ, 357, 373

Böhringer, H., Schuecker, P., Guzzo, L., et al. 2004, A&A, 425, 367

Bonafede, A., Feretti, L., Murgia, M., Govoni, F., Giovannini, G., Dallacasa, D., Dolag, K., & Taylor, G. B. 2010, A&A, 513, A30

Bonafede, A., Brüggen, M., van Weeren, R., et al. 2012, MNRAS, 426, 40

Boschin, W., Girardi, M., & Barrena, R. 2012, A&A, 547, A44

Bourdin, H., & Mazzotta, P. 2008, A&A, 479, 307

Branchesi, M., Gioia, I. M., Fanti, C., Fanti, R., & Perley, R. 2006, A&A, 446, 97

Bregman, J. N. 2007, ARA&A, 45, 221

Brentjens, M. A., & de Bruyn, A. G. 2005, A&A, 441, 1217

Brown, J. C., & Taylor, A. R. 2001, ApJ, 563, L31

Brown, J. C., Haverkorn, M., Gaensler, B. M., Taylor, A. R., Bizunok, N. S., McClure-Griffiths, N. M., Dickey, J. M., & Green, A. J. 2007, ApJ, 663, 258

Brown, S., & Rudnick, L. 2009, AJ, 137, 3158

Brown, S., Farnsworth, D., & Rudnick, L. 2010, MNRAS, 402, 2

Brown, S., & Rudnick, L. 2011, MNRAS, 412, 2

Brown, S., Emerick, A., Rudnick, L., & Brunetti, G. 2011, ApJ, 740, L28

Brown, S. D. 2011, Journal of Astrophysics and Astronomy, 32, 577

Brunetti, G. 2004, Journal of Korean Astronomical Society, 37, 493

Brunetti, G., Venturi, T., Dallacasa, D., et al. 2007, ApJ, 670, L5

Brunetti, G., Giacintucci, S., Cassano, R., et al. 2008, Nature, 455, 944

Brunetti, G., Cassano, R., Dolag, K., & Setti, G. 2009, A&A, 507, 661

Brunetti, G. 2011, Mem. Soc. Astron. Italiana, 82, 515

Brunetti, G., & Lazarian, A. 2011, MNRAS, 410, 127

Brunetti, G., Blasi, P., Reimer, O., et al. 2012, MNRAS, 426, 956

Buote, D. A., Humphrey, P. J., & Stocke, J. T. 2005, ApJ, 630, 750

Burn, B. J. 1966, MNRAS, 133, 67

Burns, J. O., Skillman, S. W., & O'Shea, B. W. 2010, ApJ, 721, 1105

Carretti, E., Brown, S., Staveley-Smith, L., et al. 2013, MNRAS, 430, 1414

Cassano, R., & Brunetti, G. 2005, MNRAS, 357, 1313

Cassano, R., Brunetti, G., & Setti, G. 2006, MNRAS, 369, 1577

Cassano, R., Brunetti, G., Setti, G., Govoni, F., & Dolag, K. 2007, MNRAS, 378, 1565

Cassano, R., Brunetti, G., Venturi, T., et al. 2008, A&A, 480, 687

Cassano, R. 2009, The Low-Frequency Radio Universe, 407, 223

Cassano, R., Ettori, S., Giacintucci, S., et al. 2010, ApJ, 721, L82

Cassano, R., Brunetti, G., Röttgering, H. J. A., & Brüggen, M. 2010, A&A, 509, A68

Cassano, R. 2010, A&A, 517, A10

Cassano, R., Brunetti, G., Norris, R. P., et al. 2012, A&A, 548, A100

Cassano, R., Ettori, S., Brunetti, G., et al. 2013, ApJ, 777, 141

Cavaliere, A., Lapi, A., & Fusco-Femiano, R. 2011, A&A, 525, A110

Cen, R., & Ostriker, J. P. 1999, ApJ, 514, 1

Chatzikos, M., Sarazin, C. L., & Kempner, J. C. 2006, ApJ, 643, 751

Cortese, L., Gavazzi, G., Boselli, A., Iglesias-Paramo, J., & Carrasco, L. 2004, A&A, 425, 429

Cioffi, D. F., & Jones, T. W. 1980, AJ, 85, 368

Clarke, T. E., Blanton, E. L., & Sarazin, C. L. 2004, ApJ, 616, 178

Clarke, T. E., & Ensslin, T. A. 2006, AJ, 131, 2900

Clarke, T. E., Kronberg, P. P., Böhringer, H. 2001, ApJ, 547, L111

Colless, M., Dalton, G., Maddox, S., et al. 2001, MNRAS, 328, 1039

Condon, J. J., Cotton, W. D., Greisen, E. W., Yin, Q. F., Perley, R. A., Taylor, G. B., & Broderick, J. J. 1998, AJ, 115, 1693

Dai, X., Bregman, J. N., Kochanek, C. S., & Rasia, E. 2010, ApJ, 719, 119

Dallacasa, D., Brunetti, G., Giacintucci, S., et al. 2009, ApJ, 699, 1288

Davé, R., Cen, R., Ostriker, J. P., et al. 2001, ApJ, 552, 473

de Bruyn, A. G., & Brentjens, M. A. 2005, A&A, 441, 931

de Zotti, G., Massardi, M., Negrello, M., & Wall, J. 2010, A&A Rev., 18, 1

Deiss, B. M., Reich, W., Lesch, H., & Wielebinski, R. 1997, A&A, 321, 55

Donnelly, R. H., Markevitch, M., Forman, W., et al. 1998, ApJ, 500, 138

Donnert, J., Dolag, K., Brunetti, G., & Cassano, R. 2013, MNRAS, 429, 3564

Durret, F., Forman, W., Gerbal, D., Jones, C., & Vikhlinin, A. 1998, A&A, 335, 41

Dursi, L. J., & Pfrommer, C. 2008, ApJ, 677, 993

Ebeling, H., Voges, W., Böhringer, H., et al. 1996, MNRAS, 281, 799

Ebeling, H., Edge, A. C., Böhringer, H., et al. 1998, MNRAS, 301, 881

Ebeling, H., Edge, A. C., Allen, S. W., et al. 2000, MNRAS, 318, 333

Eilek, J. A., & Owen, F. N. 2002, ApJ, 567, 202

Enßlin, T. A., Biermann, P. L., Klein, U., & Kohle, S. 1998, A&A, 332, 395

Enßlin, T., Pfrommer, C., Miniati, F., & Subramanian, K. 2011, A&A, 527, A99

Fanti, C., et al. 2004, A&A, 427, 465

Farnsworth, D., Rudnick, L., Brown, S., & Brunetti, G. 2013, ApJ, 779, 189

Feain, I. J., et al. 2009, ApJ, 707, 114

Feretti, L., Giovannini, G., & Böhringer, H. 1997, N.A., 2, 501

Feretti, L., Boehringer, H., Giovannini, G., & Neumann, D. 1997, A&A, 317, 432

Feretti, L., Giovannini, G., Govoni, F., & Murgia, M. 2012, A&A Rev., 20, 54

Ferrari, C., Govoni, F., Schindler, S., Bykov, A. M., & Rephaeli, Y. 2008, Space Sci. Rev., 134, 93

Fletcher, A., Berkhuijsen, E. M., Beck, R., & Shukurov, A. 2004, A&A, 414, 53

Fletcher, A., Beck, R., Shukurov, A., Berkhuijsen, E. M., & Horellou, C. 2011, MNRAS, 412, 2396

Flin, P., & Krywult, J. 2006, A&A, 450, 9

Frick, P., Sokoloff, D., Stepanov, R., & Beck, R. 2010, MNRAS, 401, L24

Fujita, Y., Tawa, N., Hayashida, K., et al. 2008, PASJ, 60, 343

Gardner, F. F., & Whiteoak, J. B. 1966, ARA&A, 4, 245

Garrington, S. T., Conway, R. G., & Leahy, J. P. 1991, MNRAS, 250, 171

Gastaldello, F., Ettori, S., Balestra, I., et al. 2010, A&A, 522, A34

Gavazzi, G., & Trinchieri, G. 1983, ApJ, 270, 410

Gavazzi, G., & Jaffe, W. 1987, A&A, 186, L1

Ghizzardi, S., Rossetti, M., & Molendi, S. 2010, A&A, 516, A32

Giacintucci, S., Dallacasa, D., Venturi, T., et al. 2011, A&A, 534, A57

Giovannini, G., Feretti, L., & Andernach, H. 1985, A&A, 150, 302

Giovannini, G., Tordi, M., & Feretti, L. 1999, N.A., 4, 141

Giovannini, G., & Feretti, L. 2000, N.A., 5, 335

Giovannini, G., & Feretti, L. 2002, Merging Processes in Galaxy Clusters, 272, 197

Giovannini, G., Bonafede, A., Feretti, L., et al. 2009, A&A, 507, 1257

Girardi, M., Bardelli, S., Barrena, R., et al. 2011, A&A, 536, A89

Goldstein, S. J., Jr., & Reed, J. A. 1984, ApJ, 283, 540

Govoni, F., & Feretti, L. 2004, International Journal of Modern Physics D, 13, 1549

Govoni, F., Murgia, M., Markevitch, M., et al. 2009, A&A, 499, 371

Govoni, F., et al. 2010, A&A, 522, A105

Guidetti, D., Murgia, M., Govoni, F., Parma, P., Gregorini, L., de Ruiter, H. R., Cameron, R. A., & Fanti, R. 2008, A&A, 483, 699

Guidetti, D., Laing, R. A., Murgia, M., Govoni, F., Gregorini, L., & Parma, P. 2010, A&A, 514, A50

Harris, D. E., Bahcall, N. A., & Strom, R. G. 1977, A&A, 60, 27

Haves, P. 1975, MNRAS, 173, 553

Heald, G., Braun, R., & Edmonds, R. 2009, A&A, 503, 409

Hoeft, M., & Brüggen, M. 2007, MNRAS, 375, 77

Hoeft, M., Nuza, S. E., Gottlöber, S., et al. 2011, Journal of Astrophysics and Astronomy, 32, 509

Hogge, T. G., Sarazin, C. L., & Wik, D. R. 2013, ApJ, in preparation

Iapichino, L., Adamek, J., Schmidt, W., & Niemeyer, J. C. 2008, MNRAS, 388, 1079

Jaffe, W. J., & Rudnick, L. 1979, ApJ, 233, 453

Jeltema, T. E., & Profumo, S. 2011, ApJ, 728, 53

Johnston-Hollitt, M., & Ekers, R. D. 2004, arXiv:astro-ph/0411045

Kang, H., Ryu, D., & Jones, T. W. 2009, ApJ, 695, 1273

Kang, H., Ryu, D., & Jones, T. W. 2012, ApJ, 756, 97

Kempner, J. C., & Sarazin, C. L. 2001, ApJ, 548, 639K

Kempner, J. C., Sarazin, C. L., & Ricker, P. M. 2002, ApJ, 579, 236

Keshet, U., Waxman, E., & Loeb, A. 2004, ApJ, 617, 281

Keshet, U., & Loeb, A. 2010, ApJ, 722, 737

Kim, K.-T., Kronberg, P. P., Dewdney, P. E., & Landecker, T. L. 1990, ApJ, 355, 29

Kim, K.-T., Kronberg, P. P., & Tribble, P. C. 1991, ApJ, 379, 80

Kushnir, D., Katz, B., & Waxman, E. 2009, Journal of Cosmology and Astroparticle Physics, 9, 24

Laing, R. A., & Bridle, A. H. 1987, MNRAS, 228, 557

Laing, R. A., Canvin, J. R., Cotton, W. D., Bridle, A. H., & Parma, P. 2006, Astronomische Nachrichten, 327, 533

Laing, R. A., Bridle, A. H., Parma, P., & Murgia, M. 2008, MNRAS, 391, 521

Lampton, M., Margon, B., & Bowyer, S. 1976, ApJ, 208, 177

Lane, W. M., Cotton, W. D., Helmboldt, J. F., & Kassim, N. E. 2012, Radio Science, 47

Law, C. J., et al. 2011, ApJ, 728, 57

Ledlow, M. J., & Owen, F. N. 1996, AJ, 112, 9

Ledlow, M. J., Voges, W., Owen, F. N., & Burns, J. O. 2003, AJ, 126, 2740

Macario, G., Venturi, T., Intema, H. T., et al. 2013, A&A, 551, A141

Marini, F., Bardelli, S., Zucca, E., et al. 2004, MNRAS, 353, 1219

Markevitch, M., Forman, W. R., Sarazin, C. L., & Vikhlinin, A. 1998, ApJ, 503, 77

Markevitch, M., Sarazin, C. L., & Vikhlinin, A. 1999, ApJ, 521, 526

Markevitch, M., Ponman, T. J., Nulsen, P. E. J., et al. 2000, ApJ, 541, 542

Markevitch, M., & Vikhlinin, A. 2007, Phys. Rep., 443, 1

Massey, R., Rhodes, J., Ellis, R., et al. 2007, Nature, 445, 286

Mazzotta, P., Edge, A. C., & Markevitch, M. 2003, ApJ, 596, 190

Mazzotta, P., & Giacintucci, S. 2008, ApJ, 675, L9

Miller, N. A., & Owen, F. N. 2003, AJ, 125, 2427

Morris, D., & Berge, G. L. 1964, AJ, 69, 641

Murgia, M., Govoni, F., Markevitch, M., et al. 2009, A&A, 499, 679

Murgia, M., Govoni, F., Feretti, L., & Giovannini, G. 2010, A&A, 509, A86

O'Sullivan, S. P., & Gabuzda, D. C. 2008, Extragalactic Jets: Theory and Observation from Radio to Gamma Ray, 386, 284

Orrú, E., Murgia, M., Feretti, L., et al. 2007, A&A, 467, 943

Owers, M. S., Nulsen, P. E. J., Couch, W. J., & Markevitch, M. 2009, ApJ, 704, 1349

Owers, M. S., Nulsen, P. E. J., & Couch, W. J. 2011, ApJ, 741, 122

Pedelty, J. A., Rudnick, L., McCarthy, P. J., & Spinrad, H. 1989, AJ, 98, 1232

Pizzo, R. F., de Bruyn, A. G., Feretti, L., & Govoni, F. 2008, A&A, 481, L91

Pizzo, R. F., & de Bruyn, A. G. 2009, A&A, 507, 639

Pizzo, R. F., de Bruyn, A. G., Bernardi, G., & Brentjens, M. A. 2011, A&A, 525, A104

Planck Collaboration, Ade, P. A. R., Aghanim, N., et al. 2013, A&A, 554, A140

Planck Collaboration, Ade, P. A. R., Aghanim, N., et al. 2013, A&A, 550, A134

Popping, A., & Braun, R. 2008, A&A, 479, 903

Pratt, G. W., Croston, J. H., Arnaud, M., Böhringer, H. 2009, A&A, 498, 361

Rau, U., & Cornwell, T. J. 2011, A&A, 532, A71

Rines, K., & Diaferio, A. 2006, AJ, 132, 1275

Rossetti, A., Dallacasa, D., Fanti, C., Fanti, R., & Mack, K.-H. 2008, A&A, 487, 865

Rossetti, M., Eckert, D., De Grandi, S., et al. 2013, A&A, 556, A44

Roy, S., Rao, A. P., & Subrahmanyan, R. 2005, MNRAS, 360, 1305

Rudnick, L., Saslaw, W. C., Crane, P., & Tyson, J. A. 1981, ApJ, 246, 647

Rudnick, L., Zukowski, E., & Kronberg, P. P. 1983, A&AS, 52, 317

Rudnick, L. 1988, ApJ, 325, 189

Rudnick, L. 2002, PASP, 114, 427

Rudnick, L. & Blundell, K. M. 2003, ApJ588, 143

Rudnick, L. & Blundell, K. 2004, in Proceedings of The Riddle of Cooling Flows in Galaxies and Clusters of Galaxies, eds. T. Reiprich, J. Kempner & N. Soker, published electronically at http://www.astro.virginia.edu/coolflow/proceedings/104.pdf

Rudnick, L., & Brown, S. 2009, AJ, 137, 145

Rudnick, L., & Lemmerman, J. A. 2009, ApJ, 697, 1341

Russell, H. R., van Weeren, R. J., Edge, A. C., et al. 2011, MNRAS, 417, L1

Ryu, D., Kang, H., Hallman, E., & Jones, T. W. 2003, ApJ, 593, 599

Ryu, D., Kang, H., Cho, J., & Das, S. 2008, Science, 320, 909

Sakelliou, I., & Ponman, T. J. 2006, MNRAS, 367, 1409

Santos, J. S., Rosati, P., Tozzi, P., et al. 2008, A&A, 483, 35

Sarazin, C. L. 1986, Reviews of Modern Physics, 58, 1

Sarazin, C. L. 2002, Merging Processes in Galaxy Clusters, 272, 1

Sarazin, C. 2006, Chandra Proposal, 2233

Saripalli, L. 2009, Astronomical Society of the Pacific Conference Series, 407, 131

Schnitzeler, D. H. F. M., Katgert, P., & de Bruyn, A. G. 2009, A&A, 494, 611

Shukurov, A., & Berkhuijsen, E. M. 2003, MNRAS, 342, 496

Simard-Normandin, M., & Kronberg, P. P. 1980, ApJ, 242, 74

Simard-Normandin, M., Kronberg, P. P., & Button, S. 1981, ApJS, 45, 97

Simmons, J. F. L., & Stewart, B. G. 1985, A&A, 142, 100

Small, T. A., Ma, C.-P., Sargent, W. L. W., & Hamilton, D. 1998, ApJ, 492, 45

Sokoloff, D. D., Bykov, A. A., Shukurov, A., Berkhuijsen, E. M., Beck, R., & Poezd, A. D. 1998, MNRAS, 299, 189

Stanimirovic, S. 2002, Single-Dish Radio Astronomy: Techniques and Applications, 278, 375

Sun, M., Murray, S. S., Markevitch, M., & Vikhlinin, A. 2002, ApJ, 565, 867

Taylor, A. N., Bacon, D. J., Gray, M. E., et al. 2004, MNRAS, 353, 1176

Taylor, A. R., Stil, J. M., & Sunstrum, C. 2009, ApJ, 702, 1230

Tian, J.-T., Yuan, Q.-R., Zhou, X., et al. 2012, Research in Astronomy and Astrophysics, 12, 1381

Tribble, P. C. 1991, MNRAS, 250, 726

Vacca, V., Govoni, F., Murgia, M., et al. 2011, A&A, 535, A82

van Weeren, R. J., Röttgering, H. J. A., Brüggen, M., & Hoeft, M. 2010, Science, 330, 347

van Weeren, R. J., Brüggen, M., Röttgering, H. J. A., et al. 2011, A&A, 533, A35

Vazza, F., Brunetti, G., Gheller, C., Brunino, R., & Brüggen, M. 2011, A&A, 529, A17

Venturi, T., Giacintucci, S., Brunetti, G., et al. 2007, A&A, 463, 937

Venturi, T., Giacintucci, S., Dallacasa, D., et al. 2008, A&A, 484, 327

Venturi, T., Giacintucci, S., Dallacasa, D., et al. 2013, A&A, 551, A24

Walker, S. A., Fabian, A. C., Sanders, J. S., George, M. R., & Tawara, Y. 2012, MNRAS, 422, 3503

Wall, J. V. 1996, QJRAS, 37, 519

Wardle, J. F. C., & Kronberg, P. P. 1974, ApJ, 194, 249

Way, M. J., Quintana, H., & Infante, L. 1997, arXiv:astro-ph/9709036

Whitaker, K. E., Kraft, R. P., Posson-Brown, J., Jones, C., & Donnelly, R. H. 2003, Bulletin of the American Astronomical Society, 35, 1282

Wolleben, M., Landecker, T. L., Hovey, G. J., Messing, R., Davison, O. S., House, N. L., Somaratne, K. H. M. S., & Tashev, I. 2010, AJ, 139, 1681

Willson, M. A. G. 1970, MNRAS, 151, 1

Young, A. 2004, PhD. Thesis, University of Minnesota

Zavala, R. T., & Taylor, G. B. 2002, ApJ, 566, L9

ZuHone, J. A., Markevitch, M., Brunetti, G., & Giacintucci, S. 2013, ApJ, 762, 78